Ferromagnetism in Wide Band Gap Materials: Mn-ZnO and Mn-Si_3N_4 Thin Films

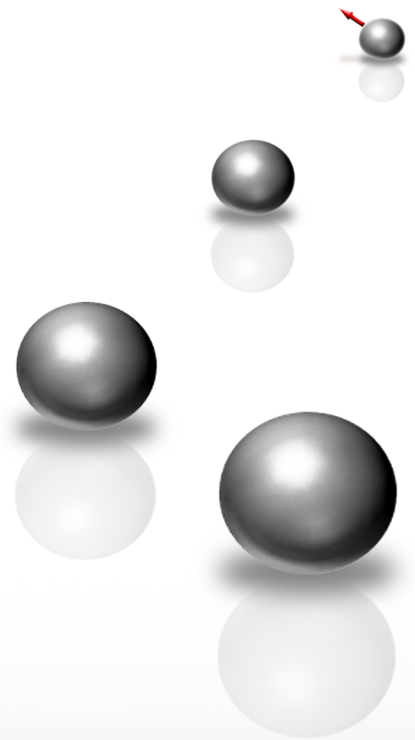

Eva Céspedes Montoya

FERROMAGNETISM IN WIDE BAND GAP MATERIALS:

Mn-ZnO AND Mn-Si_3N_4 THIN FILMS

(Ferromagnetismo en Materiales de Gap Ancho: Láminas Delgadas de Mn-ZnO y Mn-Si_3N_4)

Memoria presentada para optar al grado de Doctora en Física por:

EVA CÉSPEDES MONTOYA

Tesis dirigida por:

Prof. Carlos Prieto de Castro

Tutora:

Prof. Luisa E. Bausá López

Departamento de Física de Materiales

Facultad de Ciencias

Universidad Autónoma de Madrid

Instituto de Ciencia de Materiales de Madrid

Consejo Superior de Investigaciones Científicas

Septiembre de 2009

Summary

This dissertation is the result of a four-year doctorate on the ferromagnetism of Mn-based wide band gap thin film materials prepared by sputtering, performed at the Instituto de Ciencia de Materiales de Madrid (ICMM) under the supervision of Prof. Carlos Prieto.

The first part of this work is aimed at the study of the Mn-ZnO system. The interface-related properties as well as the influence of the particular manganese oxidation process during growth in the ferromagnetism of this system are analysed.

The second part deals with the novel Mn-Si_3N_4 system, which has been firstly studied here, reporting room temperature ferromagnetism. The origin of its ferromagnetism is ascribed to the stabilization of a slightly distorted Mn_3N_2, one of the main contributions of this research.

Finally, the work is completed with investigations of the Au nanoparticles growth in both ZnO and Si_3N_4 matrix materials.

Keywords: wide band gap semiconductors, diluted magnetic semiconductors, DMS, ferromagnetic oxides, ferromagnetic nitrides, multilayers, thin films, sputtering, XAS, XANES, EXAFS, II-VI semiconductors, MnZnO, interface, Mn oxidation state, manganese nitride, Mn_3N_2, gold nanoparticles.

Resumen

El trabajo presentado en esta memoria de Tesis Doctoral se centra en el estudio del ferromagnetismo en materiales de gap ancho preparados en forma de lámina delgada mediante la técnica de sputtering.

La primera parte de la memoria está dedicada al estudio del sistema Mn-ZnO. Se analizan varios factores relacionados con el ordenamiento magnético del sistema, como el papel que juegan las distintas intercaras y el efecto de la oxidación o reducción del manganeso durante el proceso de crecimiento.

En la segunda parte de la memoria se investiga el sistema Mn-Si_3N_4, estudiado por primera vez en este trabajo, con la observación de ferromagnetismo a temperatura ambiente. El origen del ferromagnetismo en este sistema se ha explicado por la existencia de una fase de tipo Mn_3N_2 ligeramente distorsionada.

Finalmente, el trabajo se completa con el estudio de la formación de nanopartículas de Au en ambas matrices, ZnO and Si_3N_4.

Palabras clave: semiconductores de gap ancho, semiconductores magnéticos diluidos, DMS, óxidos ferromagnéticos, nitruros ferromagnéticos, multicapas, láminas delgadas, sputtering, XAS, XAS, XANES, EXAFS, semiconductores II-VI, MnZnO, intercara, estado de oxidación de Mn, nitruro de manganeso, Mn_3N_2, nanopartículas de Au.

As a result of the work described in this dissertation, the following papers have been published:

- *Correlation between Mn oxidation state and magnetic behaviour in Mn/ZnO multilayers prepared by sputtering.*
  E. Céspedes, J. Garcia-Lopez, M. García-Hernández, A. de Andrés and C. Prieto, J. Appl. Phys. 102, 033907 (2007).

- *High temperature ferromagnetism in Mn based multilayers of wide gap semiconductors: Mn/ZnO and Mn/SnO_2: the role of interfaces.*
  A. Espinosa, E. Céspedes, C. Prieto, M. García-Hernández and A. de Andrés, J. Korean Phys. Soc 52, 5 (2008).

- *Mn local order in room-temperature ferromagnetic Mn/ZnO multilayers.*
  E. Céspedes, G. R. Castro, F. Jiménez-Villacorta, A. de Andrés and C. Prieto, J. Phys.: Condens. Matter 20, 095207 (2008).

- *X-ray absorption and magnetic circular dichroism characterization of a novel ferromagnetic MnN_x phase in Mn-Si_3N_4 multilayers.*
  E. Céspedes, Y. Huttel, L. Martínez, A. de Andrés, J. Chaboy, M. Vila, N. D. Telling, G. van der Laan and C. Prieto, Appl. Phys. Lett. 93, 252506 (2008).

- *Evolution of ferromagnetism with sputtering gas in Mn:ZnO films.*
  E. Céspedes, J. Sánchez-Marcos, J. García-López and C. Prieto, J. Magn. Magn. Mater.(2009), doi:10.1016/j.jmmm.2009.05.038.

- *Induced ferromangetism in Mn_3N_2 phase embedded in Mn/Si_3N_4 multilayers.*
  E. Céspedes, E. Román, Y. Huttel, J. Chaboy, F. J. García-López, A. de Andrés and C. Prieto, J. Appl. Phys. 106, 043912 (2009).

- *Au layer growth on amorphous Si_3N_4.*
  E. Céspedes, D. Babonneau, O. Lyon, S. Rouzière, C. Prieto, L. Olivi and A. Traverse, J. Appl. Phys. (2009) (submitted).

Additional publications in different related fields are:

- *Brillouin Light Scattering Characterization of the Surface Acoustic Waves Velocity in the ZnO/ Si_3N_4/Si(100) System.*
  E. Céspedes, R. J. Jiménez-Riobóo, M. Vila and C. Prieto, Superlattices and Microstructures 39, 75-82 (2006).

- *Interface and Mn valence effects in ferromagnetic insulating multilayers based on Mn and tin oxide.*
  A. Espinosa, E. Céspedes, C. Prieto, M. García-Hernández, J. Rubio-Zuazo and A. de Andrés, J. Appl. Phys. 103, 07D129 (2008).

- *Microstructural properties and local order around iron in granular metal-insulator Fe/Si_3N_4 granular systems prepared by magnetron sputtering.*
  A. Espinosa, E. Céspedes, C. Prieto, M. García-Hernández, J. Rubio-Zuazo and A. de Andrés, J. Appl. Phys. 103, 07D129 (2008).

- *Neutron diffraction and X-ray absorption spectroscopy study of complex oxygen deficient manganites.*
  R. Cortés-Gil, M. Hernando, M. L. Ruiz-González, E. Céspedes, C. Prieto, J. M. Alonso, M. Vallet-Regí, A. Hernando, J. M. González-Calbet, Chemistry-A European Journal 14, 9038 (2008).

A mi madre

A la memoria de mi padre

"Ciencia es aquello sobre lo cual cabe siempre discusión"

José Ortega y Gasset

Contents

Chapter 1

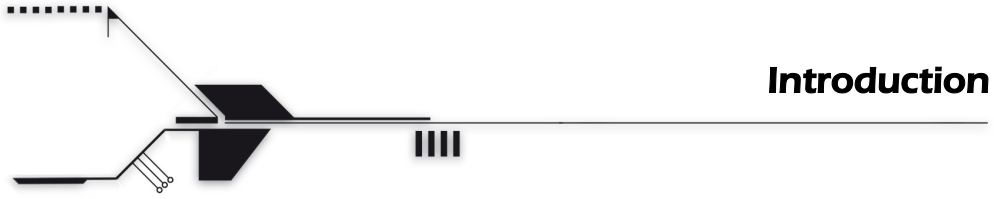

Introduction

1.1. State of the art

The theoretical prediction and observation of room temperature ferromagnetism (RTFM) in doped transition metal semiconductors is one of the most interesting and provocative scientific developments of the early 21st century.[1]

The most common approach to drive a semiconductor ferromagnetic is that of diluted magnetic semiconductors (DMSs). DMSs refer to materials obtained by doping a non-magnetic semiconductor with a few atomic percent of transition metal (TM) elements (e.g. V, Cr, Mn, Fe, Co, Ni and Cu), including TM-doped III-V (GaAs, InAs), II-VI (CdTe) or group IV (Ge and Si) types. In an actual DMS, TM cations are randomly distributed inside the semiconductor lattice, replacing a fraction of the cations of the host. In these materials, the presence of the 3d magnetic ions influences the free carrier behaviour through the sp-d exchange interaction between the localized magnetic moments and the spins of the itinerant carriers, which are introduced either by the magnetic dopant or by some secondary electronic dopant.[1,2,3]

DMSs are promising materials for applications as well as interesting from the basic-physics point of view. Possible applications exist in spin electronics (*spintronics*), which employ the spin degree of freedom of electrons in addition to their charge. This may allow the integration of data processing and magnetic storage on a single device called "*spintronic device*". This new class of spintronics devices includes spin-valves, transistors, spin light emitting diodes, non-volatile memories, magnetic sensors, etc.[1,4] Since the electronic spin is a quantum mechanical degree of freedom, the exploit of quantum interference effects in these devices could eventually lead to the design of quantum computers. The search of new materials becomes essential for both

fundamental research and practical applications.[2,5]

However, most DMSs have a low Curie temperature (T_C), which totally limits their use in practical applications. In 2000, Dietl. et al.[6] employed the original Zener model of ferromagnetism[7] to theoretically predict stable ferromagnetism and T_C values that exceeded room temperature (RT) for DMSs based on wide band gap semiconductors, i.e., ZnO and GaN, containing 5% of Mn and high hole concentration ($3.5x10^{20}$ cm^{-3}). In addition, using first-principle calculations, Sato et al.[8] theoretically showed that a ZnO matrix doped with TM atoms such as V, Cr, Fe, Co and Ni exhibited FM ordering, whereas doping with Ti and Cu resulted in a paramagnetic state, what opened a window for experimental attempts to prepared DMSs with RTFM.

Since the appearance of the Diet. et al.[6] publication, remarkable progress has been made on the realization of materials with T_C values above RT.

Ferromagnetic semiconductors with O^{2-} anions, such as TM-doped ZnO, TiO_2 or SnO_2 are also termed diluted magnetic oxides (DMOs).

Oxide semiconductors have many advantages in comparison with non-oxide semiconductors: i) wide band gap suitable for short wavelength light applications, ii) transparency and simple colouring with pigments, iii) high n-type carrier concentrations, iv) capability to be grown at low temperatures even on plastic substrates, v) ecological safety and durability and vi) low cost. In addition, strong electronegativity of oxygen is expected to produce strong p-d exchange coupling between band carriers and localized spins, pointed as an important characteristic of DMS. [9]

There are two major criteria for selecting the most promising materials for semiconductor spintronics. First, as it has been mentioned, the FM should be retained at practical temperatures, that is, above 300 K, and second, it is a major advantage if there is existing technology for the material in other applications. Fortunately, TM-doped ZnO satisfies the two criteria. TM-doped ZnO has been intensively investigated in the last years to achieve RTFM and promising magneto-transport properties.[1,2,3,10] As a low cost, wide band gap (Eg = 3.37 eV) semiconductor, ZnO itself has been focus of renewed

research applications such as UV light emitters, transparent high-power electronics, surface acoustic-wave devices, piezoelectric transducers and solar cells.[3]

So far, RTFM has been reported in ZnO samples doped with TM elements such as Sc,[11,12] Ti,[11,13] V,[14] Cr,[11,15,16] Mn,[17,18,19,20,21,22,23,24] Fe,[25,26] Co,[11,27,28,29,30] Ni[31] and Cu[32,33] for which Mn- and Co-doped ZnO are the most popular systems.

In particular, the doping of ZnO with Mn is of special interest because Mn^{2+} has the highest possible magnetic moment with the 3d band with 5 electrons among the 10 available states, creating a stable fully polarized state.[10] Furthermore, Mn metal is not ferromagnetic; it is well known to be antiferromagnetic as well as the standard manganese oxides (MnO, Mn_2O_3 and MnO_2) except Mn_3O_4 which is ferrimagnetic with T_C about 45 K,[10] what allows to discard RTFM due to the this type of precipitates in this system.

The rapid increase of the works around the world dealing with DMSs makes very difficult to summarize the progress in these multi-functional materials. Nonetheless, it should be noted that despite the large exploration performed in this field up to now, the fundamental scientific issues in these materials are still many:

First, observations of RTFM in transition metal doped oxide semiconductors are numerous. However, in spite of the great efforts, there is no firm conclusion whether ferromagnetism is an intrinsic material property or comes from the clustering of magnetic impurities, formation of secondary ferromagnetic phases, etc. Furthermore, evidences of RTFM haven been recently reported even in undoped ZnO.[34]

To date, there is no firm theoretical explanation of why and how magnetism in DMS materials works and there are controversies about the conditions required to achieve long-range magnetic order in these materials. The role of the carriers mediating ferromagnetism is equally unclear, and RTFM has been reported from highly conductive to highly insulating materials.[1,2,3]

The most popular mechanisms suggested for magnetic ordering in TM-doped ZnO are carrier-mediated exchange (electron an hole carriers),[3,6,10,35,36] and the bound magnetic polaron (BMP)[27,35] model respect to defects, including oxygen vacancies (V_O),

Zn interstitial (Zn_i) and Zn vacancies (V_{Zn}).

Early publications generally favoured carrier exchange interactions, which are characterized by strong coupling between localized d electrons of TM ions and the extended sp carriers of ZnO. The term carrier-mediated exchange refers to interactions between localized magnetic moments that are mediated by free carriers in the system, which can be divided into three cases: the Rudermann-Kittel-Kasuya-Yosida (RKKY) interaction, Zener carrier-mediated exchange and Zener double-exchange. RKKY interaction formally describes the magnetic exchange between a single localized magnetic moment and a free electron gas.[3,10] Zener carrier-mediated exchange proposes that FM ordering is driven by a decrease in carrier energy due to redistribution between spin sub-bands split by the exchange interaction.[6] Finally, the Zener double-exchange model refers to indirect coupling mediated by oxygen atoms between neighbouring ferromagnetic ions in different states.[3,36]

In addition, the observation of RTFM in insulating TM-ZnO led to elucidate the BMP mechanism,[27] where the ferromagnetic exchange coupling in diluted n-type oxides is based on the tendency of these materials to form shallow donors.

An electron associated with a particular defect will be confined in a hydrogenic orbital of radius r_H. As the donor concentration decreases, the 1s orbitals overlap to form an impurity band. The model is based on the interaction of the magnetic cations with the hydrogenic electrons in the impurity band. By coupling the localized 3d moments of the cations within the donor orbits, the donors tend to form bound magnetic polarons. A BMP is hence a quasi-particle comprised of the localized carrier and the magnetic cations encompassed within its radius, where the exchange interaction tends to align the moments parallel to one another inside the BMP. The basic idea is illustrated in Fig. 1.1, similarly to the reported in Ref. 27. The cations present an extra random potential, which extends the localized regions as the concentration of cations increases. Provided the radius of the BMP sufficiently large, overlapping BMPs become correlated and their spins align, producing long-range ferromagnetic interactions.

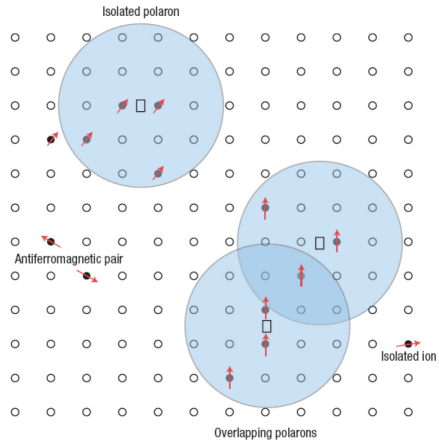

Fig. 1.1 Representation of bound magnetic polarons. An electron bound within its hydrogenic orbital couples to magnetic impurities causing them to align parallel to one another inside the orbit radius. Cation sites are represented by small circles. Oxygen is not shown and the unoccupied oxygen sites are represented by squares. The figure is drawn for a magnetic cation concentration of 0.1.

Many points and mechanisms have been additional proposed to explain the ferromagnetic ordering in these systems. For instance, it has been proposed that ferromagnetism originated at the interface ZnO/MnO_2 by Zn diffusion into the manganese oxide grains, which acts as a retardant of the $MnO_2 \rightarrow Mn_2O_3$. In this case, ferromagnetism is related to double-exchange between Mn^{3+} and Mn^{4+}, where not only coexistence of both cations is necessary but also the presence of Zn cations.[19,37]

In addition, a FM $Mn_{2-x}Zn_xO_{3-\delta}$ metastable phase has been proposed as the origin of the high-temperature FM in the Mn-Zn-O system.[17]

More recently, N. Sanchez et al.[38] have theoretically explored how the surface affects the magnetic order in diluted magnetic oxides. They have shown that the surface enhances the spin polarization induced by Co atoms, and additionally, even in the absence of magnetic ions, it promotes the formation of a p-derived extended magnetic state which has no counterpart in bulk.

From the experimental point of view, it is hard to characterize and quantitatively analyze the nature of RTFM because so many factors affect the magnetic behaviour of TM-doped ZnO. It is clear that the local structure and the magnetic behaviour of TM-

doped ZnO are strongly sensitive to preparation parameters. The sample preparation procedure, structural defects, sample shape, substrate effect, transport properties, and other important variables should be taken into account to clarify the variety of contradictory results reported for these materials.[3,4]

Most of the results reported on RTFM in wide band gap semiconductors deals with thin film materials. TM-doped ZnO films are commonly deposited by pulsed-laser deposition (PLD), magnetron sputtering (including direct current (DC), reactive and radio-frequency (RF)), molecular beam epitaxy (MBE), chemical vapor deposition (CVD), ion-beam implantation, sol-gel methods, etc. Although it is known that the magnetic behaviour of TM-doped ZnO films is sensitive to the deposition conditions, there is not conclusion on which deposition method is best for achieving RTFM in the films. For that reason, magnetron sputtering technique is increasingly popular for preparing TM-doped ZnO films owing to its low cost, high efficiency, easy control and its production of uniform films of large size.[3]

1.2. Outlook of this dissertation

The main goal of this work was to prepare and to investigate wide band gap materials that could exhibit room temperature ferromagnetism.

- Prompted by all the promising reports regarding the Mn-Zn-O system as well as the actual controversy on the origin of its ferromagnetic behaviour, a large part of this work was focussed on the study of Mn-Zn-O thin films. A double outcome was proposed here: one was to fabricate specific samples to get further knowledge of the factors involved in the reported ferromagnetism, in particular, the interface-related properties and the role of the actual manganese oxidation state. The other was to obtain actual DMS thin films based on Mn:ZnO showing RTFM for low concentrations of Mn.
- Besides the study of largely investigated ferromagnetic oxides, another important goal of this dissertation was the research of new ferromagnetic wide band gap

materials. With this motivation, the Mn/Si_3N_4 system has been studied here for the first time, reporting RTFM. The explanation in terms of a distorted non-centrosymmetric Mn_3N_2 phase constitutes one of the main novelties of this work.

- In addition, the increasing scientific attention on noble metal nanoparticles systems together with the acquired knowledge on ZnO- and Si_3N_4-based materials prompted us to complete this work with the study of Au NPs embedded in these wide band gap matrices, showing the multiple possibilities of these multifunctional materials.

A fact of great importance for the understanding of the nature of the observed RTFM in these complex systems is to perform comprehensive structural studies. Details characterizations of these materials are fundamental to find defensible structure-function relationships to contribute to clarify the actual debate on the origin of their magnetic properties, since in many cases contradictory experimental results are due to insufficient studies. A key requirement in elucidating RTFM in Mn-doped ZnO is to judge whether the magnetism originates from substitutional dopants on Zn sites or form the formation of a second ferromagnetic phase. It should be highlighted at this point that more than 10 experiments using synchrotron radiation techniques were carried out along this dissertation to obtain precise information on the Mn electronic properties and on the local environment of Mn in the prepared samples. Furthermore, a variety of characterization techniques was used in each particular study.

1.3. Dissertation structure

A brief introduction of this dissertation is given in Chapter 1, showing the state of the art in the field of diluted magnetic semiconductors and the main goals of this work.

The experimental procedure, including sample preparation method and characterization techniques is explained in Chapter 2. A summary of the families of samples studied in this dissertation and a scheme of the experimental procedure are given at the end of that chapter.

Regarding the experimental results of the studied systems, this thesis consists of three main parts:

- Part I, which is composed by Chapters 3, 4 and 5, is aimed at the study of the promising Mn-Zn-O system. Chapters 3 and 4 deal with the exploration of the interface-related properties in relation to the ferromagnetism in the system. To understand the influence of the particular manganese oxidation process during growth, two different approaches have been done: fabrication and characterization of Mn/ZnO multilayers, studied in Chapter 3, and of MnO_x/ZnO multilayers, in Chapter 4. On the other hand, Chapter 5 is based on the preparation of actual Mn:ZnO DMS films doped with approximately 5% at. Mn (labelled as $Zn_{0.05}Mn_{0.95}O$ films), where Mn^{2+} cations are expected to replace Zn^{2+} cations in the ZnO lattice. In this case, the working gasses during deposition process have been altered in order to modify the magnetic properties and to get further knowledge of the origin of the expected RTFM.

  In addition, thermal post-deposition treatments have been performed to study the effect on the ferromagnetic response. Annealing of the samples studied in Chapters 4 and 5 are treated within each chapter, while the effect of thermal treatments, as well as the substrate temperature effect, on the Mn/ZnO multilayers is shown in Appendix A, which has been included at the end of Part I.

  Details of the ZnO crystal structures are given in Appendix B, at the end of Part I, following the Appendix A.

- Part II (Chapter 6) deals with the study of two different Mn/Si_3N_4 multilayer series. It is shown the induced ferromagnetism in Mn_3N_2 phase embedded in the prepared Mn/Si_3N_4 multilayers and the evolution of the ferromagnetic response within the sample series in terms of the stabilized Mn_3N_2 phase.

- Finally, the growth of Au nanoparticles embedded in both ZnO and Si_3N_4 systems

has been included as Appendix C. The study of Au/Si_3N_4 multilayered samples and the evolution of the Au-layer morphology with the deposited Au amount have been shown in Appendix C.1, while similar studies for the Au/ZnO multilayer samples have been included in Appendix C.2.

A motivation for each particular study has been given at the beginning of each chapter. The general conclusions drawn from the current work have been summarized at the end of this dissertation and the references used in this thesis have been included at the end of each chapter.

References

[1] S. A. Chambers, *"Ferromagnetism in doped thin-film oxide and nitride semiconductors and dielectrics"*, Surface Science Reports 61, 345 (2006).

[2] S. J. Pearton, W. H. Heo, M. Ivill, D. P. Norton and T. Steiner, Topical Review: "*Diluted magnetic semiconducting oxides*" Semicond. Sci. Technol. 19 R59 (2004).

[3] F. Pan, C. Song, X. J. Liu, Y. C. Yang and F. Zeng, "*Ferromagnetism and possible application in spintronics of transition-metal-doped ZnO films*", Mat. Science and Engeneering R 62, 1-35 (2008).

[4] G. Peleckis, Doctoral Thesis *"Studies on diluted magnetic semiconductors for spin electronic applications"*, University of Wollongong (2006).

[5] C. Timm, Topical Review: "*Dissorder effects in diluted magnetic semiconductors*", J. Phys.: Condens. Matter 15, R1865 (2003).

[6] T. Dietl, H. Ohno, F. Maksukura, J. Cibert, and D. Ferrand, Science 287, 1019 (2000).

[7] C. Zener, Phys. Rev. 81, 440 (1950).

[8] K. Sato and H. Katayama-Yoshida, Jpn. J. Appl. Phys. 39, L555 (2000).

[9] T. Fukumura, Y. Yamada, H. Toyosaki, T. Hasegawa, H. Koinuma, M. Kawasaki, "*Exploration of oxide-base diluted magnetic semiconductors toward transparent spintronics*" Appl. Surf. Sci. 223, 62 (2004).

[10] C. Liu, F. Yun and H. Morkoç, "*Ferromagnetism of ZnO and GaN: a Review*", J. Mater. Sci.: Mater. Electron.16, 555 (2005).

[11] M. Venkantesan, C. B. Fitzgerald, J. G. Lunney and J. M. D. Coey, Phys. Rev. Lett. 93, 177206 (2004).

[12] J. M. D. Coey, M. Venkantesan, C. B. Fitzgerald, L. S. Dorneles, P. Stamenov and J. G. Lunney, J. Magn Magn. Mater. 290, 1405 (2005).

[13] L. S. Dorneles, D. O'Mahony, C. B. Fitzgerald, F. McGee, M. Venkantesan, I. Stanca, J. G. Lunney and J. M. D. Coey, Appl. Surf. Sci. 248, 406 (2005).

[14] N. H. Hong, J. Sakai and A. Hassini, J. Appl. Phys. 97, 10D312 (2005).

[15] K. Ueda, H. Tabata and T. Kawai, Appl. Phys. Lett. 79, 988 (2001).

[16] H. Liu, X. Zhang, L. Li, Y. X. Wang, K. H. Gao, Z. Q. LiR. K. Zheng, S. P. Ringer, B. Zhang and X. X. Zhang, Appl. Phys. Lett. 91, 072511 (2007).

[17] D. C Kundaliya, S.B. Ogale, S.E. Lofland, S. Dhar, C.J. Metting, S.R. Shinde, Z. Ma, B. Varughese, K.V. Ramanujachary, L. Salamanca-Riba, and T. Venkatesan, Nat. Mater. 3, 709 (2004).

[18] V.K. Sharma, G.D. Varmaa, J. Appl. Phys. 102, 056105 (2007).

[19] M. A. García, M. L. Ruiz-González, A. Quesada, J. L. Costa-Krämer, J. F. Fernández, S. J. Khatib, A. Wennberg, A. C. Caballero, M. S. Martín-González, M. Villegas, F. Briones, J.M. González-Calbet, and A. Hernando, Phys. Rev. Lett. 94, 217206 (2005).

[20] R. Sanz, J. Jensen, G. González-Díaz, O. Martínez, M. Vázquez and M. Hernández-Vélez, Nanoscale Res. Lett. 4, 878 (2009).

[21] W. Xu, Y. Zhou, X. Zhang, D. Chen, Y. Xie, T. Liu, W. Yan, and S. Wei, Solid State Commun. 141, 374 (2007).

[22] J-H Guo, A. Gupta, P. Sharma, K. V. Rao, M. A. Marcus, C. L. Dong, J. M. O. Guillen, S. M. Butorin, M. Mattesini, P. A. Glans, K. E. Smith, C. L. Chang, and R. Ahuja, J. Phys.: Condens. Matter 19, 172202 (2007).

[23] J. H. Kim, H. Kim, D. Kim, Y. E. Ihm, W. K. Choo, J. Appl. Phys. 92, 6066 (2002).

[24] J. C. A. Huang, H. S. Hsu, J. H. Sun, S. L. Chiu, C. H. Lee, Y. F. Liao, and H. Chou, J. Appl. Phys. 103, 07D128 (2008).

[25] J. M. D. Coey, A. P. Douvalis, B. Fitzgerald and M. Venkantesan, Appl. Phys. Lett. 84, 1332 (2004).

[26] X. X.Wei, C. Song, K. W. Geng, F. Zeng, B. He and F. Pan, J. Phys.: Condens. Matter 18, 7471 (2006).

[27] J. M. D. Coey, M. Venkantesan and C. B. Fitzgerald, Nat. Mater. 4, 173 (2005).

[28] A. B. Pakhomov, B. K. Roberts, and K. M. Krishnan, Appl. Phys. Lett. 83, 4357 (2003).

[29] Z. Jin, T. Fukumura, M. Kawasaki, K. Ando, H. Saito, T. Sekiguchi, Y. Z. Yoo, M. Murakami, Y. Matsumoto, T. Hasewaga, H. Koinuma, Appl. Phys. Lett 78, 3824 (2001).

[30] Q. Liu, C. L. Gan, C. L. Yuan, G. C. Han, Appl. Phys. Lett. 92, 032501 (2008).

[31] X. Liu, F. Lin, L. Sun, W. Cheng, X. Ma and W. Shi, Appl. Phys. Lett. 88, 062508 (2006).

[32] D. B. Buchholz, R. P. H. Chang, J. H. Song and J. B. Ketterson, Appl. Phys. Lett. 87, 082504 (2005).

[33] C. Sudakar, J. S. Thakur, G. Lawes, R. Naik and V. M. Naik, Phys. Rev. B 75, 054423 (2007).

[34] A. Sudaresan, R. Bhargavi, N. Rangarajan, U. Siddesh, and C. R. Rao, Phys. Rev. B 74, 161306 (2006).

[35] M. J. Calderon and S. Das Sarma, Annals of Physics 322, 2618 (2007).

[36] R. Janish, P. Gopal, N. A. Spaldin, J. Phys.: Condens. Matter 17, R657 (2005).

[37] A. Quesada, M. A. García, P. Crespo and A. Hernando, J. Magn. Mag. Mat. 304, 75 (2006).

[38] N. Sanchez, S. Gallego, and M. C. Muñoz, Phys. Rev. Lett. 101, 067206 (2008).

Chapter 2

Thin Film Preparation Method and Experimental Techniques

2.1. Sputtering technique

Sputtering is defined as the removal of near surface atoms from a target by energetic particle bombardment. The process was firstly reported by W. R. Grove in 1853, who observed metallic deposition within a discharge tube. However, it took over 50 years until Goldstein showed that the deposition within the discharge tube was caused by positive ions from the discharge bombarding the cathode. Nowadays, the sputtering process is a widely used method for deposition of thin films and functional coatings as for surface cleaning.[1,2,3]

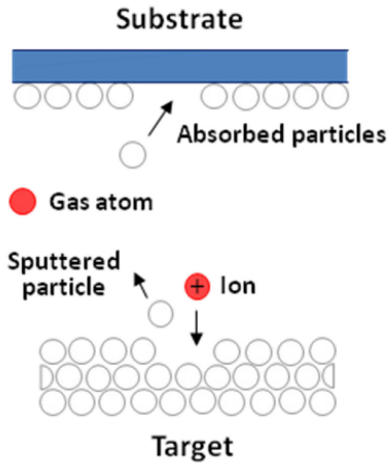

Fig. 2.1 Sputtering process scheme. Positive ions from a gas discharge are accelerated towards a target and create upon impact an atomic collision cascade in which some of the atoms from the material can leave the target and subsequently condense onto a substrate.

The sputtering deposition method, schematized in Fig. 2.1, is a physical vapour deposition (PVD) process in which a bulk starting material (target) is eroded by a particle bombardment and subsequently deposited onto a substrate. In its simplest form, a target material is placed in a vacuum chamber filled with a particular process gas at a reduced pressure and set on a negative potential. The negative potential accelerates the few electrons present in the process chamber towards the grounded chamber wall. While traversing the chamber, the electrons collide with gas molecules and generate, if the electric field sufficient strong, electron-ion pairs. The ions from the electron-ion pairs are accelerated towards the target (cathode) and create upon impact with the target surface an atomic collision cascade in which some of the target material can be ejected from the target and subsequently condense onto the surrounding surfaces.

If the electrons were only generating new charged species in the discharge, the process would quickly extinguish since the generation of electron-ion pairs would take place closer and closer to the chamber wall and cease when eventually the last electron is collected at the chamber wall. However, while the ions are not able to create electron-ion pairs to the same extent as the electrons, upon impact with the target surface they create secondary emitted electrons which again are accelerated towards the chamber wall and ionize as well the gas molecules. If the number of secondary emitted electrons per incident ion times by the number of ions created in the discharge is greater or equal to one, the discharge becomes self-sustained. The described cathodic sputtering process is also called *DC sputtering*.

A disadvantage of the above described diode sputtering is the relatively low degree of ionization of the process gas. To increase the ionization and thereby the deposition rate, a magnetic field is commonly used to confine electrons in the discharge near the target surface and hence increase their ionization efficiency. This method, widely known as *magnetron sputtering* can, apart from increasing the deposition rate, also sustain a discharge at a lower pressure compared to non-magnetron sputtering. A low process pressure is usually desirable since the sputtered particles have a long mean free path in a low pressure discharge and can therefore retain some of the kinetic energy as they traverse the process chamber. The excess energy increases the surface diffusion of the

absorbed particles at the substrate surface which improved and in many cases promoted crystal growth and the quality of the deposited film. Typical working pressures of the sputtering process are in the 10^{-3}-10^{-2} mbar range.[2,4]

A significant drawback of *DC sputtering* is that the target must consist of a conducting material in order to avoid charging and therefore, materials of high resistivity cannot be DC sputtered. The reason is that if an isolating target material is set on a negative potential, the ion bombardment quickly charges up the surface of the target, eventually resulting in an electrical breakdown in the form of arcing. However, arcing can be avoided by using a radio frequency (RF) or pulsed DC bias.

RF sputtering is similar to *DC sputtering* except for the fact that alternating current discharges are sustained instead of DC discharges. In *RF sputtering*, the target self-biases to a negative potential, sputtering atoms by the positive ion bombardment. The electrons are more mobile than the ions and hence follow the periodic changes in the AC electric field much effectively. When the AC electrical signal is applied at the target, initially a large electron current is drawn followed by a small positive ion current making the net current flow different from zero over the complete period of one cycle. Net current flow cannot be different from zero as charge cannot be transferred through a capacitor and hence at the operating point of this cycle, the target self-biases to a negative potential – where no net current flows. A combination of capacitors and inductors is used to form an impedance matching network which maximizes the power delivery by forming an effective coupling of the RF power supply and the target. The impedances of materials with high resistivity that cannot be DC sputtered drop with increasing frequency and so, high frequencies pass current through dielectric targets. RF frequencies that can be employed range from 5 to 30 MHz. But the Federal Communications Commission has reserved a frequency of 13.56 MHz for the plasma processing techniques and so is the most widely used.[2,5]

The sputtering process is typically quantified by the total *sputtering yield* (S), defined as the statistical mean number of sputtered particles per incident particle. S depends on several factors related to the incident ion and target material. These factors include ion mass, ion energy, ion angle of incidence, atomic mass of target atoms, target

atomic structure (crystal orientation/lattice system and whether target is polycrystalline, amorphous, or comprised of a single crystal), target surface binding energy, and target texture. Sputtering yield tends to increase with increasing incident ion mass. At incident ion energies below the threshold energy, E_{th}, sputtering will not occur. Above E_{th}, sputtering yield generally increases with the incident ion energy. *S* also enhances with increasing target atomic masses, roughly correlated to the target atom's location on the periodic table. As well, *S* increases with the angle of incidence, from normal incidence ($\beta = 0°$) until approximately $\beta = 60°$ (30^o from glancing), reaching a value of zero at $\beta = 90°$. As the angle of incidence increases, more of the ion's energy gets deposited closer to the surface, until the ion is at near glancing incidence when the ion begins to be increasingly repulsed by the target surface atoms. Single crystal targets "tunnel" the collision cascade (due to the repeating crystal lattices) creating "spot pattern" distributions while amorphous and polycrystalline targets behave in a more isotropic manner. Microscopic surface features and texturing create localized changes in the angle of incidence from the bulk of the surface, changing the local yield. These features may "shadow" other areas of the surface (especially at oblique incidences) thus creating localized areas of reduced sputtering. Target materials with higher surface binding energies allow fewer atoms to be sputtered, thus lowering *S*.[5]

Thin film deposition of compounds can be performed by using a reactive working gas, what is called *reactive sputtering*. This is, however, a more complex process exhibiting a nonlinear behavior with respect to the main process parameters, such as the partial pressure of the reactive gas, the discharge power etc. Moreover, compound is not only formed on the substrate but also on the target surface (target poisoning) and if the targets enter the so called compound mode, in which a compound layer is fully formed on the surface of the target, the deposition rate substantially decreases since the process efficiency is generally lower for the compound than for the elemental material.

2.1.1. Experimental equipment

All the samples studied during this work have been prepared at the sputtering laboratory at the ICMM. The specific equipment used for the thin film sputtering deposition is shown in Fig. 2.2. It consists of a PLS 500 Pfeiffer high vacuum system, equipped with a TMH 520 turbomolecular pump, what allows a base pressure of about 10^{-7} mbar. A throttle valve between the vacuum chamber and the turbomolecular pump enables to lessen pumping rate. A PKR 251 Pirani-Penning combined sensor (10^{3}-10^{-9} mbar range) from Balzers Instruments is place at the deposition chamber for the pressure measurement.

A number of three Thin Film Consulting Gmbh planar magnetrons (2" diameter) are placed inside the experimental chamber, what allows the deposit of diverse materials. They can be operated by both PFG 1500-DC or PFG 300-RF power supplies (from Hüttinger Gmbh. Electronics) for conductive or high resistive materials, respectively. A matchbox operates coupled to the RF power supply at a frequency of 13.56 MHz. All the magnetrons have a water cooling system. Circular targets from the corresponding material (2" diameter and about 3 mm thickness) are mechanically clamped to the water-cooled electrodes.

Different gasses can be introduced inside the chamber by means of UFC 1200A mass flow controllers (MFCs) from UNIT Instruments. The purity of the gases, N_2, O_2, Ar, N_2/H_2 and Ar/H_2, is 99.999%. The different MFCs allow us to set the desired atmosphere during growth.

An additional small load-lock chamber is placed at the left side of the deposition chamber (see Fig. 2.2) in order to introduce the sample-holder and take it out without opening the main chamber. This secondary chamber, connected to the main chamber by a guillotine valve, is equipped with a mechanical pump, an IMR 260 Pirari sensor (from Balzers Instruments) and with a sample transfer bar.

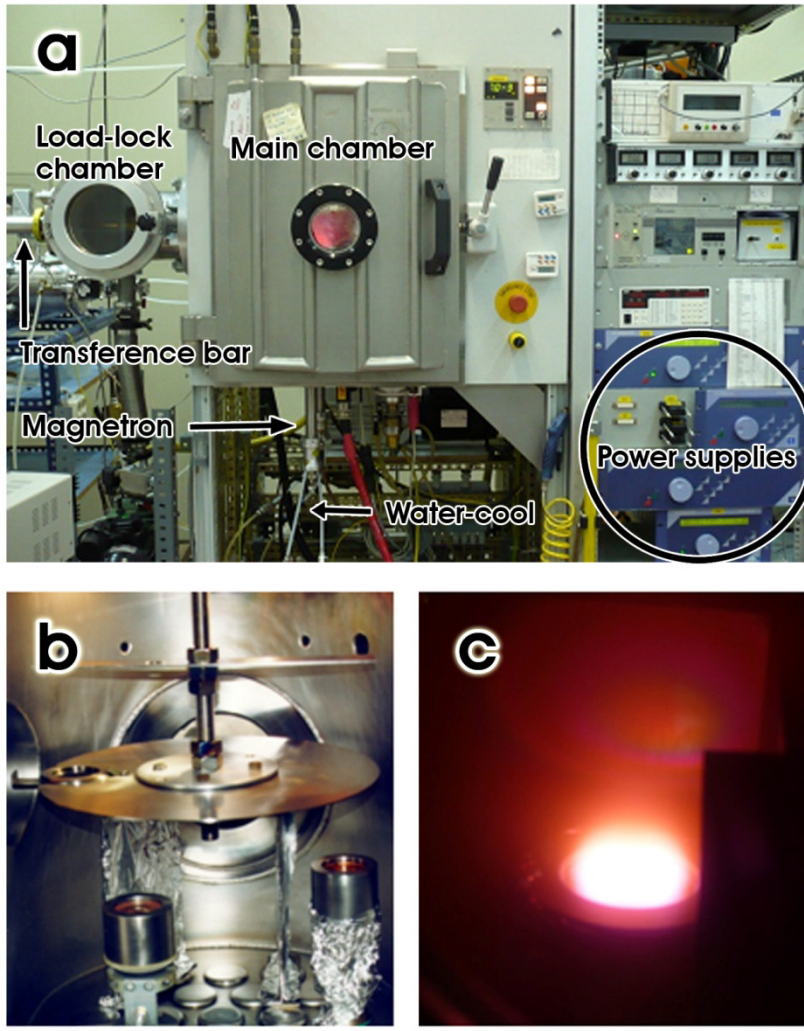

Fig. 2.2 (a) Sputtering experimental equipment from the sputtering laboratory at the ICMM used for the thin film deposition. (b) Inside of the main chamber, where the magnetrons and the rotatory disk (with the sample-holder inserted) can be observed. (c) Example of the sputtering process inside the main chamber.

The sample-holder, which is about 2" size, is introduced into the main chamber through the transfer bar and insert into a rotary disk placed at a distance of about 10 cm above the magnetron surfaces. The inside of the main chamber is shown in Fig. 2.2(b),

where the sample-holder disk and 3 magnetrons can be observed. Nitrogen plasma during a thin film sputtering deposition inside the described chamber can be seen in Fig 2.2(c).

The sputtering deposition process with this chamber was previously monitored by Dr. Angel Muñoz.[6] Thanks to these improvements, the system has a home-made software that allows to control the movement of the sample-holder disk (the substrate-holder can be alternatively from one magnetron source to another or to any pre-sputtering position), each sputtering or pre-sputtering time and the sputtering working gasses, removing the substrate-holder from each magnetron while changing the sputtering working gases during the preparation of two consecutive layers. Each layer thickness is controlled by its sputtering time, being each deposition rate previously calibrated by x-ray reflectivity measurements.

This monitored system is especially useful to prepare multilayers of different materials in a controlled way, fact that is of great importance in this work, where diverse multilayers series of different materials have been grown.

In addition, a 1.6" substrate-heater (SH-OX-R1C, from Blue Wave Semiconductors) can be also placed inside the sputtering chamber, what enables growing at a substrate temperature of about 600ºC.

In order to perform post-deposition thermal annealings of samples under controlled atmospheres, we have developed a specific chamber consisting of a vacuum quartz tube placed inside a furnace. The vacuum system of the quartz tube allows to reach a base pressure close to 10^{-6} mbar. Additionally, several MFCs permit to control the flow of different gasses inside the chamber. By means of this system, post-deposition annealings of different samples, either in vacuum or in oxygen atmosphere, have been carried out during this work.

A scheme of all the prepared samples along this work by means of the described sputtering equipment is shown in Fig. 2.6, at the end of this chapter. The prepared samples have been characterized by many different experimental techniques, including many synchrotron radiation experiments. Along this work SQUID, XRR, XRD, TEM,

RBS, NRA, XPS, XANES, EXAFS, XMCD, UV-Vis Absorption and GISAXS have been used for the thin film characterizations. In this chapter, a brief overview of several selected techniques is given. An outlook of the experimental procedures is given in the last part (Fig 2.7).

2.2. SQUID magnetometry

The magnetic characterization of samples was performed in a SQUID (Superconducting Quantum Interference Device) magnetometer (MPMS-5T from Quantum Design) at the ICMM facilities, in collaboration with Dr. Mar García Hernández. In some cases, a SQUID (MPMS-7T from Quantum Design) was employed for the magnetic measurements.

The SQUID is the most sensitive device available for measuring magnetic fields. The SQUID in the MPMS system does not detect the magnetic field from the sample directly. The measurement is performed in the MPMS instrument by moving the sample through the superconducting detection coils, which are located at the center of the superconducting magnet outside the sample chamber.[7,8] The detection coils are connected to the SQUID with superconducting wires, allowing the current from the detection coils to inductively couple to the SQUID sensor. As the sample moves through the detection coils, the magnetic moment of the sample induces an electric current in the detection coils. The detection coils, the connecting wires and the SQUID input coil form a closed superconducting loop. Any change in the magnetic flux in the detection coils produces a change in the persistent current in the detection circuit, proportional to the change in magnetic flux. Since the SQUID operates as highly linear current-to-voltage convertor, the variations in the current in the detection coils produce corresponding variations in the SQUID output voltage which are proportional to the magnetic moment of the sample. In a fully calibrated system, measurements of the voltage variation as the sample is moved through the detection coils provide a highly accurate measurement of the sample magnetic moment. The system can be accurately calibrated using a small piece of material having a known mass and magnetic susceptibility.

The Quantum Design MPMS-5T instrument with a superconducting magnet can be operated using fields up to 5 Tesla (the MPMS-7T model up to 7 Tesla) and measurements can be performed at temperatures ranging from 2 to 400 K. The system makes use of a second order derivative coil configuration to eliminate effects of stray fields. The sample chamber has low helium gas pressure, which provides thermal contact with a flow of gas outside the sample chamber pipe that is used to change and stabilize the temperature. Over 4.5 K flow impedance and a gas heater take care of the temperature control. The temperature is homogenized around the sample space by copper wires.

For the temperature dependence of magnetization, M(T), two kinds of measurements were done. In the zero field cooling measurement (ZFC) the sample was cooled down to 5 K in the absence of a magnetic field and a constant magnetic field was applied during the warm up scan (usually H = 1 kOe). In the field cooling (FC) measurements, the sample was cooled down to 5 K in the presence of the same constant magnetic field and then, a warm up scan was performed in the same magnetic field. Nonetheless, for the samples studied here, no appreciable differences were found between the ZFC and FC curves. The M vs. T curves shown here correspond generally to the FC ones.

For the hysteretic loop, M (H) measurements, the samples were subjected to a magnetic field cycling between +5 Tesla and -5 Tesla and magnetization was measured at a particular temperature (typically at 5 and 300 K).

2.3. X-Ray Diffraction (XRD)

X-ray diffraction (XRD) measurements have been performed in several Bruker D8 X-ray diffractometers from the ICMM diffraction service, by using the K_α radiation line of Cu, in order to obtain information about the structure and texture of the films. The prepared films are usually grown with textured grains. The grain size of the films in the out-of-plane direction has been obtained by measuring the full width at half maximal

(FWHM) intensity of the Bragg diffraction peak and using the Scherrer formula (Eq. 2.1)

$$l = \frac{0.9\lambda}{B\cos\theta} \tag{2.1}$$

where l is the crystallite size, λ is the wavelength of the x-radiation used, B is the peak width (in radians) due to particle size effect, and θ is the Bragg angle.

For selected samples, additional x-ray diffraction experiments have been carried out in a six-circle diffractometer especially designed for thin film characterization, using λ = 0.8857 Å, at SpLine, BM25B (Spanish CRG beamline) of the European Synchrotron Radiation Facility (ESRF), in Grenoble. In this case, apart from the usual θ-2θ diffractograms, grazing incidence (ω = 0.75°) experiments were performed in order to enhance the thin film signal and to avoid the strong peaks from the substrate.

2.4. X-Ray Reflectivity (XRR)

Additionally to the standard XRD characterization, X-ray reflectivity (XRR) measurements can be done by using well focused, monochromatic x-rays. XRR curves are possible due to the contrast in electronic density between film and air and between film and substrate (and also between layers in the case of multilayers).[9] In the hard x-ray region the refractive index n of the materials is smaller than unity. Considering the Snell equation, since the refractive index inside the material is now smaller than the one of air ($n_{air} = 1$), there will be an angle under which the x-rays are totally reflected. This angle is called the critical angle (θ_c) and it is dependent on the electronic density as:

$$\theta_c = \sqrt{\frac{4\pi\rho_e r_0}{k^2}} \tag{2.2}$$

$r_0 = e^2/mc^2$ is the classical electron radius, k is wave vector and ρ_e is the electronic density.

Above the critical angle, due to the interference between the x-ray beams scattered from the different interfaces it is possible to record a scan consisting of so-called thickness or

Kiessig fringes, i.e., intensity maxima corresponding to constructive interference and minima due to destructive interference. The position of these fringes is directly related to the thickness of the layers (d), which is in fact the Bragg equation but modified by the influence of refraction.

$$2d\sqrt{sin^2\theta_m - sin^2\theta_c} = m\lambda \tag{2.3}$$

where m is an integer.

Since, in most cases, the incident angle θ is sufficiently small, Eq (2.3) has the form:

$$\theta_m{}^2 - \theta_c{}^2 = m^2\left(\frac{\lambda}{2d}\right)^2 \tag{2.4}$$

This relation shows a simple method to determine the layer thickness from the measured reflectivity curve. Just by plotting the square of the angular positions of the intensity maxima versus the squares of the *Kiessig fringe* order. In the validity range of Eq. (2.4) it gives a straight line with the layer thickness d as slope.

Similarly to the case of a single layer, the modified Bragg law for the x-ray reflectivity of a periodic multilayer containing N periods, each consisting of a layer A with thickness t_A and a layer B with thickness t_B ; the multilayer period is $D = t_A + t_B$, can be written as:

$$2D\sqrt{sin^2\theta_m - sin^2\theta_c} = m\lambda \tag{2.5}$$

where m is an integer.

For incident angle θ sufficiently small, the equation can be simplified

$$\theta_m{}^2 - \langle\theta_c\rangle^2 = m^2\left(\frac{\lambda}{2D}\right)^2 \tag{2.6}$$

A experimental XRR spectrum from a multilayered prepared by sputtering is shown in Fig 2.3 as an example. On the experimental curve of a periodic multilayer stack, the following maxima can be resolved:

1) *Satellite maxima* (indicated by vertical arrows in the main part of Fig. 2.3), whose angular spacing depends on the multilayer period (D).

2) *Kiessig fringes* (indicated by vertical arrows in the inset of Fig. 2.3). Their period depends on the total multilayer thickness ($t = ND + t_C$), considering an additional capping layer of thickness t_C:

$$2ND\langle n\rangle sin\theta_t = p\lambda \tag{2.7}$$

where p is an integer.

If an additional capping layer is deposited on top, maxima corresponding to its thickness can be also observed. Knowing the position of these maxima, the corresponding thicknesses can be estimated using equations (2.5) and (2.7).

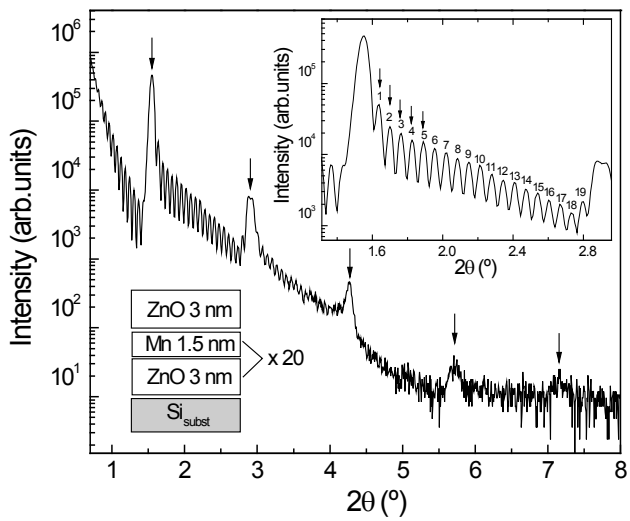

Fig. 2.3 XRR spectrum of a multilayered sample labelled as $[Mn_{(1.5nm)}/ZnO_{(3nm)}]_{20}$ (N = 20) measured on a Bruker D8 X-ray diffractometer using Cu K_α. Vertical arrows indicate the satellite maxima. The inset shows a zoom of the spectrum in the region between 2θ = 1.3º and 3º approximately, showing N-1 *Kiessig fringes* (vertical arrows) between two *satellite maxima*.

More sophisticated methods of simulating the reflectivity curves give more precise thickness values as well as information about the inter-layer roughness. For instance, XRR measurements of Mn/ZnO multilayers and their simulation by using the Xreal software developed by Dr. N. Telling can be found in section 3.4.

2.5. Rutherford Backscattering Spectroscopy (RBS)

Rutherford Backscattering Spectroscopy (RBS) is a quantitative elemental-analysis technique based on collisions between atomic nuclei (billiard-ball physics). RBS uses a monoenergetic beam of high energy ions (typically 2-3 MeV He^{2+}) to probe a thin film sample and detects those incident ions which are scattered back from sample nuclei. From the energy spectrum of the backscattered particles, elemental concentration and their depth profiles can be calculated. This technique is nondestructive since it does not sputter atoms from the surface.[2]

Each atom, when collided with an incident ion of known energy, will absorb a discrete amount of the energy from the incident ion (momentum transfer). Consequently, the incident ion backscatters at a lower energy that can be characterized by Rutherford backscattering to determine the elemental composition. This technique is very useful for measurements of low atomic number elements. Heavy elements withdraw little energy, so they are more difficult to resolve from each other, although the sensitivity for them is much higher since the backscatter cross-section increases as atomic number squared. Also, the RBS signal for atoms lighter than the substrate rides on the substrate background while heavier atoms are displayed by themselves.

The thickness of the film can be determined by the difference in backscattered ion energy. An ion that collides with an atom at the thin film surface will backscatter the ion with a different energy than when it collides with an atom deeper in the sample. In the latter case, the He ion will lose energy from the nucleus collision but also from the electron valence atoms from the sample when traveling into and out the sample before and after the scattering. Thus, the thicker the film, the broader in energy becomes the back-scattered peak that is evenly distributed through it, and variation in the peak height

with backscattering energy can be used to calculate depth profile with a resolution of about 10 nm.

Most of the RBS experiments described in this work were carried out at the Centro Nacional de Aceleradores (Sevilla, Spain) in collaboration with Dr. Javier García López in order to determine precisely the atomic composition of the samples. The experiments were done in a 3 MV Tandem accelerator, using a 2 MeV H^{2+} beam, with beam diameter ~ 1 mm and scattering angle of 165º.

Data analysis was usually performed through SIMNRA software,[10] which is up to now the most popular and refined one.

2.6. X-Ray Absorption Spectroscopy (XAS)

X-ray Absorption Spectroscopy (XAS) using synchrotron radiation is a well-established technique providing information on the electronic, structural and magnetic properties of matter. In XAS, a photon is absorbed by an atom, giving rise to the transition of an electron from a core state to an empty state above the Fermi level. The absorption cross-section depends on the energy and on the measured element. To excite an electron in a given core level, the photon energy has to be equal or higher than the energy of this core level. In XAS experiments, the photon energy is scanned from below to above this core-level energy. The energies of the absorption edges therefore correspond to the core-level energies, which are characteristic for each element, making x-ray absorption an element-sensitive technique. The $L_{3,2}$-edges are related to a 2*p* core level while the K-edge is related to a 1*s* core-level binding energy.

In general, two regions can be discerned in XAS: the near-edge region or XANES (X-ray Absorption Near-Edge Structure), which extends to an energy of the order of 50 eV above the edge and EXAFS (Extended X-ray Absorption Fine Structure), which is the oscillatory structure in the absorption coefficient whose amplitude is typically a few percent or less of the total absorption, and which extends over hundred of electron volts beyond the x-ray absorption edge. The spectral shape in the XANES region is determined by electron correlation and density of states (or multiple scattering) effects

and gives mainly information about the electronic properties of the absorbing atom. The EXAFS region is dominated by single scattering events of the outgoing electron on the neighbouring atoms, giving information about the local atomic structure around the absorbing site. For further information about XAS spectroscopy, we refer the reader to Ref. 11 and 12.

2.6.1. XAS experiments at the Mn and Zn K-edges

The absorptions at the K-edges are transitions from the core 1*s* level to the empty 3*d* states. In order to let the incident beam penetrate into the core levels of the atoms, high energy x-rays must be used. Synchrotron radiation is practically the unique source capable of producing x-rays of such high intensity. This type of source produces x-ray radiation of the order of 10^5 to 10^6 times of the intensity of a conventional source and is continuously tunable. XAS experiments were carried out at the European Synchrotron Radiation Facility (ESRF), in Grenoble, with storage ring energy of 6 GeV and an average current of 200 mA. Details of the XAS experiment carried out at the ESRF during this disertation are the following.

Several Mn K-edge experiments were performed at different beamlines: BM26A (Fluorescence detection), BM8 (Total Electron Yield, TEY) and, especially, at SpLine, BM25A (Spanish CRG beamline), where Mn and Zn K-edge were measured using fluorescence detection.

A Si(111) double crystal pseudo channel-cut monochromator was used for energy selection and sample was vertically shifted while the spectrum was collected. Incident beam was typically monitored by means of an ion chamber filled with a mixture of N_2 and He, and the Mn and Zn K□lines fluorescence yield was collected using a Si(Li) detector, from e2v Scientific Instruments. The monochromator was detuned up to 70% for those energy ranges to reject components of higher harmonics. Several spectra were collected in order to improve statistics and to have a good signal to noise ratio. Fluorescence spectra were obtained at room temperature under geometry where the angle between the detector and the incoming beam was 90º and the corresponding between the sample

and the incoming beam was 45º. The energy calibration was monitored using Mn and Zn foils. In some cases, measurements of the Zn K-edge were achieved by adding a Cr filter (6 μm foil) between the sample and detector and a smaller angle collection by increasing the sample-detector distance, in order to avoid detector saturation.

2.6.1.1. X-Ray Absorption Near-Edge Structure (XANES)

The Mn oxidation state in the prepared samples has been investigated by XANES. The edge position depends on the oxidation state of the absorber, being shifted to higher energies when increasing its formal valence. This can be observed in Fig. 2.4, which shows the XANES spectra at the Mn K-edge of metallic Mn and different oxides, where distinct differences in the form and in the position of the edges can be noticed.

From a simplified point of view, the sensitivity to valence is due to the core-hole interaction with the electron localized or quasi-localized on the excited atom. If one shifts from a valence, for example Mn^{2+} to Mn^{3+}, the filling of the 3*d* elements changes and consequently its nucleus is less well screened, resulting in an increased binding energy of the deepest core levels and therefore shifting the edge to higher energies.[13]

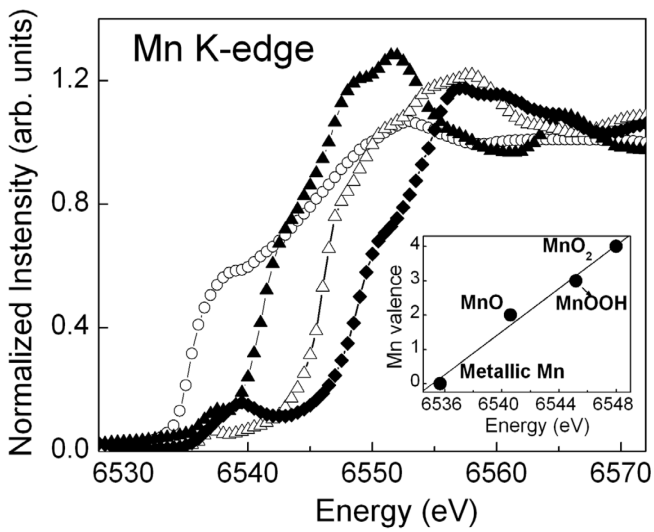

Fig. 2.4 XANES spectrum of Mn^0, Mn^{2+} (MnO), Mn^{3+} (MnOOH) and Mn^{4+} (MnO_2) references.[14] The inset shows the linear relationship between threshold energy and oxidation state.

The form of the absorption edges reflects the empty electronic density of states and is strongly dependent, for example, on the type of atomic coordination, like linear, tetrahedral (T_d) or octahedral (O_h) coordination. XANES computational methods allow to obtain important information on the sample structure. XANES calculations of the Mn K-edge XANES spectra have been carried out in collaboration with Dr. Jesús Chaboy from the Instituto de Ciencia de Materiales de Aragón, using the multiple-scattering code CONTINUUM[15] based on the one-electron full-multiple-scattering theory[16,17], obtaining significant information on the Mn/Si_3N_4 studied samples. Details of the simulations are described in section 6.8.2.

2.6.1.2. Extended X-Ray Absorption Fine Structure (EXAFS)

The origin of the EXAFS signal is related to an interference effect that evolves scattering of the outgoing photoelectron from the neighboring atoms. From a qualitative viewpoint, the probability that an x-ray photon will be absorbed by a core electron depends on both the initial and the final states of the electron. The initial state is the localized core level corresponding to the absorption edge. The final state is that of the ejected photoelectron which can be represented as an outgoing spherical wave originating from the x-ray absorbing atom. If the absorbing atom has a neighboring atom, the outgoing photoelectron wave will be backscattered by the neighboring atom, thereby producing an incoming electron wave. The final state is then the sum of the outgoing and all the incoming waves, one from each neighboring atom. It is the interference between the outgoing and the incoming waves that gives rise to the sinusoidal variation of μ vs E known as EXAFS.

By EXAFS analysis at the Mn absorption K-edge we can obtain precise information of the local environment (neighbours, coordination and bond length) around Mn, which results of great important in the field of DMS. The technique is not restricted by long-range order and is element-sensitive, being of great importance for noncrystalline solids and highly diluted materials.

The analysis of the EXAFS signal was performed in the following way. EXAFS

oscillations were obtained after removing the atomic background by a cubic spline polynomial fitting, and EXAFS signal ($\chi(k)$) was found by normalizing the magnitude of the oscillations to the edge jump. The resulting data were transformed into a function of the photoelectron wavenumber, *k*.

The pseudo Radial Distribution Function around the absorber atoms was calculated by Fourier transforming the k^n-weighted EXAFS signal ($k^n \cdot \chi(k)$) multiplied previously by a Hanning window (where typically n = 1,2 or 3). To obtain neighbours distances and coordination numbers, the back Fourier transform of first and second peaks was fitted to the well-known expression:[11]

$$\chi(k) = S_0^2 \sum_j \frac{N_j}{kR_j^2} e^{(-2k^2\sigma_j^2)} e^{(-2R_j/\lambda(k))} f_j(k) \times \sin(2kR_j + \Phi_j(k)) \qquad (2.8)$$

Eq. (2.8) describes the EXAFS oscillations for a Gaussian distribution of N_j atoms at mean distances R_j around the absorbing atom, considering single scattering and plane-wave approximation. S_0^2 is an intrinsic loss factor, N_j is the average coordination number for the Gaussian distribution of distances centered at the R_j value, σ_j is the Debye-Waller factor, and $\phi_j(k) = 2\delta(k) + \varphi_j(k)$ is the phase shift, being $\delta(k)$ and $\varphi_j(k)$ the central and backscattering atom phase shifts, respectively. $f_j(k)$ is the magnitude of the backscattering amplitude of the j^{th}-neighbour atom, and λ is the mean free path of the photoelectron traveling from the absorbing atom to the backscatterer in the j^{th}- shell and the life time of the core hole.

For all the samples, FTs were obtained over the same k^2-weighted interval (over a wave vector range from approximately 2 to 10 $Å^{-1}$) by using amplitude and phase backscattering functions calculated by the FEFF6 code,[18] where the scattering potentials are calculated in a standard way for atomic-charge densities within the muffin-tin (MT) approximation. The potential also includes the Hedin-Lundqvist self-energy with the Quinn correction to account for low-energy electron-hole losses. The conventional non-overlapping MT spheres approximation is used, since, for the EXAFS regime, the electron-atom scattering is dominated by the nearly spherical potential inside the muffin-tin and has low effect at these energies.[19]

2.6.2. XAS at the Mn $L_{3,2}$–edge

A $2p$ electron has dipole-allowed transitions to *s*- and *d*-like final states. Due to the large wavefunction overlap, the $3d$ channel is much stronger than the other channels, and the $2p$ absorption is determined by the transition probability $2p^6 3d^n \rightarrow 2p^5 d^{n+1}$. The $L_{3,2}$ absorption spectrum, which consists of a $2p_{3/2}$ (L_3) and $2p_{1/2}$ (L_2) structure, is therefore dominated by dipole transitions from the core $2p$ level to the empty $3d$ states, and because of the large Coulomb interaction between these two levels, it depends on the local electronic structure. Thus, analysis of the $L_{3,2}$ absorption structure can provide information about the oxidation state and the symmetry of the $3d$ transition metal ions.[20] There are some important $L_{3,2}$ spectral features to be mentioned:

Ions with the same number of $3d$ electrons give similar $L_{3,2}$ spectra, except for the size of the $2p$ spin-orbit separation and the absolute energy. However, the spectra of different d^n configurations are quite different and this can be used to identify the valence of an element. The energy separation between two oxidation states d^n and d^{n+1} of a particular element is equal to Q-U, where Q and U are the $2p \rightarrow 3d$ and the $3d \rightarrow 3d$ Coulomb interactions, respectively. Since Q is larger than U, the highest oxidation state (d^n) has the highest energy.

The crystal field interaction mixes states with different L values in the ground state LS term, allowing transitions to other final states with the same spin. This gives rise to a broadening of the peaks and a gradual appearance of new peaks with increasing crystal field interactions. Abrupt changes in the spectra are indicative of spin transitions.

Details of the Mn $L_{3,2}$-edge experiments are the following. Mn $L_{3,2}$-edge XAS measurements were done at beamline 5U.1 of the Synchrotron Radiation Source (SRS) at Daresbury Laboratory, in UK, in collaboration with Prof. G. Van der Laan and Dr. N. Telling. Spectra were collected between 630 and 670 eV in TEY mode.

Along this dissertation, information of the Mn ground state, Mn symmetry and crystal field has been obtained by comparison of the sample spectra with theoretical

calculations for different manganese electronic configurations (section 6.8.3).

Theoretical simulations performed by G. Van der Laan et al.[20] of the $2p$ absorption spectra of the Mn $3d^3$, Mn $3d^4$ and Mn $3d^5$ in tetrahedral (T_d) and octahedral (O_h) symmetry are shown in Fig. 2.5. In calculating the dipole transition from a $2p^6 3d^n$ state to the $2p^5 d^{n+1}$ final states, it has been taken into account the $2p$-$3d$ and $3d$-$3d$ Coulomb and exchange interactions, the $2p$ and $3d$ spin-orbit interactions and the crystal field acting on the $3d$ states.

The numbers near the spectra indicate the value of 10 Dq. The spectra for 10 Dq = 0, corresponding to spherical symmetry, are identical for T_d and O_h.

All spectra have a total intensity near to one and have been shifted vertically for clarity.

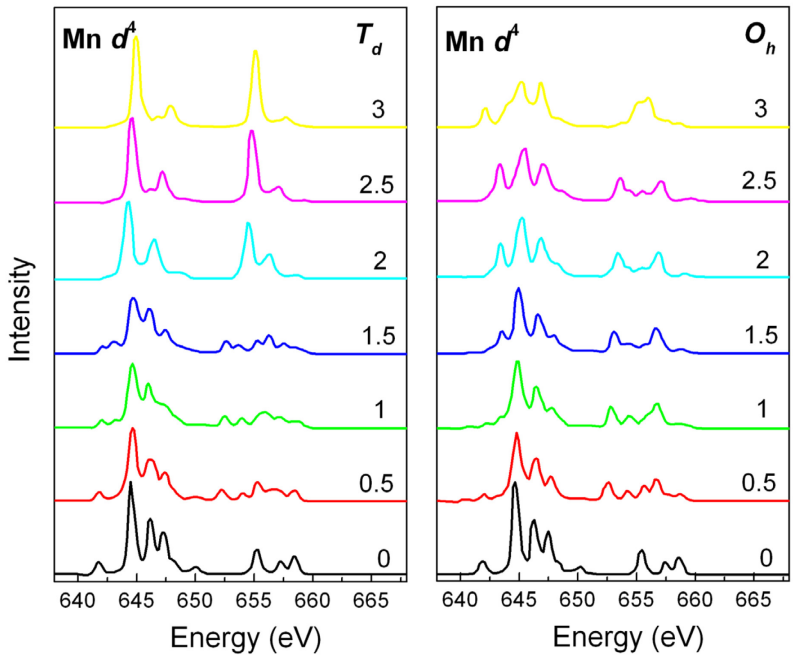

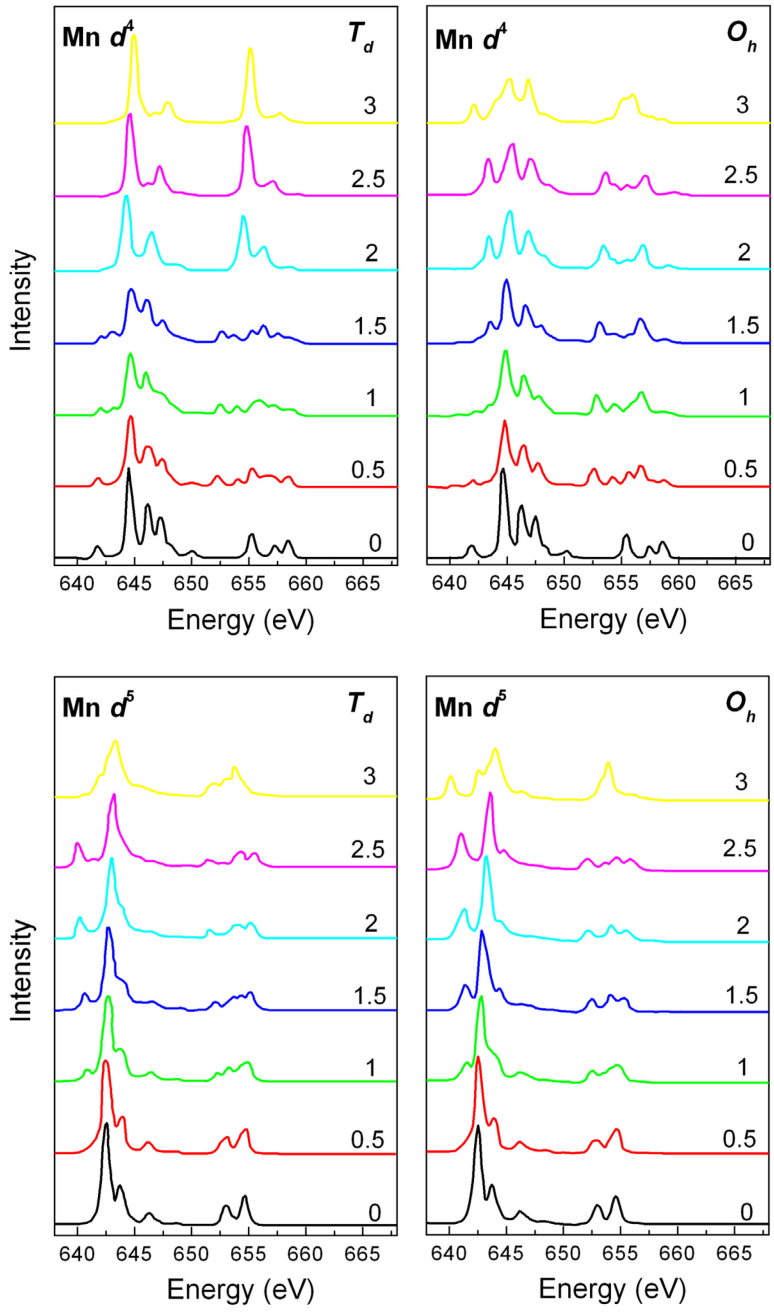

Fig. 2.5 Theoretical simulations performed by G. Van der Laan et al. [20] of the 2*p* absorption spectra of the Mn $3d^3$, Mn $3d^4$ and Mn $3d^5$ in tetrahedral (T_d) and octahedral (O_h) symmetry. The numbers close to the spectra indicate the value of 10 *Dq*. All spectra have a total intensity near to one and have been vertically shifted for clearness.

2.6.3. X-ray Magnetic Circular Dichroism (XMCD)

Dichroism with circularly polarized x-rays (X-ray Magnetic Circular Dichroism or XMCD) has become a powerful tool for the study of magnetic materials, capable to provide element specific information about spin and orbital magnetic moments.

With x-rays, in some cases, there is a difference between the absorption of left and right circularly polarized light (circular dichroism) or for different orientations of the polarization vector of linearly polarized light (linear dichroism). Magnetic dichroism occurs when the spherical symmetry of the free atom is broken due to a magnetic field, having its origin in the spin-orbit interaction. On the microscopic level, circular dichroism is given by the difference between $\Delta M_J = +1$ and $\Delta M_J = -1$ transitions, while linear dichroism is related to the difference between $\Delta M_J = 0$ and $\Delta M_J = \pm 1$ transitions.[13]

More details about the XMCD origin of the 3*d* transition-metal ions are described below.

In the spherically symmetric potential of a free ion, a small 3*d* spin-orbit interaction will split the initial state *LS* terms into levels *LSJ*. These levels are $(2J+1)$-fold degenerate, corresponding to the number of different eigenvalues $M_J = -J, -J+1, ..., J$.

The electrons are coupled to those of neighbouring atoms by exchange interactions (direct-exchange and superexchange in the case of non-metallic systems) which are usually between 0.005 and 0.1 eV. The interatomic exchange interaction in the 3*d* metal compounds can be treated as a magnetic field acting on the spin *S*. This exchange field lifts the degeneracy, making the energy of the M_J sublevels equal to $-g\mu_B H M_J$, where only the level with $M_J = -J$ is populated at T = 0 K. The factor *g* depends on the values of *L*, *S* and *J*. If the exchange interaction is of the same order of magnitude as the spin-orbit interaction, the different *J* levels within the term are strongly mixed. The energy of the final-state levels *J'* is determined by the electrostatic interactions in the $2p^5d^{n+1}$ configuration and the large core-hole spin-orbit interactions, which splits the spectrum into a $2p_{3/2}$ and $2p_{1/2}$ parts.

Magnetic dichroism is induced by the optical selection rules. For an initial state

level J, the dipole selection rule $\Delta J = +1, 0, -1$ permits only transitions to final-state levels $J' = J+1$, J and $J-1$. Excitation with left-circularly polarized radiation ($\Delta M_J = -1$) is then only allowed to $J' = J+1$ levels (the only levels which contain an $M_{J'} = -M_J + 1$ sublevel).

The levels with different total angular momentum J' in the final-state configuration have a different energy distribution due to the electronic interactions between the $2p$ core-hole and the $3d$ valence electrons, and the $2p$ core-hole spin-orbit interaction. Therefore, the spectra for left- and right-circularly polarized radiation will be different.[21]

If the absorption cross-sections for left and right circular polarizations are respectively, σ_+ and σ_-, the asymmetry (R) measured by the XMCD is:

$$R = \frac{\sigma_+ - \sigma_-}{\sigma_+ + \sigma_-} \tag{2.9}$$

The conditions necessary for a non-zero value for R are: spin-orbit coupling in the final state of the excitation, macroscopic magnetization (ferro- o ferrimagnetic samples) and a circularly polarized beam.

The degree of circular polarization of the X-ray photons is about 1% for K-edge and larger for L_2 and L_3-edges. The difference is due to the presence of a strong spin-orbit coupling in the initial state of the $L_{3,2}$ edges ($2p$ bands) which is not present in the initial state of the K edge ($1s$ band).

Details of the Mn $L_{3,2}$-edge XMCD experiments are the following. XMCD measurements were done on beamline 5U.1 of the Synchrotron Radiation Source at Daresbury Laboratory. Spectra were collected in TEY mode reversing the applied magnetic field of ± 0.6 T perpendicular to the surface at each data point for fixed photon helicity. Reversal of the XMCD signal was confirmed by switching between left and right circular polarization. Comparison between the obtained spectra with d^n calculations was done. XMCD measurements are included in section 6.8.4.

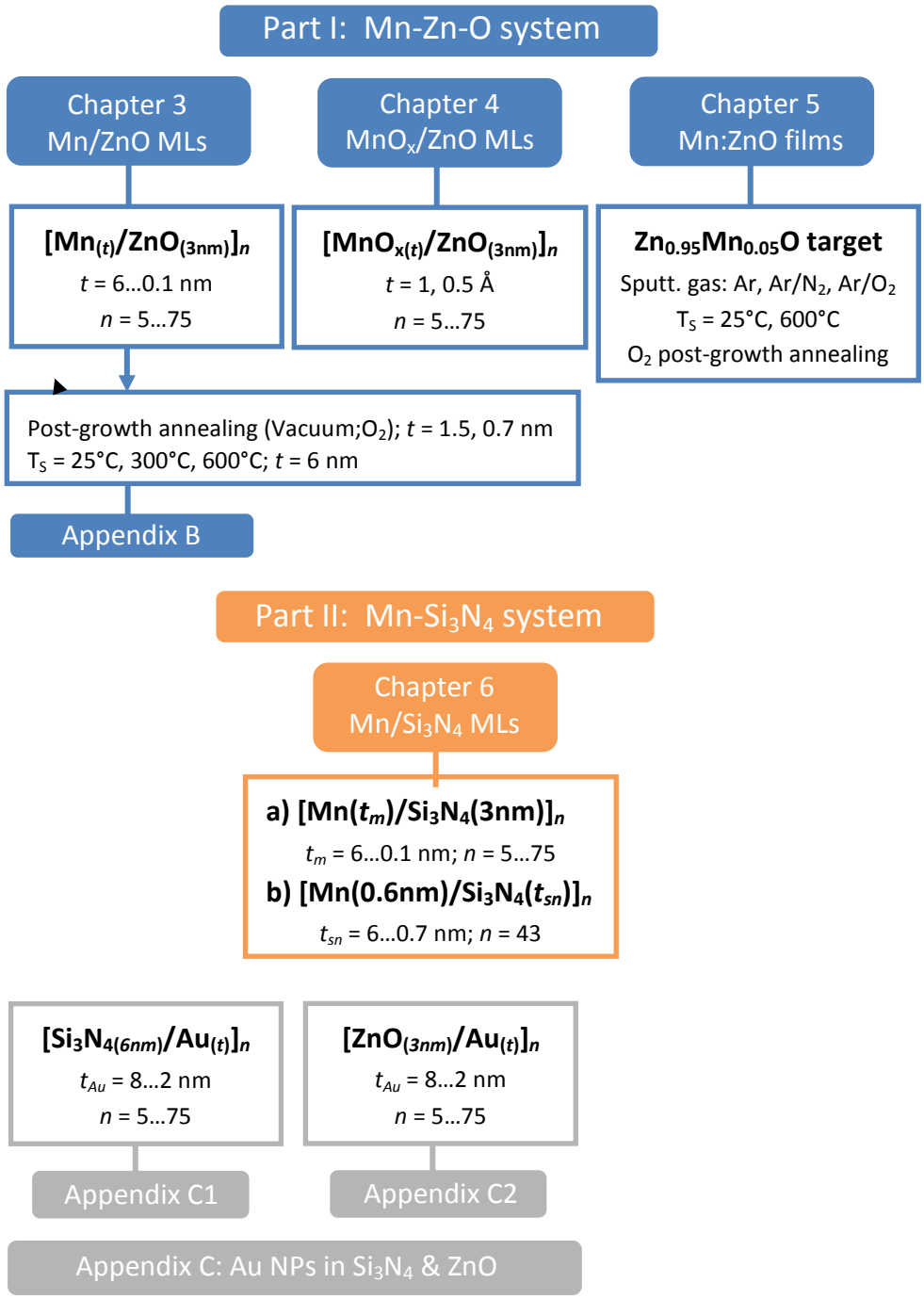

Fig. 2.6 The families of samples that have been studied in this dissertation.

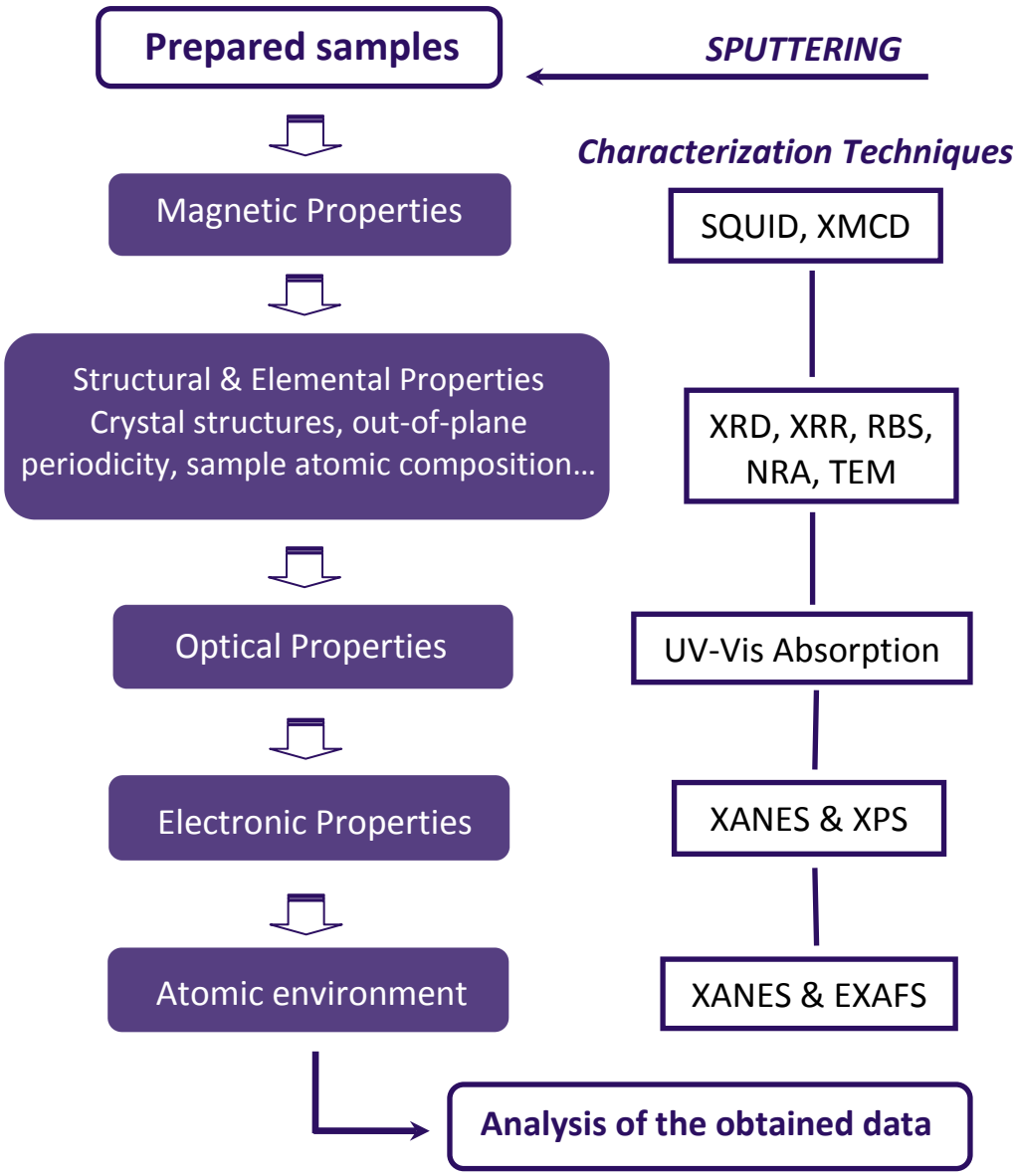

Fig. 2.7 Schematic view of the experimental procedures.

References

[1] R. Parsons, "*Thin Film Processes II*" (CA, USA: Academic Press Limited, 1991).

[2] D. L. Smith, "*Thin-Film Deposition. Principles and Practice*" (McGraw-Hill, Inc. New York, 1995).

[3] J. M. Albella, *"Láminas delgadas y recubrimientos: preparación, propiedades y aplicaciones"* (CSIC, 2003).

[4] R. Daniel, Doctoral Thesis "*Studies of the Reactive Sputtering Process and its Application in Electro-Acoustic Devices"* (Uppsala Universitet, 2006).

[5] K. A. Zoerb, Doctoral Thesis *"Differential Sputtering Yields of Refractory Metals by Ion Bombardment at Normal and Oblique Incidences"* (Colorado State University, 2007).

[6] A. Muñoz-Martín, Appendix 2 of Doctoral Thesis *"Caracterización estructural de sistemas magnéticos nanoestructurados"* (Universidad Autónoma de Madrid, 2002).

[7] MPMS-5S Quantum Design SQUID manual.

[8] A. Gupta, Doctoral Thesis *"Novel Room Temperature Ferromagnetic Semiconductors"*, Royal Institute of Technology, Stockholm (2004).

[9] V. Holý, U. Pietsch, T. Baumbach, *"High-resolution X-ray Scattering from Thin Films and Multilayers"* (Springer, 1999)-

[10] SIMNRA 6.04 User's guide, http://www.ipp.mpg.de/~mam/

[11] D.C. Koninsberger and R. Prins *"X-Ray Absorption: Principles, Applications, Techniques of EXAFS, SEXAFS and XANES"*, (Wiley, New York, 1988).

[12] B.K. Teo *"EXAFS: Basic Principles and Data Analysis"* (Springer-Verlag, Berlin Heidelberg New York Tokyo, 1986).

[13] F. Hippert, E. Geissler, J. L. Hodeay, E. Lelièvre-Berna, J. R. Regnard, "*Neutron and X-ray Spectroscopy"* (Springer, 2006).

[14] D.A. McKeown and J.E. Post, Am. Mineral. 86, 701 (2001).

[15] C. R. Natoli and M. Benfatto, (unpublished).

[16] P. A. Lee and J. B. Pendry, Phys. Rev. B 11, 2795 (1975).

[17] C. R. Natoli and M. Benfatto, J. Phys. (Paris) Colloq. 47, C8-11 (1986).

[18] S. I. Zabinsky, J. J. Rehr, Phys. Rev. B 52, 2995 (1995).

[19] J. J. Rehr and R.C. Albers, Rev. Mod. Phys. 72, 621 (2000).

[20] G. van der Laan and I. W. Kirkman, J. Phys.: Condens. Matter 4, 4189 (1992).

[21] G. van der Laan and B. T. Thole, Phys. Rev. B 43, 13401 (1991).

PART I

Mn-ZnO System

Chapter 3

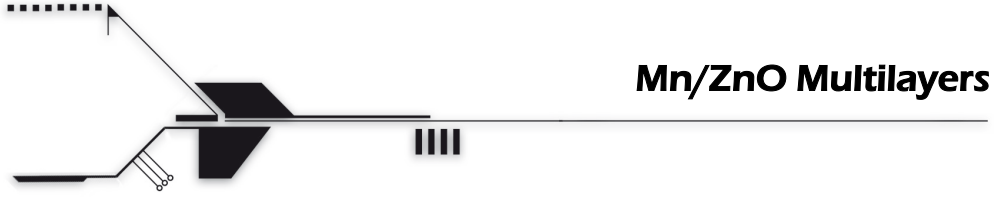

Mn/ZnO Multilayers

3.1. Motivation

The special interest of the work presented in this chapter lays in the fact that the preparation of Mn/ZnO multilayered stacks enables to study the Mn-ZnO interface and its role on the ferromagnetism of the Mn-Zn-O system. Although the interface-related properties have been claimed of great importance in the magnetic properties of this system,[1,2] to our knowledge, there has not been published any previous study dealing with Mn/ZnO interfaces.

Conversely, multilayer structure preparation has been reported for other similar ZnO-based materials, as Co/ZnO thin films by sputtering[3] and by ion-beam assisted sputtering[4] and CoFe/ZnO thin films prepared also by ion-beam sputtering,[5] where ferromagnetic behaviour has been observed. However, there has not been reported any previous study on Mn/ZnO multilayers to the one described here. Just Huang et al.[6] have lately reported investigations on $[ZnO(20Å)/Co(1Å)]_{25}$ and $[ZnO(20Å)/Mn(1Å)]_{25}$ multilayers prepared by molecular beam epitaxy (MBE), mainly based on the role of the lattice disorder caused by the different dopants on ZnO.

In addition to the novelty of this study, it should be noticed that a comprehensive structural characterization of the Mn/ZnO sample series has been performed combining different laboratory and synchrotron radiation techniques. Details characterizations are of great importance in this field since, in many cases, contradictory experimental results are due to insufficient structural studies. In particular, the use of techniques as X-ray absorption near-edge structure (XANES) and extended X-ray absorption fine structure (EXAFS) spectroscopies in these investigations should be underlined. These powerful tools have been used to show that Mn substitutes Zn in the ZnO wurtzite phase for

instance in Mn-doped epitaxial ZnO thin films,[7] or in polycrystalline sintered samples for Mn concentrations up to 5 at.%.[8] Additionally, high pressure experiments have been carried out to probe that Mn substitutes Zn in the wurtzite phase and also in the rocksalt phase after applying more than 8 GPa.[9] The magnetic behaviour has been recently correlated to the Mn lattice position in MBE prepared Mn-Zn-O films[10] where ferromagnetism is observed at low temperatures and which might be originated from substitutional Mn^{2+} in wurtzite ZnO lattice. More recently, Guo et al.[11] have reported observations of room temperature ferromagnetism in a 2.2 at.% Mn-doped ZnO thin film deposited on fused quartz substrate by pulsed laser deposition and EXAFS indicates that Mn^{2+} replaces Zn site in wurtzite.

3.2. Preparation of multilayers

$[Mn_{(t)}/ZnO_{(3nm)}]_n$ multilayers were prepared by sequential DC sputtering of ZnO and Mn on Is(100) substrates at room temperature. The base pressure provided by de vacuum system was in the $1x10^{-7}$ mbar range. ZnO layers were deposited by reactive sputtering from a pure Zn target (Goodfellow: 99.9%) using O_2/Ar mixture gas (30% O_2-rich) at a working pressure of $5.4x10^{-3}$ mbar. Mn layers were grown from a Mn target (Goodfellow: 99.95%) at $5.0x10^{-3}$ mbar pressure of pure Ar. Pre-sputtering was performed before the multilayer growth and also between two consecutive layers. The DC power supplied was about 9 W for Mn and 5.5 W for ZnO and the corresponding deposition rates were about 0.07 nm/s for Mn and 0.05 nm/s for ZnO. Following this procedure, series of Mn/ZnO multilayers was prepared, keeping the ZnO layer nominal thickness constant (3 nm) and changing the Mn layer nominal thickness (t), from 6 to 0.1 nm. An additional 3 nm ZnO layer was deposited onto each sample. The number of bilayers, n, was increased to keep the total amount of Mn approximately constant in every sample. The nominal formula, nominal thickness and bilayer number are collected in Table 3.I.

Table 3.I. Nominal sample series description.

Nominal sample $[Mn_{(t)}/ZnO_{(3nm)}]_n$	Mn-layer nominal thickness t (nm)	Number of bilayers n	Mn total nominal thickness (nm)	Nominal sample thickness (nm)
$[Mn_{(6nm)}/ZnO_{(3nm)}]_5$	6	5	30	48
$[Mn_{(3nm)}/ZnO_{(3nm)}]_{10}$	3	10	30	63
$[Mn_{(1.5nm)}/ZnO_{(3nm)}]_{20}$	1.5	20	30	93
$[Mn_{(0.7nm)}/ZnO_{(3nm)}]_{43}$	0.7	43	30	162
$[Mn_{(0.4nm)}/ZnO_{(3nm)}]_{75}$	0.4	75	30	258
$[Mn_{(0.2nm)}/ZnO_{(3nm)}]_{75}$	0.2	75	15	243
$[Mn_{(0.1nm)}/ZnO_{(3nm)}]_{75}$	0.1	75	7.5	236

3.3. Magnetic properties

Magnetic characterization of these samples is shown in Fig. 3.1, where magnetization per manganese atom has been calculated taking into account the precise amount of Mn obtained by Rutherford Backscattering Spectroscopy experiments (section 3.5). The silicon substrate diamagnetic contribution has been subtracted at the plots.

The temperature dependence of magnetization, M(T), depicted in Fig. 3.1(a), shows that the magnetic behaviour of the samples varies within the series, being the ferromagnetic order favoured by increasing the Mn layer thickness (t). Ferromagnetism over room temperature is clearly observed for the thickest Mn-layer film (t = 6 nm). As t is reduced, the ferromagnetic component of the magnetization decreases, while the paramagnetic one increases. Finally, very thin Mn-layer samples (t < 1.5 nm) exhibit paramagnetic-like behaviour. The inset of Fig. 3.1 (a) shows the Curie-Weiss behaviour for the t = 0.1 nm sample, which implies a negative Curie temperature ($\theta \approx$ -68 K), indicating that the dominant magnetic interactions between Mn atoms are antiferromagnetic in nature, in agreement with some results previously reported in the Mn-Zn-O system.[12,13] Fig. 3.1 (b) shows hysteresis loops at several temperatures of two

ferromagnetic samples. The sample with t = 6 nm exhibits about 0.05 μ_B per Mn atom, being the highest saturation magnetization among the studied samples, and a coercive field of approximately 80 Oe at 5 K. M_S of about 0.05 μ_B/Mn corresponds to about 4 emu per grame of Mn and to 10 emu/cm^3, considering the film volume.

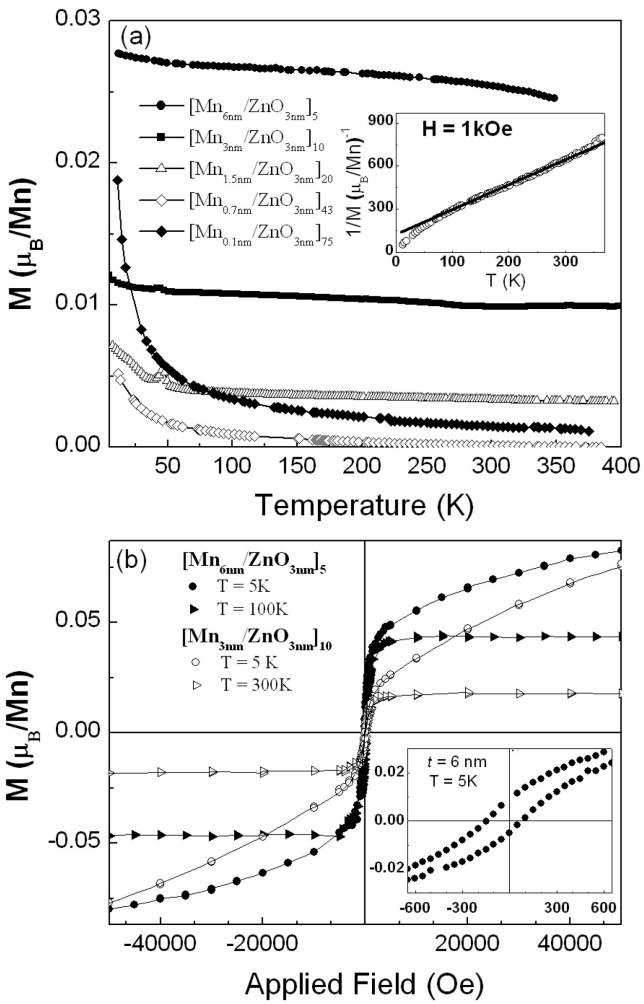

Fig. 3.1 (a) Magnetization curves (H = 1kOe) for several representative samples. The inset shows the inverse of magnetization vs. temperature for the t = 0.1 nm sample. Solid line corresponds to the linear fit from 100 to 350 K. (b) Hysteresis loops of the t = 6, 3 nm samples at different temperatures. The inset shows the low field region of hysteresis loop at 5 K (t = 6 nm sample).

These values are comparable to those previously reported in the literature. For instance, M_S of 1 emu/cm^3 and a coercive force (H_C) around 50 Oe were claimed to be obtained at 5 K for a ZnO/MnO_2 multilayer film by M. A. García et al.[2] In addition, M_S of 0.28 emu/g at (5.6 emu/g considering the Mn amount) and H_C of 78 Oe at 10 K have been obtained by Kundaliya et al.[1] for RTFM nanosized $Zn_{0.95}Mn_{0.05}O$. Finally, a higher M_S value of 0.18 μ_B/Mn has been reported by S. S. Yan et al.[14] for a 2 at.% Mn-doped ZnO sample. After these comparisons, it is possible to conclude that the here prepared ferromagnetic multilayers lay in the typical magnetization range reported for the Mn-Zn-O system.

On the other hand, it should be remarked that the possibility of ferromagnetism due to any ferromagnetic impurity in these samples can be rejected. X-ray absorption experiments performed at L-edges at beamline 5U.1 of SRS at Daresbury Laboratory, in UK, in collaboration with Prof. G. Van der Laan and Dr. N. Telling, have show that there is no appreciable Fe, Co or Ni contamination in these films. In addition, the different magnitudes of M(T) observed within the sample series also indicates that ferromagnetism cannot be due to uncontrolled magnetic impurities from the starting Mn target. M(T) normalized to the total number of Mn atoms (and therefore to the possible amount of impurity atoms) shows different magnetization values within the sample series, being dependent of the Mn layer thickness (t). This indicates that ferromagnetism due to uncontrolled ferromagnetic impurities, where the magnetization would be proportional to the impurity amount, can be discarded.

In addition, magnetic measurements were performed on several pure ZnO thin films deposited on the same type of silicon substrates to discard any possible ferromagnetic contribution. Magnetization vs. applied field measurement at 4.2 K for a pristine ZnO thin film prepared by sputtering has been shown in Fig. 3.2, where no appreciable ferromagnetic signal is observed.

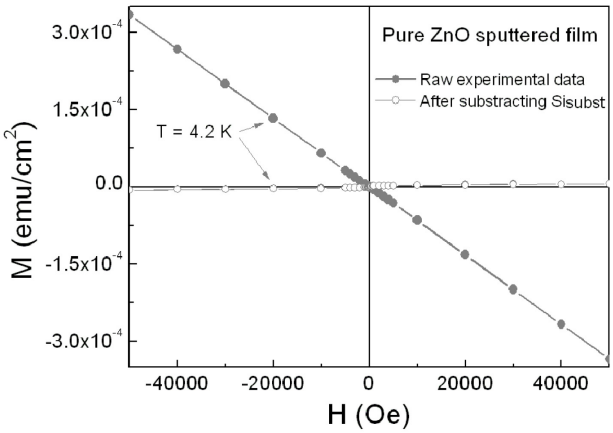

Fig. 3.2 M-H curve from a pure ZnO film prepared by sputtering with approximately 0.4 micron thickness, measured at 4.2 K. Raw experimental data as well as the data after subtracting the diamagnetic contribution from the silicon substrate have been included for comparison, showing that no appreciable ferromagnetic signal is obtained.

3.4. X-Ray Reflectivity (XRR)

X-ray reflectivity (XRR) measurements were carried out on a Bruker D8 X-ray diffractometer with a Cu K_α source at the ICMM facilities. X-ray reflectivity (XRR) sample spectra, depicted in Fig. 3.3, show **multilayer periodicity in the out-of-plane direction for all the samples, what confirms that samples are actually formed by layers of different electronic density**.

Average thickness values of Mn and ZnO-rich layers have been obtained from simulations of the reflectivity data (included in Fig. 3.3) performed with the Xreal software developed by N. D. Telling.[15] It should be noted that these simulations make possible higher accuracy in the layer thickness determination than performing just direct XRR data analysis. Simulations have been done here mainly with that purpose, being complex data fitting away from the aim of this work. That is the reason why just a short number of parameters has been used in the calculated spectra and why these simulations do not fully reproduce the experimental data. Some parameters from the simulations are,

for instance, silicon substrate roughness (rms), about 0.6 nm, reflected intensity background (~10^{-6}-10^{-5} cps), interface roughness (~0.7 nm), Mn and ZnO densities (7.3 g/cm^3 and 5.7 g/cm^3, respectively) and the thickness of each layer.

Since the calculations do not completely fit the experimental data, the comparison indicates interface roughness a bit larger in the samples as well as some additional effects not considered here, as possible in-depth variations of the parameters. Nonetheless, the interface roughness in the simulations (~0.7 nm) indicates that, at least for Mn thickness (t) smaller than 0.7 nm non-continuous Mn growth is expected, what points out to cluster formation for $t \leq 0.7$ nm samples.

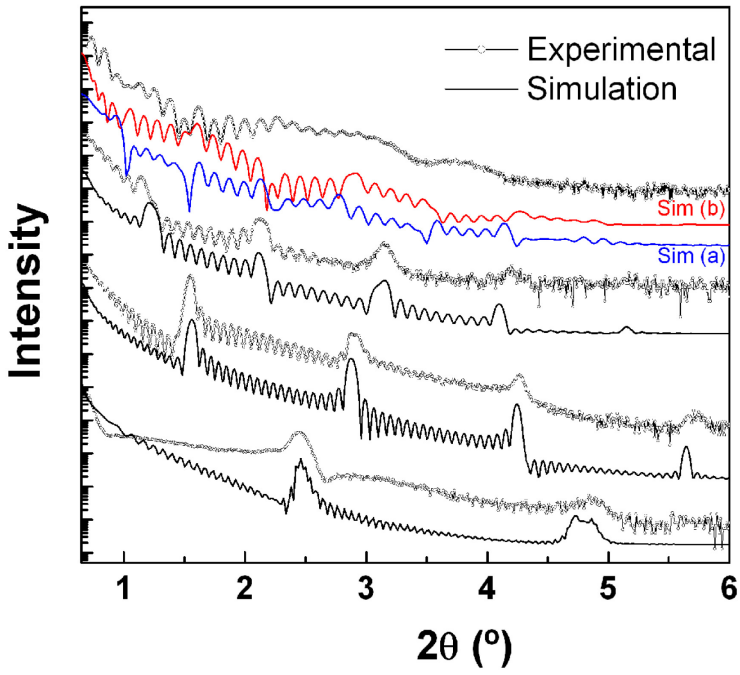

Fig. 3.3 X-ray reflectivity multilayer spectra and their simulations. From top to bottom, spectra of samples t = 6, 3, 1.5 and 0.2 nm. All spectra have been vertically shifted for clearness.

Considering the particular case of the t = 6 nm sample, simulations by using pure ZnO and Mn layers (simulation (a) of Fig 3.3, in blue) did not match very well the experimental data. For this spectrum, better agreement was obtained, especially at low

angles, by considering two mixed Mn-Zn-O layers with slightly different densities (6.5 g/cm^3 for the Mn-rich region and 6.2 g/cm^3 for the ZnO-rich one, used in simulation (b) of Fig. 3.3, in red) which is in fact the first sign of interdiffusion in the samples. It is clear that in the simulation of this t = 6 nm sample, additional structural details should be considered to simulate the reflectivity over $2\theta = 2^o$, where extra features appear. Since these simulations do not match very well the experimental XRR data, the uncertainty in the fit parameters is quite high. Nevertheless, the goodness of the bilayer thickness values, related to the maximum peaks position, is expected to be higher.

The obtained bilayer thicknesses as well as the related Mn layer thicknesses (t_m), these ones with larger uncertainties, are summarized in Table 3.II, in comparison with nominal values. The corresponding ZnO layer thickness value averaged among all samples results 4 nm, being larger than the nominal 3 nm ZnO layer. Bilayer thicknesses result about 20-30 % higher than the nominal ones for samples with $t \geq 0.7$ nm. The comparison is shown in Fig 3.4, indicating an approximately linear dependence, as it is expected.

Table 3.II. Sample bilayer thickness values (XRR-Λ) and Mn-layer thickness values (XRR-t_m) determined form XRR simulations compared to nominal values

Nominal sample $[Mn_{(t)}/ZnO_{(3nm)}]_n$ t (nm)	n	XRR-Λ (nm)	XRR- t_m (nm)
6	5	12.6	7.9
3	10	8.7	3.9
1.5	20	6.3	1.8
0.7	43	4.7	0.8
0.4	75	4.0	0.5
0.2	75	3.7	0.3
0.1	75	3.4	0.15

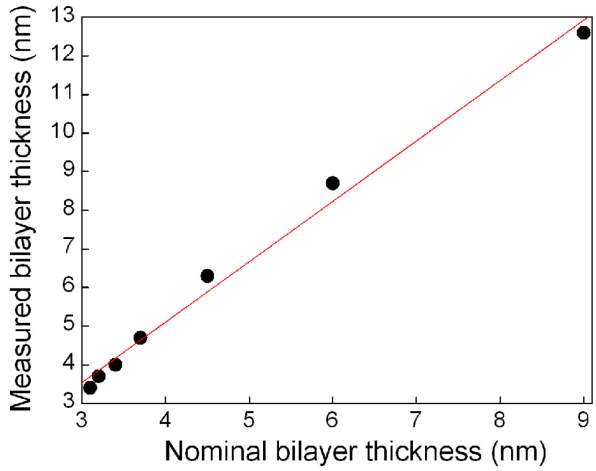

Fig. 3.4 Comparison between the nominal bilayer thickness of samples and the experimental values obtained by XRR measurements.

Considering the obtained Mn layer thickness values (t_m), further exploration of the ferromagnetic response of the samples has be done. In particular, it has been found that there exists an approximately linear dependence of the saturation magnetization at room temperature vs. t_m, which is shown in Fig. 3.5. The comparison between the M-H curves for the most ferromagnetic sample within the series (t_m = 7.9 nm) and the t_m = 0.15 nm one, showing just paramagnetic-like response, is included in the insets.

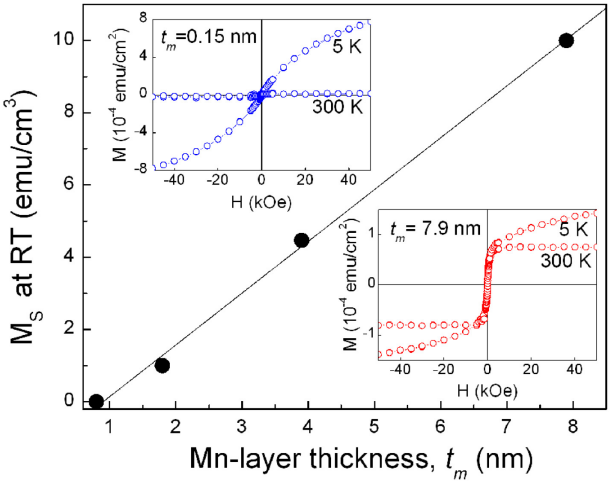

Fig. 3.5 Evolution of M_S at RT vs. t_m. The straight line corresponds to the linear fit of data. The insets show the M-H curves for the samples t_m = 0.15 and 7.9 nm.

It should be noted that, for simplicity, samples will be named by their nominal values from now on in this chapter.

3.5. Rutherford Backscattering Spectroscopy (RBS)

RBS experiments were carried out in collaboration with Dr. Javier García López at the Centro Nacional de Aceleradores (CNA) in Sevilla to evaluate the actual amount of Mn in each sample as well as the film atomic composition.

Fig. 3.6 shows experimental data and simulations of some representative samples. Fig. 3.6(a) exhibits the RBS spectra obtained with incident ions of 2 MeV and their simulations in order to obtain film composition. Additionally, RBS spectra were collected with incident ions of 8 MeV to distinguish the Mn and Zn contributions. As it can be observed in Fig. 3.6(b), Mn and Zn contributions are separated and both integrals can be easily evaluated. Nevertheless, for these energies, Mn and Zn cross sections are not known and simulation cannot be performed in a similar way as for the spectra collected at 2 MeV. However, the Mn/Zn ratio can be calculated since it is proportional to the integral ratio of both contributions, which become well separated at 8 MeV. Therefore, using the Mn/Zn ratio for the t = 6 nm sample obtained with 2 MeV (where both concentrations can be obtained by simulation) the actual ratio in the whole set of samples can be calculated. After analysis of the two used energies, the obtained film composition is given in Table 3.III. It can be noticed that, despite considering that the uncertainty in the oxygen amount determined by RBS (~10-20%) is quite higher than for heavier elements as Mn or Zn, there are considerably more oxygen atoms than zinc atoms in these samples. The obtained atomic % of oxygen, which results roughly the same for all the samples, suggests that oxygen in samples might be related to zinc from ZnO but also to manganese.

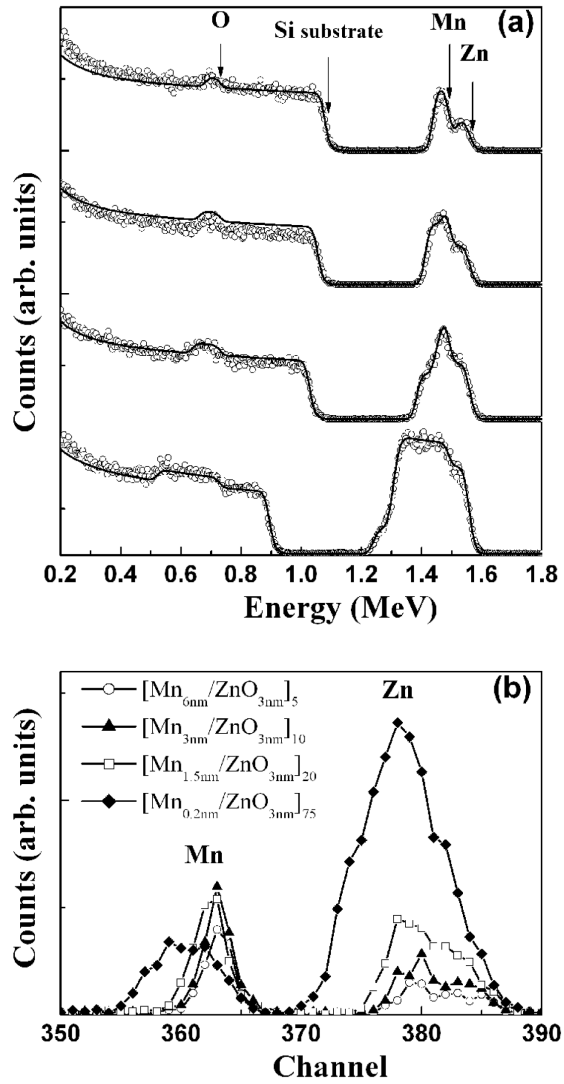

Fig. 3.6 (a) RBS spectra taken at energy of incident ions of 2 MeV (dots) and their simulations (lines) of samples t = 6 nm, t = 1.5 nm, t = 0.7 nm t = 0.1 nm, from top to bottom. All spectra have been vertically shifted for clearness. (b) RBS spectra of the same samples at 8 MeV.

Table 3.III. Number of Mn atoms per Mn layer (at./cm^2) and sample atomic composition (%) obtained from simulations of RBS data.

Nominal sample $[Mn_{(t)}/ZnO_{(3nm)}]_n$ t (nm)	Mn atoms per Mn-layer (10^{16} at./cm^2)	Atomic composition (%) [Mn]	[Zn]	[O]
6	3.71	0.35	0.12	0.53
3	2.62	0.35	0.16	0.49
1.5	1.31	0.25	0.22	0.53
0.7	0.76	0.19	0.29	0.52
0.4	0.54	0.16	0.33	0.51
0.2	0.42	0.13	0.34	0.53
0.1	0.35	0.11	0.34	0.55

A comparison between the Mn layer thickness previously obtained by XRR simulations and the calculated ones by taking into account the RBS results (where the metallic Mn density, 8.1x10^{22} at./cm^3 has been used) is shown in Fig. 3.7. The most noticeable fact is that, for samples with thick enough Mn layers, XRR-determined Mn-layer thickness is larger than the corresponding value obtained from RBS. Since XRR is a thickness direct measurement, this apparent discrepancy can be explained in terms of the considered Mn density. It means that in the thickness calculation from RBS data, the used metallic Mn density is, in fact, higher than the actual one. This fact directly points towards the existence of oxidized Mn layers in the samples. The relation between the straight-line slopes corresponding to both techniques can be used to estimate the average Mn layer density in the samples. The obtained slope, 4.4x10^{22} at./cm^3, is clearly smaller than the value corresponding to metallic Mn (8.1x10^{22} at./cm^3). **A comparison with some manganese oxides** like MnO (4.6x10^{22} at./cm^3), Mn_2O_3 (1.9x10^{22} at./cm^3) or MnO_2 (3.5x10^{22} at./cm^3) **indicates that Mn is present in a partially oxidized form**.

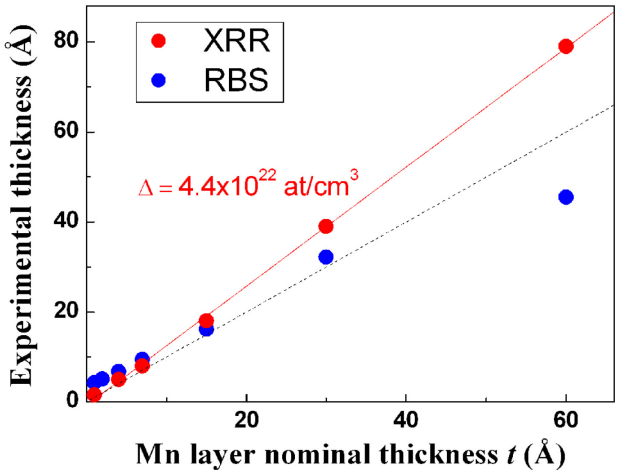

Fig. 3.7 Comparison between experimental Mn layer thickness values obtained from RBS and XRR. $4.4x10^{22}$ at./cm^3 is the Mn-layer density necessary in calculations to match RBS data with XRR results (dash line represents correspondence between the experimental and nominal values).

3.6. X-Ray Diffraction (XRD)

Diffraction measurements on the sample series were carried out in a standard laboratory Bruker D8 X-ray diffractometer by using the K_α radiation line of Cu. XRD spectra from several samples are shown in Fig. 3.8. From the possible phases in these samples, the observed peak at $2\theta \sim 34.2^o$ matches the (002) peak from the hexagonal wurtzite-ZnO (*W*-ZnO) crystal structure ($2\theta = 34.4^o$). *W*-ZnO corresponds to the stable form of zinc oxide, being the one commonly found in ZnO films prepared by sputtering, either by reactive sputtering (DC or RF-type) of a metallic Zn target[16,17,18] or by RF sputtering of ZnO.[19,20,21]

In Fig. 3.8, the (002) peak corresponding to the hexagonal wurtzite-ZnO can be clearly observed in samples with large enough ZnO content (being the samples with a number of layers sufficiently high, as the ZnO layer thickness is constant along the series but not the total ZnO thickness). Conversely, this (002) peak is not observed for samples with few ZnO layers, like $[Mn_{(6nm)}/ZnO_{(3nm)}]_5$ and $[Mn_{(1.5nm)}/ZnO_{(3nm)}]_{10}$, most likely due to the small ZnO amount. No additional information of other Mn-containing phases

can be extracted from this first XRD characterization.

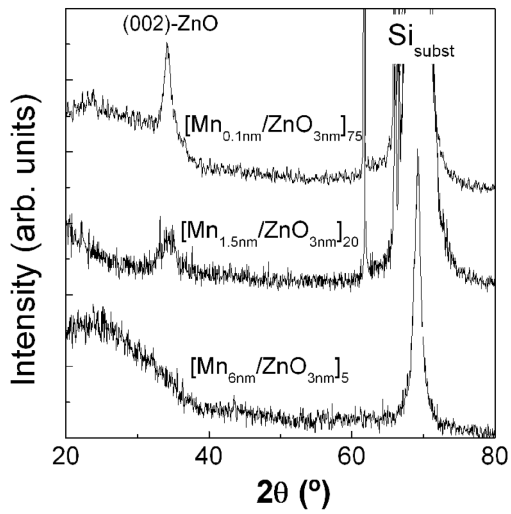

Fig. 3.8 X-ray diffractograms of several representative samples.

In order to obtain additional structural information, especially about possible Mn-Zn-O mixed phases in the $[Mn_{(t)}/ZnO_{(3nm)}]_n$ samples, X-ray diffraction experiments were carried out in an especially designed for surface and thin film characterization six-circle diffractometer with $\lambda = 0.8857$ Å, at the Spanish CRG beamline (Spline, BM25, branch B) of the European Synchrotron Radiation Facility (ESRF), Grenoble.

Spectra were measured in grazing incidence (0.75º) configuration, which was used in order to enhance the thin film signal and to avoid the very strong peaks from the Si substrate. Spectra corresponding to selected samples from the series, which are representative of thin and thick Mn layers (t = 0.1 and 6 nm respectively) are shown in Fig. 3.9(a). A ZnO sputtered thin film which has been prepared under same conditions (Ar/O_2 gas, power…) as the ZnO layers in the $[Mn_{(t)}/ZnO_{(3nm)}]_n$ has been included in the figure for direct comparison. A zoom of these spectra together with some reference spectra is also shown in Fig. 3.9(b). For the sample with t = 0.1 nm, just *W*-ZnO is

evidenced, without clear hints of other phases. Conversely, t = 6 nm sample spectrum confirms the presence of cubic MnO rocksalt (*RS*) nanocrystals, evidenced by its (200)-*RS* peak at about 23º. The broad peak at about 19.5º might correspond to (002)-*W* and (111)-*RS* peaks.

Therefore, in agreement with the previous XRR and RBS comparison, which indicated the presence of Mn partially oxidized in the samples, **MnO nanocrystals have been identified in the t = 6 nm sample by high resolution grazing incidence X-ray diffraction.**

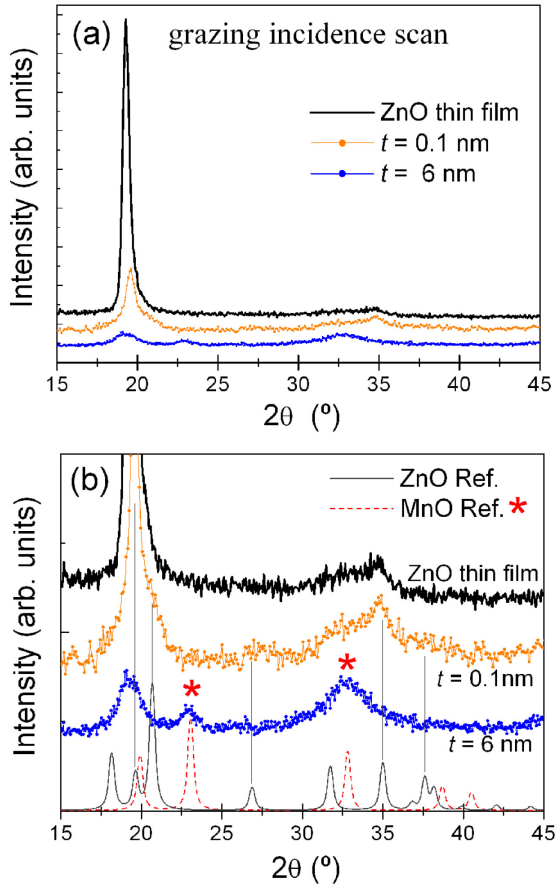

Fig. 3.9 (a) Grazing incidence (ω = 0.75º) X-ray diffraction of several studied multilayers and a 70 nm sputtered ZnO film. (b) Zoom of the grazing incidence sample spectra in comparison with XRD patterns from *W*-ZnO and *RS*-MnO references.

The θ-2θ scan of the t = 0.1 nm sample in comparison with the sputtered ZnO film is shown in Fig. 3.10, where it can be inferred that samples exhibit texture. The ZnO grain size of several samples from the series (shown in Table 3.IV) has been obtained using the Scherrer formula and the Gaussian fits of the (002)-ZnO peaks. Gaussian fits of several ZnO diffraction peaks are shown in Fig. 3.10(b).

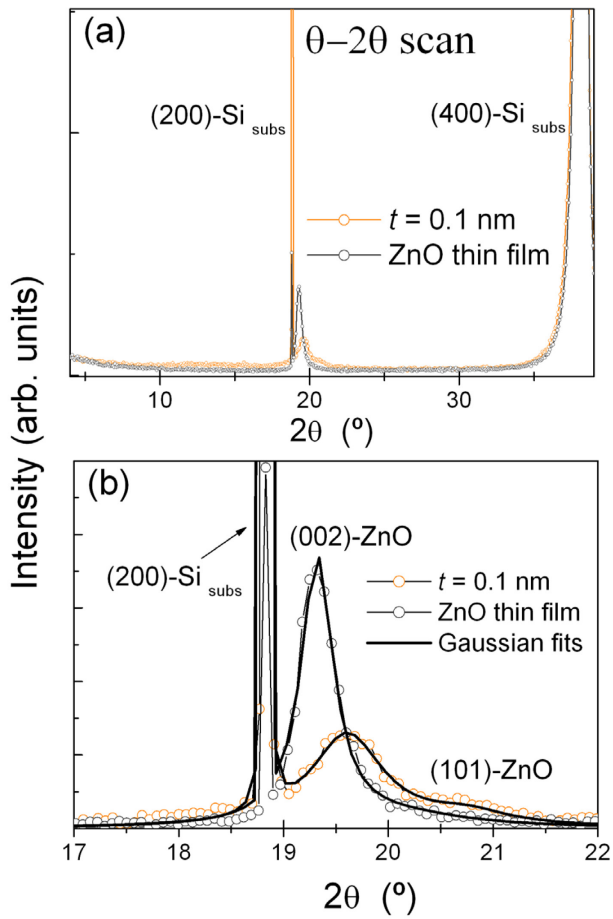

Fig. 3.10 (a) θ-2θ X-ray diffraction measurements of t = 0.1 nm sample and a 70 nm sputtered ZnO film. (b) Zoom of the same θ-2θ X-ray diffraction spectra and their corresponding Gaussian fits.

- In the case of **samples with larger *t***, the size of these nanocrystalline grains is near 3 nm, which is of the order of the ZnO layer thickness. This suggests that, even if interdiffusion is expected, **deposited Mn is actually present as a continuous Mn oxide layer**, interrupting the ZnO grain growth in the out-of-plane direction. On the other hand, no traces of metallic Mn or other Mn-Zn-O phases have been found.
- In the case of samples with very thin Mn layers, the obtained crystalline grain sizes are above 7 nm, which are considerably higher than the 3 nm ZnO layer nominal thickness and close to the grain size of a sputtered ZnO film (≈ 10 nm), evidencing no restriction to the ZnO grain size growth in the out-of-plane direction. It means that **in multilayers with these small t values, the Mn deposition does not hamper the ZnO grain growth**. This fact points towards the formation of discontinuous MnO_x layers, resulting in MnO_x clusters embedded in the ZnO matrix for the $t \leq 0.7$ nm multilayers. Either the possible amorphous character of the MnO_x clusters or the small size of the MnO_x crystalline grains can imply their non detection by diffraction measurements. No signals of metallic Mn, rocksalt nanocrystals or other Mn-Zn-O phases are observed from diffraction spectra in multilayers with $t < 1.5$ nm.

Table 3.IV. Average crystalline grain size of ZnO in the out-of-plane direction obtained by XRD.

Nominal sample $[Mn_{(t)}/ZnO_{(3nm)}]_n$ t (nm)	n	Grain size (nm)
6	5	2.3
1.5	20	2.9
0.1	75	7.7
ZnO film	70 nm (film thickness)	10.4

3.7. Transmission Electron Microscopy (TEM)

Preparation of several $[Mn_{(t)}/ZnO_{(3nm)}]_n$ samples for TEM cross-section characterization was carried out during a 2 months stay at the Department of Ceramics and Glass Engineering, CICECO, at the University of Aveiro, in Portugal. The cross section thin film preparation technique was carried out thanks to the assistance of Dr. Mercedes Vila and Dr. Augusto Barros López. Electron Microscopy studies were undertaken using a 300 kV Hitachi H9000-NA TEM.

Further high resolution TEM studies were carried out at the Electronic Microscopy Centre Luis Bru in collaboration with Dr. María Luisa Ruiz González and Prof. José María González Calbet using a FEG-electron microscopy (300 kV JEOL 300FEG) with spatial resolution of 1.7 Å for High Resolution Transmission Electron Microscopy (HRTEM).

From TEM studies, additional nano-structural details can be extracted. Bright field TEM cross-section images corresponding to t = 6 and 3 nm samples are depicted in Fig. 3.11(a) and 3.11(b). Multilayer structure can be inferred for both samples, being clearer for the former sample (Fig. 3.11(b)). The total film thickness values obtained from the TEM images are approximately 60 and 87 nm for t = 6 and 3 nm, respectively, in accordance with XRR results (Table 3.II).

Dark field image of the t = 0.7 nm sample is shown in Fig. 3.11(c). The obtained ~260 nm of total thickness is in agreement with XRR results. The electron diffraction pattern of this sample (t = 0.7 nm) is shown in Fig. 3.11(d), where the appearance of rings can be related to the polycrystalline nature of the t = 0.7 nm sample. It should be noticed that the existence of no very well-defined rings with slightly oval shapes makes difficult a reliable indexation of the rings. Nonetheless, taking into consideration the above results from XRD (see Figs. 3.8-3.10), *W*-ZnO presence is expected in this sample with small Mn layer thickness. Although strong evidences could not be inferred from the obtained electron diffraction rings, the pattern seems to match with the existence of *W*-ZnO polycrystalline grains in the t = 0.7 nm sample (Fig. 3.11(d)).

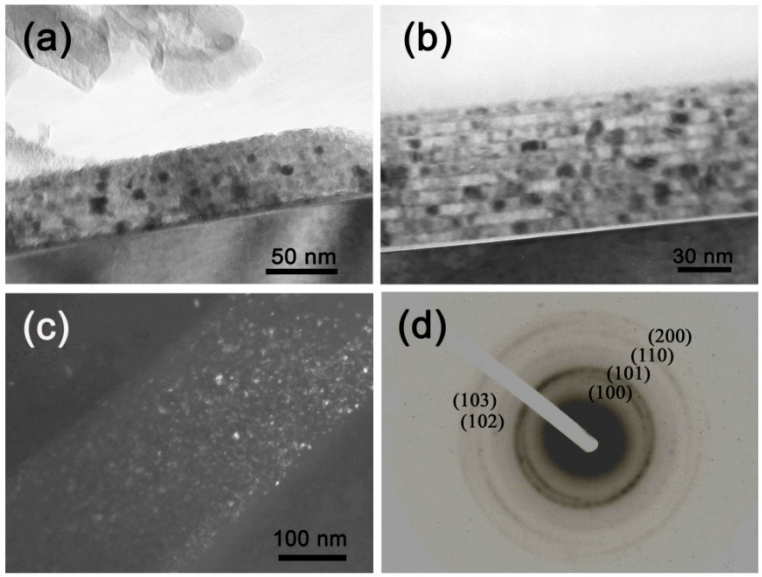

Fig. 3.11 (a) Cross-sectional TEM image of sample t = 6 nm, (b) t = 3 nm and (c) t = 0.7 nm. Electron diffraction patterns of t = 0.7 nm sample are shown in (d). The pattern seems to correspond to the wurtzite structure of ZnO.

TEM image of the t = 3 nm sample evidences the presence of 10 layers (as shown in the low resolution image depicted in Fig. 3.12(a) as well as its nanocrystalline nature (Fig. 3.12(b)). The HREM study indicates the presence of nanocrystals (Fig. 3.12(c)) whose periodicities and their corresponding FFT, fit with a cubic NaCl type (rocksalt) unit cell along [011] zone axis. Therefore, **HREM evidences the presence of nanocrystalline *RS* phase in the t = 3 nm sample**.

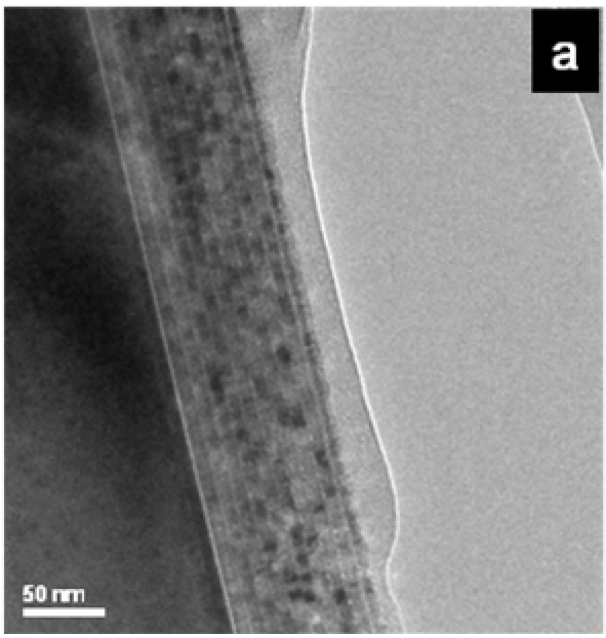
a
50 nm

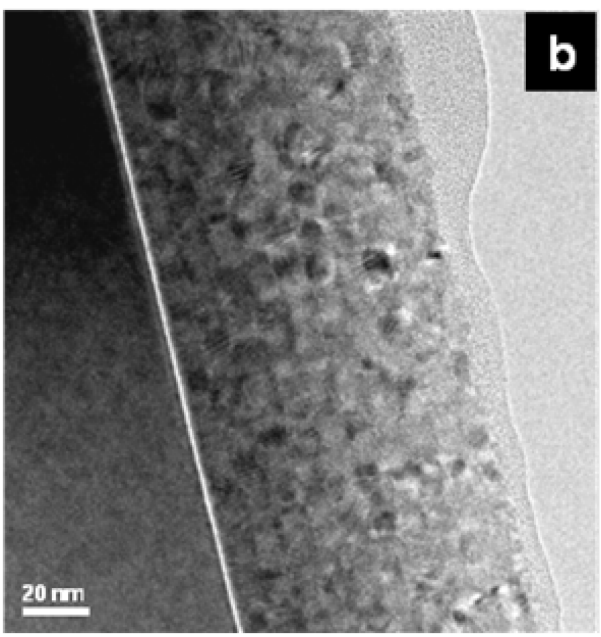
b
20 nm

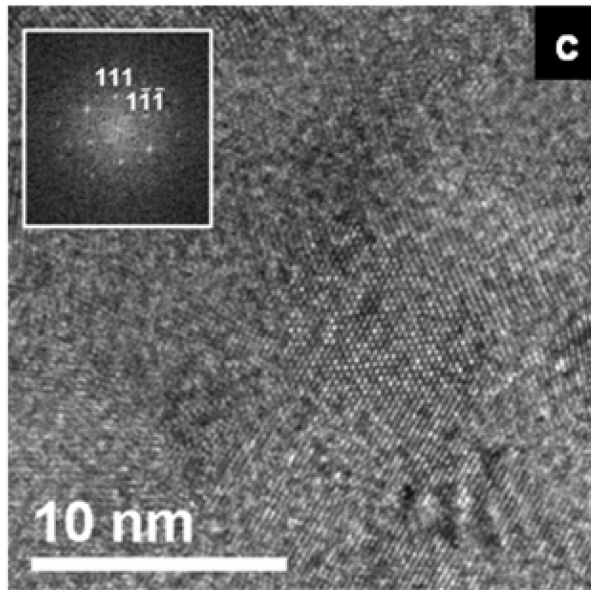

Fig. 3.12 Cross-sectional TEM (a) and (b), and HRTEM (c) images of the t = 3 nm sample.

3.8. X-Ray Absorption Spectroscopy (XAS)

Mn electronic states and local structure of the Mn/ZnO multilayers have been investigated by means of X-ray absorption spectroscopy. XAS experiments were carried out at the BM25 beamline (SpLine) of the European Synchrotron Radiation Facility (ESRF), Grenoble. Several spectra were collected in order to improve statistics and to have a good signal to noise ratio. The fluorescence spectra were obtained at room temperature under a configuration where the detector formed an angle of 90º respect to the incoming beam. Further experimental details can be found in section 2.6.1.

3.8.1. X-Ray Absorption Near-Edge Spectroscopy (XANES)

XANES experiments were performed in order to obtain information on the manganese charge state.

Mn K-edge XANES spectra of the samples series in comparison with a Mn metal foil and MnO_2 are displayed in Fig. 3.13. The Mn absorption K-edge energy was calibrated by measuring a Mn foil and setting its E_0 value as in Ref. [22] to be compared with the reported relative edge positions of the Mn compounds with different oxidation states. After edge jump normalization, direct comparisons can be made among the XANES spectra for all samples. The most important fact is that the sample series spectra exhibit a shift of the main edge energy, higher than 3.5 eV, from the thickest Mn-layer sample (t = 6 nm) to the thinnest one (t = 0.1 nm), indicating an increase of the oxidation state as the Mn-layer thickness decreases. Arrows have been plotted at the threshold energy in Fig. 3.13.

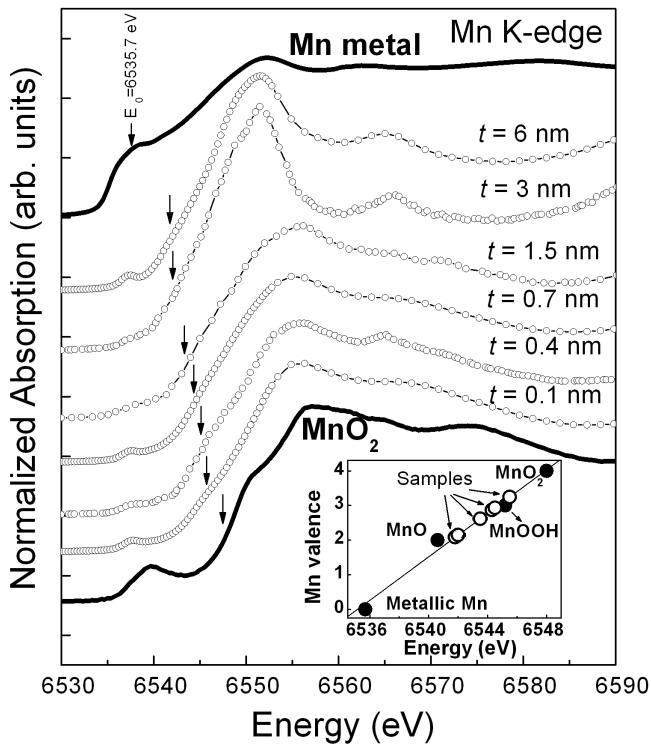

Fig. 3.13 Mn K-edge spectra of samples compared with Mn foil and MnO_2. The inset shows the evolution of the Mn oxidation state compared with Mn^0, Mn^{2+} (MnO), Mn^{3+} (MnOOH) and Mn^{4+} (MnO_2) references[22].

Edge-energy values instead of pre-edge or white-line features have been used here to obtain the average Mn oxidation state, since for the obtained data this approach is more sensitive to Mn valence and least sensitive to structural effects. Taking into account the linear relationship between threshold energy and oxidation state for the reference compounds,[22] the average oxidation state of Mn in these ML samples can be easily determined by measuring the threshold energy (inset of Fig. 3.13). It is worth to comment that in manganese oxides, the threshold energy values obtained from the maximum of the first derivative, results to be troubled by the splitting of the 1*s*-4*p* transition,[23] which affects to the first maximum position of the first derivative. For this reason, the threshold energy has been estimated in all cases as the energy corresponding to one third of the jump.

Table 3.V. Average Mn oxidation states calculated from XANES.

Nominal sample $[Mn_{(t)}/ZnO_{(3nm)}]_n$ t (nm)	n	Average Mn oxidation state
6	5	+2.1 ± 0.2
3	10	+2.2 ± 0.2
1.5	20	+2.6 ± 0.2
0.7	43	+2.9 ± 0.2
0.4	75	+3.0 ± 0.2
0.1	75	+3.3 ± 0.2

Results, summarized in Table 3.V, indicate a **variation of the average Mn oxidation state with *t*, ranging the Mn oxidation states between Mn^{2+} and Mn^{4+}**. Samples with larger *t* in the series are related to Mn valence near to +2, while the ones with small *t* values present oxidation states higher than +3. It is important to remark that under the experimental measuring conditions, the entire depth of the film is explored, contributing all Mn atoms from each sample to the Mn K-edge XAS signal. It means that

the obtained oxidation state value corresponds to the average of the actual distribution present in the whole film. The gentle slope that can be observed at the XANES threshold spectra indicates that Mn in the samples is not present in a pure oxidation state. **XANES results are therefore in agreement with the previous XRR-RBS comparison** (section 3.5) and definitely, the so-called **Mn layers are in fact formed by oxidized Mn with a manganese oxidation state that increases within the sample series.**

3.8.2. Extended X-Ray Absorption Fine Structure (EXAFS)

In order to obtain precise information about the local environment (neighbours, coordination and bond length) around Mn and Zn EXAFS analysis was carried out at the Mn and Zn absorption K-edges.

Standard analysis was performed with the VIPER software.[24] For all the samples, FTs were obtained over the same k^2-weighted interval (over a wave vector range from 2 to 10 $Å^{-1}$) by using amplitude and phase backscattering functions calculated by the FEFF6 code.[25] Addition details can be found in section 2.6.1. Fig. 3.14 shows the Fourier transform (FT) magnitude of the EXAFS signal at the Mn K-edge of the studied samples. Several manganese oxides, a standard Mn metal foil and a Mn thin film grown by sputtering were also measured for comparison. It can be observed that all FT sample spectra present a first peak at ~1.5 Å. This contribution is compatible with a Mn-O distance of about 2 Å, indicating the presence of oxidized Mn in the samples, in agreement with XANES studies. A noticeable difference between the FT magnitude of samples with thicker Mn layers (t = 6, 3 nm) and the other samples with thinner Mn layers can be observed in the graph.

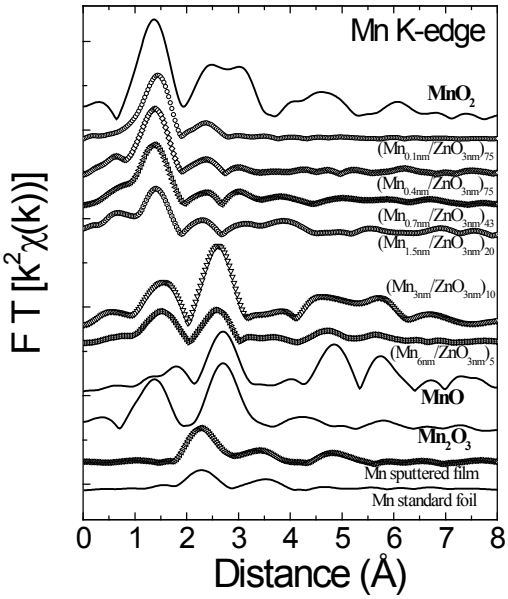

Fig. 3.14 Experimental EXAFS Fourier Transforms (FT) of the Mn/ZnO multilayer samples. FT of manganese oxides, a Mn foil and a Mn sputtered thin film are shown for comparison.

The position and shape of the FT peaks for samples with t = 6, 3 nm clearly differ from the corresponding to samples with $t \leq 1.5$ nm, all of them very similar, evidencing differences in the structural properties between these two samples with thicker Mn layers and the others. From the magnetic measurements, a noticeable difference was also observed between the magnetic behaviour of these two samples and the others. Multilayers with $t \geq 3$ nm exhibit ferromagnetic behaviour over room temperature while for samples with t below this value, the paramagnetic contribution increases and the magnitude of magnetization becomes negligible. This fact suggests a direct relation between the ferromagnetic behaviour of these samples and the different Mn local structure that they exhibit.

Standard EXAFS analysis at the Mn K-edge provides the pairs and distances summarized in Table 3.VI, corresponding to the first and second coordination spheres. A comparison between experimental data and simulations for three representative samples can be observed in Fig. 3.15.

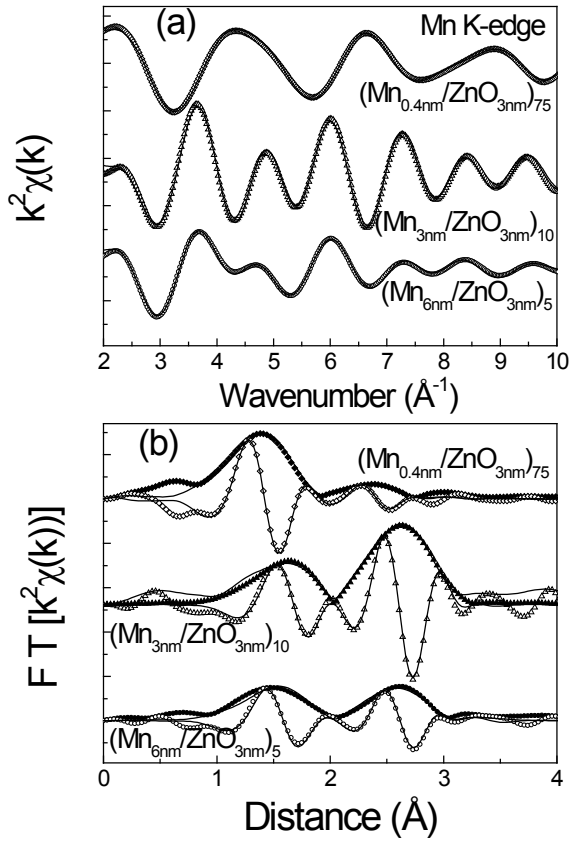

Fig. 3.15 (a) k-space comparison between the filtered EXAFS signal (dots) and simulations (lines) at Mn K-edge of samples t = 6, 3 and 0.4 nm. (b) Fourier transform of the (a) plotted signals; modulus and imaginary parts have been presented for dual comparison with calculated contributions (lines).

TABLE 3.VI. Summary of XAS results corresponding to references and samples: Average Mn oxidation states and R, N, σ^2 EXAFS parameters (distance (R), number of neighbours (N) and the Debye-Waller factor, respectively). * M stands for Mn or Zn since they result indiscernible by XAS in this XAS experiments.

References	Mn oxid.state	Pair	R (Å)	N
MnO	+2	Mn-O	2.22	6
		Mn-Mn	3.14	12
Mn_3O_4	+2	Mn-O	2.04	4
	+3	Mn-O	1.93	4
			2.28	2
Mn_2O_3	+3	Mn-O	1.89-2.25	6
β-MnO_2	+4	Mn-O	1.89	6
		Mn-Mn	2.89	2
		Mn-Mn	3.40	8
ZnO		Zn-O	1.99	4
		Zn-Zn	3.23	12

Samples	Mn oxid.state	Pair *	R (Å)	N	σ^2 (10^{-3}Å^2)
sputtered ZnO film		Zn-O	1.97±0.02	4	0.4±0.5
		Zn-Zn	3.18±0.02	12	12±1
$[Mn_{6nm}/ZnO_{3nm}]_5$	+2.1±0.2	Mn-O	2.03±0.02	1.7	4±0.5
		Mn-O	2.18±0.02	1.6	5±0.5
		Mn-M	3.11±0.02	4.3	15±1
		Mn-M	3.37±0.02	4.0	18±1
		Zn-O	1.98±0.02	4.5	18±0.5
		Zn-M	3.12±0.02	7.5	17±1
		Zn-M	3.37±0.02	4.0	6±1
$[Mn_{3nm}/ZnO_{3nm}]_{10}$	+2.2±0.2	Mn-O	2.16±0.02	5.0	8±0.5
		Mn-M	3.12±0.02	7.3	11±1
		Mn-M	3.37±0.02	2.7	9±1
$[Mn_{1.5nm}/ZnO_{3nm}]_{20}$	+2.6±0.2	Mn-O	1.94±0.02	3.6	2.5±0.5
		Mn-M	2.86±0.02	1.6	20±1
		Zn-O	2.05±0.02	2.9	1.4±0.5
		Zn-Zn	3.14±0.02	5.0	4.5±1
$[Mn_{0.7nm}/ZnO_{3nm}]_{43}$	+2.9±0.2	Mn-O	1.92±0.02	2.9	3±0.5
		Mn-M	2.91±0.02	1.9	30±1
$[Mn_{0.4nm}/ZnO_{3nm}]_{75}$	+3.0±0.2	Mn-O	1.91±0.02	4.5	2.5±0.5
		Mn-M	2.88±0.02	1.0	50±1
$[Mn_{0.1nm}/ZnO_{3nm}]_{75}$	+3.3± 0.2	Mn-O	1.93±0.02	4.5	5±0.5
		Mn-M	2.91±0.02	1.0	40±1

From the obtained results and in agreement with XANES data, shorter Mn-O distances are achieved from thinner Mn-layer samples, evidencing higher Mn oxidation states in the samples with $t \leq 1.5$ nm. For all these films the local environment around Mn is very similar. Mn-O and Mn-Mn obtained distances present values of 1.91 - 1.94 Å and 2.86 – 2.91 Å, respectively, which are very close to those in -MnO_2 structure.[26] Both, the high Mn oxidation state and the pair distances ($R_{Mn-O} \sim 1.92$ Å and $R_{Mn-Mn} \sim 2.9$ Å) indicate mostly MnO_2 formation in samples with very thin Mn layers.

It should be commented that direct comparison between the FT corresponding to films with $t < 1.5$ nm and MnO_2 reference does not match in magnitude for the second coordination sphere. The small magnitude observed for the peaks corresponding to second coordination spheres is, undoubtedly, due to the very small MnO_2 grains obtained in the small Mn layers. This fact makes a significant reduction of the coordination number for coordination spheres further than the first one,[27] which provides an amorphous-like FT magnitude. For that reason, even if second FT peaks are not comparable in magnitude, the second peak position for samples with $t < 1.5$ nm matches with MnO_2 since the fitted distances, given in Table 3.VI, do.

Conversely and also in agreement with XANES results, in the case of samples with $t \geq 3$ nm, the obtained Mn-O distances ($R_{Mn-O} \sim 2.1$ Å) reveal an average Mn oxidation state near Mn^{2+} when comparing with MnO reference, where $R_{Mn-O} \sim 2.2$ Å. Following a more refined EXAFS analysis, it is found that the $t = 3$ nm sample presents mostly one Mn-O contribution at $R_{Mn-O} = 2.16$ Å, while for the $t = 6$ nm sample, two different Mn-O distances are provided by the fit, being 2.03 and 2.18 Å. Fits of both samples also show second neighbour distances $R_{Mn-M} \sim 3.1$ Å and $R_{Mn-M} \sim 3.4$ Å, being M = Mn, Zn. It is important to underline that, for the analysed k-range interval, no significant differences were obtained when considering Mn or Zn as backscatterer atoms. It means that, at least under the achieved experimental conditions, there is no possibility to fairly distinguish between them (for this reason, only a R_{Mn-M} distance contribution is reported, where M stands for Mn or Zn).

Regarding the EXAFS analysis of these multilayers with larger t values ($t \geq 3$ nm)

it should be considered that on one hand, MnO formation has been evidenced by the above XRD and HRTEM experiments. Therefore, MnO phase, which has a rocksalt-type structure (*RS*), with octahedral Mn coordination (O_h), is expected to be detected by EXAFS.

In addition, diffusion of Mn cations into the close ZnO layers could be also possible in these samples and consequently, the presence of Mn in the ZnO wurtzite (*W*) structure, with tetrahedral Mn coordination (T_d) might be found. Hence, stabilization of a Zn-O-Mn mixed phase (*W*-type) at the ZnO rich regions should be also considered in the analysis.

On the other hand, diffusion of Zn cations into the MnO phase should be also taken into account. In fact, it must be noted that, although it is well known that the hexagonal wurtzite (*W*) is the stable form of ZnO, under specific conditions, like high pressure, the cubic rocksalt phase (*RS*) could be induced for ZnO. (More details of the *W* to *RS* phase transitions in ZnO are included in Appendix B). When the relative content of Mn in ZnO phase is high, an enhanced stability of this rocksalt phase is expected since *RS* is the stable form of MnO. Therefore, stabilization of a mixed phase named as Mn-O-Zn (*RS*-type) at the MnO-rich regions seems in fact quite probable.[i]

All these points should be considered when analysing the complicated EXAFS results obtained for the samples with larger *t* values ($t \geq$ 3 nm), where the complex situation of non-homogenously intermixed layers with coexistence of Mn-Zn-O mixed phases having both *W* and *RS* structures, maybe expected.

The obtained results for the t = 3 nm sample are well in agreement with *RS* structure: the obtained $R_{Mn\text{-}O}$ = 2.16 Å is slightly smaller than the corresponding to the pure MnO rocksalt (2.22 Å) but it is in full agreement with the obtained distance (2.17 Å) by EXAFS in $Zn_{1-x}Mn_xO$ thin films with *RS*-stabilized structure reported by Pellicer-Porres et al.,[28] what supports the existence of Mn-O-Zn *RS* mixed phase. In addition,

i Notice that "Zn-O-Mn (*W*)" refers to the mixed phase with Mn diffused into the majority *W*-ZnO phase while "Mn-O-Zn (*RS*)" refers to the mixed phase with Zn diffused into the majority *RS*-MnO phase. "Mn-Zn-O mixed phases" refer to both.

second neighbours, found at R_{Mn-M} = 3.11 Å, match the geometrical condition between first and second distances in rocksalt structure ($\sqrt{2}$ ratio). Besides, there is a minor contribution with R_{Mn-M} = 3.37 Å, that also appears in the t = 6 nm sample, and that will be explained below.

Results for the t = 6 nm sample indicate the same distance contributions as t = 3 nm sample corresponding to *RS* structure, but in addition, EXAFS analysis shows here extra contributions with distances R_{Mn-O} = 2.03 Å and R_{Mn-M} = 3.37 Å, that can be identified with Mn substituting Zn in wurtzite phase.[28,29] The obtained Mn-O distance is slightly larger than Zn-O in wurtzite structure, what is in fact expected since the Mn^{2+} ionic radius is higher than the Zn^{2+} one. In addition, this distance coincides again with the EXAFS obtained value in $Zn_{1-x}Mn_xO$ thin films[28] with low Mn content and wurtzite phase (labelled here as Zn-O-Mn (*W*)). No much attention should be paid to the obtained coordination numbers for these samples (especially for the second shell); its high correlation with Debye-Waller factors, the small grain size effect as well as experimental difficulties due to self-absorption and short available k-space can considerable increase its own uncertainty.

Additional measurements were performed at the Zn K-edge of several samples. Fig. 3.16 shows the Fourier transform magnitude of two samples (t = 6, 1.5 nm) and a ZnO sputtered film. The evaluation of the Zn-environment in the t = 1.5 sample and the ZnO sputtered film by comparing its corresponding FT shape should be made just in its wide sense. On one hand, the ZnO layers thickness in these samples are only 3 nm, what allows finite size effects and besides, strains in the samples seem likely (a slightly shifted (002)-ZnO peak was found in section 3.6), having both influence on the TF magnitude.

Standard EXAFS analysis provides Zn-O and Zn-M pairs and distances summarized in Table 3.VI, corresponding to the first and second coordination spheres. Experimental data and simulations for the Fourier transform and back Fourier transform of the EXAFS signal at the Zn K-edge are shown in Fig. 3.17.

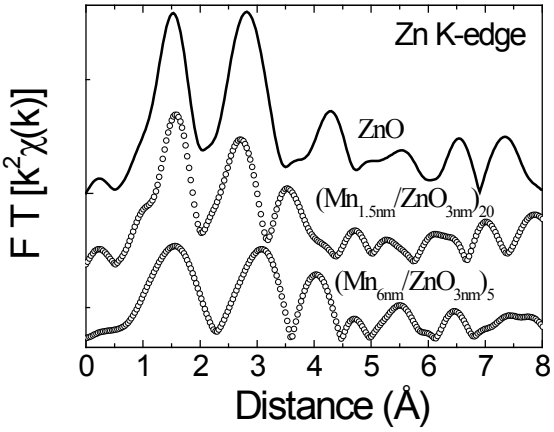

Fig. 3.16. Fourier Transforms (FT) of Zn K-edge EXAFS oscillation function $k^2\chi(k)$ of samples t = 6, 1.5 nm and a 100 nm ZnO film.

It can be observed that in the case of the t = 6 nm sample, the second peak of the FT magnitude reveals a second-neighbour contribution at higher atomic distances. Data analysis provides an additional Zn-M contribution at 3.37 Å. This distance is in full agreement with the Mn-M contribution found in the Mn K-edge analysis of the multilayer samples with t > 1.5 nm. Both results put together indicate that this sample is composed by layers containing Mn in both, wurtzite and rocksalt phases in the t = 6 nm sample. Therefore, distances corresponding to *W*-ZnO, Zn-O-Mn (*W*) and MnO (*RS*) are found by EXAFS analysis of the t = 6 nm sample. The non-detection at the Zn K-edge of Zn-O contribution at distances ~ 2.1 Å, which would be related to Mn-O-Zn (*RS*) phase, can be assigned to the short available k-range as well as the small fraction of Zn in the Mn-O-Zn phase compared to the majority of Zn in *W*-ZnO phase. A small amount of Mn-O-Zn (*RS*) phase in comparison with Zn-O-Mn (*W*) phase is consequently expected for the t = 6 nm sample.

The situation is different for the t = 3 nm sample, where Mn-O distance corresponding to Mn in *W*-ZnO phase is not detected (although Mn-M contribution is observed at 3.37 Å, exactly as for the t = 6 nm sample). The non distinction between the

two similar Mn-O distances expected in the t = 3 nm sample is, in all likelihood, due to the low fraction of Zn-O-Mn (W) compared to *RS* phase. Small amount of Zn-O-Mn (W) phase in comparison with *RS* phase is therefore expected for the t = 3 nm sample.

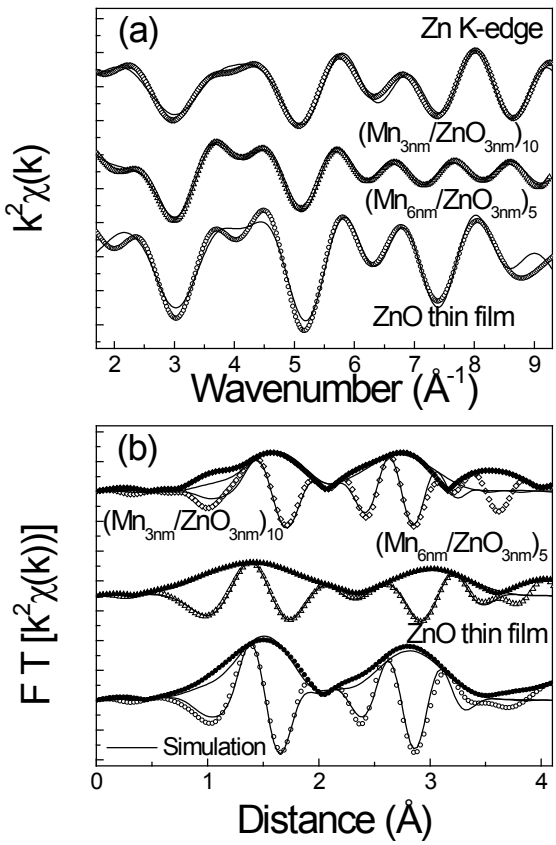

Fig. 3.17 (a) k-space comparison between the filtered EXAFS signal (dots) and simulations (lines) at Mn K-edge of samples t = 6, 1.5 nm and a 100 nm ZnO film. (b) Fourier transform of the (a) plotted signals; modulus and imaginary parts have been presented for dual comparison with calculated contributions (lines).

Summarizing these results, the complex EXAFS analysis of the samples with $t \geq 3$ nm indicates the formation of Zn-Mn-O mixed phases in non-homogenously intermixed

layers, where Mn-rich phase (*RS*), named as Mn-O-Zn and Zn-rich phase (*W*), named as Zn-O-Mn, coexist. For the t = 6 nm sample, majority of *W* mixed phase in comparison with the *RS* phase is evidenced, while the opposite occurs for the t = 3 nm sample. The obtained EXAFS distances fully agree with the ones reported by Pellicer et al.[28] for $Zn_{1-x}Mn_xO$ thin films with *W* or *RS*-stabilized structures.

The analysis is much more simple for samples with t < 1.5 nm, where mostly MnO_2 formation inside *W*-ZnO is identified. Sample with t = 1.5 nm, laying in the barrier between both different situations, shows similarities with both behaviours, being closer to the $t \leq 0.7$ nm one.

3.9. Structural and magnetic scheme

According to the growth conditions, the following model is proposed to explain all the obtained results. For all the samples, the oxygen excess at the surface of the lately deposited ZnO layer can provide a highly oxidized state to the very close Mn atoms and therefore, a very small Mn^{4+} fraction might be expected at the first growth stage of the Mn layers.

For samples with very thin Mn layers, no appreciable differences are expected between top and bottom of the Mn layer, leading to the formation of MnO_2 in the entire non-continuous layer. The formation of MnO_2 nano-clusters inside the ZnO matrix has been evidenced jointly by XRR simulations, X-ray diffraction and EXAFS results. Either the amorphous character of the MnO_2 clusters or the small size of its crystalline grains (indicated by their EXAFS amorphous-like FT magnitudes) implies their non detection by diffraction measurements. The tendency of MnO_2 to be present in a non-stoichiometric state with Mn^{4+} vacancies, Mn^{3+} replacing Mn^{4+} cations and OH^- species replacing O^{2-} anions explains the obtained oxidation states smaller than +4 obtained by XANES. In this case of small t values, due to big differences in the ionic radii, neither Mn^{4+} diffusion into ZnO nor Zn^{2+} diffusion in MnO_2 are expected[30]. Consequently, for $t \leq 0.7$ nm, all the obtained results indicate the formation of amorphous MnO_2

nanoclusters inside the *W*-ZnO matrix, presenting these samples paramagnetic-like behaviour. A scheme of the situation is represented in Fig. 3.18 (right).

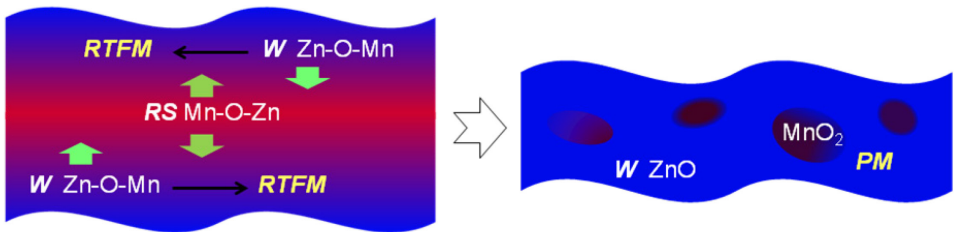

Fig. 3.18 Sample series structural schemes. The images show the simplified structure of samples wit $t \geq 3$ nm (on the left) and with $t \geq 0.7$ nm (on the right).

Conversely, in the case of samples with thicker Mn layers (nominally 3 nm and 6 nm) just the firstly deposited Mn is likely to be highly oxidized. The average Mn oxidation states in these two samples have been found to be +2.1 and +2.2 respectively, and although a small Mn^{4+} amount is expected, this fraction should be very small compared to the dominant phase, being the reason why it is not detectable by EXAFS.

For these large t values, high reactivity of freshly deposited Mn along with competition between Mn and Zn to share oxygen can explain inter-diffusion and the formation of mixed Mn-Zn-O double oxides, where Mn-rich phase (*RS*), named as Mn-O-Zn and Zn-rich phase (*W*), named as Zn-O-Mn, coexist. The mixed *RS* phase formation is favoured by the amount of MnO rocksalt phase as well as the non equilibrium growth conditions, what allows, for instance, stresses in the films. The coexistence of these two phases in the samples with Mn average oxidation states near +2 is corroborated by EXAFS and X-ray diffraction studies, which also discard the existence of appreciable amount of other Mn-Zn-O phases. A schematic representation of this complex situation has been done in Fig. 3.18 (left) for easier understanding.

For the t = 6 nm sample, mainly *W* mixed phase is evidenced, while the contrary occurs for the t = 3 nm sample. In principle, the relative content of both phases should be

related to the obtained coordination numbers, but the nanostructured character makes unattainable to deduce it from EXAFS data because of the finite size effect. Nevertheless, it has been evidenced that the Zn-O-Mn wurtzite phase content is higher in the t = 6 nm sample, confirmed by the relationship between second neighbour coordination numbers. It is worth to note that, unfortunately, the low relative ratio of Zn-O-Mn wurtzite phase wurtzite mixed phase in the t = 3 nm sample does not allow to resolve the two similar Mn-O distances expected.

Finally, in order to prove the validity of this model, the multilayer XANES spectra with large t values should be fitted by a linear combination of the XANES spectra corresponding to Mn in each different phase, wurtzite and rocksalt, whose relative content would be obtained from the fit.

Fig. 3.19 shows the fits of XANES spectra of samples t = 6 and 3 nm. Spectra of Mn in *RS* (Mn in O_h coordination) and Mn in *W* (Mn in T_d coordination) phases used as references (thick solid lines) have been taken from experimental data in Ref. 28, where both phases were obtained in the Mn-Zn-O system under transformation induced by hydrostatic pressure.

First of all, it is important to remark an experimental hint that comes from the pre-edge peak. The existence of this pre-edge (at 6537 eV in Fig. 3.19) indicates tetrahedral (T_d) coordination since it is related to *p-d* hybridization, which is allowed when the Mn site symmetry does not present an inversion center, as in T_d configuration. This pre-edge peak loses most of its intensity in the *RS* phase, with octahedral symmetry (O_h), since it contains an inversion center.[28] The clear existence of this pre-peak for t = 6 nm sample, with majority of *W* phase, as well as the considerable decrease of the pre-peak intensity for t = 3 nm sample should be underlined here, sustaining the obtained EXAFS results.

Finally, as it can be observed in Fig. 3.19, just by linear combination of Mn replacing Zn into the *W* and *RS* phases, the experimental spectra are quite well reproduced, fact that corroborates the coexistence of these two phases for $t \geq 3$ nm samples. The obtained relative content of both phases are $[RS]$ = 25% and $[W]$ = 75% for t = 6 nm sample and $[RS]$ = 70 % and $[W]$ = 30 % for t = 3 nm sample.

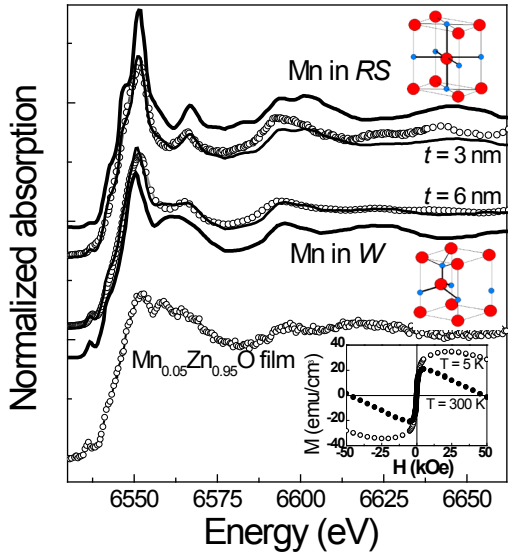

Fig. 3.19 XANES spectra at the Mn K-edge of t = 6 and 3 nm samples and their fits obtained by linear combination of the Mn substituting Zn in wurtzite (W) and rocksalt (RS) reference spectra. Additionally, data from a 100 nm $Mn_{0.05}Zn_{0.95}O$ sputtered thin film, which exhibits RTFM, is given for comparison. Its XANES main features are similar to Mn in wurtzite phase. The inset shows the hysteresis loops of $Mn_{0.05}Zn_{0.95}O$ film at 5 and 300 K. Schematic representations of W and RS crystallographic structures show the corresponding tetrahedral symmetry (T_d) and the octahedral symmetry (O_h).

Furthermore, analysis of magnetic and XAS results shows a direct relation between the Mn-Zn-O wurtzite phase amount and the obtained saturation magnetization value in these multilayers. The obtained ratio between the wurtzite content $[W]$ in the two FM samples, $[W]_{t=6nm}/[W]_{t=3nm}$ is approximately 2.5.

Considering the magnetic properties of these two samples, the ratio between saturation magnetization values of samples, $[M_S]_{t=6nm}/[M_S]_{t=3nm}$, results to be the same value (2.5). **This fact suggests that only Zn-O-Mn wurtzite phase contributes to the observed ferromagnetism**. This is supported by the fact that the XANES spectrum of the 100 nm $Mn_{0.05}Zn_{0.95}O$ sputtered sample, which exhibits RTFM (inset of Fig. 3.19), shows clear similarities with Mn in wurtzite phase (Fig. 3.19). Although ferromagnetism due to Mn oxide with Zn interdiffused cannot be totally discarded, results strongly point

towards RTFM related here to the formation of a Zn-Mn-O double oxide wurtzite phase. Despite the fact that the obtained normalized Mn moments are very small, it should be remarked that results indicate that not all the Mn-Zn-O phases contribute to ferromagnetism. It means that normalizing to the total amount of Mn when calculating magnetization values involves Mn moment values lower than the actual ones.

Recently, B. Gu et al.[31] have performed quantum Monte Carlo calculations in the p-type (Zn,Mn)O compound to determine how the crystal structure influences the impurity bound state, which plays an important role in the development of the FM correlations between the impurities. They have found that the FM correlations are strongly influenced by the crystal structure. In particular, they have observed FM correlations for wurtzite $[W]$ and zinc-blenda $[ZB]$ crystal structures, while no FM correlations between the impurities have been found for the rocksalt $[RS]$ structure.

3.10. Conclusions

Concerning the magnetic properties of Mn multilayered systems, the main conclusion of this chapter is the relevance of the Mn oxidation state in the diffusion process and consequently in the magnetic properties of the films. The role that each particular type of interface plays in the ferromagnetism of this Zn-Mn-O system has been shown.

An evolution of the magnetic response depending on the Mn layer thickness (t) has been observed within the sample series, where room temperature ferromagnetism has been clearly found for $[Mn_{(t)}/ZnO_{(3nm)}]_n$ multilayers with larger values of t (nominally t = 6, 3 nm).

Different Mn electronic states within the sample series, depending on the Mn layer thickness (t) have been revealed by XANES, showing that the average oxidation state ranges from +2.1 to +3.3. Diffraction studies agree with absence of metallic Mn in the samples.

For Mn/ZnO samples with very thin Mn layers ($t \leq 0.7$ nm), conversely to what it was expected, X-ray absorption spectroscopy results have shown that Mn is not diluted into the ZnO layers. Conversely, the formation of amorphous MnO_2 nano-clusters inside the ZnO matrix has been evidenced together by XRR simulations, XAS and XRD results. No sign of metallic Mn, rocksalt nanocrystals or other Mn-Zn-O phases is found.

For the obtained ferromagnetic samples ($t \geq 3$ nm), EXAFS, XANES, HREM and XRD results indicate the coexistence of Mn^{2+} in rocksalt and wurtzite phases. Non-homogenously intermixed layers are expected, with Mn and Zn highly diffused into both ZnO and Mn oxide rich regions. In these samples showing FM, the obtained quantity of Mn in $[W]$ phase (Zn-O-Mn phase) scales with the saturation magnetization, pointing towards this Zn-O-Mn double oxide wurtzite phase as the responsible of the observed RTFM, in agreement with theoretical calculations.

References

[1] D. C Kundaliya, S.B. Ogale, S.E. Lofland, S. Dhar, C.J. Metting, S.R. Shinde, Z. Ma, B. Varughese, K.V. Ramanujachary, L. Salamanca-Riba, and T. Venkatesan, Nat. Mater. 3, 709 (2004).

[2] M. A. García, M. L. Ruiz-González, A. Quesada, J. L. Costa-Krämer, J. F. Fernández, S. J. Khatib, A. Wennberg, A. C. Caballero, M. S. Martín-González, M. Villegas, F. Briones, J.M. González-Calbet, and A. Hernando, Phys. Rev. Lett. 94, 217206 (2005).

[3] S. S. Yan, C. Ren, X. Wang, Y. Xin, Z. X. Zhou, L. M. Mei, M. J. Ren, Y.X. Chen, Y. H. Liu, and H. Garmestani, Appl. Phys. Lett. 84, 2376 (2004).

[4] A. B. Pakhomov, B. K. Roberts, and K. M. Krishnan, Appl. Phys. Lett. 83, 4357 (2003).

[5] J. C. A. Huang, H. S. Hsu, Y. M. Hu, C. H. Lee, Y. H. Huang, and M. Z. Lin, Appl. Phys. Lett. 85, 3815 (2004).

[6] J. C. A. Huang, H. S. Hsu, J. H. Sun, S. L. Chiu, C. H. Lee, Y. F. Liao, and H. Chou, J. Appl. Phys. 103, 07D128 (2008).

[7] Z-W Jin, Y-Z Yoo, T. Sekiguchi, T. Chikyow, H. Ofuchi, M. Oshima, and H. Koinuma, Appl. Phys. Lett. 83, 39 (2003).

[8] M. Kunisu, F. Oba, H. Ikeno, I. Tanaka, and T. Yamamoto, Appl. Phys. Lett. 86, 121902 (2005).

[9] J. Pellicer-Porres, A. Segura, J. F. Sánchez-Royo, J. A. Sans, J. P. Itié, A. M. Flank, P. Lagarde, and A. Polian, Appl. Phys. Lett. 89, 231904 (2006).

[10] W. Xu, Y. Zhou, X. Zhang, D. Chen, Y. Xie, T. Liu, W. Yan, and S. Wei, Solid State Commun. 141, 374 (2007).

[11] J-H Guo, A. Gupta, P. Sharma, K. V. Rao, M. A. Marcus, C. L. Dong, J. M. O. Guillen, S. M. Butorin, M. Mattesini, P. A. Glans, K. E. Smith, C. L. Chang, and R. Ahuja, J. Phys.: Condens. Matter 19, 172202 (2007).

[12] Z. Gu, M- Lu, J. Wang, D. Wu, S. Zhang, X. Meng, Y. Zhu, S. Zhu, and Y. Chen, Appl. Phys. Lett. 88, 082111 (2006).

[13] J. Lu, J.K. Liang, Q.L. Liu, F.S. Liu, Y. Zhang, B.J. Sun, and G.H. Rao, J. Appl. Phys. 97, 086106 (2005).

[14] S. S. Yan, C. Ren , X. Wang, Y. Xin, Z. X. Zhou , L. M. Mei, M. J. Ren, Y. X. Chen, Y. H. Liu, H. Garmestani, Appl. Phys. Lett. 84, 2376 (2004).

[15] N. D. Telling, S. J. Guilfoyle, D. R. Lovett, C. C. Tang, M- D. Crapper, and M. Petty, J. Phys.

D: Appl. Phys. 31, 472(1998).

[16] N. Mehan,V. Gupta, K. Sreenivas, and A. Mansingh J. Appl. Phys. 96, 3134 (2004).

[17] Z. Li and W. Gao, Mater Lett 58, 1363 (2004).

[18] J.J. Chen, Y. Gao, F. Zeng, D. M. Li and F. Pan, Appl. Surf. Sci. 223, 318 (2004).

[19] J. Jou , M. Han and D. Cheng, J. Appl. Phys. 71, 4333 (1992).

[20] J. Lee, Z. Li , M. Hodgson , J. Metson , A. Asadov, W. Gao, Current. Appl. Phys. 4, 398 (2004).

[21] S. Takada, J. Appl. Phys. 73, 4739 (1993).

[22] D.A. McKeown and J.E. Post, Am. Mineral. 86, 701 (2001).

[23] M. Croft, D. Sills, M. Greenblatt, C. Lee, S.-W. Cheong, K. V. Ramanujachary and D. Tran, Phys. Rev. B 55, 8726 (1997).

[24] K. V. Klementiev, VIPER for Windows, freeware: www.desy.de/~klmn/viper.html; J. Phys. D 34, 209 (2001).

[25] S. I. Zabinsky, J. J. Rehr, Phys. Rev. B 52, 2995 (1995).

[26] B. Gilbert, B.H. Frazer, A. Beltz, P.G. Conrad, K.H. Nealson, D. Haskel, J.C. Lang, G. Srajer, and G. De Stasio, J. Phys. Chem. A 107, 2839 (2003).

[27] N. Gay-Sanz, C. Prieto, A. Muñoz-Martín, A. de Andrés, M. Vázquez and Seong-Cho Yu, J. Mater. Res., 14, 3882-3888 (1999).

[28] J. Pellicer-Porres, A. Segura, J. F. Sánchez-Royo, J. A. Sans, J. P. Itié, A. M. Flank, P. Lagarde, and A. Polian, Appl. Phys. Lett. 89, 231904 (2006).

[29] B. Mokili, Y. Charreire, R. Cortes, and D. Lincot, Thin Solid Films 288, 21 (1996).

[30] M. Peiteado, A.C. Caballero and D. Makovec, J. Solid State Chem. 180, 2459 (2007).

[31] B. Gu, N. Bulut and S. Maekawa, J. Appl. Phys. 104, 103906 (2008).

Chapter 4

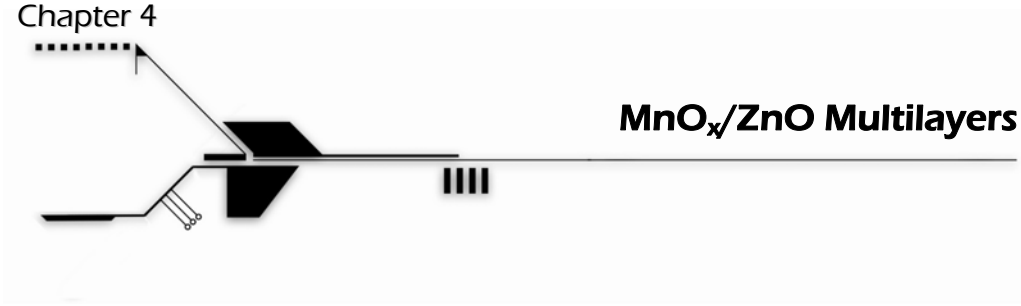

MnO_x/ZnO Multilayers

4.1. Motivation

Prompted by the relevance of the Mn oxidation state found in the diffusion process and consequently in the magnetic properties of the Mn/ZnO multilayers, we have also prepared MnO_x/ZnO multilayers under similar conditions as the former Mn/ZnO ones. A detailed magnetic, electronic and structural characterization is presented aimed at studying how this early Mn oxidation during the preparation process influences the magnetic behaviour of this system.

4.2. Preparation of MnO_x/ZnO multilayers

$[MnO_{x\,(t)}/ZnO_{(3nm)}]_{75}$ multilayers were prepared also by sequential DC sputtering of ZnO and Mn on Si(100) substrates at room temperature. The experimental conditions for the ZnO deposition were the same as described in section 3.2. The DC power supplied for Mn was also about 9 W. However, instead of using Ar gas to sputter Mn, an O_2/Ar mixture gas (30% O_2-rich, same as for the ZnO) was employed for the Mn sputtering. The main differences in the preparation process of these multilayers are, firstly, that the same gases were used here for the different layers, and secondly, that just a very short pre-sputtering was performed between layers (5 s before each layer compared to 1 min in the case of Mn/ZnO multilayers). The Mn sputtering times were the same as in t = 0.4 and 0.2 nm samples. However, the expected Mn thickness is considerably smaller here since the O_2 sputtering efficiency is minor than the Ar one. The principal growth parameters are collected in Table 4.I.

Table 4.I. Parameters of the MnO_x/ZnO multilayer growth and sample description.

Nominal sample $[MnO_{x\ (t)}/ZnO_{(3nm)}]_n$	Mn $t_{sputtering}$ (s)	Mn DC power (W)	O_2/Ar sputtering P (mbar)	Sample label
$[MnO_{x\ (1Å)}/ZnO_{(3nm)}]_{75}$	7	9	$5.4x10^{-3}$ mbar	A
$[MnO_{x\ (0.5Å)}/ZnO_{(3nm)}]_{75}$	4	9	$5.4x10^{-3}$ mbar	B

4.3. Magnetic properties

Magnetic hysteresis loops of samples A and B are shown in Fig. 4.1, where the magnetization per manganese atom has been calculated taking into account the precise amount of Mn obtained by Rutherford Backscattering Spectroscopy experiments. The silicon substrate diamagnetic contribution has been subtracted at the plots.

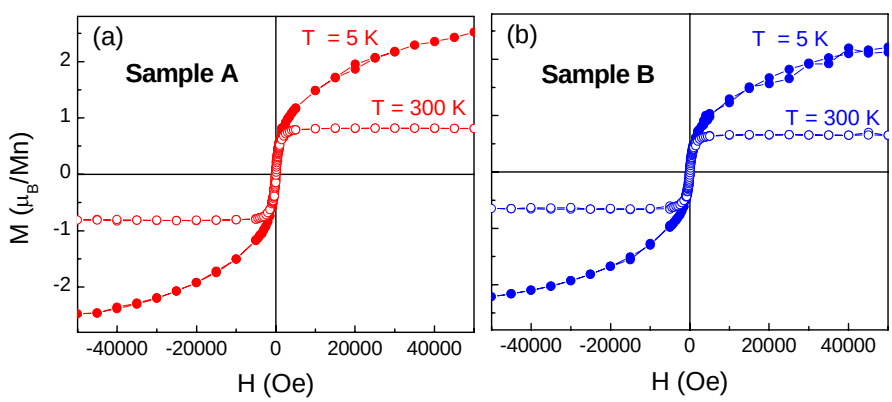

Fig. 4.1 M-H curves of samples A and B at different temperatures.

For the two studied samples, a clear ferromagnetic component as well as an additional paramagnetic one, which appears at the low temperature regime, can be observed. Saturation magnetization values as large as 0.8 μ_B per Mn atom at 300 K have been found for sample A and nearly 0.7 μ_B per Mn atom for sample B. These values correspond to approximately 2.4 x 10^{-4} emu/cm^2 and 1.8 x 10^{-4} emu/cm^2 for samples A

and B, respectively. The magnetization versus temperature is depicted in Fig. 4.2, where a T_C higher than 400 K can be inferred for both samples.

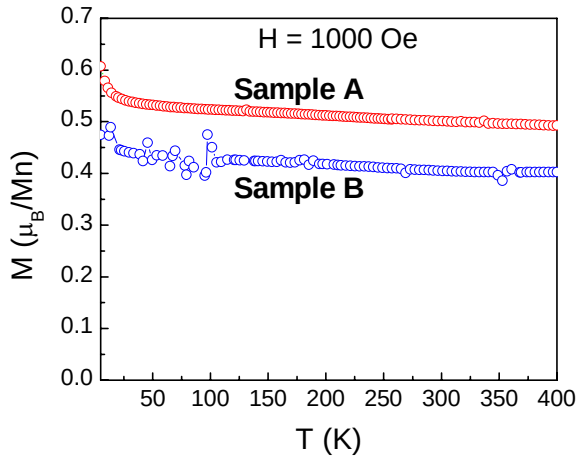

Fig. 4.2 Magnetization curves (H = 1kOe) for samples A and B.

It should be underlined the fact that considerably higher M_S values have been obtained for these samples in comparison with the previous Mn/ZnO multilayers. At first sight, though, this fact does not seem to agree with the results aforementioned, where none appreciable ferromagnetism was expected for higher Mn oxidation states. However, the Mn oxidation during the growth process can involve dissimilar electronic and structural properties. A structural and electronic characterization of these samples is presented here to study the origin of these exciting magnetic properties.

4.4. Rutherford Backscattering Spectroscopy (RBS)

RBS experiments were performed to evaluate the actual amount of Mn sample as well as the film atomic composition of each MnO_x/ZnO sample. Data acquisition and simulations were performed in the same way as for the Mn/ZnO samples (described in section 3.5), and the spectra were measured with incident ions of 2 and 8 MeV. RBS spectra collected at 8 MeV to distinguish the Mn and Zn contributions are exhibited in Fig. 4.3, where spectra corresponding to the ZnO/Mn multilayers t = 0.2 and 0.1 nm

have been included for comparison. The film composition calculated after analysis of the two energies is given in Table 4.II. By means of RBS, a fair approximation of the small concentration of Mn in each sample is obtained. Anyway, it should be remarked that the small % of Mn atoms obtained for samples A and B (about 2%) is near the resolution limit order of this technique. The uncertainty in the calculated value is therefore considerably large, what means that, for instance, small differences between the atomic compositions of sample A and B, that are in fact expected, might not be distinguished.

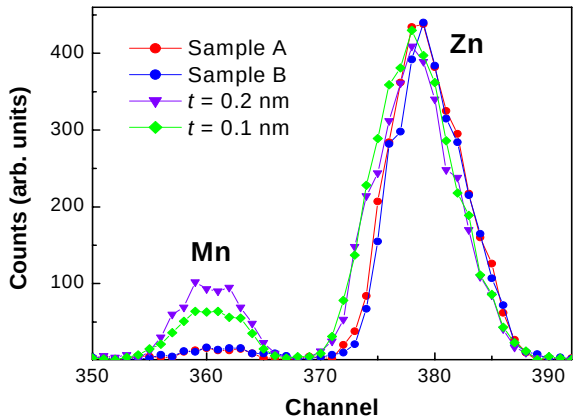

Fig. 4.3 (a) RBS spectra taken at energy of incident ions of 8 MeV of samples A and B. Spectra of previous t = 0.2 and 0.1 nm samples are included for comparison.

Table 4. II. Mn-layer atomic density and sample composition obtained from simulations of RBS data.

Sample	Total Mn atomic density (10^{16} at./cm^2)	Composition (%)		
		[Mn]	[Zn]	[O]
A	3.2	0.02	0.49	0.49
B	3.0	0.02	0.49	0.49
t = 0.2 nm	26.3	0.13	0.34	0.53
t = 0.1 nm	25.8	0.11	0.34	0.55

4.5. X-Ray Reflectivity (XRR)

X-ray reflectivity spectra of samples A and B, performed on a Bruker D8 X-ray diffractometer with a Cu K_α source, are shown in Fig. 4.4. No appreciable peaks of heterostructure periodicity in the out-of-plane direction are observed for samples A and B, where the Mn amount deposited was very small and non-continuous growth is expected.

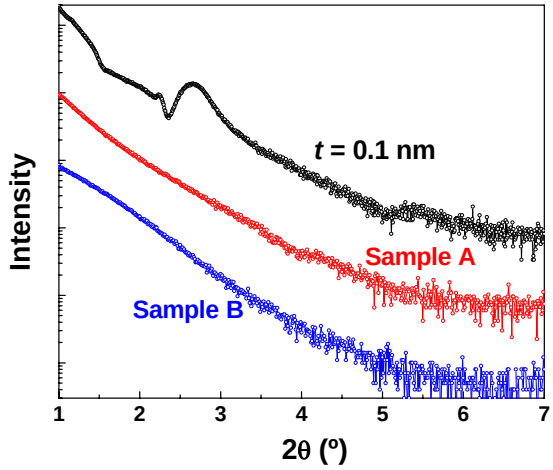

Fig. 4.4 (a) X-ray reflectivity spectra and of samples A, B and previous t = 0.1 nm (included for comparison). All spectra have been vertically shifted for clearness.

Some periodicity features can be distinguished, by contrast, in the t = 0.1 nm spectrum, consisting of MnO_2 clusters inside the ZnO matrix, included for comparison. Conversely to the t = 0.1 nm sample, samples A and B do not show superstructure. Different facts as the very small size of the Mn-rich particles, random particle distribution, Mn dilution into ZnO or large film roughness can be the reason for these dissimilar A and B sample spectra, showing clear differences with the Mn/ZnO multilayers.

4.6. X-Ray Diffraction (XRD)

Diffraction measurements on the sample series were carried out in a standard laboratory diffractometer by using the K_α radiation line of Cu in θ-2θ configuration. XRD spectra of samples A and B and the former t = 0.1 nm sample are shown in Fig. 4.5. The (002) peak corresponding to the hexagonal wurtzite-ZnO (*W*-ZnO) crystal structure can be clearly observed for samples A and B, which exhibit very similar XRD diffractograms. Moreover, their (002) peak intensities are considerably high compared to the t = 0.1 nm sample, which has approximately the same ZnO content, showing a higher texturation degree. No additional phases are detected by this first XRD characterization.

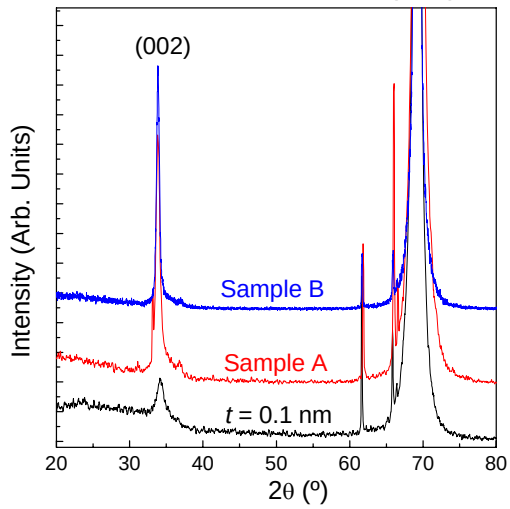

Fig. 4.5 X-ray diffractograms of samples A, B, where the (002)-ZnO and (400)-Si_{subst} peaks can be observed. The spectrum of the t = 0.1 nm sample (from the Mn/ZnO multilayer series) has been included for comparison.

In order to obtain more structural information, X-ray diffraction experiments were carried out in a six-circle diffractometer especially designed for thin film characterization with λ = 0.8857 Å, at the Spanish CRG beamline (Spline, BM25, branch B) of the European Synchrotron Radiation Facility (ESRF), Grenoble.

Grazing incidence and θ-2θ X-ray diffraction spectra of sample A and a ZnO sputtered film under same experimental conditions, included for comparison, are depicted in Fig. 4.6. Similar grazing incidence spectra (omega-angle geometry with ω=0.75º) are observed for both films, in agreement with the ZnO reference (Fig. 4.6(a)). Regarding the θ-2θ scan (Fig. 4.6(b)), it can be observed that the (002)-wurtzite peak position of sample A is in agreement with the ZnO reference, showing that there is not any noticeable shift respect to pure *W*-ZnO. However, slight differences between sample A and the ZnO film crystalline quality can be noticed. Table 4.III summarizes the size of the ZnO wurtzite nanocrystalline grains along the out-of-plane direction obtained for different samples by using the Scherrer formula.

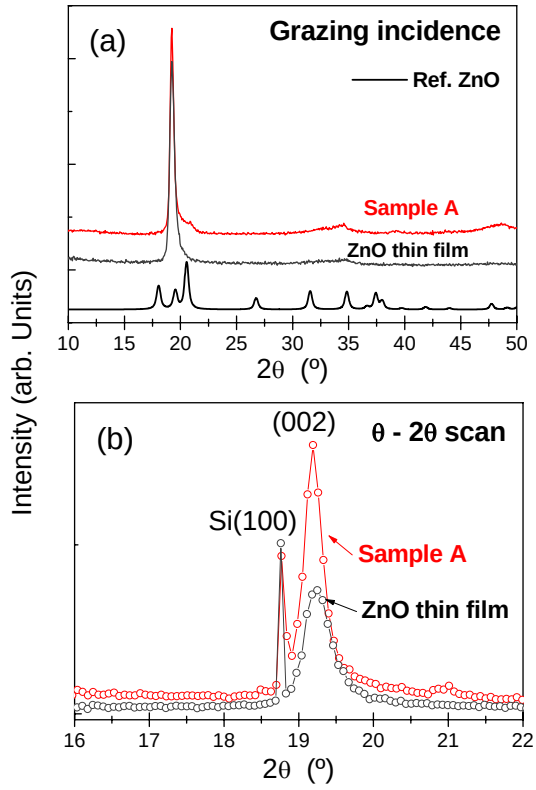

Fig. 4.6 (a) Grazing incidence (ω = 0.75º) X-ray diffraction of sample A and a 70 nm sputtered ZnO film. (b) θ-2θ X-ray diffraction of the same samples.

The obtained crystalline grain size for samples A and B (about 20 nm) are much larger than the 3 nm corresponding to the ZnO layer nominal thickness, showing no restriction to the ZnO grain size growth in the out-of-plane direction, in agreement with XRR measurements. Furthermore, the A and B grain sizes are even considerably larger than the obtained for the sputtered ZnO film (≈ 10 nm), what signals that the **MnO_x deposition favours the ZnO nanocrystalline grain growth in the out-of-plane direction**. This fact agrees more with MnO_x nanoparticles formation acting as surfactants for the ZnO grain growth than with Mn dilution into the ZnO nanocrystals. Moreover, no (002)-wurtzite peak shift was found from θ-2θ measurements for sample A. Either the possible amorphous character of the MnO_x nanoparticles or the small size of the MnO_x crystalline grains can imply their non detection by diffraction measurements.

Table 4.III. Average crystalline grain size in the out-of-plane direction obtained by θ-2θ measurements.

Sample	*n*	Grain size (nm)
A	75	17
B	75	20
t = 0.1 nm	75	7.7
ZnO film	70 nm (film thickness)	10.4

4.7. X-Ray Absorption (XAS)

Mn electronic states of the MnO_x/ZnO multilayers have been investigated by means of X-ray absorption spectroscopy at the Mn K-edge and the Mn $L_{3,2}$-edge.

4.7.1. XANES at the Mn K-edge

The Mn K-edge XANES spectrum of samples A and B in comparison with Mn metal, Mn^{2+}, Mn^{3+} and Mn^{4+} from references, are shown in Fig 4.7. Firstly, it is important to remark that nearly identical XANES spectra are observed for both samples. Since very similar magnetic behaviours were obtained for both samples, this fact suggests that the small differences in the magnetization values are more related to the number of Mn cations evolve in the ferromagnetism than to differences in the Mn oxidation states of both samples.

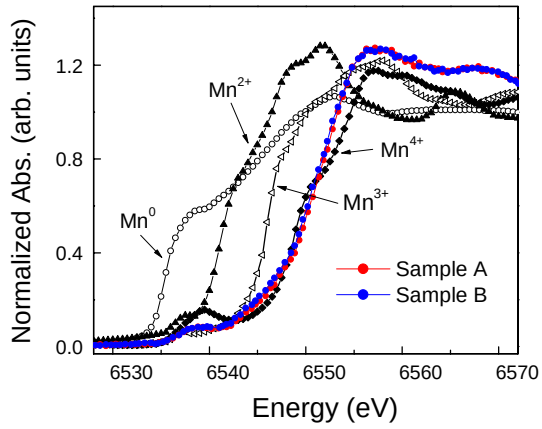

Fig. 4.7 Mn K-edge XANES spectra of samples compared with Mn^0, Mn^{2+} (MnO), Mn^{3+} (MnOOH) and Mn^{4+} (MnO_2) references1.

Considering the XANES shape and threshold energy, it can be inferred dominant Mn^{4+} contribution in both samples and probably a small contribution from Mn^{3+}, since samples A and B present absorption higher than the corresponding to Mn^{4+} reference at 6445 eV, where Mn^{3+} has an important signal. In order to estimate the average Mn oxidation state, as it was described in section 3.8.1 for the Mn/ZnO multilayers, calculation is troubled by the splitting of the 1*s*-4*p* transition,[2] what affects to the first maximum position of the first derivative. Thus, estimation was done by using the threshold energy corresponding to one third of the jump. Following the same procedure, an average Mn valence close to +3.8 ± 0.2 can be inferred for samples A and B. Several XANES features, as differences in the pre-peak region, the slight energy shift and some

XANES shape dissimilarities respect to Mn^{4+} seem to be indicative of mixed Mn oxidation state. Nevertheless, in order to obtain more information about this fact, additional soft energy XAS measurements have been done at the Mn $L_{3,2}$-edge.

4.7.2. XAS at the Mn $L_{3,2}$-edge

The Mn $L_{3,2}$ XAS structure is a fingerprint for the 3*d* count, giving reliable information on the Mn oxidation state and symmetry. (Details of the Mn $L_{3,2}$ XAS spectra characteristics and calculations are described in section 2.6.2)

Figure 4.8 shows the normalized XAS spectrum of sample A measured at RT, where the L_3 and L_2 step edges have been subtracted from the experimental XAS spectrum. It can be observed that the L_3 edge exhibits complex multiple absorption peaks, what is a hint of mixed charge states in sample A. Theoretical calculations for the Mn^{3+} (d^4) and Mn^{4+} (d^3) electronic configurations in T_d environment[3] are included in the figure for comparison. The multiple experimental features of the spectrum indicate that **$3d^n \rightarrow 2p^5 3d^{n+1}$ absorption spectrum corresponds to a mixed Mn^{3+}/Mn^{4+}** ground state, as it was pointed by the Mn K-edge XANES measurements.

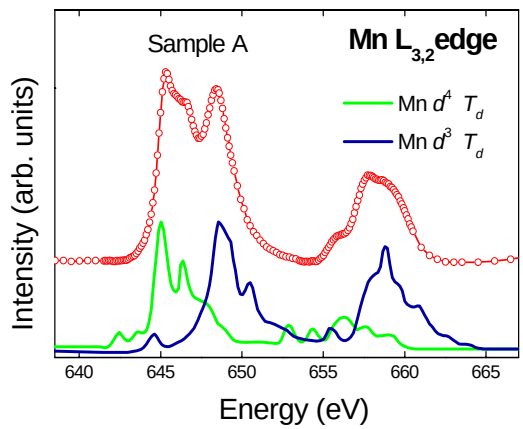

Fig. 4.8 Normalized Mn $L_{3,2}$ XAS spectra of sample A measured at RT. The L_3 and L_2 step edges have been subtracted by two atan functions after background removal. Calculations of Mn^{3+} (d^4) and Mn^{4+} (d^3) in T_d crystal symmetry and appreciable crystal field ($10Dq$ = 1-3 eV) are included for comparison.

4.8. Thermal post-deposition annealing

With the purpose of modifying their magnetic response, thermal post-annealing of the samples was carried out. Samples were annealed in a vacuum system furnace, firstly evacuated up to 1 x 10^{-6} mbar. The thermal treatment was performed under oxygen atmosphere of 1 x 10^{-2} mbar, during two hours at 750 ºC. The XANES spectra at the Zn K-and at the Mn K-edge as well as the obtained evolution of the magnetic properties are given in Fig. 4.9.

The Zn K-edge XANES spectra of sample A, as-grown and after annealing, shown in Fig 4.9(a), are nearly identical, and they do not present any significant difference in comparison with the included ZnO spectrum. Just a nearly negligible enhance of the signal amplitude for the annealed sample, which can be assigned to the increase of the ZnO crystal quality after the thermal treatment, could be inferred.

Looking at the Mn K-edge spectra of the samples, by contrast, we can found remarkable changes in the spectra (Fig. 4.9(b)). After annealing, a clear energy threshold shift towards lower energies is obtained. This fact evidences that, even if oxygen gas was introduced in the vacuum furnace during all the thermal treatment, annealing leads to a decrease of the Mn average oxidation state in the samples. Considering the spectral shape and threshold energy, it can be inferred that after annealing, the dominant Mn^{4+} contribution turns into Mn^{3+}. Comparing with the Mn^{3+} spectrum, there are several spectral dissimilarities which indicate that manganese in the annealed samples is not in a pure Mn^{3+} valence state. **The coexistence of mixed Mn^{3+} and Mn^{4+} valences with major presence of Mn^{3+} is pointed out by XANES**. Furthermore, it is important to remark that sample A and B exhibit extremely similar XANES as-grown spectra. After the thermal treatment, their spectral shape is considerably modified, but in the same manner for both samples, which show again nearly identical XANES spectra, what is a clear sign of the reproducibility of the process.

The evolution of ferromagnetism with the annealing treatment is shown in Fig. 4.9(c). Although RTFM is still observed, thermal treatment of samples involve a noticeably worsen of the ferromagnetic properties, leading to a reduction of the

magnetization of about one half. According to the XANES results for the as-grown and annealed samples, **RTFM here seems to be related mostly to Mn^{4+}, which coexists with Mn^{3+}**. Additional effects from annealing, as for instance improvement of crystallinity or film texture, can modify the magnetic behaviour. However, all these facts seem to point more towards the enhancement of the magnetic anisotropy and consequently improve ferromagnetism, than to the outcome decrease.

A more detailed discussion is presented below to examine the origin of the RTFM obtained for these ZnO/MnO_x samples (A and B) in comparison with the previous ZnO/Mn ones.

4.9. Discussion and remarks: The origin of FM in MnO_x/ZnO multilayers versus the origin in the so-called Mn/ZnO multilayers.

The obtained results indicate de **formation of $MnO_{2-\delta}$ nanoparticles embedded in *W*-ZnO** for the two similar samples (A and B) prepared by oxidizing Zn and Mn by sequential reactive sputtering.

XANES measurements at the Mn K-edge have indicated an average Mn oxidation state slightly smaller than + 4 in both samples. In addition, XRD measurements have shown that there is not any shift in the (002)-wurtzite peak of these samples with respect to the pure *W*-ZnO, according to no Mn inclusion into the ZnO lattice. In fact, the big differences between the Zn^{2+} and the Mn^{4+} ionic radii make Mn^{4+} diffusion into ZnO not very likely[4]. Either the amorphous character of the $MnO_{2-\delta}$ nanoparticles or the small size of the crystalline grains can imply their non detection by XRD.

RBS measurements have shown that the atomic composition of both samples is approximately $Mn_{0.02}Zn_{0.49}O_{0.49}$, confirming the small Mn relative ratio in the films. Both the small Mn amount and the small $MnO_{2-\delta}$ particle size agree with the XRR spectra, which exhibited lack of heterostructure periodicity in the out-of-plane direction.

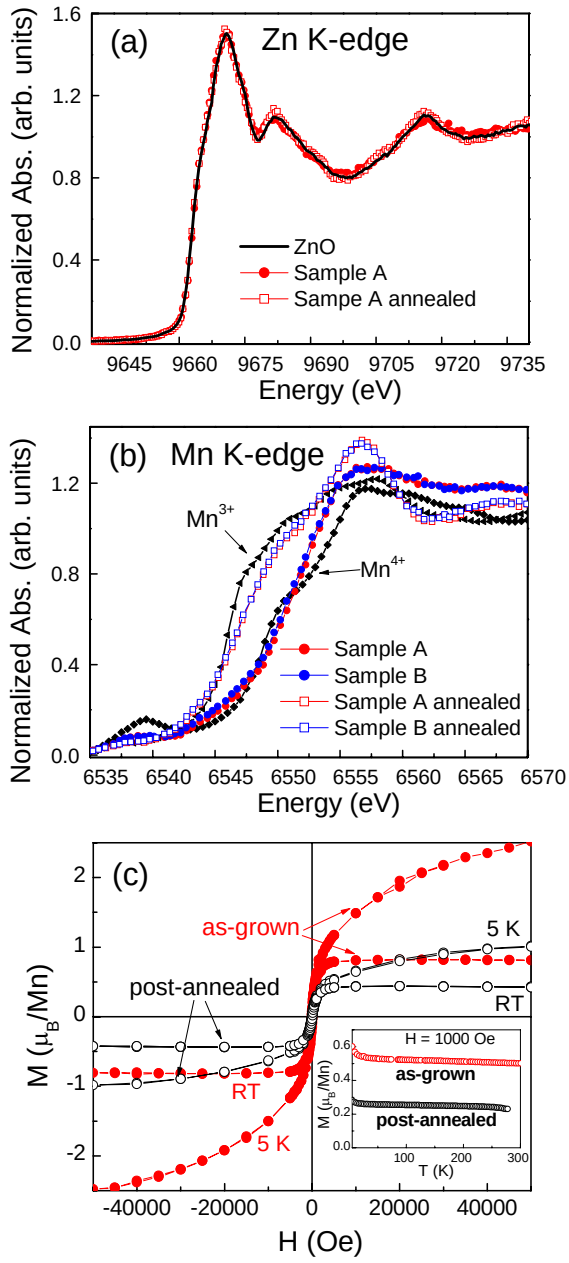

Fig. 4.9 (a) Zn K-edge XANES spectra of sample A annealed and as-grown. A ZnO sputtered film is also included for comparison. (b) Mn K-edge XANES spectra of samples A and B annealed in oxygen compared with samples as grown and Mn^{2+} (MnO) and Mn^{3+} (MnOOH) references[1]. (c) Comparison between the hysteresis loops at different temperatures of sample A as grown and post-annealed. The inset shows the magnetization vs. temperature at H = 1 KOe.

Apart from that, it has been shown by XRD that the presence of these small manganese oxide grains favours the ZnO crystalline grain growth in the out-of-plane direction, increasing the ZnO grain size in this axis a factor of 2. This fact is a sign of the **$MnO_{2-\delta}$-ZnO interface interaction**, which relaxes possible stresses appearing during growth and allows larger ZnO grains.

Regarding the magnetic properties, ferromagnetic ordering above RT has been found for the two similar samples. The M_S values obtained here, in comparison with the found for the ZnO/Mn samples, are significantly larger, more than one order of magnitude. However, these results seem to completely disagree with the former ones explained for the Mn/ZnO samples, since no appreciable ferromagnetic order was expected for these higher Mn oxidation states. In order to resolve this apparent discrepancy, several facts should be taken into consideration.

Firstly, the obtained magnetization values have been normalized to the total amount of Mn in each case. However, in the case of Mn/ZnO samples, it was found that not all the Mn-Zn-O phases contribute to ferromagnetism, being responsible just Mn in the wurtzite phase. Therefore, the actual effective magnetizations per Mn atom in these samples become somewhat larger.

For the MnO_x/ZnO samples, though, considering the small Mn/Zn ratio (about 4 at. %) and the lack of experimental evidences of coexistence of different phases, it seems reasonable to think that most of the $MnO_{2-\delta}$ nanoparticles are in the same crystallographic phase, all contributing similarly to the ferromagnetic order. In this case, however, a higher uncertainty in the calculation of the effective magnetization per Mn atom can come from the small value of the Mn atomic density obtained by RBS, which is one order of magnitude smaller than in the Mn/ZnO samples and close to the resolution limit. Small variations in the number of Mn atoms can lead to big differences in the calculated magnetization per Mn atom. However, the Mn amount in the samples cannot be much larger than the obtained by RBS.

Nevertheless, all these facts are not enough to explain the large magnetization values found for these samples (M_S of 2 x 10^{-4} emu/cm^2 compared to 6 x 10^{-5} emu/cm^2, obtained for the most ferromagnetic ZnO/Mn sample, both values are normalized to the sample area and without normalizing to the Mn amount).

Actually, the obtained results indicate that the origin of the interaction governing the magnetic properties of the previous Mn/ZnO films, where freshly deposited Mn with high reactivity becomes oxidized prompted by the ZnO presence, clearly differs from the case of intentional Mn oxidation during the growth process. Besides, **the smaller grain size of the $MnO_{2-\delta}$ particles here enhances the effect of the surrounding ZnO**.

While in the case of Mn/ZnO layers, RTFM was due to the formation of Wurtzite Mn-Zn-O phase in a mixed *W-RS* oxide, it seems that in this case RTFM is not associated with a phase but with the interface between nonferromagnetic phases.

Previous works carried out by M. A. García et al.5 and J. F. Fernández et al.6 on Mn-Zn-O bulk samples prepared from ZnO-MnO_2 mixed powders (2%MnO_2-98%ZnO and 10%MnO_2-90%ZnO) have shown that the presence of the ZnO around MnO_2 modifies the kinetics of $MnO_2 \rightarrow Mn_2O_3$ reduction and favours the coexistence of both Mn oxidation states.

In our samples, the $MnO_{2-\delta}$-ZnO interaction at the interface has been evidenced by XRD while the coexistence of Mn^{4+} and Mn^{3+} has been confirmed by Mn K-edge and Mn L-edge XANES measurements.

The origin of the ferromagnetism here agrees with the new class of surface magnetism proposed by M. A. García and co-workers[5]: **double-exchange mechanism, at the interface between two compounds containing Mn atoms in different oxidation states**. The presence of Mn^{3+} cations in the MnO_2 is not sufficient for the appearance of FM response. The FM is by contrast related to the coexistence of Mn^{3+} and Mn^{4+} ions at the Zn diffusion front, into the manganese oxide grains, being the presence of **Zn cations required for the double-exchange mechanism**.

The explanation of the process is the following:

The double exchange mechanism is based on the fact that Mn^{4+} and Mn^{3+} separated by an O can share an electron (reducing in this way their energy) by simultaneous transfer of an electron from one Mn atom to the O and from the O to the other Mn atom, as illustrated in Fig 4.10, similarly to the reported in Ref. 7. Because the spin cannot change in this transfer, a condition for this itinerancy is that both manganese ions must be polarized. Therefore, it implies a reduction of the energy associated to magnetic order that is responsible for ferromagnetic behaviour. Apart from the Mn^{4+} and Mn^{3+} coexistence, a particular geometry on the Mn-O-Mn bonds must be satisfied for the interaction.

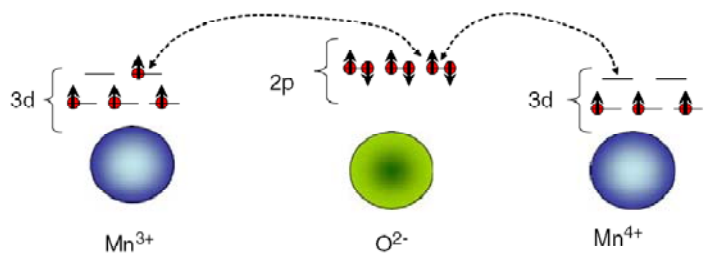

Fig. 4.10 Representation of the double exchange mechanism between Mn^{3+} and Mn^{4+}

It has been also reported[6] that, at higher temperatures, the stable Mn-Zn-O form is the spinel phase ($Zn_xMn_{3-x}O_4$), which allows the incorporation of excess Mn. As the spinel phase progress, it has been obtained the reduction of the M_S, what corroborates that the FM response is not associated with the formation of such a phase. In our experiments, **thermal treatment of the $MnO_{2-\delta}$ nanoparticles inside the *W*-ZnO** matrix showing RTFM, have also led to a **marked reduction of the FM signal,** what has been related to the considerable **increased of Mn^{3+}**, what is in agreement with these reports, according to the proposed **double-exchange mechanism**.

Considering the double exchange mechanism in the Mn-Zn-O system, the smaller amount of manganese in the mixture (to a certain limit), the larger the ferromagnetic response, since FM is increased by maximizing the interface. Taking into account the

observed magnetic differences between the MnO_x/ZnO and Mn/ZnO series, this fact can clarify the absence of ferromagnetism in those Mn/ZnO samples consisting of MnO_2 clusters inside the ZnO matrix. **Both the much higher Mn/Zn relative ratio in the Mn/ZnO samples that present MnO_2 clusters** (about 30 at. % for the t = 0.1 nm sample) in comparison with the MnO_x/ZnO ones (about 4 at. %) and the associated **smaller effect of the neighbouring ZnO** can explain the **absence of ferromagnetism**.

Summarizing, regarding both sample series, we have found that the **ZnO presence has a significant influence either on the deposited Mn or MnO_2.** On one hand, considering the reactive sputtering process, possible oxygen excess at the surface of the former deposited ZnO layer together with the high reactivity of the freshly deposited Mn can imply the oxidization of the very close Mn atoms. On the other hand, the ZnO that surrounds small highly oxidized manganese grains seems to favour the MnO_2 reduction, which usually starts at a lower temperature in the presence of Zn. In both situations, a thermodynamically stable MnO_x-ZnO state seems to be reached. Our experimental results show that the origin of the ferromagnetism is different in both cases. The first mechanism consists on magnetic interactions between the Mn^{2+} cations of a wurtzite Mn-Zn-O phase via the conduction electrons, what leads to "soft" ferromagnetism, while the second one is associated with the coexistence of Mn^{3+} and Mn^{4+} that interacts via double exchange mechanism.

Therefore, **two different approaches to the study of the role of interfaces and the relevance of the Mn valence state in the Mn-Zn-O system have led to two different types of magnetism** that can be possible in this system. Since these mechanisms are not incompatible, taking both into consideration can contribute to clarify the controversy on the ferromagnetic origin of this system.

4.10. Conclusions

In this chapter, the relevance of the Mn oxidation state in the ferromagnetic response of the Mn-Zn-O system as well as the important role played by the ZnO-MnO_x interface region has been confirmed once more.

$MnO_{2-\delta}$ nanoparticles embedded in *W*-ZnO (with Mn/Zn ratio of approximately 4 at. %) have been obtained by oxidizing Zn and Mn by sequential reactive sputtering.

The presence of these small manganese oxide grains greatly favours the ZnO crystalline grain growth in the out-of-plane direction, what is a sign of the $MnO_{2-\delta}$-ZnO interface interaction.

Ferromagnetic response over room temperature has been found for these samples, showing M_S values as large as 0.8 μ_B per Mn atom at RT.

Experimental results signal that the origin of the ferromagnetism in these $MnO_{2-\delta}$-ZnO samples comes from the simultaneous presence of Mn^{3+} and Mn^{4+} ions that, under the effect of the neighbouring ZnO, interact via double-exchange mechanism. The coexistence of Mn^{4+} and Mn^{3+} has been confirmed by Mn K-edge and Mn $L_{3,2}$-edge XANES measurements.

Looking into these $MnO_{2-\delta}$-ZnO samples together with the former Mn/ZnO multilayers, it has been evidenced that the ZnO presence has a significant influence either on the deposited Mn or MnO_2, being the origin of the ferromagnetism different in both cases.

Two different approaches to the study the Mn-Zn-O system have led to two different types of magnetism. One mechanism is based on magnetic interactions between the Mn^{2+} cations of a wurtzite Zn-Mn-O phase while the second one is associated with double exchange mechanism between Mn^{4+} and Mn^{3+}.

The obtained RTFM assigned to double exchange mechanism is nearly one order of magnitude stronger than the RTFM achieved to the Mn-Zn-O wurtzite phase

formation. Nevertheless, the two mechanisms are not incompatible, fact that should be considered to clarify the controversy on the ferromagnetic origin of this system.

References

1 D.A. McKeown and J.E. Post, Am. Mineral. 86, 701 (2001).

2 M. Croft, D. Sills, M. Greenblatt, C. Lee, S.-W. Cheong, K. V. Ramanujachary and D. Tran, Phys. Rev. B 55, 8726 (1997).

3 G. van der Laan and I. W. Kirkman, J. Phys.: Condens. Matter 4, 4189 (1992).

4 M. Peiteado, A.C. Caballero and D. Makovec, J. Solid State Chem. 180, 2459 (2007).

5 M. A. García, M. L. Ruiz-González, A. Quesada, J. L. Costa-Krämer, J. F. Fernández, S. J. Khatib, A. Wennberg, A. C. Caballero, M. S. Martín-González, M. Villegas, F. Briones, J.M. González-Calbet, and A. Hernando, Phys. Rev. Lett. 94, 217206 (2005).

6 J. F. Fernández, A. C. Caballero, M. Villegas, S. J. Khatib, M. A. Bañares, J. L. G. Fierro, J. L. Costa-Kramer, E. López-Ponce, M. S. Martín-González, F. Briones, A. Quesada, M. García and A. Hernando, Phys. Rev. Lett. 94, 217206 (2005).

7 A. Quesada, M. A. García, P. Crespo and A. Hernando, J. Magn. Mag. Mat. 304, 75 (2006).

Chapter 5

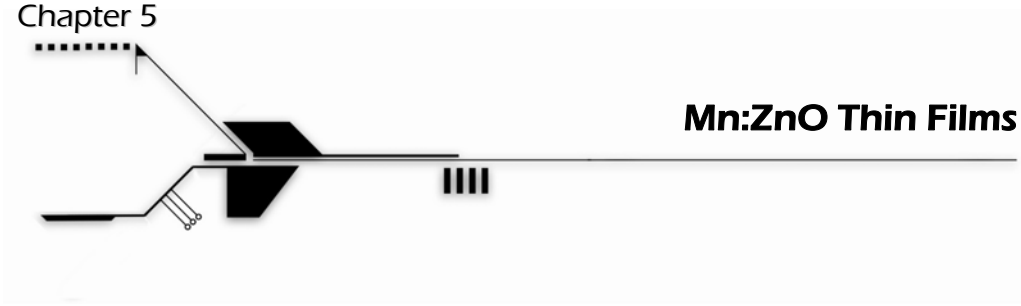

Mn:ZnO Thin Films

5.1. Motivation

Differing from the type of studies carried out along Chapters 3 and 4, where multilayered samples were prepared in order to study the role of Mn-ZnO and MnO_x-ZnO interfaces on the ferromagnetism of the Mn-Zn-O system, this chapter focuses on the basic study dealing with Mn:ZnO in the field of DMS, that is, preparation of actual DMS thin film samples. In particular, the aim of this chapter is to obtain actual DMS by preparing Mn:ZnO thin films doped with approximately 5% at. Mn (labelled as $Zn_{0.05}Mn_{0.95}O$ films), where Mn^{2+} cations are expected to replace Zn^{2+} cations in ZnO. In this case, different gases atmospheres have been used during the sputtering process in order to modify the magnetic properties of the prepared samples and to get further knowledge of the nature of the expected RTFM.

Regarding the role of carrier density in ZnO-based DMS, first theoretical calculations predicted RTFM in n-type Co^{2+}:ZnO while a hole-rich environment was predicted for RTFM in Mn^{2+}:ZnO DMS's.[1,2] However, experimental results on Mn:ZnO have been very controversial[3,4] and RTFM has been also obtained in n-type Mn:ZnO samples.[5,6,7,8] Very recently, experiments performed by Z. Yang et al.[9] on n-type ZnO:Mn thin films prepared with plasma-assisted molecular-beam epitaxy using different amounts of Ga dopant incorporation have shown evidences of electron-mediated RTFM in n-type Mn:ZnO, contradicting the initial theory.

Whereas in general, ZnO is intrinsically n-type conducting due to shallow donors associated with low-energy native point defects, such as oxygen vacancies (V_O) and Zn interstitials (Zn_i), it has been shown that nitrogen is a promising acceptor impurity for p-type ZnO.[10] However, although there is a report of experimental success in obtaining p-

type ZnO using a pure nitrogen source,[11] it is still difficult to achieve high hole densities due to compensation by O vacancies, N_O-Zn_O or N_O-$(N_2)_O$ complexes, even if an active plasma N_2 is used.[12] Nonetheless, reduction of the n-type sample character is expected by partial oxygen substitution by nitrogen.

On the other hand, S. Lee et al.[13] have reported that the electron carrier concentration in $Zn_{1-x}Mn_xO$ thin films prepared by RF magnetron sputtering drastically decreases with increasing P_{O2}, up to an Ar/O_2 ratio of 1:1, while the photoluminescence peaks related to oxygen vacancies (V_O) gradually diminish, showing that the carrier concentration can be controlled by varying P_{O2}, as observed similarly in the host ZnO material.

With the aim of modifying the carrier density in the $Zn_{0.05}Mn_{0.95}O$ thin films, samples have been deposited with different sputtering working gases (pure Ar, Ar/N_2 and Ar/O_2) under the same working pressure. In this chapter, the magnetic properties of the prepared $Zn_{0.05}Mn_{0.95}O$ films have been associated firstly, with the Mn short range order in the lattice, and secondly, with the different gas during the deposition process.

5.2. Preparation of Mn:ZnO films

A series of Mn-ZnO thin films was prepared by DC sputtering on Si(100) and fused quartz substrates at RT. Special attention was paid to the starting material and different pellets were sintered from mixing ZnO and different Mn oxides to be used as sputtering targets. The films described here were sputtered from $Zn_{0.95}Mn_{0.05}O$ pellets obtained from mixing ZnO and Mn_2O_3.

The $Zn_{0.95}Mn_{0.05}O$ ceramic targets were sintered following this procedure: Appropriate amounts of Mn_2O_3 (325 mesh, 99% ALDRICH) and ZnO (<1μ, 99.9% ALDRICH) to obtain 5% at. of Mn were mixed and grind using acetone in an agate mortar. The obtained powders were uniaxially pressed at 2000 N/cm^2. The resulting

pellets (2.5 inch diameter) were sintered in air at 800 ºC for 6 hours. The annealing ramp is represented in Fig. 5.1.

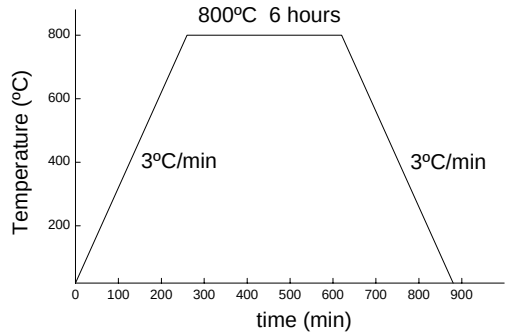

Fig. 5.1 Annealing ramp for the $Zn_{0.95}Mn_{0.05}O$ ceramic target sintering.

After sintering, targets colour turned a little bit yellowish, what might be attributed to the presence of oxygen defects. These final $Zn_{0.95}Mn_{0.05}O$ ceramic targets, very close to the 2 inch magnetron size, were used as starting bulk material for the sputtering deposition process, described below.

The base pressure provided by the vacuum system was in the 10^{-7} mbar range. The sputtering deposition was performed under a working pressure of $6.0x10^{-3}$ mbar with a RF power of 30 W to obtain a deposition rate in the 2-4 nm/min range, depending on the working gas. With the aim of modifying the carrier density, samples were deposited with different sputtering working gases (pure Ar, Ar/N_2 and Ar/O_2) under the same working pressure. The sample series description and main deposition parameters are summarized in Table 5.I.

Additionally some annealing treatments were performed after film growth. The post-deposition thermal treatments were carried out inside a quartz tube previously evacuated up to 1×10^{-6} mbar, under oxygen atmosphere flow of 1×10^{-2} mbar during two hours at 750 ºC. The description of the annealed samples is shown in Table 5.II.

Table 5.I $Zn_{0.95}Mn_{0.05}O$ sample series summary and deposition parameters as substrate temperature (T_S), RF power, sputtering deposition time (t_{sputt}), film thickness (Λ) and deposition rate (Δ).

target	T_S (ºC)	Sputtering gas (P = $6x10^{-3}$ mbar)	Power (W)	t_{sputt} (min)	Λ (nm)	Δ (nm/min)	Sample label $Zn_{0.95}Mn_{0.05}O$
$Zn_{0.95}Mn_{0.05}O$	25	100% Ar	30	30	108	3.6	-Ar
$Zn_{0.95}Mn_{0.05}O$	25	83% Ar; 17% N_2	30	30	102	3.4	-Ar/N_2
$Zn_{0.95}Mn_{0.05}O$	25	83% Ar; 17% O_2	30	30	61	2.0	-Ar/O_2
$Zn_{0.95}Mn_{0.05}O$	600	83% Ar; 17% O_2	30	60	42	0.7	-Ar/O_2-T_S=600ºC

Table 5.IIAnnealed $Zn_{0.95}Mn_{0.05}O$ samples description: annealing temperature (T_A), oxygen pressure during annealing (P_{O2}) and sample thickness after annealing.

As-grown sample	Annealing conditions			Λ (nm)	Sample label $Zn_{0.95}Mn_{0.05}O$
	T_A (ºC)	P_{O2} (mbar)	t_A (h)		
$Zn_{0.95}Mn_{0.05}O$-Ar	750	$1x10^{-2}$	2	94	-Ar-750ºC-O_2
$Zn_{0.95}Mn_{0.05}O$-Ar/N_2	750	$1x10^{-2}$	2	92	-Ar/N_2-750ºC-O_2

In addition, 1 μm thick films were grown afterwards under identical experimental conditions (gas pressure, RF power, substrate temperature) as described above (Table 5.I), with two purposes: the increase of the XRD intensity for a better detection of possible additional extrinsic phases and the enhancement of the XAS spectra threshold jump intensity for a more detailed XANES study.

5.3. X-Ray Reflectivity (XRR)

X-ray reflectivity (XRR) measurements were carried out on a Bruker D8 X-ray diffractometer with a Cu K_α source at the ICMM facilities. XRR film spectra, shown in Fig. 5.2, reveal different deposition rates depending on the sputtering gas.

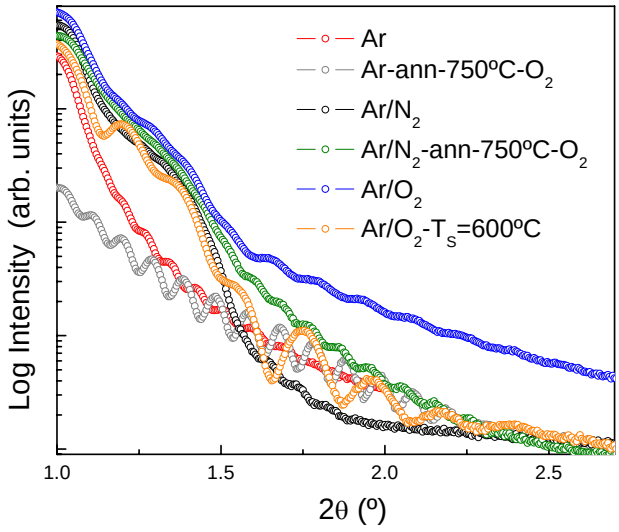

Fig. 5.2 XRR spectra of the $Zn_{0.95}Mn_{0.05}O$ films prepared using different gas atmospheres and after thermal treatments in oxygen atmosphere.

The obtained film thickness and deposition rates for the as-grown samples are given in Table 5.I. It can be observed that the sputtering gas efficiency decreases from samples prepared with Ar, Ar/N_2 to Ar/O_2. While deposition rates using 100% Ar and Ar/N_2(17%) are very similar (3.6 and 3.4 nm/min), a remarkably diminution of about 45% is obtained for Ar/O_2(17%), becoming 2.0 nm/min.

The sputtering yield (S = number ejected atoms / number incident atoms) depends basically on the target material (binding energy, mass of atoms), the sputtering gas (mass of atoms, increasing S for heavier gasses and incident energy, increasing S for higher energies) and the geometry (most efficient 20-30 degrees from glancing), as it was explained in section 2.1. Therefore, under the same geometry (normal incidence sputtering), and the same target material, it is expected that S increases as the mass of the gas atoms becomes bigger. The atomic mass of argon is 40, while the oxygen and nitrogen molecular mass are 32 and 28, respectively.

For the same working pressure, the deposition rate, which is directly related to S, increases with S. The larger sputtering yield for Ar may explain the small difference found

in the deposition rates using 100% Ar and Ar/N_2(17%), 3.6 and 3.4 nm/min, respectively. Conversely, the noticeable diminution in the deposition rate when introducing oxygen, Ar/O_2(17%), can be related to the higher reactivity of the oxygen gas and the expected chemical reactions on substrate and target, which can substantially modify the process dynamics.

Additionally, if deposition process takes place under higher substrate temperature (T_S = 600ºC, instead of 25ºC, see Table 5.I) without modifying other growth parameters (same gas atmosphere, Ar/O_2 (17%)), the deposition rate is drastically modified, decreasing to 0.7 nm/min (~80% diminution). This seems to be related to the diminution of the sticking coefficient as the substrate temperature is more elevated. Furthermore, the observed increased amplitude in the XRR spectrum of $Zn_{0.95}Mn_{0.05}O$-T_S=600ºC sample in comparison with the others (Fig. 5.2) might be associated with a decrease of the film surface roughness for higher substrate temperature, probably due to the increase of the adatom mobility.

On the other hand, post-deposition annealing at 750ºC in oxygen atmosphere of the Ar and Ar/N_2-prepared samples, summarized in Table 5.II also leads to a slight reduction of the film thickness (~10%), what can be interpreted as a sample compaction, increasing the film density.

5.4. Rutherford Backscattering Spectroscopy (RBS)

Rutherford backscattering spectroscopy (RBS) experiments were carried out in order to determine the actual Mn content inside the films. Fig. 5.3 shows the RBS spectra of several samples, what allows to compare the relative Mn concentration among them. It is observed a nearly constant Mn/Zn ratio independently of the preparation conditions, with values a bit larger but very similar to the nominal ones in the target; **the experimental Mn/Zn ratio obtained after fitting, close to 6%**, is displayed in the legend of Fig. 5.3.

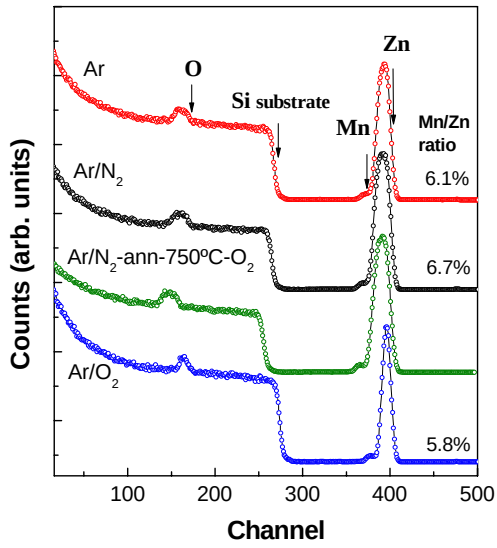

Fig. 5.3 RBS spectra of several $Zn_{0.95}Mn_{0.05}O$ thin films. The Mn/Zn ratio is given for each sample.

5.5. X-Ray Diffraction (XRD)

Diffraction measurements on the sample series were carried out in a standard laboratory Bruker D8 TT X-ray diffractometer by using the K_α radiation line of Cu at the ICMM facilities. Fig. 5.4 shows X-ray diffraction spectra corresponding to several $Zn_{0.95}Mn_{0.05}O$ films and a ZnO film deposited from a ZnO target under similar pressure and RF power using pure Ar gas (all of them in the 100 nm thick range). The prepared films show just the (002) peak corresponding to the typical wurtzite ZnO crystallographic structure, showing different texturation degrees. **No additional extrinsic phases are detected by XRD, even for identically prepared 1 μm thick films**. However, (100) and (110)-ZnO peaks were additionally identified in the XRD spectrum of the Ar/O_2–prepared 1 μm sample, evidencing lower texture in the Ar/O_2-sample.

Results from XRD analysis are given in Table 5.III. The position of the observed (002)-ZnO diffraction peaks for the as-grown samples under different atmospheres (Ar, Ar/N_2 and Ar/O_2) is approximately the same ($2\theta \sim 33.7^o$), which is smaller than the

expected (002)-ZnO peak position in wurtzite structure (2θ = 34.4º). A close 2θ value (as well as an increase of the crystalline grain size) is only obtained after post-deposition annealing in oxygen.

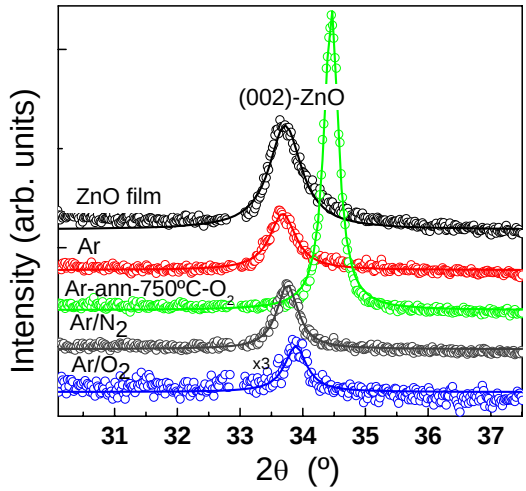

Fig. 5.4 X-ray diffraction patterns of the $Zn_{0.95}Mn_{0.05}O$ samples.

Table 5.III Annealed $Zn_{0.95}Mn_{0.05}O$ XRD results summary: (002)-ZnO peak position (2θ) and full width at half maximum (FWHM) from Gaussian fits and the corresponding grain size in the out-of-plane direction obtained by the Scherrer equation.

Sample	XRD (002)-ZnO		
	2θ (º)	FWHM (º)	grain size (nm)
ZnO-Ar	33.7	0.56	14.8
Ar	33.7	0.47	17.7
Ar-ann-750ºC-O_2	34.4	0.28	29.7
Ar/N_2	33.75	0.40	20.8
Ar/O_2	33.9	0.44	18.9

Besides, it should be noticed that the ZnO film deposited with pure Ar gas (ZnO-Ar) under similar conditions presents (002)-ZnO peak also at 33.7º, differing from

expected position. All these facts suggest the presence of tensile stresses in the as-grown films, both in ZnO and $Zn_{0.95}Mn_{0.05}O$ films. Sample annealing at 750ºC in oxygen atmosphere would lead to stress relaxation, what agrees with $2\theta = 34.4^{o}$ obtained for the Ar-ann-750ºC-O_2 sample, coinciding with the stress-free powder value.

Additionally it can be observed that the Ar/O_2–prepared sample presents a small shift to higher angles in the (002) peak ($2\theta = 33.9^{o}$) compared to the ZnO–Ar film ($2\theta = 33.7^{o}$). Just under the hypothesis that stress affects similarly all the as-grown Mn:ZnO films because of their similar thickness (~ 100 nm), the observed shift might be associated with the presence of oxygen vacancies in the ZnO–Ar film, as well as in the $Zn_{0.95}Mn_{0.05}O$ films prepared with Ar ($2\theta = 33.7^{o}$) and with Ar/N_2 ($2\theta = 33.75^{o}$), since the presence of oxygen vacancies in the ZnO lattice involve a shift to smaller angles.[14] Anyway, it should be keep in mind that this is just a lucubration only valid under the considered assumptions (similar tensions in the films and Mn occupying the same lattice position in the compared as-grown films (Mn:ZnO films).

The calculated (002)-ZnO crystalline grain sizes in the out-of-plane direction by using the Scherrer formula (shown in Table 5.III) range between 15 and 30 nm approximately. The obtained sizes for the $Zn_{0.95}Mn_{0.05}O$ films are larger than for the ZnO–Ar film. While crystalline grain sizes close to 20 nm have been found for the Ar, Ar/N_2 and Ar/O_2–as grown $Zn_{0.95}Mn_{0.05}O$ samples, approximately 15 nm of average size has obtained for the ZnO–Ar film. As well, post-deposition annealing of the Ar/N_2 sample in oxygen atmosphere leads to an noticeable increase of the crystalline grain size (from 21 to 30 nm).

5.6. Magnetic properties

The magnetic characterization, performed with a SQUID magnetometer (MPMS-7T from Quantum Design) is shown in Fig. 5.5. Magnetization per manganese atom has been calculated, after subtracting the diamagnetic Si contribution, taking into account the precise amount of Mn obtained by RBS. It should be noted here that the selected

samples have similar thickness and hence normalization to film volume or area gives similar results.

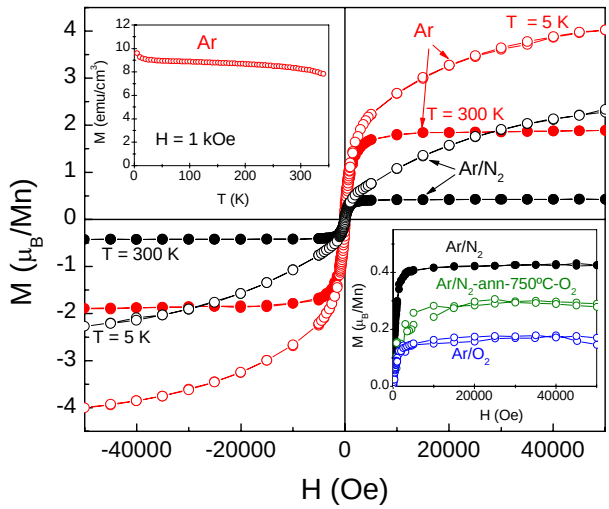

Fig. 5.5 Hysteresis loops of the Ar— and Ar/N_2—prepared $Zn_{0.95}Mn_{0.05}O$ films. Additionally, right inset shows the comparison among room temperature hysteresis loops corresponding to Ar/N_2, Ar/O_2 and Ar/N_2-ann-750ºC-O_2 samples. Left inset shows the temperature dependence of magnetization normalized to film volume for the Ar—prepared $Zn_{0.95}Mn_{0.05}O$ film.

Apart from a paramagnetic contribution at low temperature, **ferromagnetism over RT is observed** for all the studied samples. However, clear differences can be observed depending on the preparation conditions. **The sample prepared with 100% of Ar as sputtering gas presents the highest magnetization saturation (~ 2 μ_B/Mn)** along the sample series. This value is considerably large even compared to the highest reported ones by other authors.[15] The upper-left inset of Fig. 5.5 shows a nearly flat dependence of magnetization with temperature recorded after field cooling (FC), evidencing a temperature well above RT. It is worth to comment that no differences have been observed between FC and zero field cooling (ZFC) curves.

In comparison, the RT saturation magnetization obtained for the sample prepared with the Ar/N_2 mixture is nearly four times smaller, indicating that **nitrogen has an important role in the magnetic properties, weaken the ferromagnetic response**. M-H curves from two additional samples (Ar/O_2 and Ar/N_2-ann-750ºC-O_2 films) have been included in the bottom-right inset of Fig. 5.5, in comparison with the Ar/N_2–prepared sample.

It can be observed that, although both of them exhibit a weak ferromagnetic signal at RT, saturation magnetization values in this case are considerably much lower, corresponding the smallest signal to the Ar/O_2– prepared sample. In addition, no appreciable FM response was found for the sample prepared with Ar/O_2 flow at higher substrate temperature (Ar/O_2-T_S=600 ºC sample).

Regarding the magnetic characterization of these samples, a **strong dependence of the ferromagnetic response in terms of the sputtering gasses and deposition temperature** conditions has been revealed.

5.7. X-Ray Absorption Near-Edge Structure (XANES)

As we have emphasized along this work, the local order around Mn becomes of fundamental importance in Zn-Mn-O system studies. For that purpose, we have performed XAS experiments at the Mn K-edge. XANES spectra were measured in the fluorescence yield detection mode at the Spanish CRG beamline (SpLine, BM25) of the ESRF. A Mn foil and several manganese oxides were also measured to be used as references. For these experiments, we have used additional 1 μm thick films which were grown under identical experimental conditions as the 100 nm ones. The aim is to enhance the intensity of the collected XAS threshold jump to be able to fulfil a more thorough XANES study.

Fig. 5.6(a) shows XANES spectra corresponding to 1 μm thick films prepared with Ar, Ar/N_2 and Ar/O_2 sputtering gases.

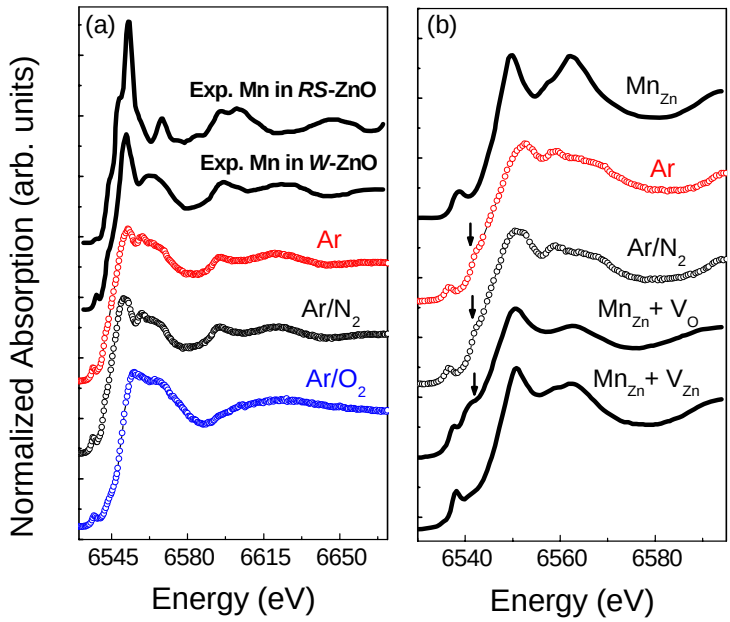

Fig. 5.6 XANES spectra of Ar, Ar/N_2 and Ar/O_2-prepared $Zn_{0.95}Mn_{0.05}O$ films firstly compared to experimental data reported in Ref. 16 for Mn in rock-salt (*RS*) and in wurtzite (*W*) structures. (b) More detailed comparison of the $Zn_{0.95}Mn_{0.05}O$-Ar and Ar/N_2 XANES spectra with calculations reported in Ref. 17 for Mn substituting Zn in stoichiometric *W* structure (Mn_{Zn}), *W* with oxygen vacancies ($Mn_{Zn}+V_O$), and *W* with zinc vacancies ($Mn_{Zn}+V_{Zn}$).

Considering the previous XANES analysis reported along this work (sections 3.8.1 and 4.7.1), the obtained threshold energy shift with respect to metal **Mn in the films prepared with Ar and Ar/N_2 gases indicates that manganese appears mostly in the Mn^{2+} oxidation state.** Moreover, XANES comparisons with these other works discard appreciable presence of extrinsic phases as MnO or even Mn_3N_2. By contrast, manganese presents a higher oxidation state (near Mn^{4+}) when preparing under Ar/O_2 atmosphere. Details of the obtained threshold shift can be observed in Fig. 5.7, which shows a zoom of the low energy region of the XANES spectra of these samples as well as the Ar-ann-750ºC-O_2 film, compared to a Mn metal foil.

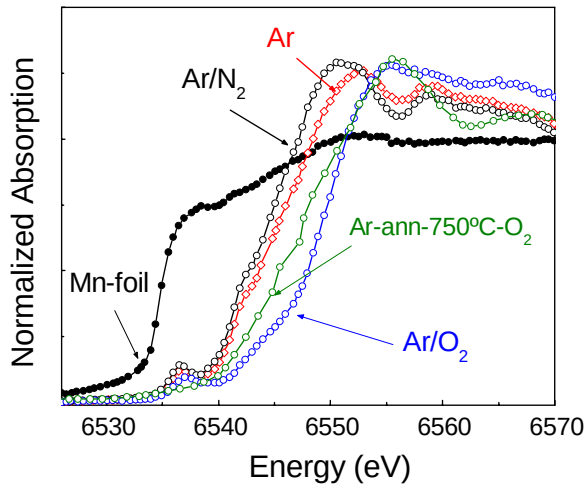

Fig. 5.7 XANES spectra of the Ar, Ar/N_2 , Ar/O_2 and Ar/N_2-ann-750ºC-O_2 $Zn_{0.95}Mn_{0.05}O$ films in comparison with a Mn metal foil.

It is worth to comment that the observed shift within the series (between Ar/N_2, Ar samples and the Ar/O_2 one) seems quite independent of the manganese oxide used in the target preparation, since similar results have been found for samples sputtered from targets sintered from ZnO-MnO (see additional information at the end of this chapter).

It can be observed a small difference between the Ar- and the Ar/N_2– prepared sample spectra (Fig. 5.7) that may be described mainly by a steeper slope in the absorption jump shape of the corresponding Ar/N_2– prepared sample spectra. This feature could be explained by a more narrow distribution of Mn^{2+} environments in the Ar-prepared sample. Slightly different Mn^{2+} sites can give rise to different threshold energies and consequently, broader distributions can imply less steep jump edges, showing more gradual slopes in the normalized XANES spectra. On the other hand, the fact that the spectrum of the Ar/N_2–prepared sample is slightly shifted to smaller energies (see Fig 5.7, jump region) indicates a small decrease in the Mn oxidation state, which is actually the first hint pointing towards the fact that nitrogen has entered in the lattice. O^{2-} substitution by N^{3-} would entail longer distances for the Mn-(O/N) shell and consequently, smaller Mn formal oxidation state.

For the sample grown with Ar/O_2 atmosphere, it appears that high oxygen reactivity during deposition process favours the stabilization of a highly oxidized manganese phase (and likely, also the diminution of the oxygen vacancies in the ZnO). The small ionic radius of Mn^{4+} in addition to the considerable charge mismatch, makes rather unfeasible the substitution of Zn^{2+} by Mn^{4+} in the ZnO lattice. Nevertheless, XANES results are compatible with the presence of minor Mn^{2+} and Mn^{3+} contributions.

For the thin films grown with Ar and Ar/N_2 gases, with Mn oxidation states close to +2, based on a direct comparison with reported experimental spectra of CVD prepared $Zn_{0.95}Mn_{0.05}O$ samples[16] (shown Fig. 5.6(a)) and according to Mn/ZnO multilayers (section 3.9), it can be deduced that Mn^{2+} substitutes Zn^{2+} in the wurtzite structure. In addition, by comparison of the XANES spectra of these samples with other XANES studies carried out on Mn/ZnO multilayers (section 3.8.1) and Mn/Si_3N_4 multilayers (section 6.8.1), the presence of appreciable extrinsic phases, as MnO or even Mn_3N_2, can be discarded.

Besides, a more detailed study of XANES structure of these two films allows to characterize the Mn environment more precisely. Yan et al.[17] have performed calculations of XANES spectra for different environments of Mn^{2+} replacing Zn^{2+} in wurtzite where vacancies or interstitials are considered. In fact, the substitution of Zn by Mn gives slightly different spectra in three interesting cases: a stoichiometric crystal (Mn_{Zn}), a crystal with additional oxygen vacancies ($Mn_{Zn}+V_O$) and with additional zinc vacancies ($Mn_{Zn}+V_{Zn}$). Fig. 5.6(b) shows the comparison between the Ar– and Ar/N_2–prepared films with the calculated spectra. It can be observed that the corresponding $Mn_{Zn}+V_O$ calculated spectrum presents a characteristic feature in the middle of the jump (marked with an arrow in Fig. 5.6(b), which also appears in the two studied sample spectra. By comparison, it can be noted **that films prepared by sputtering with Ar and Ar/N_2 are compatible with an appreciable amount of oxygen vacancies** and consequently, both samples are expected to show n-type conduction.

Summarizing, XANES results indicate that, for the Ar/O_2–prepared sample as well as for the oxygen-annealed films, manganese is mostly in an high oxidation state and

almost certainly placed out of the ZnO wurtzite structure. However, the existence of additional minor Mn^{2+} and Mn^{3+} contributions could be expected, especially for the Ar-ann-750ºC-O_2 sample, with smaller average Mn oxidation state. This would explain the weak ferromagnetic signal observed for the Ar/N_2-ann-750ºC-O_2 and for the Ar/O_2–prepared samples, being smaller for the Ar/O_2 one, as expected.

Conversely, XANES spectra corresponding to the films prepared with Ar and Ar/N_2 gases (oxygen deficient atmospheres) indicate that the majority Mn^{2+} are placed in the cation sites of an oxygen defective wurtzite structure. Moreover, it seems that, when N_2 is introduced in the sputtering gas, nitrogen has entered in the lattice because Mn^{2+} presents a slightly smaller K-edge threshold energy. Since nitrogen would act as an acceptor impurity here, this would imply a reduction of the n-type character and therefore, a variation of the carrier density would be expected for the Ar– and Ar/N_2–prepared samples, being the $Zn_{0.95}Mn_{0.05}O$-Ar sample the richest one in electron carriers between both. Regarding the magnetic properties, the highest saturation magnetization has been found for the $Zn_{0.95}Mn_{0.05}O$-Ar sample, diminishing significantly the ferromagnetic response when using Ar/N_2 gases.

5.8. UV-VIS Absorption

Optical absorption measurements were carried out in order to obtain additional information about the above supposition, before a direct evidence of the charge carrier variation could be checked by transport measurements.

The visible - ultraviolet optical absorption of the films deposited on fused quartz was measured with a Cary 4000 UV-Vis spectrophotometer in the 190-900 nm range. Fig. 5.8 shows the optical absorption coefficient as a function of wavelength of the same studied $Zn_{0.95}Mn_{0.05}O$ films (about 100 nm thick) prepared on fused silica substrates to be measured by transmission mode. A ZnO film prepared by sputtering from a pure ZnO target with Ar gas is presented also for comparison. An estimation of the gap energy of this ZnO film gives a value of 3.28 eV, in agreement with reported values. Additionally,

the excitonic character of the optical absorption edge can be clearly observed by the feature at 352 nm in this undoped sample.[18]

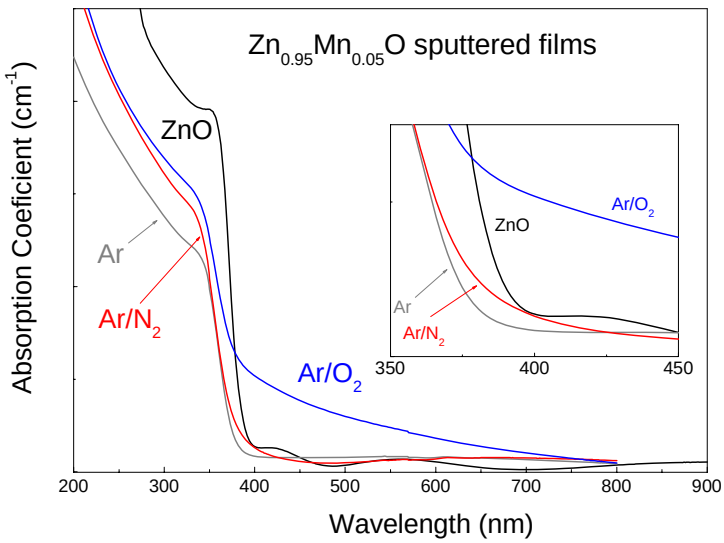

Fig. 5.8 Optical absorption coefficient of the studied samples.

Both, the Ar– and Ar/N_2– prepared Mn:ZnO films show a slightly shifted absorption edge respect to the ZnO film. Moreover, the noticeable reduction of the excitonic feature has been related to the presence of Mn^{2+} in $Zn_{1-x}Mn_xO$ due to the increase of disorder and subsequent lattice distortion.[18] A more detailed study of the optical edge (inset of Fig. 5.8) shows that Ar/N_2– prepared films have a slightly larger absorption coefficient in the 370 - 420 nm range, in agreement with the reported by Gu et al.[14] This increment might be due to the presence of nitrogen in the lattice structure, providing additional levels in the gap. Therefore, **optical measurements agree with the inclusion of nitrogen in the wurtzite structure**.

On the other hand, the Ar/O_2– prepared Mn:ZnO film presents a higher absorption from 800 nm, being in agreement with the presence of MnO_2, as it has been reported in MnO_2/TiO_2 nanocomposites.[19]

Taking into account UV-Vis characterization together with X-ray diffraction and XANES measurements, results point towards the presence of Mn^{2+} in the wurtzite lattice for $Zn_{0.95}Mn_{0.05}O$-Ar and $Zn_{0.95}Mn_{0.05}O$-Ar/N_2 films, both of them with similar amount of oxygen vacancies. The presence of intrinsic oxygen vacancies in ZnO conferred sample n-type character but as nitrogen acts as an acceptor impurity in the ZnO lattice, substitution of O^{2-} by N^{3-} entails a reduction of the ZnO electron density. Therefore, **results suggest a variation of the electron carrier density of these $Zn_{0.95}Mn_{0.05}O$ n-type films where mostly Mn^{2+} cations substitute Zn^{2+} in the ZnO-*W* structure**. Since the highest ferromagnetic signal within the series has been found for the $Zn_{0.95}Mn_{0.05}O$-Ar sample (with higher n-type carrier density) and it becomes significantly reduced for the $Zn_{0.95}Mn_{0.05}O$-Ar/N_2 film (with smaller one) these results suggest the existence of **electron mediated RTFM in Mn:ZnO films**. Additional electrical measurements are planned to prove the proposed association.

For the Ar/O_2–prepared sample, XRD, XANES and optical measurements suggest the formation of a highly oxidized manganese phase ($MnO_{2-\delta}$-type) coexisting with ZnO-*W* structure. However, extra Mn^{2+} and Mn^{3+} minor contributions could be expected for this sample as well as for the oxygen-annealed films (with smaller Mn oxidation state). This might explain the small ferromagnetic signal observed for both the Ar/N_2-ann-750ºC-O_2 and the Ar/O_2–prepared samples, being smaller for the Ar/O_2 one, what seems consistent regarding its higher average Mn oxidation state.

5.9. Conclusions

Room temperature ferromagnetism has been obtained in Mn:ZnO films prepared by sputtering from a $Zn_{0.95}Mn_{0.05}O$ target.

A strong variation of the ferromagnetic response has been found by modifying the working gas type (Ar, Ar/O_2, Ar/N_2) in films prepared from the same $Zn_{0.95}Mn_{0.05}O$ target under the same sputtering working pressure.

The highest saturation magnetization values have been obtained for the Ar– and Ar/N_2–prepared Mn:ZnO films (about 2 and 0.5 μ_B/Mn at room temperature, respectively), being the only samples where it has been found that there is mostly Mn^{2+} located in the wurtzite structure.

Both the film preparation in oxygen atmosphere (Ar/O_2) and the annealing treatments after deposition in oxygen flow lead to highly oxidized Mn, close to Mn^{4+}. The oxygen effect is a significant reduction of the ferromagnetic signal.

X-ray diffraction, XANES and optical absorption characterizations point towards the existence of nitrogen in the wurtzite lattice for the Ar– and the Ar/N_2–prepared $Zn_{0.95}Mn_{0.05}O$ films, both of them with similar amount of oxygen vacancies. This indicates that the two samples present n-type character, and that the electron density in the Ar–prepared film is higher than in the Ar/N_2–one. The observed difference in the magnetic properties can be therefore related to different carrier density, being in agreement with room temperature ferromagnetic ordering in n-type Mn:ZnO mediated by electron carriers.

ADITTIONAL INFORMATION

XANES spectra of additional thin films also prepared with different sputtering working gases (pure Ar, Ar/N_2 and Ar/O_2) under the same working pressure, from a $Zn_{0.95}Mn_{0.05}O$ target. In this case, the $Zn_{0.95}Mn_{0.05}O$ sputtering target has been obtained from mixing ZnO and MnO, differing from the above studied case, where ZnO and Mn_2O_3 powders have been used.

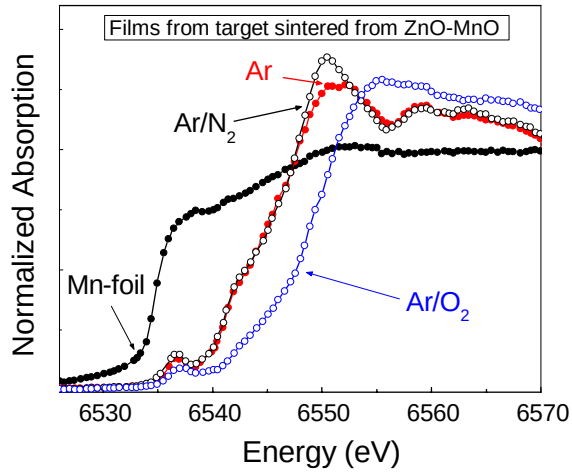

Fig. 5.9 XANES spectra of the Ar, Ar/N_2 , Ar/O_2 and Ar/N_2-ann-750ºC-O_2 $Zn_{0.95}Mn_{0.05}O$ films in comparison with a Mn metal foil. These films have been deposited from a $Zn_{0.95}Mn_{0.05}O$ target sintered from ZnO and MnO starting powders.

References

[1] T. Dietl, H. Ohno, F. Matsukura, J. Cubert, and D. Ferrand, Science 287, 1019 (2000).

[2] K. Sato and H. Katayama-Yoshida, Semicond. Sci. Technol. 17, 367–376 (2002).

[3] C. Liu, F. Yun, H. Morkoc, "*Ferromagnetism of ZnO and GaN: A Review*", J. Mat. Science: Materials in Electronics 16, 555 (2005).

[4] F. Pan, C. Song, X. J. Liu, Y. C. Yang, F. Zeng, "*Ferromagnetism and possible application in spintronics of transition-metal-doped ZnO films*", Mat. Science and Engineering R 62 1-35 (2008).

[5] P. Sharma, A. Gupta, K. V. Rao, Frank J. Owens, R. Sharma, R. Ahuja, J. M. Osorio Guillen, B. Johansson, and G. A. Gehring, Nat. Mater. 2, 673 (2003).

[6] Y. W. Heo, M. P. Ivill, K. Ip, D. P. Norton, S. J. Pearton, J. G. Kelly, R. Rairigh, A. F. Hebard, and T. Steiner, Appl. Phys. Lett. 84, 2292 (2004).

[7] S. W. Jung, S. J. An, G. G. Yi, C. U. Jung, S. I. Le and S. Cho, Appl Phys Lett 80, 4561 (2002).

[8] Y. M. Kim, M. Yoon, I. W. Park, Y. J. Park, and J. H. Lyou, Solid State Commun. 124, 175 (2004).

[9] Z. Yang, J. L. Liu, M. Biasini, W. P. Beyermann, Apl. Phys. Lett. 92, 042111 (2008).

[10] Q. Xu, H. Schmidt, L. Hartmann, H. Hochmuth, M. Lorentz, A. Setzer, P. Esquinazi, C. Meinecke, M. Grundmann, Apl. Phys. Lett. 91, 092503 (2007).

[11] A. Tsukazaki, A. Ohtomo, T. Onuma, M. Ohtani, T. Makino, M. Sumiya, K. Ohtani, S. F. Chichibu, S. Fuke, Y. Segawa, , H. Ohno, H. Koinuma, and M. Kawasaki, Nat. Mat. 4, 42 (2005).

[12] E. C. Lee, Y. S. Kim, Y. G. Jin, and K. J. Chang, Phys. Rev. B 64, 85120 (2001).

[13] S. Lee, H. S. Lee, S. J. Hwang, Y. Shon, D. Young, Y. Kim and E. K. Kim, J. Cryst. growth 286, 223 (2006).

[14] Z. Gu et al. Appl. Phys. Lett., 88, 082111 (2006).

[15] F. Pan, C. Song, X. J. Liu, Y. C. Yang and F. Zeng, "*Ferromagnetism and possible application in spintronics of transition-metal-doped ZnO films*", Mat. Science and Engeneering R 62, 1-35 (2008).

[16] J. Pellicer-Porres, A. Segura, J. F. Sánchez-Royo, J. A. Sans, J. P. Itié, A. M. Flank, P. Lagarde, and A. Polian, Appl. Phys. Lett. 89, 231904 (2006).

[17] W. Yan, Z. Sun, Q. Liu, Z. Pan, J. Wang, S. Wei, D. Wang, Y. Zhou, and X. Xhang, Appl. Phys. Lett., 91, 062113 (2007).

[18] K. J. Kim, Y.R. Park, J. Appl. Phys., 94, 867 (2003).

[19] M. Xue et al., Nanotechnology, 19, 185604 (2008).

Appendix A

Effect of Thermal Treatments and Substrate Temperature on Mn/ZnO Multilayers

Annealing can have a great effect on the magnetization of TM-doped ZnO, largely because it can modify the microstructure and local structure of samples. For instance, the post-deposition annealing treatment may lead to a more even distribution of substitutional Mn^{2+} and minimize antiferromagnetic coupling in $Zn_{1-x}Mn_xO$ thin films.[1]

Regarding ZnO defects, annealing in vacuum or in a reducing atmosphere might enhance FM of these samples due to introduction of V_O and Zn_O defects, which have been claimed of great importance in the RTFM of TM-doped ZnO. The formation of this type of intrinsic defects is evolved to FM since electrons locally trapped by V_O or Zn_O can occupy an orbital overlapping with the *d* shells of the TM neighbours to form a bound magnetic polaron (BMP), recently related to intrinsic RTFM.[2] Similarly, annealing of samples in oxidation atmospheres can lead to a decrease in V_O concentration, with a large detrimental effect on FM.

However, experimental results in the DMS field are diverse and highly dependent on sample preparation. Especially, the thermodynamics in $Zn_{1-x}Mn_xO$ thin films has not been clarified yet; thus it is difficult to understand the thermodynamic behaviour of the components, the magnetic ions, and the carriers for $Zn_{1-x}Mn_xO$ samples.

V. K. Sharma et at.[3] investigated thermal treatments of non-homogeneous $Zn_{1-x}Mn_xO$ bulk polycrystalline samples with x ranging from 0.02 to 0.25, where the magnetization increases as the Mn content increases. They found that annealing in hydrogenated argon (oxygen-deficient atmosphere) further enhances ferromagnetism, whereas annealing in air (oxygen-rich atmosphere) deteriorates the ferromagnetic signal.

By contrast, B. Babić-Stojić et al.[4] observed RTFM in non-homogeneous Mn-Zn-O bulk polycrystalline samples with 10% of Mn that were thermally treated at 400 and

500°C for 12 h in air. They suggested that RTFM could arise from interactions between the Mn^{2+} ions and p-type defects incorporated in the ZnO crystal lattice during the thermal treatment.

E. Chikoidze et al.[5] reported that, contrary to pure ZnO films, Mn-Zn-O alloy is highly unstable under annealing in O_2, starting from temperatures as low as 300°C. They found that the oxygen annealing modifies the mean cation-cation distance, and the Mn^{2+} distribution without formation of any ferromagnetic phase.

Conversely, the ferromagnetic properties of $Zn_{0.93}Mn_{0.07}O$ films were dramatically improved after rapid thermal annealing at 900°C in nitrogen atmosphere (S. Lee et al.[6]). Their results suggest that FM of Mn-Zn-O films can be improved by modifying the crystal magnetic anisotropy through post-growth thermal treatments.

Y. W. Heo et al.[7] studied the effect of post deposition annealing on the ferromagnetic properties of Mn implanted ZnO film deposited on Al_2O_3 at 400°C. Samples were annealed in the PLD chamber at temperatures ranging from 425 to 600°C in O_2 ambient (~10^{-1} mbar) for 60 min. A significant enhancement in the magnetization after annealing at 600°C was observed, which was attributed to the improvement of crystalline quality.

On the other hand, substrate temperature can importantly affect the magnetization of TM-ZnO films since it can also modify structural defects. For instance, P. Sharma et al.[8] reported that Mn-Zn-O films prepared at low processing temperature exhibited RTFM, whereas clustering and no RTFM was obtained for samples prepared at high substrate temperatures (T_S > 700°C).

Besides, A. K. Pradhan et al.[9] showed that $Zn_{1-x}Mn_xO$ films grown at a substrate temperature of 500°C exhibited RTFM and beyond 500°C, the crystalline quality of the film increased at the expense of a decrease in the magnetization due to the formation of Mn related clusters.

Aimed at studying the effect of temperature on the ferromagnetic response of Mn/ZnO samples, i) annealing treatments and ii) sample growth under different

substrate temperatures were carried out. Electronic, structural and magnetic characterizations of representative samples were performed to find reliable magnetic-structural associations in this system.

Experimental details:

i) Thermal annealing of Mn/ZnO samples

Annealing of samples was performed in a vacuum quartz tube evacuated up to 1 x 10^{-6} mbar, placed inside a furnace. Samples were annealed during two hours at temperatures of 600ºC and 750ºC, with heating and cooling rates of about 5ºC/min. The thermal treatments were performed both in vacuum (P = 1 x 10^{-6} mbar) and in controlled oxygen flow (P = 1 x 10^{-2} mbar). In this former case, the oxygen flow was regulated by means of a mass flow controller (MFC) to obtain a steady regime at constant pressure with vacuum evacuation.

Experimental results corresponding to the annealing of t = 3 nm and 0.7 nm samples from the Mn/ZnO series (described in Chapter 3), with nominal formulas $[Mn_{(1.5nm)}/ZnO_{(3nm)}]_{20}$ and $[Mn_{(0.7nm)}/ZnO_{(3nm)}]_{43}$ respectively, are described in this appendix. The studied samples are summarized in Table A.I.

ii) Mn/ZnO deposition at different substrate temperatures (T_S)

Samples were prepared under the same experimental conditions that were used for the Mn/ZnO multilayer growth described in section 3.2, but modifying the substrate temperature. Deposition was performed at three different substrate temperatures: T_S = 25ºC, 300ºC and 550ºC. ZnO and Mn sputtering deposition times were the same for the three samples (160 s and 107 s for ZnO and Mn, respectively), corresponding to the previously described t = 6 nm nominal sample, with nominal formula $[Mn_{(6nm)}/ZnO_{(6nm)}]_5$. These samples have been included in Table A.I.

Table A.I Summary of selected i) annealed Mn/ZnO samples and ii) Mn/ZnO samples deposited at different temperatures.

$[Mn_{(t)}/ ZnO_{(3nm)}]_n$ as-grown parameters		T_S (ºC)	Annealing conditions		Label
			Atmosphere	T_A (ºC)	
t (nm)	*n*				
1.5	20	25	-	-	*t* = 1.5 nm as-grown
			Vacuum	600ºC	*t* = 1.5 nm-ann-600ºC-V
			Vacuum	750ºC	*t* = 1.5 nm-ann-750ºC-V
			Oxygen	600ºC	*t* = 1.5 nm-ann-600ºC-O_2
			Oxygen	750ºC	*t* = 1.5 nm-ann-750ºC-O_2
0.7	43	25	-	-	*t* = 0.7 nm as-grown
			Vacuum	600ºC	*t* = 0.7 nm-ann-600ºC-V
			Oxygen	600ºC	*t* = 0.7 nm-ann-600ºC-O_2
			Oxygen	750ºC	*t* = 0.7 nm-ann-750ºC-O_2
6	5	25	-	-	*t* = 6 nm T_S=25ºC
			Oxygen	600ºC	*t* = 6 nm T_S=25ºC ann-600ºC-O_2
		300	-	-	*t* = 6 nm T_S=300ºC
		550	-	-	*t* = 6 nm T_S=550ºC

The effect of temperature on the XRR spectra of the Mn/ZnO samples is shown in Fig. A.1. Fig A.1(a) depicts the comparison among *t* = 1.5 nm sample as-grown and after different vacuum an oxygen annealing treatments and Fig A.1(b) shows the comparison among *t* = 6 nm sample prepared at different substrate temperatures, T_S = 25ºC, 300ºC and 550ºC.

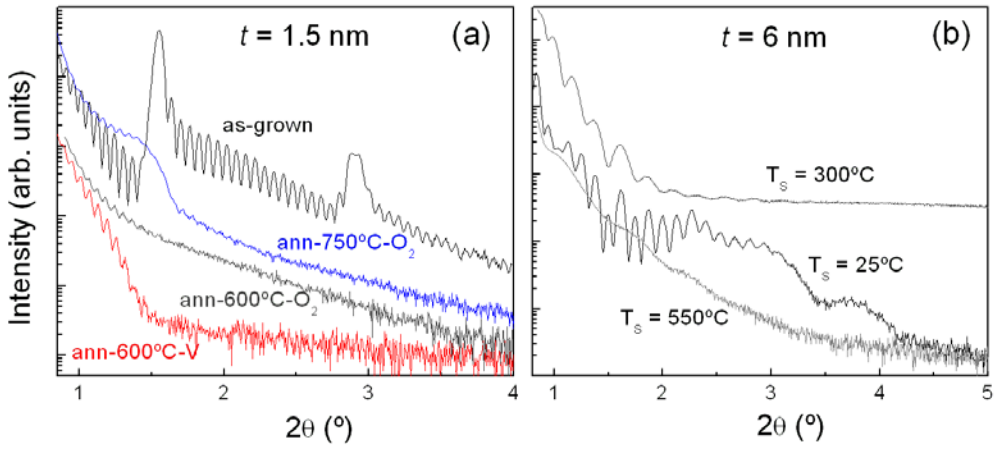

Fig. A.1 (a) XRR spectra of sample t = 1.5 nm under different thermal treatments in comparison with as-grown sample. (b) XRR spectra of sample t = 6 nm prepared at different substrate temperatures, T_S = 25ºC, 300ºC and 550ºC.

As it can be inferred from the graphs, **multilayer features, which are clearly observed for the as-grown samples (T_S = 25ºC), disappear when increasing temperature**. The loss of heterostructure periodicity is observed for i) annealing at a temperature of 600ºC and higher (either in oxygen or vacuum) and also ii) when growing at a substrate temperature of 300ºC or higher.

The fact that heterostructure features vanish at significant low temperature (T_S = 300ºC) evidences high interdiffusion and strong interaction between the different layers. These results suggest that, interface interaction, which becomes greatly favoured by increasing temperature, also occurs in the as-grown samples. Therefore, moderate diffusion in the Mn/ZnO samples series deposited at 25ºC could be then related to the obtained coexistence of Mn-Zn-O wurtzite and rocksalt mixed phases in Mn/ZnO multilayers with thicker Mn-rich layer thickness, supporting the obtained results in Chapter 3.

Two additional facts from the XRR graphs should be mentioned.

i) On one hand, the total thickness of t = 1.5 nm sample does not appreciably change after annealing treatments. This has also been checked for t = 0.7 nm sample annealed at 600ºC in oxygen flux, supporting the idea that thermal treatments do no noticeably modify sample composition.

ii) On the other hand, sample thickness is significantly dependent of the substrate temperature during growth. The deposition rate remarkably diminishes when growing at T_S higher than 25ºC, fact that we also observed in the case of $Zn_{0.95}Mn_{0.05}O$ films grown with T_S = 600ºC (section 5.6). The thickness of these samples prepared with identical growth parameters except T_S, has the following behaviour: thickness of t = 6 nm sample prepared at T_S = 25ºC is 68 nm, it becomes nearly one half (36.7 nm) for T_S = 300ºC and it is finally reduced to 15.5 nm for T_S = 550ºC.

For the sake of clarity, it should be noted that this sample series has been named as "t = 6 nm" which corresponds to the nominal Mn layer thickness at 25ºC ($t_{sput(Mn)}$ = 107 s, see Table A.I). For T_S = 300ºC and 550ºC, although samples are named in the same manner (t = 6 nm) in fact, expected Mn layer thickness are smaller for these larger T_S values. Moreover, it should be kept in mind that, for the two sample series, i) and ii), no heterostructure arrangement was observed.

The Mn electronic states of several samples have been investigated by means of X-ray absorption spectroscopy at the Mn K-edge and also at the Mn $L_{3,2}$-edge.

The Mn K-edge XANES spectra of t = 1.5 nm as-grown as well as after annealing treatments samples are shown in Fig A.2(a), in comparison with Mn^0, Mn^{2+}, Mn^{3+} and Mn^{4+} spectra, from references.

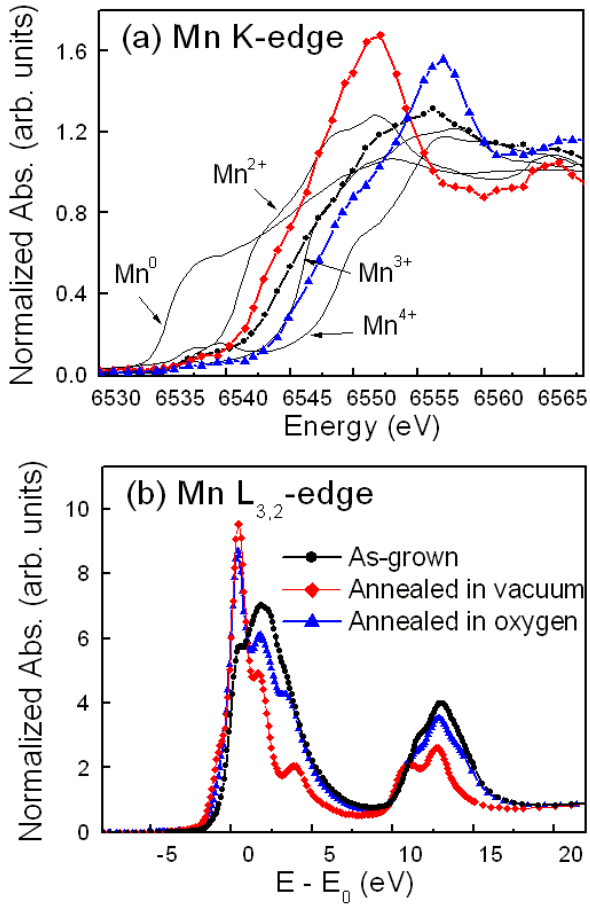

Fig. A.2 (a) Mn K-edge XANES spectra of t = 1.5 nm as-grown sample (● in black), annealed in vacuum at 600ºC (♦ in red) and annealed in oxygen at 750ºC (▲ in blue), compared to metallic Mn, Mn^{2+} (MnO), Mn^{3+} (MnOOH) and Mn^{4+} (MnO_2) references10 (b) Mn $L_{3,2}$-edge XANES spectra of t = 1.5 nm as-grown sample, annealed in vacuum at 750ºC and annealed in oxygen at 600ºC.

The XANES spectra of the annealed samples show remarkable differences compared to the as-grown one, both in the spectral position and in the signal amplitude**. After annealing in vacuum,** a clear energy threshold shift towards lower energies is obtained, evidencing a **reduction of the average Mn oxidation state** in the sample. By contrast**, annealing in high oxygen flux** (under the same vacuum base pressure) leads

to a threshold energy shift towards higher energies, what can be understood as an **enhancement of the average Mn oxidation state** in the samples.

It should be commented here that the type of modification in the Mn oxidation state induced by each kind of thermal treatment (sample annealing in reducing or oxidazing atmosphere) depends on the particular sample type, not pointing always towards the same direction. For instance, the former observation can be compared to the case of MnO_x/ZnO samples (section 4.8), where annealing with oxygen flux under identical conditions, implies a reduction of the Mn valence of the initially highly oxidized Mn (instead of further oxidation).

The average Mn oxidation states in these samples have been calculated considering the linear dependence between threshold energy and oxidation state for the reference compounds, performed in the same way as it was done in section 3.8.1. The estimated values are given in Table A.II. A total variation from +2.2 to +3.3 is found in the Mn oxidation state, from the vacuum-annealed sample to the oxygen-annealed one.

Furthermore, the noticeable enhance of the white line observed for the annealed samples might be assigned to an increase of the film crystal quality after thermal treatment, what leads to a narrower distribution of Mn crystal environments.

Additional soft X-ray absorption experiments have been done at the Mn $L_{3,2}$-edge in order to obtain more information about the Mn electronic states in the samples. Fig. A.2(b) shows the normalized XAS spectra measured at RT corresponding to t = 1.5 nm as-grown sample and after annealing in vacuum at 750ºC and in oxygen at 600ºC.

It should be remarked that an experimental energy shift during data acquisition made unattainable to know the precise energy threshold for each spectrum. For that reason, E_0 has been set as the maximum of the first derivate in Fig. A.2(b). Although the actual energy shift among the different spectra cannot be inferred, a significant difference in the Mn $L_{3,2}$-edge spectral shape is clearly evidenced for the three samples. Hence, we can still obtain important electronic information by analyzing the Mn $L_{3,2}$-edge spectral shapes, albeit being a bit more complicated.

By considering the Mn $L_{3,2}$ XAS theoretical calculations for Mn^{2+} (d^5), Mn^{3+} (d^4) and Mn^{4+} (d^3) electronic configurations, which are described in section 2.6.2, we have reasonably simulate the experimental spectra, simply by a linear combination of the calculated ones in T_d geometry under different crystal fields. It should be noted that the assessment of the quality of the calculations is based on the correct reproduction of the energy position of the different spectral features, relative energy separation and intensity ratio. The linear combinations of the three Mn electronic states considered as well as the obtained Mn oxidation state values are summarized in Table A.II, in comparison with the above-estimated values from the Mn K-edge. Results are in rather good agreement. It can also be noticed that the crystal field interaction magnitude included in the simulations becomes smaller for the annealed samples, what might be associated with strain relaxation during the annealing process.

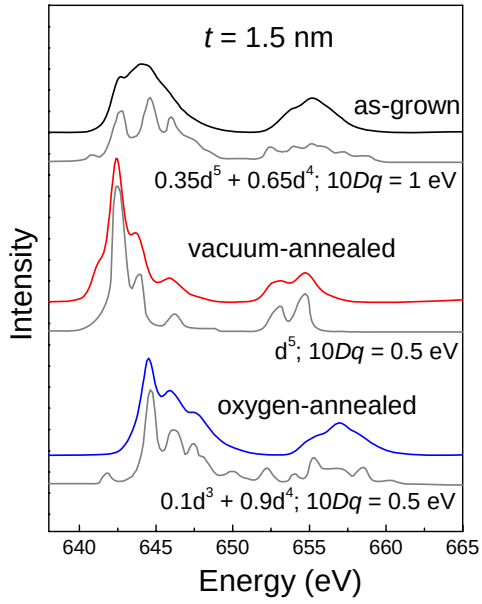

Fig. A.3 Mn $L_{3,2}$ XAS spectra measured at RT of t = 1.5 nm sample, as grown, annealed in vacuum at 750ºC and annealed in oxygen at 600ºC. Spectra have been normalized and the L_3 and L_2 step edges have been subtracted by two arctangent functions after background removal. Simulations (grey solid-lines) obtained by linear combinations of the calculations for Mn^{2+} (d^5), Mn^{3+} (d^4) and Mn^{4+} (d^3) in T_d crystal symmetry under different crystal field11 ($10Dq$ = 0.5-1 eV) are included for comparison. More calculation details are given in section 2.6.2.

Table A.II. Comparison between the Mn average oxidation state values estimated through the Mn K- and $L_{3,2}$- edges.

$[Mn_{(t)}/ZnO_{(3nm)}]_n$ t = 1.5 nm; n = 20	Mn oxidation state (K-edge)	Mn oxidation state ($L_{3,2}$-edge)
as-grown	+2.6 ± 0.2	+2.65 (0.35Mn_d^5+0.65Mn_d^4; 10Dq=1)
ann-600ºC-V	+2.2± 0.2	-
ann-750ºC-V	-	+2.0 (Mn_d^5; 10Dq=0.5)
ann-600ºC-O_2	-	+3.1 (0.1Mn_d^3+0.9Mn_d^4; 10Dq=0.5)
ann-750ºC-O_2	+3.3± 0.2	-

In addition, EXAFS experiments at the Mn- and Zn K-edges were performed for several samples. The EXAFS Fourier Transforms (FT) at the Mn K-edge for representative t = 1.5 nm as-grown and after different thermal treatments samples can be seen in Fig. A.4. EXAFS analysis provides the pairs and distances summarized in Table A.III, corresponding to the first and second coordination spheres. For the analysed k-range interval, no significant differences were obtained when considering Mn or Zn as backscatterer atoms. For that reason, only R_{Mn-M} distance contribution, where M may be both, Mn or Zn, is reported.

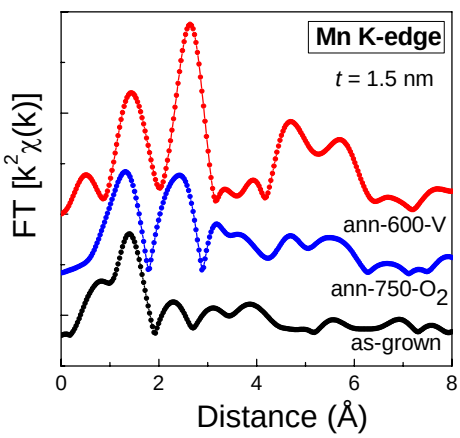

Fig. A.4 EXAFS Fourier Transforms (FT) of for t = 1.5 nm as-grown, vacuum-annealed at 600ºC and oxygen-annealed at 750ºC samples.

In Table A.III, results for t = 1.5 nm as-grown sample, annealed in vacuum at 600ºC and in oxygen flux at 750ºC, as well as t = 0.7 nm as-grown sample and annealed in oxygen at 750ºC, are compared with references of manganese oxides and zinc oxide.

From the obtained results and in agreement with the above XANES data, **shorter Mn-O distances are achieved for oxygen annealing while larger Mn-O distances are found for vacuum annealing**. Comparing with the manganese oxides references, **Mn-O and Mn-M distances in the vacuum-annealed t = 1.5 nm sample** (Mn-O = 2.21 Å and Mn-M = 3.13 Å) **becomes very similar to those ones in MnO** (Mn-O = 2.22 Å and Mn-M = 3.14 Å).

The local environment around Mn for the **oxygen-annealed t = 1.5 nm and t = 0.7 nm samples** is very similar. For these samples, **distances from the fits are Mn-O = 1.91 Å and Mn-M = 2.94 Å, being compatible, for instance, with MnO_2 presence**.

In comparison with t = 1.5 nm as-grown sample, Zn-O distances do not appreciably change after vacuum annealing (2.04 Å), while they are reduced for oxygen annealing (1.95 Å), becoming closer to those ones obtained in ZnO thin film (1.97 Å).

In general, it is found that coordination number increases after annealing, especially for the second shell, what seems to be related to the crystalline quality improve due to thermal treatment. The increase of the film crystal quality after thermal treatment was also pointed above by the XANES spectra at the Mn K-edge.

Table A.III. Summary of XAS results at the Mn and Zn K-edges corresponding to references and samples: XANES-obtained Mn oxidation values and R, N and σ^2 EXAFS parameters (distance (R), number of neighbours (N) and Debye-Waller factor, respectively).

	Mn oxid.state	Pair	R (Å)	N	σ^2 (10^{-3}Å^2)
References					
MnO	+2	Mn-O	2.22	6	
		Mn-Mn	3.14	12	
Mn_3O_4	+2	Mn-O	2.04	4	
	+3	Mn-O	1.93	4	
			2.28	2	
Mn_2O_3	+3	Mn-O	1.89-2.25	6	
β-MnO_2	+4	Mn-O	1.89	6	
		Mn-Mn	2.89	2	
		Mn-Mn	3.40	8	
ZnO		Zn-O	1.99	4	
		Zn-Zn	3.23	12	
Samples					
sputtered ZnO film		Zn-O	1.97±0.02	4	0.4±0.5
		Zn-Zn	3.18±0.02	12	12±1
t = 1.5 nm as-grown	+2.6	Mn-O	1.94±0.02	3.6	2.5±0.5
		Mn-M	2.86±0.02	1.6	20±1
		Zn-O	2.05±0.02	2.9	1.4±0.5
		Zn-Zn	3.14±0.02	5.0	4.5±1
t = 1.5 nm-ann-600-V	+2.2	Mn-O	2.21±0.02	4.0	16.0±0.5
		Mn-M	3.13±0.02	7.9	12±1
		Zn-O	2.04±0.02	2.4	1.0±0.5
		Zn-Zn	3.22±0.02	12.0	13±1
t = 1.5 nm-ann-750-O_2	+3.3	Mn-O	1.91±0.02	3.2	1.0±0.5
		Mn-M	2.93±0.02	9.2	23±1
		Zn-O	1.95±0.02	4.0	9.6±0.5
		Zn-Zn	3.30±0.02	10.0	8.5±1
t = 0.7 nm as-grown	+2.9	Mn-O	1.92±0.02	2.9	3.0±0.5
		Mn-M	2.91±0.02	1.9	30±1
t = 0.7 nm-ann-750-O_2	+3.3	Mn-O	1.91±0.02	3.1	1.0±0.5
		Mn-M	2.95±0.02	10.2	30±1

In order to obtain more structural information, XRD experiments were carried out using synchrotron radiation. Grazing incidence (omega-angle geometry with $\omega = 0.75^{o}$) as well as θ-2θ x-ray diffraction measurements (with $\lambda = 0.8857$ Å) were performed.

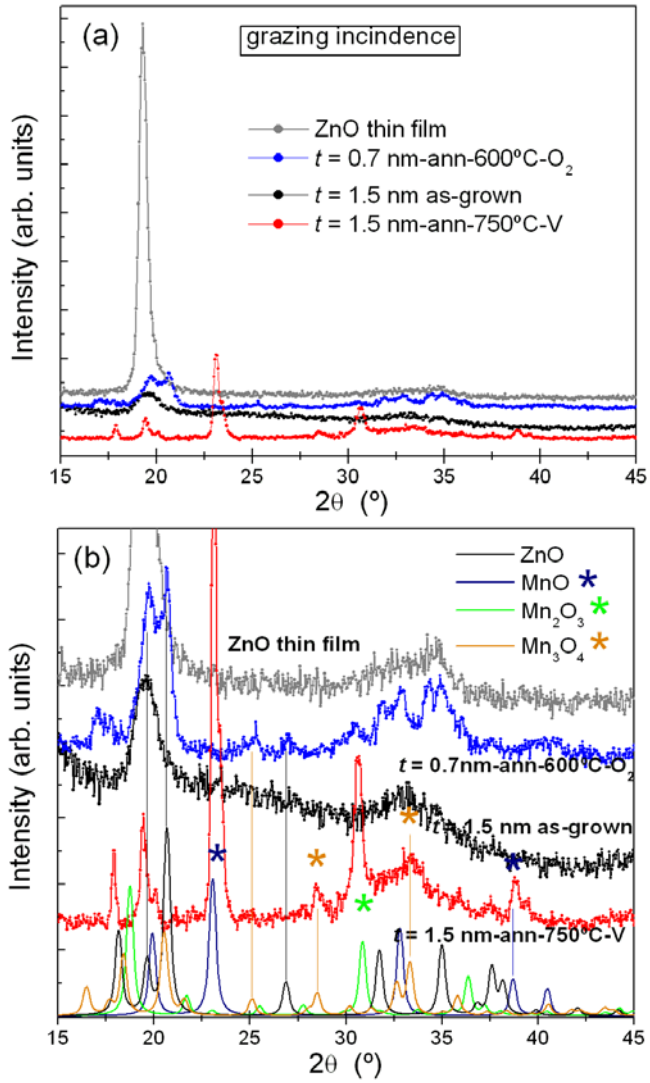

Fig. A.5 (a) Grazing incidence ($\omega = 0.75^{o}$) x-ray diffraction of t = 1.5 nm sample (as-grown and annealed in vacuum at 750°C), oxygen-annealed (600°C-O_2) t = 0.7 nm sample and a 70 nm sputtered ZnO film. (b) Zoom of the grazing incidence sample spectra in comparison with XRD patterns of *W*-ZnO, MnO, Mn_2O_3 and Mn_3O_4 references.

Fig. A.5(a) shows grazing incidence spectra of t = 1.5 nm as-grown and vacuum-annealed (ann-750ºC-V) samples, oxygen-annealed (ann-600ºC-O_2) t = 0.7 nm sample and a ZnO sputtered film (70 nm thickness), included for comparison. A zoom of these spectra, where ZnO MnO, Mn_2O_3 and Mn_3O_4 references have been included for comparison, is depicted in Fig. A.5(b).

As it can be observed from both the XRD spectra, there exist important differences among these samples. The comparison of the grazing incidence sample spectra with reference spectra, in Fig. A.5(b), leads to the following results:

For the as-grown t = 1.5 nm sample, besides the major ZnO nanocrystals presence, there are vestiges of Mn_3O_4 nanocrystalline grains. Since Mn^{2+} and Mn^{3+} cations coexist in the Mn_3O_4, this result is in accordance with the average Mn oxidation state estimated for this sample ($+2.6 \pm 0.2$) and with the obtained EXAFS distances.

Vacuum-annealing of t = 1.5 nm sample at 750ºC greatly favours the formation of MnO rocksalt nanocrystals, resulting in the principal crystalline phase within the film, as it was found from EXAFS simulations. Apart from MnO, nanocrystalline grains of **ZnO, Mn_2O_3 and Mn_3O_4** are detected by XRD measurements. The MnO crystal majority is consistent with the average Mn oxidation state calculated for this sample ($+2.2 \pm 0.2$).

From the spectrum of the oxygen-annealed sample (t = 0.7 nm-ann-600ºC-O_2), although a direct comparison with t = 1.5 nm sample cannot be made, it is possible to deduce structural information. **Thermal treatment in oxygen atmosphere leads to an increase of the ZnO grain size, especially noticeable for the (101)-ZnO grains**. Although the major crystalline contribution comes from ZnO, there are also hints of Mn_3O_4 in this sample. On the other hand, similarly to the case of Mn/ZnO as-grown samples (Chapter 3), no traces of MnO_2 grains have been found here, maybe due to their amorphous character or the small crystalline grain size. Nevertheless, the obtained results are compatible with the average Mn valence afore-estimated for this sample ($+3.3 \pm 0.2$) and with the EXAFS results.

In addition, the following results can be obtained from the θ-2θ sample scan, shown in Fig. A.6.

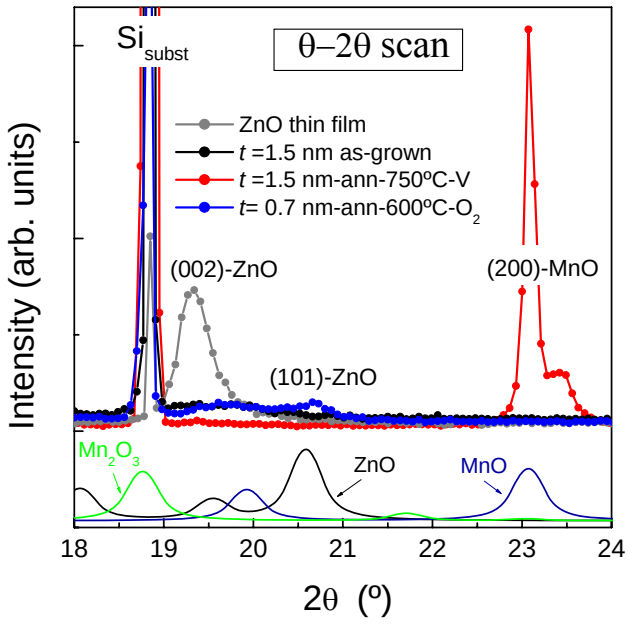

Fig. A.6 θ-2θ x-ray diffraction measurements of t = 1.5 nm sample (as-grown and annealed in vacuum at 750ºC), oxygen-annealed (600ºC-O_2) t = 0.7 nm sample and a 70 nm sputtered ZnO film in comparison with XRD patterns of *W*-ZnO, MnO and Mn_2O_3 references.

It should be remarked here that from the θ-2θ scan of the as-grown samples (Chapter 3) it was obtained that the Mn/ZnO multilayered samples show (002) texture. For t = 1.5 nm as-grown sample, the obtained crystalline grain size in the out-of-plane direction, calculated by the Scherrer formula, was near 2.9 nm, coinciding with the expected ZnO layer thickness (3 nm of nominal layer).

By contrast, after thermal annealing, it was shown by XRR measurements that different layers mixed together with the consequently lost of the heterostructure character.

θ-2θ scan of t = 0.7 nm sample after annealing at 600ºC in O_2 shows (002)-ZnO as well as (101)-ZnO peak, which corresponds to the most intense ZnO reference peak.

The obtained grain size in the out-of-plane direction is about 6 nm for (002)-ZnO, not showing the 3 nm ZnO layer thickness restriction, and it reaches 9 nm size for (101)-ZnO nanocrystalline grains.

On the other hand, θ-2θ scan of t = 1.5 nm sample after annealing at 750ºC in vacuum does not exhibit any ZnO peak. By contrast, it shows (200)-MnO texture. The calculated MnO grain size in the out-of-plane direction is 42.5 nm, which is considerably larger than, for instance, the 10.4 nm ZnO grain size.

No signs of metallic Mn or other Mn-Zn-O phases in these samples are evidenced from XRD measurements. The main XRD results are summarized in Table A.IV.

Table A.IV Crystalline phases detected by grazing incidence XRD measurements for t = 1.5 nm sample (as-grown) and vacuum-annealed (750ºC-V), oxygen-annealed (600ºC-O_2) t = 0.7 nm sample and a ZnO sputtered film. Crystalline grain sizes in the out-of-plane direction, calculated from θ-2θ diffraction peaks by means of the Scherrer equation, are also included.

$[Mn_{(t)}/ZnO_{(3nm)}]_n$	XRD-detected phases	Out-of-plane grain size
t = 1.5 nm (as-grown)	ZnO, Mn_3O_4	(002)-ZnO: 2.9 nm
t = 1.5 nm ann-750ºC-V	MnO, ZnO, Mn_2O_3, Mn_3O_4	(200)-MnO: 42.5 nm
t = 0.7 nm ann-600ºC-O_2	ZnO, Mn_3O_4	(101)-ZnO:9 nm; (002)-ZnO:6 nm
ZnO film (70nm)	ZnO	(002)-ZnO: 10.4 nm

Regarding the magnetic properties of these thermally treated samples, it can be observed that, **sample annealing, either in oxygen atmosphere or vacuum, leads to a clear weakening of the ferromagnetic response**. Magnetization versus temperature dependence of t = 1.5 nm sample, as grown and after annealing, is shown in Fig. A.7.

M(T) curve of vacuum-annealed t = 1.5 sample reveals a magnetic transition around 50 K, which can be related to the presence of Mn_3O_4 (T_C = 43 K). Furthermore, the existence of Mn_3O_4 grains has been verified in this sample by the above XRD results.

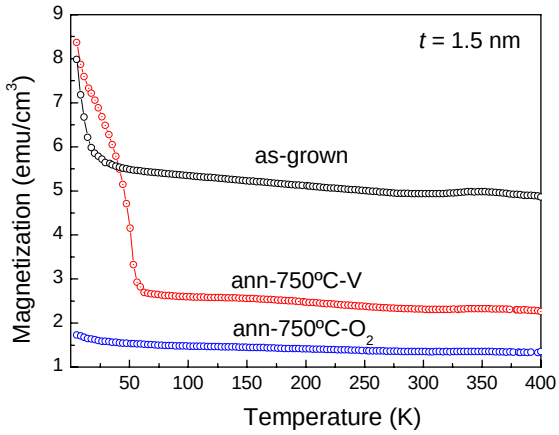

Fig. .A.7 (a) M-T curves for t = 1.5 nm sample as-grown and after different annealing treatments.

Another fact to remark from the obtained M-T curves (Fig. A.7) is that **the ferromagnetic signal diminution is stronger when annealing in oxygen atmosphere than in vacuum**. It should be underlined that the significant reduction of the ferromagnetic response by the oxygen effect is commonly found in the Mn-Zn-O system. For instance, we have also observed this effect for $Zn_{0.95}Mn_{0.05}O$ films prepared in oxygen atmosphere, as well as after annealing treatments in oxygen flow (section 5.6), what evidences a generally unfavourable oxygen effect on the ferromagnetism of this system.

We can relate these results to the origin of the ferromagnetic response found in Chapter 3 for Mn/ZnO multilayers. For the as-grown samples which exhibit ferromagnetic order, Mn oxidation states close to +2 as well as coexistence of wurtzite (*W*) and rocksalt (*RS*) phases were obtained. Nonetheless, the origin of the RTFM was only ascribed to the presence of Zn-O-Mn, in the form of *W* phase. For the case of smaller *t* values, high Mn oxidation states were obtained, resulting in the formation of MnO_2 nano-grains with no appreciable FM signal. Keeping that in mind, the diminution of the FM signal after annealing could be understand in the following way:

Vacuum annealing at temperatures between 600-750ºC leads to a clear decrease of the Mn oxidation state, which becomes near to +2. Mn oxidation states closer to +2 were found to favour FM in Mn/ZnO multilayers. However, coexistence of Mn-Zn-O in *W*

and *RS* phases was obtained in samples with mostly Mn^{2+}, being just Zn-O-Mn wurtzite phase the responsible of the observed FM. Here, XRD has shown that MnO crystals (*RS*-phase) are greatly favoured by vacuum annealing at these temperatures, as well as crystallization of minority Mn_2O_3 or Mn_3O_4 phases. Both promoting *RS* phase over *W* phase and the stabilization of additional crystalline phases can explain the detrimental effect on FM by vacuum annealing.

Annealing in oxygen flux at these temperatures, by contrast, leads to a clear increase of the Mn oxidation state, which becomes about +3.3. Comparing with as-grown Mn/ZnO multilayers with similarly oxidized Mn, mostly MnO_2 nanograins embedded in the *W*-ZnO matrix and no appreciable FM was obtained for these samples. Therefore, the obtained diminution of the FM response after oxygen annealing agrees with the origin of FM proposed in Mn/ZnO multilayers. The reduction of the ferromagnetism by the oxygen effect has been commonly observed in the Mn-Zn-O system. V. K. Sharma et al.3 showed that annealing in oxygen atmosphere at 800ºC reduced the magnetization and sample became completely paramagnetic and E. Chikoidze et al.[5] did not observe any ferromagnetism in oxygen-annealed Mn-Zn-O films, which became highly unstable at temperatures as low as 300ºC. Along the presented work, we have also observed deterioration of the ferromagnetic signal due to oxygen in $Zn_{0.95}Mn_{0.05}O$ films prepared in oxygen atmosphere, as well as after annealing treatments in oxygen flow (section 5.6).

It should be noticed that in both cases, vacuum and oxygen annealing, additional factors related to the loss of the heterostructure periodicity or to the strong modifications of the crystalline grains after annealing can complicate this simplified image.

On the other hand, Fig A.8 shows the M(T) curves obtained for t = 6 nm samples prepared at different substrate temperatures (T_S = 25ºC and 300ºC) as well as oxygen-annealed at 600ºC (T_S = 25ºC). As it was found above for t = 1.5 nm sample, oxygen annealing of t = 6 nm sample involves a significant reduction of the magnetization. Furthermore, sample growth under similar experimental conditions but at moderate substrate temperatures does not favour FM ordering in these samples. The obtained results are compatible with the investigations performed by Pradhan et al.[9], where they

found that for substrate temperatures over 500ºC, the crystalline quality of the $Zn_{1-x}Mn_xO$ films increased at the expense of a decrease in the RTFM due to the formation of Mn related clusters. The declination of the FM occurs here even at lower substrate temperatures.

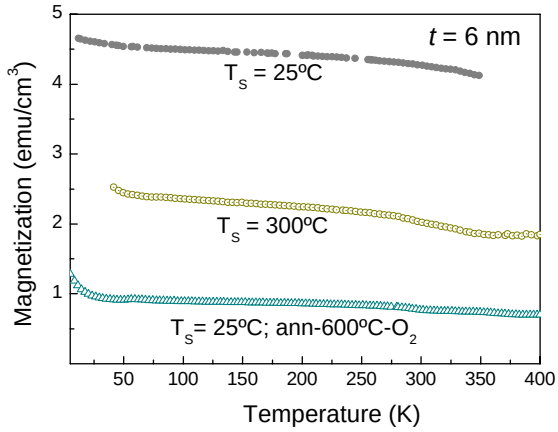

Fig. A.8 (a) M-T curves for t = 6 nm sample grown at different substrate temperature and after oxygen annealing.

Conclusions

Post-deposition annealing of Mn/ZnO samples at temperatures around 600-750ºC notably modifies the Mn electronic state in these samples. While a reduction of the average Mn oxidation state is found after annealing in vacuum, annealing with high oxygen flux leads to an enhancement of the average Mn oxidation state.

In addition, both post- deposition annealing at these temperatures (either in oxygen or vacuum atmosphere) and growing at substrate temperature of 300ºC (or higher) cause the loss of the heterostructure periodicity, clearly observed for as-grown samples (T_S = 25ºC).

Furthermore, the structural properties and crystalline quality of samples are significantly modified by the annealing treatments.

The ferromagnetic response of these samples is considerable weaken after annealing, being the signal diminution stronger for annealing in oxygen atmosphere than in vacuum.

Vacuum-annealing promotes the formation of rocksalt nanocrystals over wurtzite phase, what seems related to the ferromagnetic signal reduction. This fact holds with Zn-O-Mn wurtzite phase as the responsible of the RTFM observed in Mn/ZnO multilayers.

Oxygen-annealing favours the formation of highly oxidized manganese phase coexisting with *W*-ZnO, what leads to a decrease of FM, in accordance to the case of Mn/ZnO multilayer with very thin Mn layers. The reduction of the ferromagnetic response by the oxygen effect has been commonly observed in the Mn-Zn-O system.

Moreover, annealing favours the crystallization of additional phases, as Mn_2O_3 or Mn_3O_4.

In addition to the Zn-O-Mn wurtzite phase declination, different facts as, loss of the heterostructure periodicity, improvement of the crystal quality and formation of additional crystal phases as Mn_2O_3 or Mn_3O_4 worsen the ferromagnetic order in the Mn-Zn-O system.

References

1 H. K. Yadav, K. Sreenivas and V. Gupta, J. Appl. Phys. 99, 083507 (2006).

2 F. Pan, C. Song, X. J. Liu, Y. C. Yang and F. Zeng, Materials Science and Engeneering R 62, 1-35 (2008).

3 V. K. Sharma and G. D. Varma, J. Alloy. Compd. 458, 523 (2008).

4 B. Babić-Stojić, D. Milivojević, J. Blanuša, V. Spasojević, N. Bibić, B. Simonović and D. Arandelović J. Phys.: Condens. Matter 20, 235217 (2008).

5 E. Chikoidze, Y. Dumont, H. J. von Bardeleben, J. Gleize, O. Gorochov, J. Magn. Magn. Mater. 316, e181 (2007).

6 S. Lee, Y. Shon, S-W Lee, S. J. Hwang, H. S. Lee, T. W. Kang and D. Y. Kim, Apl. Phys. Lett. 88, 212513 (2006).

7 Y. W. Heo, M. P. Ivill, K. Ip, D. P. Norton, Appl. Phys. Letter 84, 2292 (2004).

8 P. Sharma, A. Gupta, K. V. Rao, F. J. Owens, R. Sharma, R. Ahuja, J. M. Osorio, Gullen, B. Johansson, G. A. Gehring, Nat. Mater. 2, 673 (2003).

9 A. K. Pradhan, K. Zhang, S. Mohanty, J. B. Dadson, and D. Hunter, Appl. Phys. Lett 86, 152511 (2005).

10 D. A. McKeown and J.E. Post, Am. Mineral. 86, 701 (2001).

11 G. van der Laan and I. W. Kirkman, J. Phys.: Condens. Matter 4, 4189 (1992).

Appendix B

ZnO Crystal Structures

Most of the II-VI semiconductors crystallize in either cubic zinc-blende (ZB) or hexagonal wurtzite (W) structure where each cation is surrounded by four anions at the corners of a tetrahedron and vice versa. This tetrahedral (T_d) coordination is typically of sp^3 covalent bonding, but these materials also have a substantial ionic character. ZnO is a II-VI semiconductor whose ionicity resides at the borderline between covalent and ionic semiconductor. In fact, there are three reported crystal structures for ZnO, wurtzite (W), zinc-blende (ZB) and rocksalt (RS), which have been schematically represented in Fig. B.1.[1]

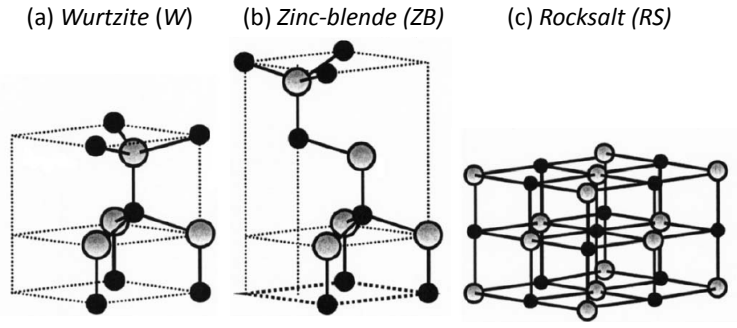

Fig B.1 Representation of the ZnO crystal structures: (a) hexagonal wurtzite (W), (b) cubic zinc-blende (ZB) and (c) cubic rocksalt (RS). The shaded grey and black spheres indicate Zn and O atoms, respectively.

At room conditions, the thermodynamically stable phase is *W*-ZnO. The *W* structure has a hexagonal unit cell with two lattice parameters, *a* and *c*, in the ratio c/a = 1.633 and belongs to the $P6_3mc$ space group. A representation of the *W*-ZnO structure has been shown in Fig. B.2. This structure is composed by two interpenetrating

hexagonal-close-packed (*hcp*) sublattices, each of which consists of one atom displaced with respect to each other along the threefold *c*-axis by the amount of $u = 3/8 = 0.375$, in an ideal *W* structure. Each atom type (group II or VI) is surrounded by 4 atoms of the other kind, which are coordinated at the edges of a tetrahedron. In a real ZnO crystal, the *W* structure deviates from the ideal arrangement by changing the c/a ratio or the u value. There is a strong correlation between the c/a ratio and the u parameter. When the c/a ratio decreases, the u parameter increases in such a way that those four T_d distances remain nearly constant through a distortion of tetrahedral angles due to long-range polar interactions.[1,2]

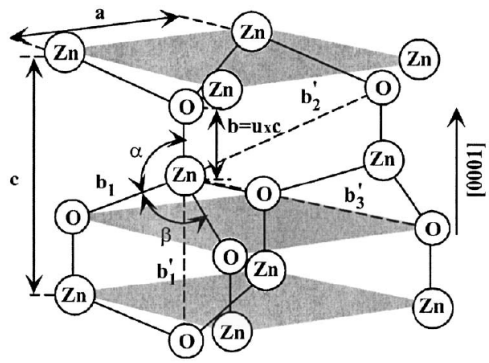

Fig B.2 Schematic representation of a ZnO wurtzite structure with lattice constants *a* in the basal plane and *c* in the basal direction; *u* parameter is expressed as the bond length or the nearest-neighbour distance *b* divided by *c* (0.375 in an ideal crystal) and α and β (109.47° in an ideal crystal) are the bond angles.

The *ZB*-ZnO structure is metastable and can be stabilized only by heteroepitaxial growth on cubic substrates, such as ZnS.[3] The symmetry of the *ZB* structure is given by space group $F\bar{4}3m$ and consists of two interpenetrating face-centered-cubic (fcc) sublattices shifted along the body diagonal by one-quarter of a body diagonal. There are four atoms per unit cell and every atom (group II) has T_d coordination of atoms of the other type (group VI), and vice versa. Because of the T_d coordination of *W* and *ZB*

structures, the 4 nearest neighbours and 12 next-nearest neighbours have the same bond distance in both structures. The main difference between them lies in the stacking sequence of the closed-packed biatomic planes. While *W*-ZnO exhibits triangularly arranged alternating biatomic closed-packed (0001) planes (*AaBbAaBb*…) in the <0001> direction, *ZB*-ZnO consists of triangularly arranged atoms in the closed-packed (111) planes along the <111> direction with a stacking order of *AaBbCcAaBbCc*… , referring small and large letters to the two different constituents.[1]

Additionally, as it happens in other II-VI semiconductors, *W*-ZnO can be transformed to the *RS*-ZnO structure (*NaCl*) at relatively modest external pressures. The reason for this is that the reduction of the lattice dimensions causes the interatomic Coulomb interaction to favour the ionicity more over the covalent nature. The space-group symmetry of the *RS* phase is *Fm*3*m*, and the structure is sixfold coordinated, having octahedral (O_h) symmetry.[1] However, the *RS*-ZnO structure cannot be stabilized by epitaxial growth. Usually, the pressure induced phase transition occurs at approximately 10 GPa, with a volume decrease of about 17%.[4] Authors have reported metastability of this phase for long periods of time even at room pressure and above 100ºC, and more recently, even when the pressure is released.[1,5,6] By contrast, it has been also reported that this transition is reversible at room temperature.[1,7] Recently, *ab initio* calculations[8] have been performed to study the mechanism responsible for the *W*-to-*RS* structural phase transition in ZnO. It has been shown that the commonly observed transition from the fourfold coordinated *W* to the sixfold coordinated *RS* phase occurs through a *quasitetragonal* deformation which links, in a crystallographic simple way, the two endpoint structures. The recently suggested *hexagonal* path does not seem favorable for ZnO, although it seems possible in wurtzite semiconductors such as AlN or SiC). The discussed paths for the phase transformation in the *ab* angle (γ) - *u* internal coordinate plane is shown in Fig. B.3.

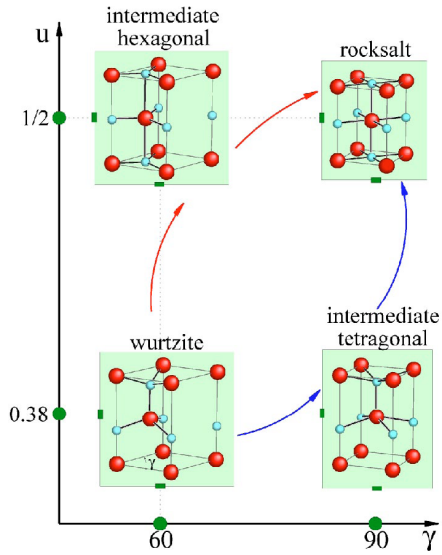

Fig B.3 Evolution of the u parameter ($u = b/c$) versus γ (ab angle) in the two different routes ("hexagonal" and "tetragonal" paths) proposed for the transformation of a wurtzite structure into a rocksalt phase. The optima c/a ratio is about 1.61 and 1.74 for the wurtzite and tetragonal structures (bottom), where $u \sim 0.38$ and 1.29 and $\sqrt{2}$ for the hexagonal an rocksalt structures (top), where $u = 1/2$. Recent calculations have shown that the intermediate tetragonal one is the energetically favourable one.[8]

For the *W*-ZnO, the reported lattice constants range from 3.2475 to 3.2501 Å for the a parameter and from 5.2042 to 5.2075 Å for the c parameter. The c/a ratio and u parameter vary in a slightly wider range, from 1.593 to 1.6035 and from 0.383 to 0.3856, respectively. The deviation from that of the ideal wurtzite crystal is probably due to lattice stability and ionicity. The point defects such as zinc antisites (Zn_O) oxygen vacancies (V_O) and extended defects, such as threading dislocations, also increase the lattice constant. For the *ZB*-ZnO, the lattice contants of ZnO epilayers grown on ZnS were between 4.37 and 4.47 Å. Finally, the high-pressure phase transition from the *W* to the *RS* structure decreases the lattice constant down to the range of 4.271–4.294 Å.[1]

References

1 Ü. Özgür, Ya. I. Alivov, C. Liu, A. Teke, M. A. Reshchikov, S. Dogan, V. Avrutin, S. J. Cho, and Morkoç, Applied Physics Reviews, J. Appl. Phys. 98, 0141301 (2005).

2 E. Kisi and M. Elcombe, Acta Crystallogr., Sect. C: Cryst. Struct. Commun. C45, 1867 (1989).

3 T. Kogure and Y. Bando, Y. Electron Microsc. 47, 7903 (1993).

4 C. H. Bates, W. B. White, and R. Roy, Science 137, 993 (1962).

5 L. Gerward and J. S. Olsen, J. Synchrotron Radiat. 2, 233 (1995).

6 J. M. Recio, R. Pandey, and V. Luaña, R. Pandey, L. Gerward, and J. Staun Olsen, Phys. Rev. B 58, 8949 (1998).

7 J. C. Jamieson, Phys. Earth Planet. Inter. 3, 201 (1970).

8 A. M. Saitta and F. Decremps, Phys. Rev. B 70, 035214 (2004).

PART II

Mn-Si_3Ni_4 System

Chapter 6

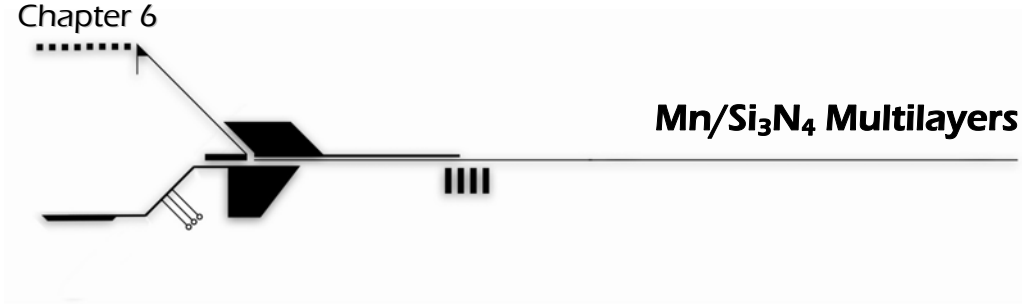

Mn/Si_3N_4 Multilayers

6.1. Motivation

Manganese nitrides have gained attention among the 3d transition metal nitrides for their variety of electronic and magnetic properties which are suitable for potential applications.[1,2,3] Recently, these materials have also generated interest in the field of diluted magnetic semiconductors (DMS) with high Curie temperatures, as potentially magnetic secondary phases forming within films of Mn-doped III-V semiconductors such as Mn:GaAs, MnInN and especially Mn:GaN.[4,5,6]

The manganese nitrides form a variety of stoichiometric phases (ε, ζ, η, θ) exhibiting different magnetic properties. The most N rich phase, mononitride θ-MnN, has a tetragonally distorted rocksalt (NaCl) structure with an antiferromagnetic (AF) ground state. It usually contains a considerable amount of N vacancies and is often labeled as Mn_6N_{5+x}.[7] The closely related η-Mn_3N_2 phase is also of the NaCl structure but with an ordered array of N vacancies.[7,8] The ζ-phases (Mn_5N_2 and Mn_2N) have hexagonal closed packed arranges and present ferromagnetic (FM) and AF order, respectively[9]. Finally, the ε-Mn_4N phase consists basically in a Mn face-centered cubic structure with an interstitial N and exhibits ferrimagnetism with a curie temperature (T_C) as high as 745 K.[10]

These MnN_x phases are currently related to inhomogeneities in ternary nitride-based alloys as the possible origin of the observed ferromagnetism. Recent studies have pointed towards Mn_4N as a segregation phase showing the ferromagnetic behaviors in Mn:GaN films.[11] Special attention has been also directed to the θ-MnN phase, since possible inclusions or MnN-rich regions in the matrix can have the same crystallographic structure as the semiconductor host. Although MnN has an AF ground state, it has been

theoretically shown that FM order can be established depending on the polymorph of MnN and lattice parameters.[6] A number of band-structure calculations have been performed considering MnN in the hypothetical zinc-blende (ZB) and wurtzite (W) structures in order to get a better comprehension of these ternary nitride-based DMS systems.[6,12] Ferromagnetism with T_C of 354 K due to Mn-rich precipitates in the zinc-blende phase has been recently predicted in Mn:GaN by using the mean-field approximation.[4] More recently, simulations of GaN/MnN superlattices have been developed as a new way to obtain the FM *W*-MnN on GaN as an alternative to the (Ga,Mn)N DMS approach.[13] These calculations based on spin-density-functional theory have suggested that this system can be used for new spintronics devices as they can provide spin-polarized carriers in the wide-gap nitride systems. A FM ground state has been predicted in these GaN/MnN heterostructures, which comprise a thin layer of biaxially strained *W*-MnN intercalated with layers of GaN, due to the structure relaxation at the GaN-MnN interface.

Despite all these exciting properties, up to date there have not been reported experimental efforts to obtained FM semiconductor/manganese nitride heterostructures. Even the interesting magnetic properties of MnN_x films have hardly been experimentally studied, probably due to difficulties in sample preparation. Just a few attempts of fabrication of MnN by reactive sputtering[9] and ion-assisted deposition[2], Mn_3N_2 using reactive sputtering[3] and molecular beam epitaxy[1] and Mn_4N, also by reactive sputtering,[3,14] have been reported.

Here, because of its similarities, instead of GaN, we use Si_3N_4, which also possesses a wide-band-gap semiconducting behavior and can be an excellent host material due to its possible high dopant concentration.[15,16] Furthermore, Si_3N_4 has been extensively used in materials science for its good performance in resistance to thermal shock and oxidation, great chemical stability, low density, and high fracture toughness.[17,18] Recently, there have been reported successful researches on Si_3N_4 films, nanowires and nanobelts, which are very promising for the synthesis of nanostructured Si_3N_4 on a large scale.[19,20,21]

In the present chapter, the magnetic properties of several series of Mn/Si_3N_4 multilayered films have been explored and ferromagnetism above room temperature has been found in this system for the first time. The structural and electronic properties of the samples have been studied using a number of techniques as x-ray reflectivity, x-ray absorption and x-ray photoemission spectroscopies and x-ray magnetic circular dichroism to investigate the magnetic-structural relationship in the Mn/Si_3N_4 system.

Different sets of Mn/Si_3N_4 multilayers have been prepared by varying the Mn:Si_3N_4 relative ratio. The evolution of the magnetic properties has been studied for multilayers with nominal formula $[Mn(t_m)/Si_3N_4(3nm)]_n$, being "t_m" the nominal Mn layer thickness and "n" the number of bilayers, as well as for samples labeled as $[Mn(0.6nm)/Si_3N_4(t_{sn})]_{43}$, being "$t_{sn}$" the nominal Si_3N_4 layer thickness, in order to find the most suitable conditions to stabilize the ferromagnetic ordering in this system.

4.2. Preparation of multilayers

Mn/Si_3N_4 multilayers were prepared by sequential sputtering of Si_3N_4 and Mn on Si(100) substrates at RT. The residual pressure in the vacuum system was in the 1 x 10^{-7} mbar range. The Si_3N_4 layers were deposited by reactive RF-sputtering from a pure Si target (Goodfellow: 99.999 %) with N_2 as reactive sputtering gas.[22] The deposition rate was 2 nm/min for a RF power of 100 W. Mn was grown by DC-sputtering from a Mn target (Goodfellow: 99.95 %) with Ar as sputtering gas and a deposition rate of ~4 nm/min for a DC power of ~ 10 W.

Samples with nominal formula $[Mn(t_m)/Si_3N_4(3nm)]_n$ as well as samples named $[Mn(0.6nm)/Si_3N_4(t_{sn})]_{43}$ were prepared. For the first set of samples, the Si_3N_4 layer thickness was maintained constant while the Mn layer (t_m) was modified between 6 and 0.1 nm of nominal thickness. In this case, the number of bilayers (n) was progressively increased (from 5 to 75) as the Mn layer thickness was reduced in order to maintain the total amount of Mn approximately constant. In the case of $[Mn(0.6nm)/Si_3N_4(t_{sn})]_{43}$ samples, the Mn layer thickness was kept approximately constant while the Si_3N_4 layer

thickness (t_{sn}) was modified from 6 nm to 0.7 nm. In the former case, the number of bilayers was always the same (n = 43). For the two sets of multilayers the growth process began with a Si_3N_4 layer and terminated by depositing an additional 3 nm Si_3N_4 layer on top.

6.3. X-Ray Reflectivity (XRR)

X-ray reflectivity measurements were done in a standard X-ray diffractometer (Bruker D8) working with the Cu K_α wavelength, at the ICMM facilities. XRR spectra of the studied multilayers are shown in Fig. 6.1 for both samples series prepared with different Mn-layer thickness (t_m) (Fig. 6.1(a)) and with variable Si_3N_4 layer thickness (t_{sn}) (Fig 6.1 (b)).

Well-defined peaks of **heterostructure periodicity in the out-of-plane direction** can be observed in the spectra from samples with larger t_m and t_{sn} thicknesses, while these periodicity features become smoother as t_m and t_{sn} are reduced. In fact, non-continuous Mn layers are expected for very small t_m values, where Mn layer thickness and interface roughness become comparable. It should be noted in Fig. 6.1(a) that samples with a large bilayer number, as for instance 75 bilayers, have a total thickness too large to exhibit the short oscillations corresponding to finite size film interferences.

Sample description and microstructural features such as average bilayer thickness are summarized in Tables 6.I and 6.II for samples with variable t_m and t_{sn}, respectively. Measured layer thickness is approximately 15 % higher than nominal.

For the sake of clarity, samples will be named from now on by their XRR experimentally obtained thickness values.

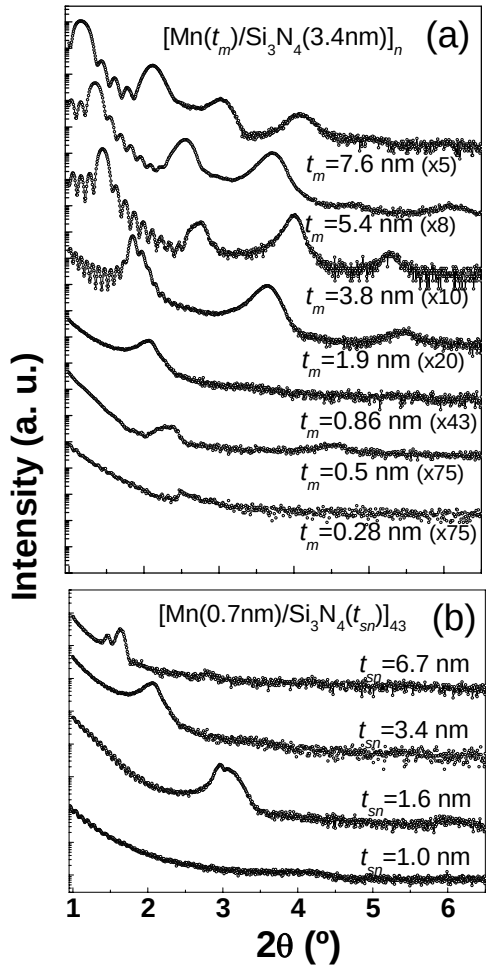

Fig. 6.1. (a) XRR spectra of some of the multilayer samples with different Mn-layer thickness (t_m). Experimental t_m values are shown in the figure. (b) XRR spectra of the prepared samples with different Si_3N_4-layer thickness (t_{sn}). Experimental t_m values are shown in the figure. All spectra have been vertically shifted for clearness.

Table 6.I. Description of selected $[Mn(t_m)/Si_3N_4(3nm)]_n$ nominal samples: nominal Mn thickness (t_m), number of bilayers (n), nominal bilayer thickness (Λ), XRR- obtained bilayer thickness (XRR-Λ), XRR- obtained Mn thickness (XRR-t_m) and atomic composition, obtained from simulation of RBS and NRA.

Nominal t_m (nm)	n	Nominal Λ (nm)	XRR-Λ (nm)	Mn-layer atomic density (at./cm^2)	XRR-t_m (nm)	Composition (% at)		
						[Mn]	[Si]	[N]
6	5	9	11	$4.6x10^{16}$	7.6	0.42	0.14	0.44
6	5	9	10.7	-	7.3	-	-	-
4	8	7	8.8	-	5.4	-	-	-
3	10	6	6.9	$2.2x10^{16}$	3.8	0.31	0.16	0.53
3	10	6	6.6	-	3.5	-	-	-
1.5	20	4.5	5.3	$1.1 x10^{15}$	1.9	0.25	0.18	0.57
0.7	43	3.7	4.2	$5.9 x10^{16}$	0.86	0.17	0.25	0.58
0.4	75	3.4	3.6	$4.1 x10^{15}$	0.5	0.13	0.28	0.59
0.2	75	3.2	3.4	$2.9 x10^{15}$	0.28	0.10	0.30	0.60
0.1	75	3.1	3.1	$1.9 x10^{15}$	0.17	0.07	0.35	0.59

Table 6.II. Description of selected $[Mn(0.6nm)/Si_3N_4(t_{sn})]_{43}$ nominal samples: nominal Si_3N_4 thickness (t_{sn}), number of bilayers (n), nominal bilayer thickness (Λ), XRR- obtained bilayer thickness (XRR- Λ), XRR- obtained Si_3N_4 thickness (XRR- t_{sn}) and atomic composition, obtained from simulation of RBS and NRA.

Nominal t_{sn} (nm)	n	Nominal Λ (nm)	XRR-Λ (nm)	Mn-layer atomic density (at./cm^2)	XRR-t_{sn} (nm)	Composition (% at)		
						[Mn]	[Si]	[N]
6	43	6.6	7.4	$4.7x10^{15}$	6.7	0.08	0.34	0.58
3	43	3.6	4.1	$4.8x10^{15}$	3.4	0.13	0.27	0.60
1.5	43	2.1	2.3	$4.8x10^{15}$	1.6	0.20	0.20	0.60
0.7	43	1.7	1.7	$4.7x10^{15}$	1.0	0.25	0.14	0.61

6.4. Transmission Electron Microscopy (TEM)

For several samples, the **multilayer periodicity** has been additionally **confirmed by transmission electron microscopy** studies performed in collaboration with Dr. Augusto Barrós and Dr. Mercedes Vila from the Department of Ceramics and Glass Engineering, CICECO, at the University of Aveiro, in Portugal. The TEM cross-section images corresponding to t_m = 3.8 nm and 0.86 nm samples are depicted in Fig. 6.2(a) and 6.2(b) respectively. For the t_m = 3.8 nm sample, the image shows continuous layers of similar thickness corresponding to the Mn-rich and Si_3N_4 layers. An interface roughness enhance as the number of layers increases is evidenced in Fig. 6.2(a). The total thickness obtained by TEM is approximately 70 nm for this sample, which is slightly smaller but quite in agreement with XRR measurements. Conversely, although z-axis periodicity is still observed from TEM image of the t_m = 0.86 nm sample, the image suggests non-continuous growth in this former case. Non-continuous layers Mn-rich layers are hence expected for samples with t_m < 0.86 nm.

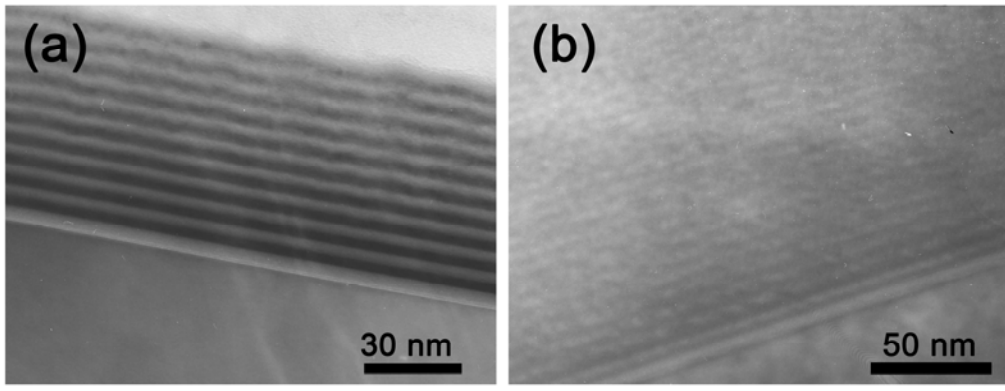

Fig. 6.2 (a) Cross-sectional TEM image of the sample labeled as $[Mn(3.8nm)/Si_3N_4(3.4nm)]_{10}$ and (b) $[Mn(0.86nm)/Si_3N_4(3.4nm)]_{43}$ sample, performed in a 300 kV Hitachi H9000-NA microscope.

6.5. Rutherford Backscattering Spectroscopy (RBS) and Nuclear Reaction Analysis (NRA)

Rutherford backscattering spectroscopy (RBS) and Nuclear Reaction Analysis (NRA) experiments were carried out at the Centro Nacional de Aceleradores (Sevilla, Spain) in collaboration with Dr. Javier García López to determine precisely the atomic composition of the samples. For the RBS experiments, a 2 MeV H^{2+} beam was employed, with beam diameter ~ 1 mm and scattering angle of 165º. The NRA measurements were done using the $^{14}N(d,\alpha_1)^{12}C$ nuclear reaction with a 1.4 MeV D^+ beam and a detection angle of 150º. A 13 μm thick mylar foil was placed in front of the detector in order to stop the backscattered deuterons to avoid saturation of the electronic set-up. For absolute N quantification of our samples, we have used as standard a 100 nm thick Si_3N_4 film grown on Si substrate.

Fig. 6.3(a) and 6.3(b) show the obtained RBS spectra and their corresponding simulations using the SIMNRA simulation software package. The calculated Mn atomic density and film atomic composition obtained jointly by RBS and NRA for some representative samples are summarized in Tables 6.I and 6.II.

A comparison between the experimental manganese layer thickness values obtained from XRR spectra and the ones calculated from RBS data considering pure metal manganese density is shown in Fig. 6.4. The obtained difference means that, even if pure Mn was sputtered, **layers do not consist of pure metallic Mn**, since to obtain the actual thickness (given by the XRR data) a smaller Mn density should be considered in calculations from RBS. On the other hand, no appreciable oxygen amount was detected by RBS and NRA experiments (less than 5 at. %). Both, the reduced Mn density evidenced from RBS simulations and the small oxygen content indicate that **manganese nitridation occurs at the Mn-rich layers**.

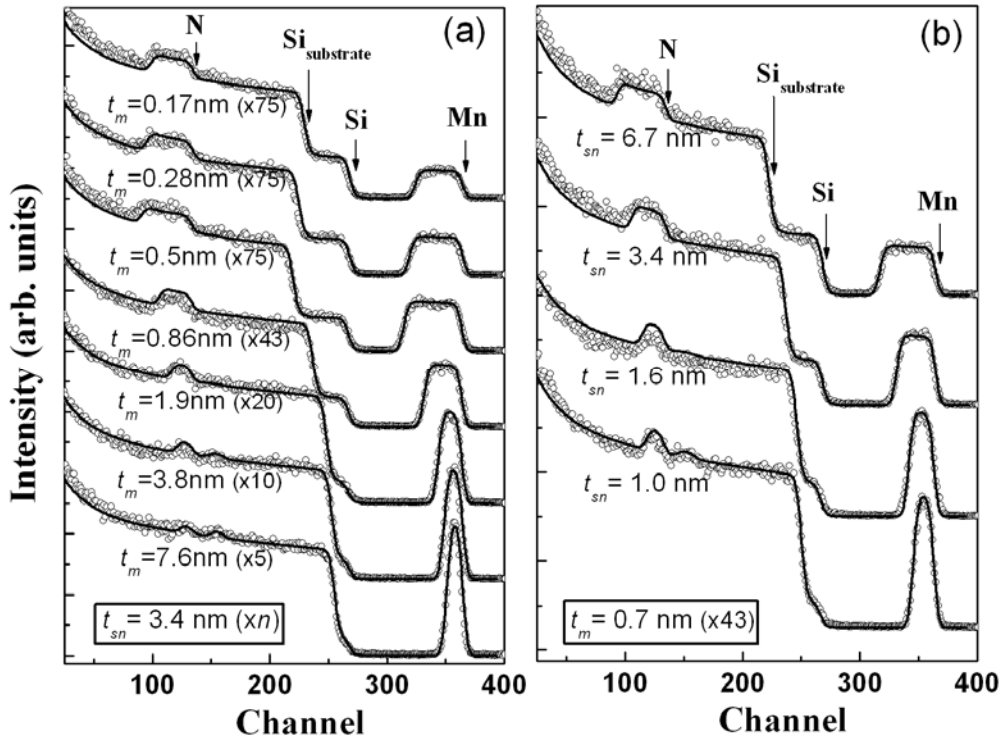

Fig. 6.3 (a) RBS spectra taken at energy of incident ions of 2 MeV (dots) and their simulations (lines) of several Mn/Si_3N_4 samples with different Mn-layer thickness (t_m). (b) RBS spectra of several samples with different Si_3N_4-layer thickness (t_{sn}). All spectra have been vertically shifted for clearness. (c) Comparison between experimental Mn layer thickness values obtained from XRR and calculation from RBS.

The oxygen amount in silicon nitride films has been related to the deposition methods in different works. These works are based on the tendency of Si_3N_4 to develop the corresponding oxy-nitride which can lead to the strong modification of its physical properties. However, it has been shown that, contrary to silicon nitride deposition from Si_3N_4 ceramic targets, reactive sputtering from pure Si targets, as it has been done here, leads to near oxygen free films[22,23].

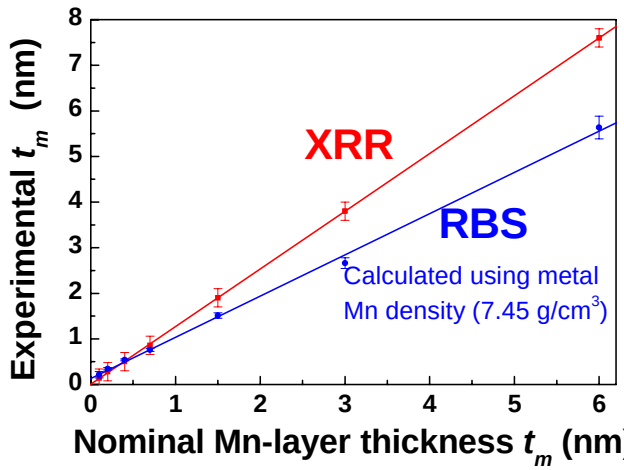

Fig. 6.4 Comparison between experimental Mn layer thickness values obtained from XRR and calculations from RBS.

6.6. *Magnetic properties*

Magnetic characterization of samples was performed by means of a commercial SQUID magnetometer (Quantum Design MPMS-5S) in the temperature range from 5 to 400 K at the ICMM facilities.

A **ferromagnetic-like signal has been observed for most of the prepared samples**. The magnetic characterization results of the Mn/Si_3N_4 films are displayed in Fig. 6.5. The magnetization per Mn atom has been calculated accounting for the precise amount of Mn as obtained by RBS measurements. Fig. 6.5(a) shows the hysteresis loops recorded at RT and 5 K for selected samples with t_m ranging from 3.5 to 0.14 nm. In all cases the diamagnetic contribution of the silicon substrate has been subtracted from the recorded data. For the t_m = 0.14 nm sample, a high paramagnetic-like component is observed at first glance. While this sample exhibits a very weak ferromagnetic ordering, the room temperature magnetization of the t_m = 3.5 nm sample indicates the existence of an average magnetic moment of ~ 0.4 μ_B per Mn atom.

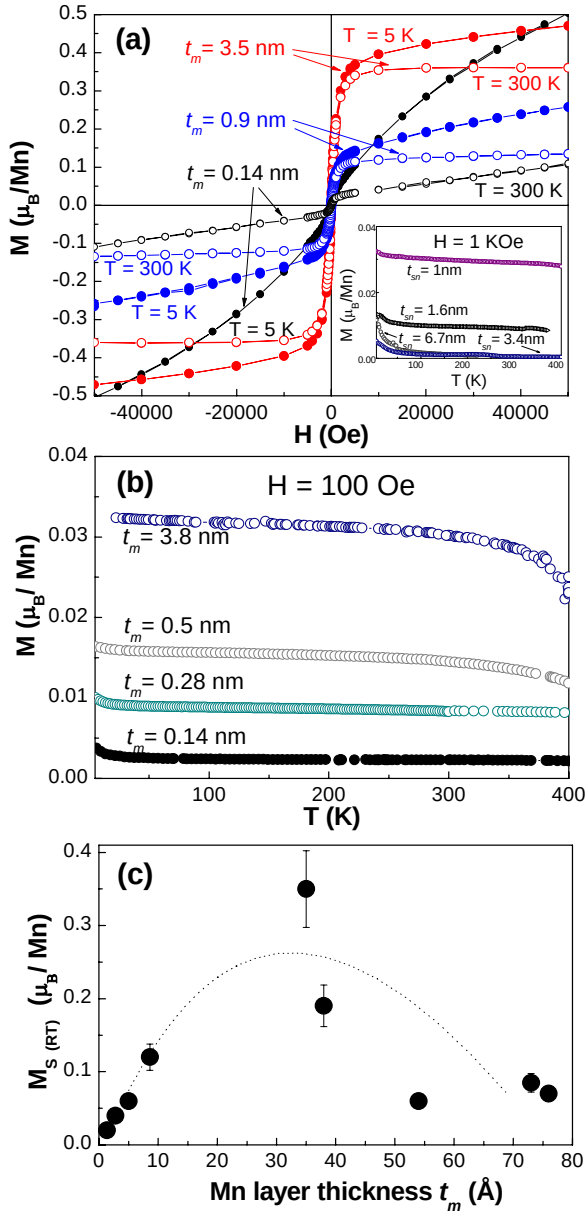

Fig. 6.5 (a) Hysteresis loops of several samples measured at 5 K and room temperature. The inset shows the effect of modifying the Si_3N_4 layer thickness on the magnetization curves (H = 1kOe) for a Mn layer thickness constant (t_m = 0.7 nm). (b) Magnetization vs. temperature (H = 100 Oe) for several samples with different Mn layer thickness (t_m) values. (c) Variation of the saturation magnetization at room temperature with the Mn layer thickness (t_m) for all the FM samples obtained. A dot-line is included just as a guide to the eye.

This value corresponds to about 110 emu/cm^3 of film at RT, being this value the highest saturation magnetization among the samples studied here. This sample shows a coercive field (H_C) ~ 60 Oe at RT. Similar H_C values at RT, between 50 and 80 Oe approximately, are found for the whole set of samples, while they range between 80 and 130 Oe at 5 K.

The temperature dependence of magnetization, M(T), measured under an applied magnetic field of 100 Oe, can be seen in Fig. 6.5(b). An ordering temperature well above 400 K can be inferred for samples with $t_m \geq 0.5$ nm. For samples with smaller t_m, although an enhancement of T_C could be evoked from the M-T curves, their smaller ferromagnetic response together with the complexity of M versus T measurements over 400 K for thin film samples, make difficult to assert an increase of T_C. The evolution of the saturation magnetization (M_S) at room temperature versus the measured Mn layer thickness (t_m) for all the obtained FM samples is represented in Fig. 6.5(c)**. For small Mn layer thickness, M_S increases with t_m, exhibiting a maximum for a Mn layer thickness of the order of the Si_3N_4 one (~3.5 nm) while M_S decreases for further t_m increase**.

The importance of the Si_3N_4 layer thickness into the magnetic properties is also evidenced in the inset of Fig. 6.5(a), that shows the M(T) curves of several samples prepared with constant Mn layer thickness (t_m = 0.7 nm), same number of repetitions (n = 43) and different Si_3N_4 layer thickness, t_{sn} (ranging from 6.7 to about 1 nm). Although it should be remarked that smaller magnetization values are found for this type of samples, the highest FM signal within this series is obtained for the sample labeled as $[Mn(0.7nm)/Si_3N_4(1nm)]_{43}$. Considering that the sample having the highest M_S value is sample is $[Mn(3.5nm)/Si_3N_4(3.4nm)]_{10}$, it seems that the ferromagnetic alignment is favored when both, the manganese-rich and the silicon nitride layers have comparable thicknesses.

It should be also underlined that, for extra samples series prepared under similar experimental conditions, FM ordering and magnetization values of the same order were always found in the case of samples prepared with silicon nitride layers of about 3 nm and

sufficiently thick Mn layers. However, magnetic properties were not always reproducible when preparing additional similar samples with very thin layers, especially for Mn layers (t_m) thinner than 2 nm. None appreciable FM or mostly paramagnetic behaviour was sometimes found in this case, suggesting either the metastability or the high sensitivity to specific experimental conditions of the developed ferromagnetic phase, whose instability appears to be enhanced in the non-continuous growth regime.

Additional characterizations, as XPS and XAS, have been focused in this work on understanding the origin of the observed RTFM in this multilayer system.

6.7. X-Ray Photoemission Spectroscopy (XPS)

XPS measurements were carried out in collaboration with Dr. Elisa Román and Dr. Yves Huttel at the ICMM. The measurements were performed in an ultra high-vacuum (UHV) chamber with a base pressure of 1 x 10^{-10} mbar. The angle between the hemispherical analyzer (Specs-PHOIBOS100) and the plane of the surface was kept at 60° and the x-ray radiation was the Mg K_α line (1253.6 eV). XPS spectra were recorded at the core levels of the elements present in the samples (Mn, Si, N); in the case of Mn, Mn 3p spectra were recorded with a photon energy step of 0.1 eV and pass energy of 15 eV in order to optimise the energy resolution for further fitting analysis and Mn species identification. Prior to the data analysis, the contributions of the Mg K_α satellite lines were subtracted and the spectra were subjected to a Shirley background subtraction formalism. The binding energy (BE) scale was calibrated with respect to the Si peak at 101.6 eV. Fittings were carried out using Gaussian-Lorentzian doublets (GL). Within the experimental conditions, the sensitivity to the surface is rather limited and it can be assumed that the XPS spectra give information of the electronic structure that corresponds to the bulk.

In order to study the electronic properties of Mn-rich layers, we have performed an XPS study of two samples, the t_m = 7.6 nm sample, representative of the thick Mn layer samples, and the t_m = 0.5 nm one, where non-continuous Mn is expected. Depth profiles

were performed by removing thin layers of material with a calibrated sputtering gun operated with Ar+ ions of 1.4 eV of kinetic energy. The photoemission spectra were collected after each sputtering sequence in order to follow the evolution of the electronic structure as a function of depth into the samples. The depth-profile Si, N and Mn compositions of the t_m = 7.6 nm sample are shown in Fig. 6.6. It can be observed that the depth-profile concentrations of the different elements are in rather good agreement with the layer period for the t_m = 7.6 nm sample. As stated above, XPS spectra of the different elements present in the samples have been measured after each sequence of sputtering. In Fig. 6.7 we display the Mn 3p spectra of these 2 samples that were measured at the experimental point located at the depth of 5.4 nm (cf. Fig. 6.6). For the case of t_m = 0.5 nm sample, since Mn layers are very thin and embedded into Si_3N_4 layers, it is not possible to distinguish different Mn layers from the XPS signal and therefore, this depth is not very significant. Anyway, it was chosen to be the same in both cases. The Figure 6.7 also displays the corresponding peak decomposition into the different Mn valence states.

Through the fitting analysis it clearly appeared that the samples exhibit different Mn valence states. **For the t_m = 7.6 nm sample, majority of Mn metal and Mn^{2+} contributions has been obtained** (about 40 % Mn metal, 31 % Mn^{2+}, 22 % Mn^{3+} and 7 % Mn^{4+} are given from the fits, where an uncertainty between 5-10 % can be expected). Despite the small additional contribution from higher oxidized species, if we consider the majority species, the metallic Mn/Mn^{2+} ratio is about 4/3. **For the t_m = 0.5 nm sample, mostly Mn^{2+} contribution** was deduced from the XPS analysis (about 6 % Mn metal, 65 % Mn^{2+}, 20 % Mn^{3+} and 9 % Mn^{4+}). The extra Mn^{3+} and Mn^{4+} high valence contributions are approximately the same in both samples. However, the Mn metallic phase is drastically reduced in this former sample, being the Mn^{2+} valence state the dominant one. The obtained **Mn average oxidation states are about +1.9 for the t_m = 7.6 nm sample and +2.3 for the t_m = 0.5 nm one**.

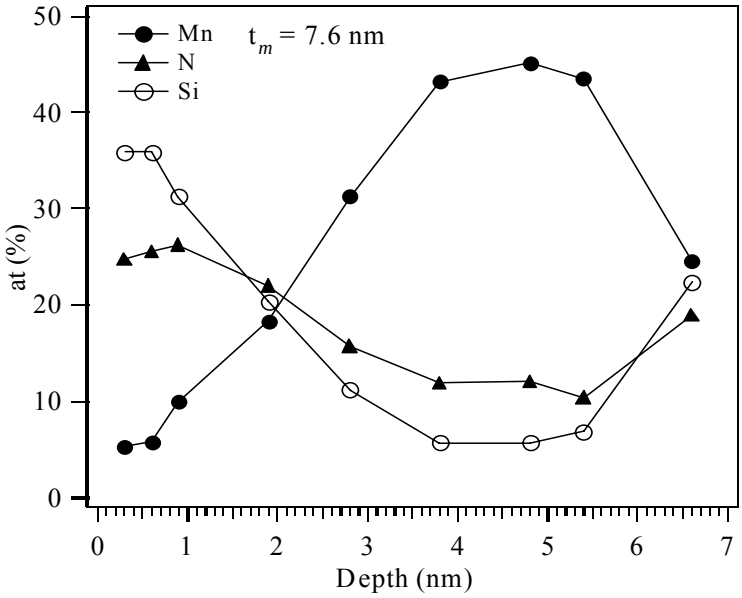

Fig. 6.6 XPS depth profile of the t_m = 7.6 nm sample.

6.8. X-Ray Absorption Spectroscopy (XAS)

Aimed at determining the Mn electronic state, the local structure of the Mn sites and the presence of Mn-N alloys, we have performed a combined XANES and EXAFS study of the $[Mn(t_m)/Si_3N_4(3.4nm)]_n$ and $[Mn(0.7nm)/Si_3N_4(t_{sn})]_{43}$ samples.

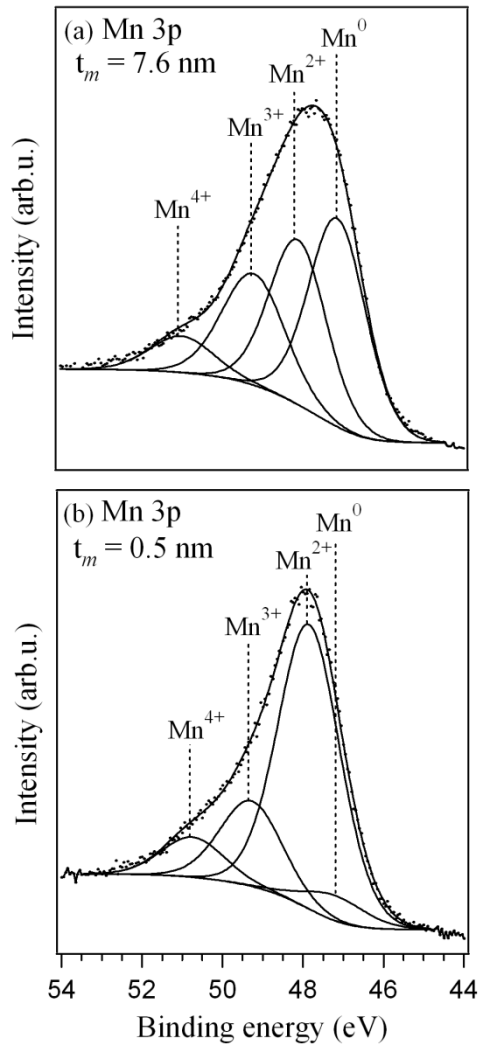

Fig. 6.7 Mn 3p XPS spectra of the t_m = 7.6 nm and t_m = 0.5 nm samples with the corresponding decomposition analysis into the different Mn valence states.

6.8.1. X-Ray Absorption Near-Edge Structure (XANES)

XAS experiments at the Mn K-edge have been performed to study the Mn electronic structure as well as the Mn atomic surrounding. The experiments were carried

out at the BM26 and BM8 beamlines of the European Synchrotron Radiation Facility (ESRF) in Grenoble. Samples were measured in fluorescence and TEY modes, respectively. No appreciable differences were found between the two detection modes and spectra are included here without distinction. Further details of the experimental set-up are given in section 2.6.1

The normalized Mn K-edge XANES spectra of representative samples are shown in Fig. 6.8. The threshold energy position evidences an **average Mn oxidation state close to 2+**, in agreement with XPS results. Details of the pre-peak region can be seen in the inset, showing an evolution of the pre-peak intensity from the manganese foil reference to the samples with thinner Mn layer. As shown in Fig. 6.8 **the shape and the main spectral features of the spectra change as t_m is varied**.

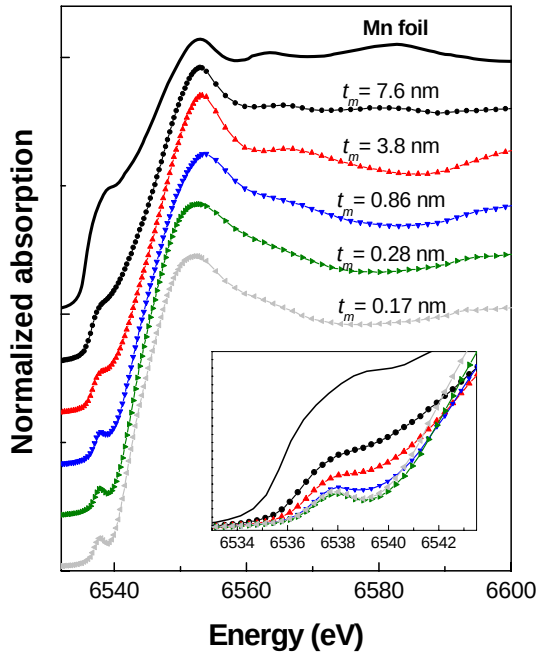

Fig. 6.8 Mn K-edge XANES spectra of Mn/Si_3N_4 samples with different Mn layer thickness (t_m) values as well as a Mn foil spectrum included for comparison. All spectra have been vertically shifted for clearness. The inset shows a zoom of the pre-peak region.

6.8.2. Computational methods: XANES simulations

To obtain further information about possible formation of Mn-N alloys in the samples, we have performed additional studies by comparing the experimental Mn K-edge XANES spectra and the results of theoretical simulations. This work has been done in collaboration with Dr. Jesus Chaboy Nalda from the Instituto de Ciencia de Materiales de Aragón.

The computation of the Mn K-edge XANES spectra was carried out using the multiple-scattering code CONTINUUM24 based on the one-electron full-multiple-scattering theory[25,26]. For a complete discussion of the XANES simulation procedure we refer the reader to Refs. 27 and 28.The potential for the different atomic clusters was approximated by a set of spherically averaged muffin-tin (MT) potentials built by following the standard Mattheis' prescription[29]. The muffin-tin radii were determined following the Norman's criterion[30]. The Coulomb part of each atomic potential was generated using charge densities obtained from a non-local self-consistent Dirac-Fock code[31,32]. The atomic orbitals were chosen to be neutral for the ground state potential, whereas different choices were used to build the final state potential and we have found during the present calculations that the screened and relaxed Z+1 option[33] lead to the best performance for the simulation of the experimental absorption spectra at the Mn K-edge. The calculated theoretical spectra have been further convoluted with a Lorentzian shape function to account for the core-hole lifetime[34] (Γ = 1.2 eV) and the experimental resolution (Γ = 1 eV).

It should be noted that despite the current progress in XANES computation several problems, as the treatment of the inelastic losses of the photoelectron, still remains an open problem. By this reason we have started the computation on a reference material, metallic α-Mn, in order to fix the main parameters of the calculations.

The first step of the calculations was deserved to determine the size of the cluster needed to reproduce all the spectral features present in the experimental XANES spectra. To this end we have performed the computation of the Mn K-edge XANES in the case of

α-Mn (I-43m) by increasing progressively the number of atoms in the cluster. It should be noted that because Mn occupies four different crystallographic positions 2a (Mn1), 8c (Mn2), 24f (Mn3), 24g (Mn4) XANES computations have to be performed for four different clusters in which the absorbing Mn atom lies at the different Mn_i sites, being the theoretical spectrum made up from the weighted sum of these contributions according the crystallographic statistical ratio. In this way, we have determined that the computations performed for clusters including contributions from neighboring atoms located within the first 7 Å around photoabsorbing Mn account for all the observed spectral features, and the addition of further coordination shells does not contribute significantly to the XANES spectrum. We have also studied the effect of both the maximum angular momentum quantum number, l_{max}, and the overlapping factor imposed to the muffin-tin spheres to build up the potential into reproducing the Mn K-edge XANES spectrum. We have found that the best reproduction of the experimental spectrum is obtained by using l_{max} = 4 and a 1% overlapping factor to build up a 7 Å cluster. The results of these computations are shown in Fig. 6.9(a). The agreement between the computations and the experimental signal is noticeable as the calculations reproduce the step-like profile at the threshold (A), the main peak (B) and the two structures located at 28 (C) and 47 eV (D) above the edge. During the calculations we have tested the performance of the energy dependent Hedin-Lundqvist (HL) and Dirac-Hara (DH) exchange and correlation potentials (ECP) potentials. Moreover, we have also made computations by using only the real part of the HL ECP (hereafter, real HL) and, in addition, we have built a "complex" DH one by adding to it the imaginary part of the HL one. As shown in Fig. 6.9(a), the performance of the different EPC potentials is similar although in the case of the HL the calculated absorption maxima falling short of the observed ones. By contrast, computations performed by using the DH ECP show a better reproduction of the relative energy position among the peaks. This is evidenced by the reproduction of the main resonance D and the negative dip E located, respectively, at 47 eV and 62 eV above the edge. Moreover, the addition of the imaginary part of the HL

potential improves the calculations yielding the use of the complex DH ECP the best reproduction of the intensity ratio among the different spectral features.[i]

Possessing these results we have further performed the computation of the Mn K-edge spectrum in the case of both θ-MnN (Mn O_h environment) and η-Mn_3N_2 (Mn in two different environments: fivefold pyramids and linear twofold coordination with a ration of 2:1).

In the case of MnN, computations have been performed for a cluster containing 179 atoms that includes all the contributions from neighbouring atoms located within the first 7.4 Å around the absorbing Mn atom. In the case of Mn_3N_2, Mn occupies two different crystallographic sites 2a (Mn1) and 4e (Mn2). Hence, XANES computations have been performed for two clusters in which the absorbing Mn atom lies at the different Mn1 and Mn2 sites. These clusters include the scattering contributions within the first 7.5 Å around the absorber and contain 153 and 150 atoms for Mn1 and Mn2, respectively. The Mn K-edge absorption of Mn_3N_2 has been calculated by adding the theoretical computations obtained for both clusters according the crystallographic statistical ratio.

The results of these computations are compared to the experimental spectrum of the t_m = 0.28 nm sample in Fig. 6.9(b). The computed spectra show similar oscillations in the high energy region. However, their spectral profiles at the threshold region differ, especially concerning the pre-edge peak (A). This peak is experimentally observed and typically assigned to a non-centrosymmetric environment of the absorbing site, such as in tetrahedral coordination (T_d) symmetry. The **theoretical simulation reproduces this peak for η-Mn_3N_2, while it is absent for MnN**. These results suggesting the presence of η-Mn_3N_2 in our samples have been verified by studying the modification of the XANES spectra as a function of the thickness

[i] It should be noted that the assessment of the quality of the theoretical computations is based on the correct reproduction of the shape and energy position of the different spectral features and of their relative energy separation and intensity ratio as well.

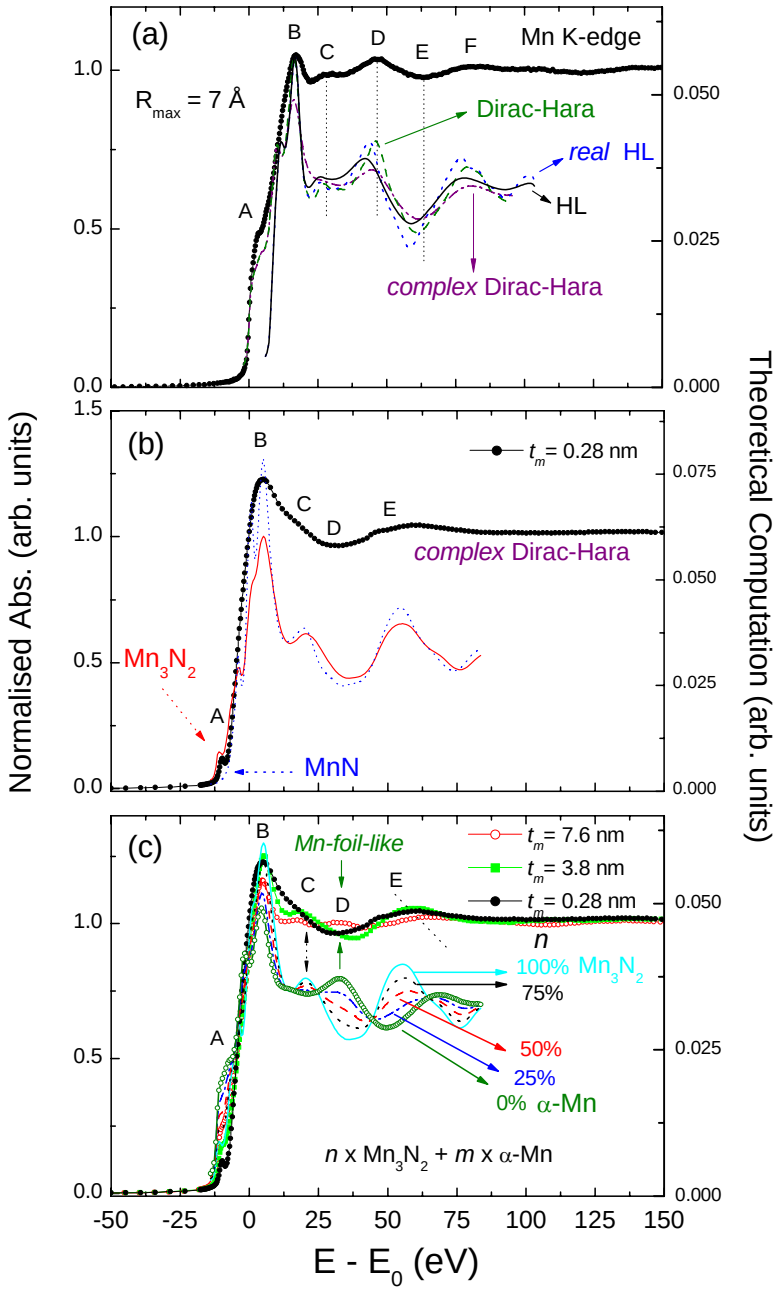

Fig. 6.9 (a) Comparison between the Mn K-edge of a Mn metallic foil (●) and the theoretical spectra calculated on a 7 Å cluster by using l_{max} = 4 and different ECP potentials: real HL (blue, dots), real DH (green, dash line), complex HL (black, solid line) and complex DH (purple, dot-dash).

(b) Comparison between the experimental Mn K-edge XANES of the t_m = 0.28 nm Mn sample (●) and the theoretical computation performed for both MnN (blue, dots) and Mn_3N_2 (red, solid line) by using the complex Dirac-Hara ECP potential.

(c) Comparison between the experimental Mn K-edge XANES of the t_m = 0.28 nm (black, ●), t_m = 3.8 nm (green, □) and t_m = 7.6 nm (red, ○) samples and the theoretical signals calculated as the weighted sum of the computed spectra for both Mn_3N_2 and α-Mn (see text for details) as a function of the Mn_3N_2 fraction n: 100 % (cyan, solid line), 75% (black, dots), 50% (red, dash), 25% (blue, dot-dash) and 0% (green, ○).

Indeed, as the Mn thickness increases the η-Mn_3N_2 contribution should be hindered as the XANES would be made by the superposition of the XANES spectra of both η-Mn_3N_2 and bulk-Mn-like. This is shown in Fig. 6.9(c) where the XANES spectra of the samples with different Mn thickness (t_m) are compared to the theoretical spectra calculated as the weighted addition of the computed spectra for η-Mn_3N_2 and α-Mn in the form: n x Mn_3N_2 + m x α-Mn. As shown in the figure, the modification of the Mn thickness strongly changes the spectral profile in the high energy region. For example, in the case of the sample wit the small Mn thickness (t_m = 0.28 nm) the spectrum shows a negative dip (D) at ~ 33 eV above the edge. As the Mn thickness increases, samples t_m = 3.8 nm and t_m = 7.6 nm, this spectral feature evolves up to yield a positive resonance. This is exactly the situation obtained in the theoretical simulation of Fig. 6.9(c): whereas the Mn_3N_2 dominates the spectrum, feature D remains negative but, however, as the contribution of bulk Mn increases, the sign of this contribution is reversed. Similar analysis can be followed for the energy position of the main resonance E at ~57 eV above the edge. Experimentally, this feature is shifted towards higher energies as the Mn thickness increases in the samples, in identical manner to the behaviour of the theoretical signal constructed by varying the weight of the η-Mn_3N_2 and α-Mn contribution to the XANES spectra. The obtained evolution agrees with the Mn_3N_2:Mn ratio obtained by RBS and XPS.

Therefore, the ***ab-initio* calculations have evidenced the presence of both metallic and Mn_3N_2 phase (with Mn T_d symmetry) in sample t_m = 7.6 nm, while no sign of Mn metallic phase appears in the t_m = 0.28 nm spectrum, which presents just nitride contribution**. The Mn metal/Mn_3N_2 ratio indicated by XANES simulations for

sample t_m = 7.6 nm is compatible with the previous one estimated by XPS and EXAFS (about 3:2 of metal/nitride). The fact that increasing the Mn-layer thickness lead to a reduction of the relative contribution of η-Mn_3N_2 compared to the bulk-like Mn indicates that the Mn nitride formation in the sputtered Mn layer is related to the Si_3N_4 interfaces, leading, for thin enough Mn layers, to all the deposited Mn turned into manganese nitride.

6.8.3. Extended X-Ray Absorption Fine Structure (EXAFS)

Further confirmation of these results has been obtained by studying the Mn local environment from the analysis of the EXAFS part of the spectra by using the VIPER software.[35] Additional details of the analysis procedure are given in section 2.6.1.2.

Figure 6.10 shows the evolution of the Fourier transform (FT) magnitude of the EXAFS signal at the Mn K-edge along the series with t_m variable and a Mn metal foil, given for comparison. At first glance, clear differences between the FT magnitude of the t_m = 7.6 nm sample and the others, as well as the loss of the FT second peak for small t_m values, are observed.

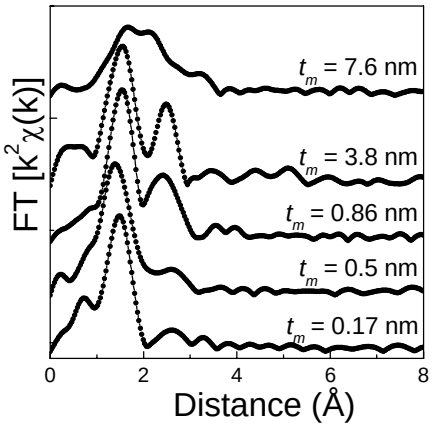

Fig. 6.10 Experimental EXAFS Fourier Transforms (FT) of some representative $[Mn(t_m)/Si_3N_4(3nm)]_n$ samples.

The comparison between experimental data and simulations is shown in Fig. 6.11,

and the obtained results are summarized in Table 6.III. Analysis shows a complex situation that can be explained as follows. A contribution around **2.05 Å corresponding to Mn-N distance is present for all the samples** from the series and besides, samples with t_m higher than 0.5 nm present a second Mn-Mn near 3 Å. Those **distances agree with Mn_3N_2 compounds with slightly compressed distances**.[8] Additionally, a small Mn-Si contribution at about 3.1 Å has been found for t_m = 0.86 nm and t_m = 3.8 nm samples, what can be assigned to the link between the Mn_3N_2 and Si_3N_4 phases. Finally, **the Mn-Mn distance found at 2.67 Å in sample t_m = 7.6 nm is in agreement with distances in metallic Mn.** The expected small size of Mn_3N_2 clusters explains the disappearance of the FT second peak for $t_m \leq 0.5$ nm and does not allow to obtain Mn-Mn and Mn-Si distances for these samples. In the case of the t_m = 7.6 nm sample, EXAFS results are in agreement with previous XANES conclusions. For this sample, significant presence of metallic Mn (with Mn-Mn distances widely spread around 2.7 Å) is found; this additional phase as well as the small number of layers make very hard to obtain the minority Mn-Si contribution.

At this point, it is important to note that the observation of this Mn-Si EXAFS distance supports the fact that Mn_3N_2 phase is formed at the interface between the Mn and Si_3N_4 layers, suggesting that the Si_3N_4 has a definitive influence in the development of a strained Mn_3N_2 phase. Within the error in the neighbor number determination, the Mn metal/Mn_3N_2 ratio obtained by EXAFS is compatible with the one extracted by both XPS and XANES data (4:3).

By contrast, no appreciable Mn metal contribution is obtained from the EXAFS analysis of the t_m = 3.8 nm sample. In comparison with the other samples, slightly higher Mn-Mn distances (3.06 Å) are found in the Mn_3N_2 phase of the t_m = 3.8 nm sample, being one of the most ferromagnetic ones. Results from EXAFS simulations of samples with different Si_3N_4 layer thickness (Fig. 6.12) are included in Table 6.III. As expected, similar Mn-N distances are obtained when varying t_{sn}. It can be observed that the change in the atomic environment when varying t_{sn} is smaller than the resulting when modifying t_m, where larger magnetization values were found. Just very small differences are detected by EXAFS for the

samples with different t_{sn} values.

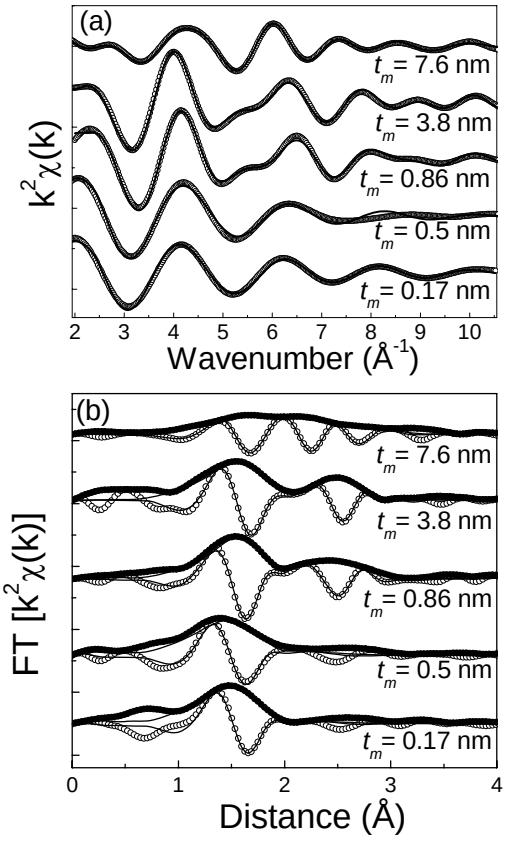

Fig. 6.11 (a) k-space comparison between the filtered EXAFS signals (dots) and simulations (lines) at Mn K-edge of samples with different Mn layer thickness (t_m). (b) Fourier transform of the (a) plotted signals; modulus and imaginary parts have been presented for dual comparison with calculated contributions (lines).

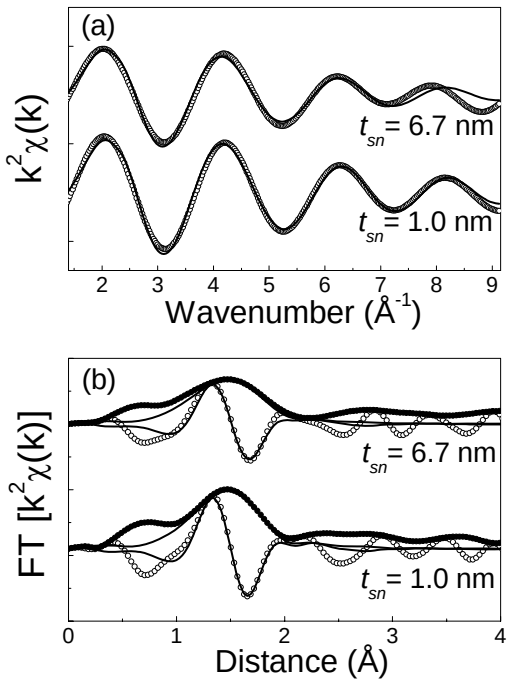

Fig. 6.12 (a) k-space comparison between the filtered EXAFS signal (dots) and simulations (lines) at Mn K-edge of samples with different Si_3N_4 layer thickness (t_{sn}). (b) Fourier transform of the (a) plotted signals; modulus and imaginary parts have been presented for dual comparison with calculated contributions (lines).

6.8.4. XAS at the Mn $L_{3,2}$-edge and XMCD

Additional XAS and XMCD experiments at the Mn $L_{3,2}$ edge have been carried out since they become of great interest here. On one hand, the Mn $L_{3,2}$ XAS structure is a fingerprint for the 3*d* count, giving information on the Mn valence state and on the other hand, XMCD provides an element-specific tool sensitive to the magnetic states. Further information of these techniques can be found in section 2.6.3.

Mn $L_{3,2}$ edge XAS and XMCD measurements were done on beamline 5U.1 of the Synchrotron Radiation Source at Daresbury Laboratory (UK) in collaboration with Dr. Neil Telling and Dr. Gerrit Van Der Laan.

Table 6.III. EXAFS results summary: atomic distance (R), number of neighbors (N) and Debye-Waller factor (σ^2).

Sample	pair	R (Å)	N	σ^2 (× 10^{-3}Å^2)
[Mn(t_m)/Si_3N_4(3.4nm)]$_n$				
t_m = 7.6 nm	Mn–N	2.03±0.02	2.4±1	5±1
	Mn–Mn	2.67±0.02	4.2±1	25±1
	Mn–Mn	2.98±0.02	6.0±1	29±1
t_m = 3.8 nm	Mn–N	2.06±0.02	3.1±1	9±1
	Mn–Mn	3.06±0.02	3.4±1	17±1
	Mn–Si	3.12±0.02	2.3±1	7±1
t_m = 0.86 nm	Mn–N	2.04±0.02	2.6±1	7±1
	Mn–Mn	2.98±0.02	2.8±1	7±1
	Mn–Si	3.10±0.02	1.1±1	9±1
t_m = 0.5 nm	Mn–N	2.02±0.02	2.9±1	12±1
t_m = 0.28 nm	Mn–N	2.06±0.02	3.1±1	22±1
t_m = 0.17 nm	Mn–N	2.04±0.02	2.7±1	8±1
[Mn(0.7nm)/Si_3N_4(t_{sn})]$_{43}$				
t_{sn} = 6.7 nm	Mn–N	2.04±0.02	2.9±1	10±1
t_{sn} = 1.0 nm	Mn–N	2.03±0.02	3.2±1	6±1

Spectra were collected in TEY mode reversing the applied magnetic field of ±0.6 T perpendicular to the surface at each data point for fixed photon helicity. Figure 6.13 shows the XAS and XMCD spectra of the t_m = 0.28 nm sample measured at RT. Comparison of the experimental XAS spectrum with theoretical calculations for different electronic configurations indicates that the **$3d^n \rightarrow 2p^5 3d^{n+1}$ absorption spectrum corresponds to a Mn^{2+} d^5** ground state. For further information, theoretical simulations performed by G. Van der Laan et al.[36] of the 2*p* absorption spectra of the Mn $3d^3$, Mn $3d^4$ and Mn $3d^5$ in tetrahedral (T_d) and octahedral (O_h) symmetry are shown in Fig 2.3

(section 2.6.2). The obtained results sustain a non-centrosymmetric T_d Mn environment with a crystal field close to $10Dq \approx 0.5$ eV, in agreement with the above XANES and EXAFS results.

The difference between the XAS spectra recorded for parallel and antiparallel alignment of magnetic field and photon helicity results in a small XMCD signal for the t_m = 0.28 nm sample. Reversal of the XMCD signal was confirmed by switching between left and right circular polarization. A seven-points smooth of the dichroic signal is shown in Fig. 6.14, in comparison with the d^5 calculation. The **XCMD signal shows that the magnetism arises from a Mn d^5 contribution (Mn^{2+})**, which has its largest value at the photon energy position of the XAS peak maximum.

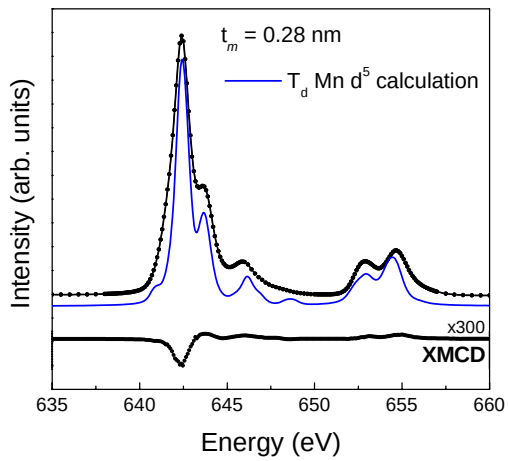

Fig. 6.13 Mn $L_{3,2}$ XAS and XMCD spectra of $[Mn(0.28nm)/Si_3N_4(3.4nm)]_{75}$ sample measured at RT compared to XAS calculations for Mn d^5 in T_d symmetry. The L_3 and L_2 step edges have been subtracted from the experimental XAS spectrum.

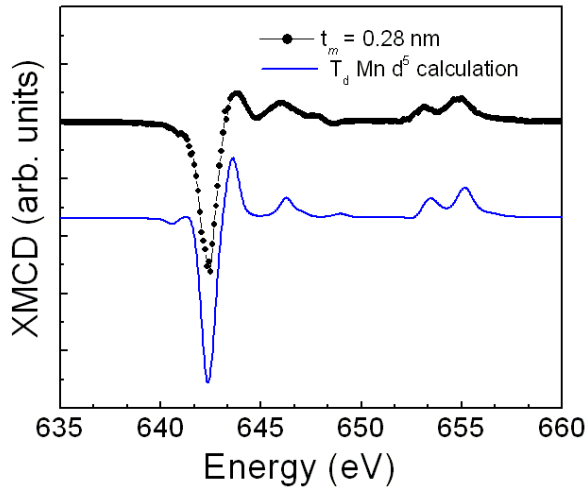

Fig. 6.14 Comparison between Mn XMCD spectrum of $[Mn(0.28nm)/Si_3N_4(3.4nm)]_{75}$ sample measured at RT and calculations for Mn d^5 in T_d symmetry.

6.9. Remarks and discussion

The combined results allow us to deduce how the Mn^{2+} cations bonded to nitrogen lead to FM order and what the role is of the silicon-nitride matrix. Firstly, ferromagnetism caused by Mn metallic clusters can be clearly ruled out by XMCD results. Furthermore, FM due to formation of ternary phases, such as $MnSiN_2$,[37] seems quite doubtful due to the silicon film content extracted from the RBS measurements. On the other hand, substitution of Si^{4+} by Mn^{2+} in Si_3N_4 seems rather unlikely due to the difference in ionic radii and considerable charge mismatch. Si sites are four-fold coordinated in Si_3N_4, with Si-N distances of ~1.74 Å. The Mn^{2+} ionic radius (0.80 Å) in T_d symmetry greatly differs from the Si^{4+} radius (0.40 Å). Large lattice distortions, which could accomplish a reduction of the coordination number and relieve the possible charge mismatch, might be considered. Even though, the large Mn-N distances (2.05 Å), obtained by EXAFS hardly match with the Mn^{2+} replacement in Si_3N_4. Therefore, FM due to Mn^{2+} substitution into the Si_3N_4 matrix can be also ruled out.

Significant contribution from manganese nitrides such as ε-Mn_4N, ζ-Mn_2N, or ζ-

Mn_5N_2 phases, can be rejected due to the large dissimilarity in the Mn-N atomic distance.

Therefore, all the obtained results points towards induced ferromagnetism in the Mn_3N_2 stabilized phase evidenced by XANES and EXAFS results at the Mn K-edge, with a manganese oxidation state of +2.

The situation seems very similar to the theoretically reported ferromagnetism in a distorted θ-MnN phase. This compound has a tetragonally distorted rocksalt structure, where Mn has octahedral (O_h) symmetry and a Mn-N distance of 2.098 Å[9], with an AF ground state.[2] However, depending on the polymorph and lattice constant, theoretical calculations have predicted FM order, e.g., in the zinc-blende structure, which would exhibit shorter Mn-N distances and Mn T_d symmetry. In fact, the θ-MnN compound has a tendency to lose nitrogen, forming the η-Mn_3N_2 phase which presents similar Mn-N distances.[8]

In the case of Mn/Si_3N_4 films, the Mn-N distances of 2.05 Å obtained by EXAFS are slightly shorter than the average in η-Mn_3N_2 (2.1 Å), where Mn is coordinated by fivefold nitrogen pyramids. Hence, taking into consideration the changes in the unit cell volume commonly considered for accounting for theoretical transitions to a FM phase with Mn in T_d symmetry from the AFM ground state in manganese nitrides, [6,12,13] the obtained results suggest that the origin of the FM behaviour in Mn/Si_3N_4 multilayers is the formation of a **slightly distorted non-centrosymetric η-Mn_3N_2 phase at the interfaces, what seems to be favored by the Si_3N_4 tetrahedral structure**.

Regarding all the obtained results, the evolution of M_S within the multilayer series can be qualitatively understood.

For samples with Mn-rich layers smaller than 0.86 nm, mostly Mn^{2+} contribution was obtained by XPS, being this Mn^{2+} average oxidation state corroborated by XANES measurements at the Mn K-edge. The Mn_3N_2 phase formation has been verified by EXAFS and XANES simulations. EXAFS results have shown the disappearance of the second neighbour shell for these samples, indicating the presence of Mn_3N_2 clusters of small size. The decrease of the magnetization for these samples is explained in terms of

the superparamagnetic size limit, which becomes important for particle sizes around 1 nm. Looking at the hysteresis loops at low temperature (cf Fig. 6.5(a)) it can be noticed how the superparamagnetic component becomes significant as t_m is reduced.

On the other hand, for large Mn-rich layer thickness samples, major contributions of both, metallic Mn and Mn^{2+}, have been found by XPS. The metallic Mn presence and the Mn_3N_2 formation, favoured by the surrounded Si_3N_4, have been corroborated by the EXAFS results and XANES calculations. In this case, the reduction of M_S is understood through the formation of the metallic Mn phase that reduces the specific magnetization per Mn atom.

A scheme of the situation described is represented in Fig. 6.15. It should be noticed that minor contributions from possible additional phases (MnN or Mn_4N, for instance) can complicate this image. However, it is important to remark that the origin of ferromagnetism in this system has been ascribed to Mn d^5 contribution (Mn^{2+}) by XMCD.

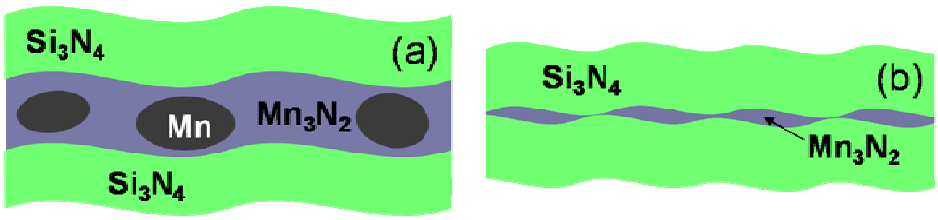

Fig. 6.15 Simplified structural image of multilayer samples (a) with higher Mn layer thickness (t_m), where Mn metal and Mn_3N_2 phases coexist and (b) with t_m < 0.86 nm, where formation of discontinuons Mn_3N_2 layers is expected.

In order to estimate the reduction of the M_S due to the presence of metallic Mn, we have calculated the effective saturation magnetization at RT of sample t_m = 7.6 nm by normalizing only to the Mn coming from Mn_3N_2 (about 30 % from XPS data), instead of all the Mn atoms (previously considered in Fig. 6.5(c)). This leads to about 0.23 μ_B per Mn atom at RT, being closer to the maximum value of Ms within the series, about 0.35 μ_B per Mn atom. Another factor, like small differences in the lattice parameters (Mn-Mn

distances larger than 3 Å were found for the t_m = 3.8 nm sample) seems to be directly related to variations in the FM order established in the Mn_3N_2 distorted phase. The role of the Si_3N_4 layer thickness in the ferromagnetism has been also evidenced in the $[Mn(0.7nm)/Si_3N_4(t_{sn})]_{43}$ series, even if higher M_S values and stronger variation were obtained when varying the Mn layer thickness (t_m). The stabilization of the FM Mn_3N_2 distorted phase results favored when both, the manganese-rich and the silicon nitride layers are comparable in thickness, where slightly larger Mn-Mn distances were found. This point is consistent with the fact of finding Mn-Si EXAFS contribution in samples with intermediate t_m, what evidences a clear relationship between the Mn_3N_2 distorted phase and the surrounded Si_3N_4 for these similar thicknesses, where the imprinted stresses seem to promote the stabilization of the Mn_3N_2 distorted phase.

6.10. Conclusions

The magnetic, structural and electronic properties of Mn/Si_3N_4 multilayer samples prepared by reactive sputtering have been investigated using SQUID, XRR, TEM, RBS, NRA, XPS, XAS, and XMCD.

RTFM has been obtained in Mn/Si_3N_4 multilayer samples with different $Mn:Si_3N_4$ relative ratio for the first time.

XMCD has shown that the magnetism in the films is due to the Mn d^5 (Mn^{2+}) state and XANES calculations have confirmed the presence of a Mn_3N_2 phase with Mn T_d symmetry, what seems to be favored by the Si_3N_4 tetrahedral structure.

The origin of ferromagnetism here has been assign to the formation of a distorted non-centrosymmetric Mn_3N_2 phase with slightly shorter Mn-N distances. This type of changes in the unit cell volume has been commonly theoretically considered in order to obtain transitions from the AFM ground state to a FM phase in manganese nitrides.

An evolution of the magnetic properties has been found depending on the Mn and

Si_3N_4 layer thickness. The variation of the ferromagnetic component has been explained in terms of the Mn_3N_2 phase.

For small Mn layer thickness, in the cluster growth regime, the Mn_3N_2 clusters size limits the magnetization magnitude, leading to a decrease of Ms as the cluster size is reduced.

By contrast, for thicker Mn layer thickness samples, the formation of metallic Mn phase results in diminishing the magnetization per Mn atom. The coexistence of metallic Mn and manganese nitride has been deduced by XPS, XAS and XANES calculations.

The most suitable condition found here to stabilize the ferromagnetic ordering in this system seems when the manganese and silicon nitride layers are continuous and their thickness are comparable and close to 3.5 nm. Several factors as, small differences in the atomic distances, contributions from possible additional phases (MnN or Mn_4N, for instance) or the inherent instability of the formed phase can lead to more complicated magnetic behaviours.

References

[1] H. Yang, H. Al-Britten, R. Smith, J. A. Borchers, R. L. Cappelletti and M. D. Vaudin, Appl. Phys. Lett. 78, 3860 (2001).

[2] S. Granville, B.J. Ruck, F. Budde, A. Koo, J.E. Downes, H.J. Trodahl, A. Bittar, N. Strickland, G.V.M. Williams, W.R.L. Lambrecht, T. Learmonth, K.E. Smith, V.J. Kennedy, A. Markwitz and T. Schmitt, Phys. Rev. B 72, 205127 (2005).

[3] M. Chiba and S. Naito, Surf. Sci. Nanotech. 6, 115 (2008).

[4] J. A. Chan, J. Z. liu, H. Raebiger, S. Lany and A. Zunger, Rev. B 78, 184109 (2008).

[5] B. K. Rao and P. Jena, Phys. Rev. Lett. 89, 185504 (2002).

[6] M. Marques, L.K. Teles, L.M.R. Scolfaro, J. Furthmüller, F. Bechstedt, and L.G.Ferreira, Appl. Phys. Lett. 86, 164105 (2005).

[7] H. Yang, H. Al-Britten, E. Trifan, D. C. Ingram and A. R. Smith, J. Appl. Phys. 91, 1053 (2002).

[8] M. Hasegawa, T. Yagi, J. Alloys Comp. 403, 131 (2005).

[9] K. Suzuki, T. Kaneko, H. Yoshida, Y. Obi, H. Fujimori and H. Morita, J. Alloys Comp. 306, 66 (2000).

[10] A. F. Guillerment and G. Grimvall, Phys. Rev. 40, 10582 (1989).

[11] B. K. Rao and P. Jena, Phys. Rev. Lett. 89, 185504 (2002).

[12] H.-M. Hong Y.-J. Kang, J. Kang, E.-C. Lee, Y.-H. Kim, and K. J. Chang, Phys. Rev. B 72, 144408 (2005).

[13] M. Marques, L. M. R. Scolfaro, L. K. Teles, J. Furthmüller, and F. Bechstedt, Appl. Phys. Lett. 88, 022507 (2006).

[14] S. Nakagawa, M. Naoe, J. Appl. Phys. 75, 6568 (1994).

[15] F. Munakata, K. Matsuo, K. Furuya, Y. Akimune, J. Ye and I. Ishikawa, Appl. Phys. Lett. 74, 3498 (1999).

[16] A. R. Zanatta and L. A. O. Nunes, Appl. Phys. Lett. 72, 3127 (1998).

[17] Y. Zhang et al., J. Mater. Res. 15, 1048 (2000).

[18] I. W. Cheng and A. Rosenflanz, Nature 389, 701 (1997).

[19] Z. Dong, G. You, P. Zhou, C. Zhang, K. Liu, Y. Yang and S. Quian, J. Phys. D: Appl. Phys. 39, 4766 (2006).

[20] J. Farjas et al Appl. Phys. Lett. 87, 192114 (2005).

[21] L. W. Yin, Y. Bando, Y. C. Zhu abd Y. B. Li, Appl. Phys. Lett. 83, 3584 (2003).

[22] M. Vila, D. Cáceres and C. Prieto, J. Appl. Phys. 94, 7868 (2003).

[23] M. Vila, E. Román and C. Prieto, J. Appl. Phys. 97, 113710 (2005).

[24] C. R. Natoli and M. Benfatto (unpublished).

[25] P. A. Lee and J. B. Pendry, Phys. Rev. B 11, 2795 (1975).

[26] C. R. Natoli and M. Benfatto, J. Phys. (Paris) Colloq. 47, C8-11 (1986).

[27] See for example J. Chaboy and S. Quartieri, Phys. Rev. B 52, 6349 (1995) and references therein.

[28] C. R. Natoli, M. Benfatto, S. Della Longa and K. Hatada, J. Synchrotron Rad. 10, 26 (2003).

[29] L. F. Mattheis, Phys. Rev. A 133, 1399 (1964); Phys. Rev. A 134, 970 (1964).

[30] J. G. Norman, Mol. Phys. 81, 1191 (1974).

[31] A. L. Ankudinov, B. Ravel, J. J. Rehr and S. D. Conradson, Phys. Rev. B 58, 7565 (1998).

[32] J. P. Desclaux, Comp Phys Comm. 9, 31 (1975).

[33] P. A. Lee and G. Beni, Phys. Rev. B 15, 2862 (1977).

[34] M. O. Krause and J. H. Oliver, J. Phys. Chem. Ref. Data 8, 329 (1979).

[35] K. V. Klementiev, VIPER for Windows, freeware: www.desy.de/~klmn/viper.html; J. Phys. D. 34, 209 (2001).

[36] G. van der Laan and I. W. Kirkman, J. Phys.: Condens. Matter 4, 4189 (1992).

[37] S. Esmaeilzadeh, U. Hålenius, and M. Valldor, Chem. Mat. 18, 2713 (2006).

Appendix C

From Ferromagnetism to Noble Metal Nanoparticles Formation in the Si_3N_4 and ZnO Systems

C.1. Au/Si_3N_4 Multilayers

The study of noble metal nanoparticles embedded in ceramic matrices shown here is the result of an international scientific stay at the Laboratoire de Chimie Physique (LCP) at the University of Paris-Sud, in France, under the supervision of Dr. Agnès Traverse, who conceived this research project.

The increasing scientific interest on noble metal nanoparticles systems added to the acquired experience of the research group in Si_3N_4 and ZnO films as well as in sequential deposition of metal/ceramic material by sputtering, has prompted us to complete this thesis based on the ferromagnetism in wide band gap materials with the study of NPs embedded in wide band gap matrices. The multiple possibilities of these multifunctional materials are therefore highlighted here.

C1.1. Motivation

Metallic nanoparticles (NPs) are of great interest in chemistry,[1,2] medical sciences[3,4] or material sciences.[1,5,6] As a consequence of reducing the size and the dimensionality of a material, its density of states changes drastically as the spatial length scale of the electronic motion is reduced.[7,8,9] The energy eigenstates are determined by the system's boundaries, and therefore, surface effects become very important. For that reason, NPs of subnanometer to nanometer size present exciting properties which are strongly different from those of bulk materials. As a result, possible future applications of NPs include the areas of ultrafast data communication and optical data storage,[5] solar

energy conversion,[6] and the use of metallic NPs as catalysts due to their high surface-to-volume ratios.[5]

In particular, noble metal NPs exhibit surface plasmon resonance (SPR) phenomenon when excited at an appropriate wavelength, usually located in the visible range. These are pronounced resonance lines in the optical spectra caused by collective excitations of conduction electrons, induced by the interacting electromagnetic field.[1] The optical properties are known to be controlled by a variety of effects. Specifically, the SPR spectral position depends on the NP metal; for instance, silver NPs generally have higher particle-plasmon energies than gold NPs.[1,10] The spectral position also depends on the size, shape and organization of NPs.[11,12]

It is possible to incorporate NPs within ceramic matrices in order to form composite materials. These materials, called nanocermets, exhibit additional properties particularly interesting for applications in linear and non-linear regimes. One can mention the existence of a strong absorption band, second[13] and third-order nonlinear susceptibility[14,15] and a femtosecond response[16] that make them potential candidates for the realization of optoelectronic components.

The refractive index of the matrix is known to play an important influence on the SPR energy. In general, increasing the refractive index of the surrounding medium leads to an enhancement of the plasmon band intensity and bandwidth as well as to a red shift of the resonance energy.[9] Regarding the ceramic matrix, significant research has been done already on Au NPs embedded in oxide matrices such as SiO_2 and TiO_2.[17]

A precise characterization of these nanocermets from the structural point of view is a prerequisite to fully interpret their properties. In this work, we present a study of the Au NPs growth and optical properties in the transparent nitride Si_3N_4, with a refractive index of 2, intermediate between the one of SiO_2 (1.5) and TiO_2 (2.7).

Au NPs inside Si_3N_4 matrix have been prepared here by sequential sputtering of Au and Si_3N_4. Among the techniques to prepare embedded metal NPs, alternative sputtering allows the experimentalists to vary parameters such as the total amount of

deposited material, the layer thickness and deposition rate in order to monitor NP growth.[12] The control of the growth mode together with NP size, morphology and organization are of fundamental importance to prepare samples with the optimised optical properties. For that reason, thorough structural characterizations to understand growth mechanisms are essential here.

In this appendix, a structural and optical characterization of a series of Au/Si_3N_4 samples is presented. Several experimental techniques have been combined to determine the growth mode and to provide a fine description of the Au NPs in terms of average size, size distribution, morphology and organization in the matrix.

C.1.2. Preparation of samples

Au/Si_3N_4 multilayered films were prepared by sequential sputtering of Si_3N_4 and Au on Si(100) substrates at room temperature. The residual pressure was near $1x10^{-7}$ mbar. Si_3N_4 layers were deposited by RF sputtering from a pure silicon target (99.999%) using N_2 as reactive sputtering gas at a pressure of $6.0x10^{-3}$ mbar. The deposition rate was about 4 nm/min for a RF power of 100 W. Au layers were grown from a Au target (99.999%) at $5.0x10^{-3}$ mbar pressure of pure Ar. The deposition rate was about 5 nm/min for a DC power of ~10 W. Pre-sputtering was developed before multilayer growth and also between two consecutive layers. The sequence of deposition was always started and finished with a Si_3N_4 layer so Au grows always on the same type of surface and becomes protected against atmospheric contamination.

Following the described procedure, a series of five Au/Si_3N_4 samples, labelled as $[Si_3N_{4(70s)}/Au_{(t\text{-sput})}]_n$ was prepared. Whereas the Si_3N_4 sputtering time per layer was maintained constant in every sample, the Au layer sputtering time (t-sput) was varied between 88 s and 7 s. The expected Si_3N_4 layer thickness is therefore approximately constant in every sample (about 6 nm) while the expected Au layer thickness (t_{Au}) ranges from 8 to 1 nm. The number of bilayers (n) was increased in order to maintain the Au total amount approximately constant in the five samples. The prepared samples are

summarized in Table C.1.I. Calculated effective thickness of samples has been included in the table, where for all samples (either formed by continuous or discontinuous Au-layers) the effective Au-layer thickness has been obtained from the Au bulk density (ρ_{Au} = 5.9x10^{22} at/cm^3) considering hypothetical Au continuous layers formed by the same Au amount as if present as NPs.

Table C.1.I Sample series description: sputtering time for the Si_3N_4 and Au-layer deposition and number of bilayers (n), XRR-obtained bilayer thickness (XRR-Λ), GISAXS-obtained bilayer thickness (GISAXS-Λ), number of Au atoms per Au-layer measured by RBS (at/cm^2), calculated effective Au-layer thickness (t_{Au}) using RBS data and Au metal bulk density (ρ_{Au} = 5.9x10^{22} at/cm^3), total number of Si atoms measured by RBS (at/cm^2) and sample effective thickness values considering RBS-t_{Au} and the Si_3N_4-layer thickness average among all the samples, from Λ and t_{Au}.

Sample $[Si_3N_{4(70s)}/Au_{(t\text{-}sput)}]_n$	XRR -Λ (nm)	GISAXS -Λ (nm)	RBS Au atoms per layer (at./cm^2)	RBS t_{Au} (nm)	RBS total Si atoms (at./cm^2)	Sample effective thickness
$[Si_3N_{4(70s)}/Au_{(88s)}]_5$	13.2	14.0	4.9x10^{16}	8.3	3.7x10^{16}	$[Si_3N_{4(6nm)}/Au_{(8.3nm)}]_5$
$[Si_3N_{4(70s)}/Au_{(44s)}]_{10}$	8.5	-	2.75x10^{16}	4.7	9.3x10^{16}	$[Si_3N_{4(6nm)}/Au_{(4.7nm)}]_{10}$
$[Si_3N_{4(70s)}/Au_{(22s)}]_{20}$	10.4	9.8	1.73x10^{16}	2.9	2.7x10^{17}	$[Si_3N_{4(6nm)}/Au_{(2.9nm)}]_{20}$
$[Si_3N_{4(70s)}/Au_{(11s)}]_{40}$	8.6	-	1.26x10^{16}	2.1	5.0x10^{17}	$[Si_3N_{4(6nm)}/Au_{(2.1nm)}]_{40}$
$[Si_3N_{4(70s)}/Au_{(7s)}]_{75}$	6.7	7.7	9.4x10^{15}	1.6	9.4x10^{17}	$[Si_3N_{4(6nm)}/Au_{(1.6nm)}]_{75}$

C.1.3. X-Ray Reflectivity (XRR)

The XRR curves of the Au/Si_3N_4 samples, measured with a Bruker D8 X-ray diffractometer with a Cu K_α source at the ICMM facilities, are shown in Fig. C.1.1. Maxima corresponding to heterostructure periodicity can be observed for all samples, indicating that films are actually formed by alternated Si_3N_4 and Au-rich regions, leading to out-of-plane periodicity. It should be noted in the figure that the spectra of samples with shortest bilayer numbers, named as $[Si_3N_{4(70s)}/Au_{(88s)}]_5$ and $[Si_3N_{4(70s)}/Au_{(44s)}]_{10}$,

also exhibit the short oscillations corresponding to finite size film interferences, not appearing for the other samples due their large thickness, which overpass the XRR thickness measurement range. In the particular case of $[Si_3N_{4(70s)}/Au_{(88s)}]_5$ sample, maxima coming from bilayer period together with the total film thickness peaks lead to less pronounced maxima and a slightly different spectrum. The effect of the extra Si_3N_4 layer deposited on top, more noticeable for this thinnest sample, makes more complex the spectral shape.

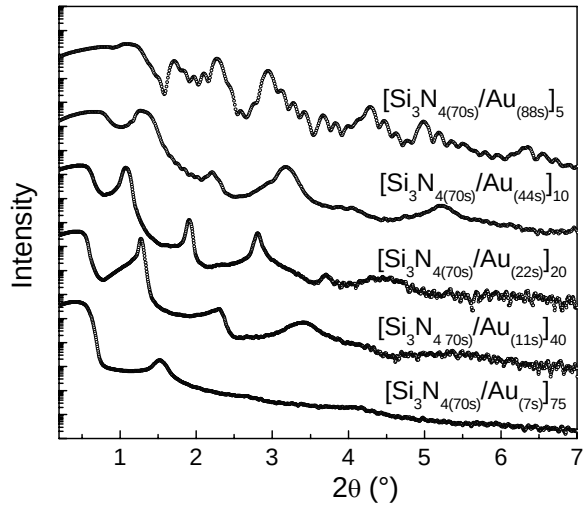

Fig. C.1.1 X-ray Reflectivity (XRR) spectra of the Si_3N_4/Au sample series. Curves have been vertically shifted for clearness.

Calculated bilayer thickness values from the XRR spectra analysis are shown in Table C.1.I (XRR-Λ). It can be noticed that the bilayer thickness obtained for $[Si_3N_{4(70s)}/Au_{(44s)}]_{10}$ sample (Λ = 8.5 nm) is very closed to the one found for $[Si_3N_{4(70s)}/Au_{(11s)}]_{40}$ sample (Λ = 8.6 nm). Moreover, $[Si_3N_{4(70s)}/Au_{(22s)}]_{20}$ sample shows Λ = 10.4 nm, which is larger than the 8.5 nm obtained for $[Si_3N_{4(\ 70s)}/Au_{(44s)}]_{10}$ sample, prepared with double Au deposition time. It should be taken into account that these differences are too big to be ascribed to uncertainties in the Λ magnitude. Furthermore, considerably similar Λ values have been found by both XRR and GISAXS experiments (see Table C.1.I), with completely different experimental set-up.

In order to clarify this apparent contradiction, the evolution of Λ within the sample series has been further studied. Fig. C.1.2 shows the bilayer thickness versus the sputtering time, where it can be seen that there exist two different slopes. These dissimilar slopes seem to be related to two different growth regimes, suggesting that the Au-layer morphology changes with the deposited Au thickness. Since formation of Au continuous layer is expected for Au sputtering times longer than 44 s, Au deposition shorter than 22 s seems to lead to non-continuous Au inside the Si_3N_4 matrix. From Table C.1.I, these Au sputtering times correspond to effective Au-layer thickness (t_{Au}) of 4.7 and 2.9 nm, respectively. The percolation threshold would be somewhere between these two values. This is the first sign of Au NPs formation within the sample series for small Au-layer deposition times (≤ 22 s), what means Au-layer thickness t_{Au} ≤ 2.9 nm.

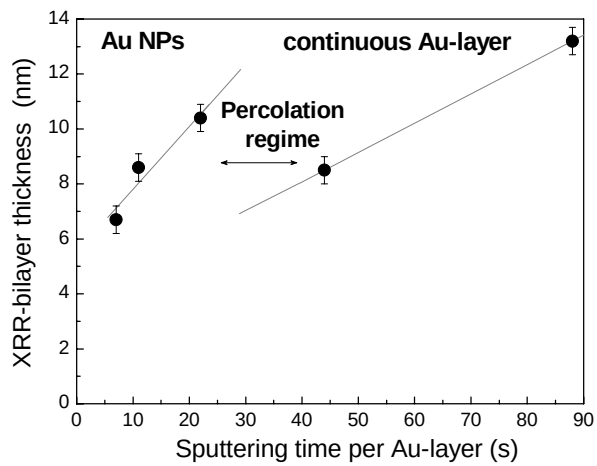

Fig.C.1.2 Bilayer thickness values measured by XRR (XRR-Λ) versus sputtering time per Au-layer deposition. Different slopes can be related to different growth type, continuous Au-layer or discontinuous growth, depending on the Au-layer deposition time.

C.1.4. Rutherford Backscattering Spectroscopy (RBS)

RBS experiments were done on the ARAMIS accelerator[18] in Orsay (France) using a 1.2 MeV He^+ beam.

Experimental data and simulations of the RBS experiments performed by the RBX software[19] are shown in Fig. C.1.3. For the sake of clearness, from now on, samples will be named by their sample effective thickness (given in table C1.I).

The atomic density per Au-layer (at/cm^2) and the corresponding Au-layer thickness calculated considering the Au metal bulk density (ρ_{Au} = 5.9x10^{22} at/cm^3) are given in Table C.1.I. The atomic compositions obtained from the RBS simulations have been also included in the table, where it appears that the Au relative concentration in the films ranges from 72 to 25 % within the sample series.

Another important result from RBS is that, as it was assumed, the amount of deposited gold is in fact proportional to its sputtering time. The linear dependence is shown in Fig. C.1.4, where the number of Au atoms per square centimetre in each Au-layer obtained from RBS is represented as a function of the sputtering time per Au-layer.

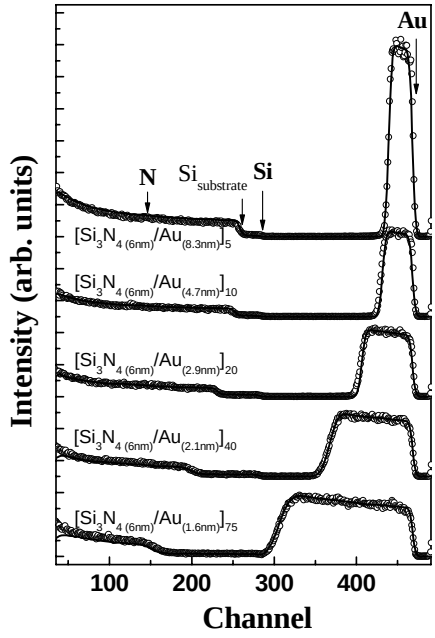

Fig. C.1.3 RBS spectra corresponding to the Au/Si_3N_4 samples. Simulation by using RBX code is given for comparison (solid line).

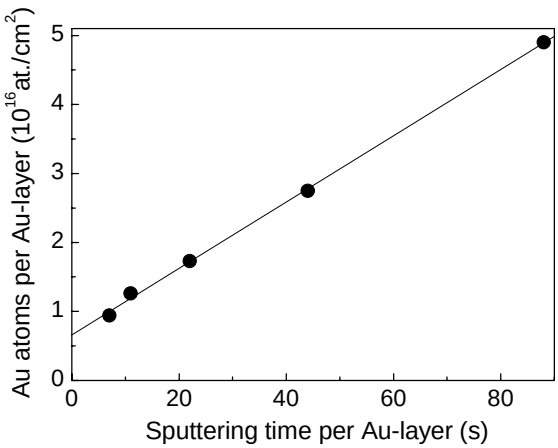

Fig. C.1.4 Number of Au atoms per square centimetre in each Au-layer obtained from RBS versus Au-layer deposition time.

C.1.5. X-Ray Absorption Spectroscopy (XAS)

XAS experiments at the Au L_{III}-edge were performed on representative samples in order to obtain additional information about the Au electronic state and local environment in the sample series. Room temperature experiments were performed in total electron yield mode on the XAFS beamline at ELETTRA (Trieste, Italy) in collaboration with Dr. Luca Olivi.

C.1.5.1. X-Ray Absorption Near-Edge Structure (XANES)

Au L_{III}-edge X-ray absorption near-edge structure (XANES) spectra of several Au/Si_3N_4 samples and a gold foil are displayed in Fig. C.1.5. Direct comparison with the Au metal reference spectrum clearly evidences that Au is present in the metallic form since, except for a slight decrease in the XANES features amplitude, no appreciable differences between the sample spectra and the metallic Au reference are found.

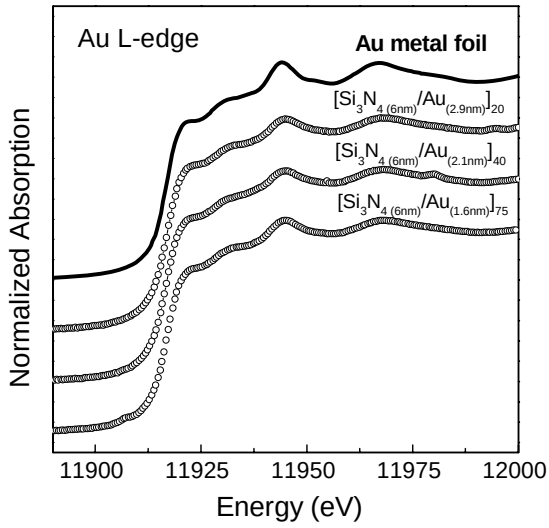

Fig.C.1.5. XANES of several samples in comparison with the Au metal reference spectra.

C.1.5.2. Extended X-Ray Absorption Fine Structure (EXAFS)

EXAFS analysis was performed using the standard procedure described in section 2.6.1.2. Simulations of the experimental data for three representative samples and a standard Au metal foil can be observed in Fig. C.1.6. Pairs and distances obtained from the data analysis are summarized in Table C.1.II.

Table. C.1.II Au atomic surrounding given by EXAFS analysis. R, N and σ^2 correspond to the atomic distance, number of neighbours and Debye-Waller factor, respectively.

Sample	Au-Au		
	R (Å)	N	σ^2 (10^{-3}Å^2)
Au foil	2.85±0.01	11.5±0.5	8.9±0.5
$[Si_3N_{4(6nm)}/Au_{(8.3nm)}]_5$	2.85±0.01	10.5±1.0	9.5±1.0
$[Si_3N_{4(6nm)}/Au_{(2.9nm)}]_{20}$	2.84±0.01	10.4±0.5	9.7±0.5
$[Si_3N_{4(6nm)}/Au_{(2.1nm)}]_{40}$	2.84±0.01	10.2±0.5	9.8±0.5

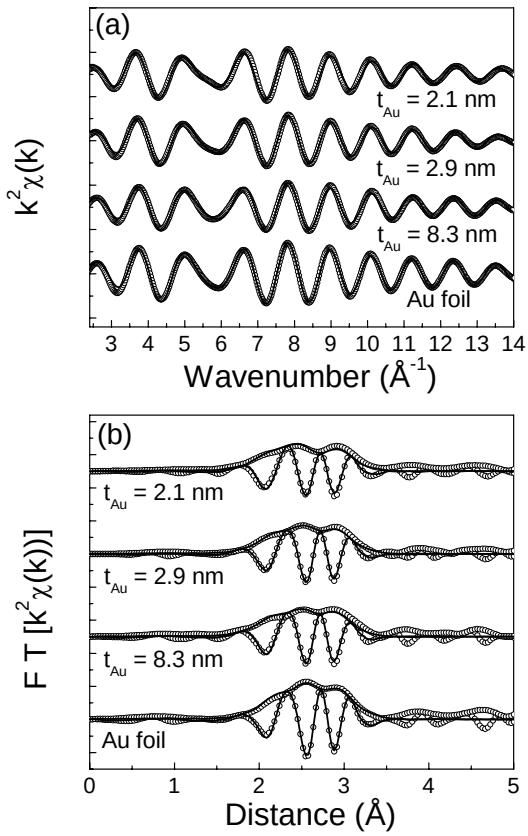

Fig. C.1.6 (a) k-space comparison between the experimental EXAFS signal (dots) and simulations (lines) at Au L-edge of samples t_{Au} = 8.3, 2.9, 2.1 nm and a Au foil. (b) Fourier transform of the (a) plotted signals; modulus and imaginary parts are shown for dual comparison with the simulated contributions (lines).

It can be observed that the Au-Au distances obtained for each sample, about 2.85 Å, coincide with the Au metal reference. Considering additional Au-N or Au-Si contributions in the simulations is not necessary since Au-Au simulations reproduce the experimental data. Therefore, possible Au/Si_3N_4 interdiffusion in the samples is too small to be detected. The EXAFS results clearly indicate Au metal formation, either as continuous layer or as NPs, in all the sample series. However, it should be noted that the decrease of t_{Au} entails a slight decrease of the Au-Au coordination number N and a slight

increase of the amplitude loss factor σ^2. Moreover, it appears that for t_{Au} = 8.3 nm, the N value is strongly dependent on the σ^2 value. An uncertainty in the Au coordination number of the order of $\pm$ 1 is thus expected here whereas it is of $\pm$ 0.5 for the other samples.

It can be noted that the fact that the Au-Au distance obtained by EXAFS for each sample agrees with the Au metal reference value (about 2.85 Å) supports the above consideration of the Au bulk density (ρ_{Au} = 5.9x10^{22} at/cm^3) for the calculation of the effective Au-layer thickness in these samples.

C.2.7. Grazing Incidence Small Angle X-ray Scattering (GISAXS)

More precise information about the Au morphology and NP dimensions was obtained by GISAXS measurements, carried out on the SWING beamline at SOLEIL synchrotron (France) in collaboration with Dr. David Babonneau and Dr. Olivier Lyon.

The energy of the incident X-ray beam was set at 9.03 keV (λ = 0.137 nm), the angle of incidence was slightly higher than θ_c in order to achieve good surface sensitivity, and the sample-to-detector distance was varied between 1.305 and 2.425 m. The transmitted and specularly reflected beams were masked by a vertical beam-stop and the scattered intensity was collected as a function of the in-plane ($2\theta_f$) and out-of-plane (α_f) exit angles with a 2D charge-coupled device (CCD) detector. The experimental data were analysed with the FitGISAXS package developed within the IGOR Pro analysis software (WaveMetrics, Inc.) by David Babonneau.

The 2D GISAXS patterns of the samples with t_{Au} = 8.3 nm, 2.9 nm and 1.6 nm are shown in Fig. C.1.7.

For t_{Au} = 8.3 nm, only Bragg peaks characteristics of a rough multilayer[20] can be seen in the vicinity of the vertical beam-stop (Fig. C.1.7a). Thus the presence of isolated NP is unlikely. A vertical cut at $2\theta_f$ = 0.32° showing 5 Bragg peaks with a q-period of about 0.45 nm^{-1} (Fig. C.1.7b) enables the period of the multilayer to be estimated as Λ = 14.0 nm, quite in agreement with the period of 13.2 nm determined by XRR.

For t_{Au} = 2.9 nm, in addition to Bragg peaks indicating layering with a *q*-period of about 0.64 nm^{-1} corresponding to Λ = 9.8 nm (also in agreement with the value determined by XRR). The pattern presents typical features of a distribution of isolated NP with in-plane spatial correlation indicating that short-range order has taken place (Fig. C.1.7c). The quantitative analysis of the GISAXS intensity within the distorted wave Born approximation[21] was performed on the basis of a horizontal cut at α_f = 0.19° using the local monodisperse approximation[22] and assuming spherical NPs with no vertical correlation between NPs (i.e., each layer has a morphology which is completely independent from the adjacent layers.[23,24] As seen in Fig. C.1.7d, the experimental data are well reproduced with a Gaussian size distribution of NPs with an average diameter ϕ = 6.9 nm, a full width at half maximum of 3.2 nm, and an interparticle distance of 9.6 nm.

For t_{Au} = 1.6 nm, the pattern is typical of a distribution of isolated NPs without spatial correlation (Fig. C.1.7e). The horizontal cut at α_f = 0.29° (symbols) and fit (red line) taking into account spheres with a Gaussian size distribution leads to an average diameter ϕ = 5.1 nm with a full width at half maximum of 2.1 nm (Fig. C.1.7f). A vertical cut at $2\theta_f$ = 0.32° showing 2 Bragg peaks gives a *q*-period of about 0.82 nm^{-1} corresponding to Λ = 7.7 nm close to 6.7 nm as found by XRR.

The bilayer thicknesses and NP sizes measured with the GISAXS technique are given in Table C.1.I and in Table C.1.III, respectively. Also given in Table C.1.III are the average diameters determined from XRD measurements of the (111) Au reflection (not shown) by using the Scherrer formula. It can be seen that the agreement between these ϕ values and those determined by GISAXS is quite good. The areal NP density given in Table C.1.III is equal to the number of Au atoms per square centimetre in each Au-layer (obtained by RBS) divided by the number of atoms per NP (obtained from the volume calculated with the diameter, ϕ, measured by GISAXS and considering the Au bulk density of 5.9×10^{22} at/cm^3). Estimated average interparticle distance (L) has been also included in the table.

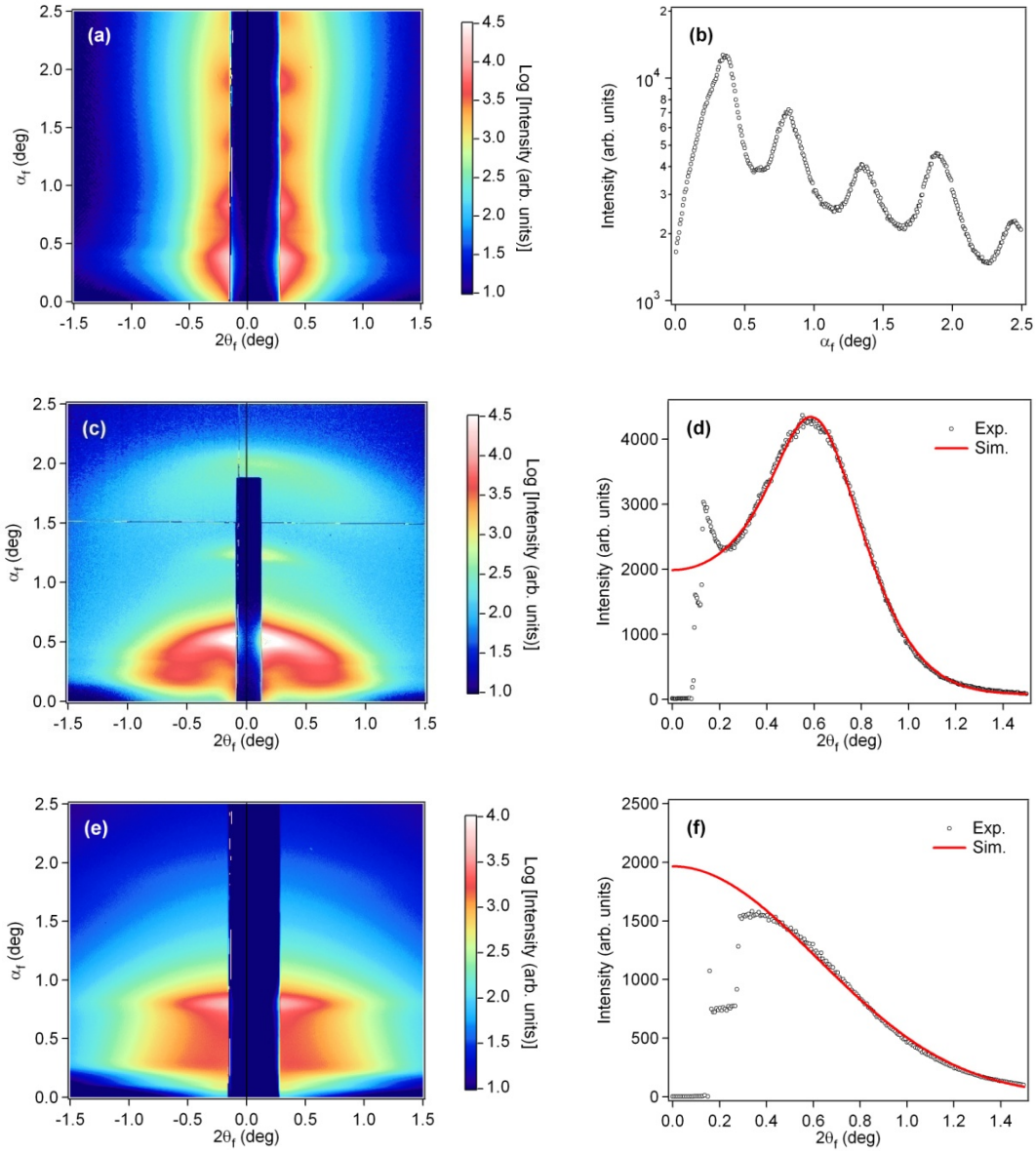

Fig. C.1.7 2D GISAXS patterns of $[Si_3N_{4(6nm)}/Au_{(t)}]_n$ multilayers for (a) t_{Au}= 8.3 nm, (c) t_{Au} = 2.9 nm, (e) t_{Au} = 1.6 nm, (b) vertical cut for t_{Au} = 8.3 nm ($2\theta_f = 0.32°$) and (d) and (f) horizontal cuts for t_{Au} = 2.9 nm ($\alpha_f = 0.19°$) and t_{Au} = 1.6 nm ($\alpha_f = 0.29°$), respectively.

Table. C.1.III Au NP average diameter obtained by XRD (XRD-ϕ) and by GISAXS (GISAXS-ϕ). Number in brackets corresponds to the diameter distribution (FWHM assuming a Gaussian size distribution, in nm). Au-layer NP density (NP/cm^2) has been calculated using GISAXS-ϕ, the number of Au atoms per square centimetre in each Au-layer obtained by RBS and considering Au bulk density (ρ_{Au} = 5.9x10^{22} at/cm^3). In plane interparticle distance (L) has been obtained from Au NPs density and considering both square and hexagonal NP arranges. The given L value corresponds to the average.

Sample	XRD-ϕ (nm)	GISAXS-ϕ (nm)	Au NPs (NP/cm^2)	L (nm)
$[Si_3N_{4(6nm)}/Au_{(8.3nm)}]_5$	-	continuous Au-layer		
$[Si_3N_{4(6nm)}/Au_{(2.9nm)}]_{20}$	7.5	6.9 (3.2)	1.7x10^{12}	9.6
$[Si_3N_{4(6nm)}/Au_{(2.1nm)}]_{40}$	7.5	-	-	-
$[Si_3N_{4(6nm)}/Au_{(1.6nm)}]_{75}$	6.7	5.1 (2.1)	2.3x10^{12}	8.3

Therefore, GISAXS results corroborate the change in the Au-layer morphology with the deposited Au thickness evidenced above by XRR results (Fig C.1.2) and give us additional information about the Au NPs morphology. Formation of approximately spherical isolated Au NPs is expected for all samples with $t_{Au} \leq 2.9$ nm. However, while Au NPs with in-plane spatial correlation are found for t_{Au} = 2.9 nm sample, NPs without spatial correlation are found for sample with t_{Au} = 1.6 nm. In view of these results, a more thorough scheme of the Au morphology within the sample series has been depicted in Fig. C.1.8.

The obtained Au morphology can be compared to the growth of Au thin films (from 0.2 to 12 nm) on TiO_2 investigated by L. Zhang et al.[25], where the Au was evaporated under UHV conditions onto TiO_2(110). They found that Au grows initially as 3D islands on TiO_2. At RT, the Au film morphology evolves with increasing average Au thickness (t_{Au}), from hemispherical islands (t_{Au} < 1 nm) to partially coalesced island structures (t_{Au} > 1.5 nm), to percolation at t_{Au} ~ 8 nm and finally, a continuous and rough film for t_{Au} = 12 nm.

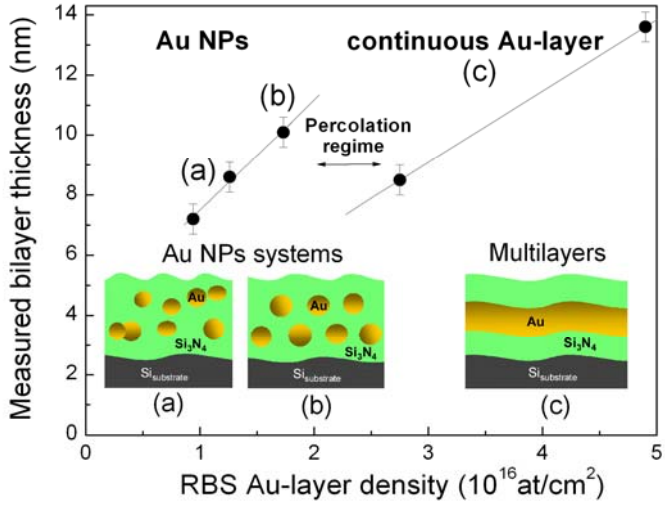

Fig. C.1.8 Bilayer thickness values (averaged XRR-Λ and GISAXS-Λ) versus the number of Au atoms per square centimetre in each Au-layer measured by RBS. Au continuous layers are obtained for Au-layer atomic densities ≥ 2.75 x 10^{16} at/cm^2 (t_{Au} ≥ 4.7 nm) leading to Si_3N_4/Au multilayered samples. For Au-layer atomic density = 1.73 x 10^{16} at/cm^2 (t_{Au} = 2.9 nm), Au NPs with short-range order are obtained while no in-plane correlation is obtained for the smallest Au-layer atomic density, 9.4 x 10^{15} at/cm^2 (t_{Au} = 1.6 nm).

In addition, they found that the inter-island distance reaches a saturation value after deposition of 1.5 nm average thickness of Au (close to 10 nm) and remains constant afterwards. In our case of sequential deposition, it has been obtained similar growth type and percolation values between t_{Au} of 2.9 and 4.7 nm, which are smaller but comparables to those reported ones.

Further details of the different Au NPs distribution can be observed in Fig. C.1.9, where structural parameter obtained by GISAXS and XRR for t_{Au} = 1.6 nm (Fig. C.1.9(a)) and t_{Au} = 2.9 nm (Fig. C.1.9(b)) samples are shown for comparison. The differences found in the average diameter values in comparison with nominal values (for example, ϕ = 5.1 nm for t_{Au} = 1.6 nm) were similarly found in Ag NPs embedded in Si_3N_4 prepared by ion beam sputtering, where NPs of 6 nm of average height were found for nominal t_{Ag} = 1 nm.[12]

It can be observed in Fig C.1.9, for instance, that NPs are separated in plane approximately by 3/2 of ϕ distance in both cases. For each sample, the obtained average in-plane interparticle distance (L) and out-of-plane periodicity (Λ) have similar values, being close to the saturation value of 10 nm reported by L. Zhang et al.[25] for an effective gold thickness of 1.5 nm. By contrast, we have not reached a saturation value for L for the studied samples.

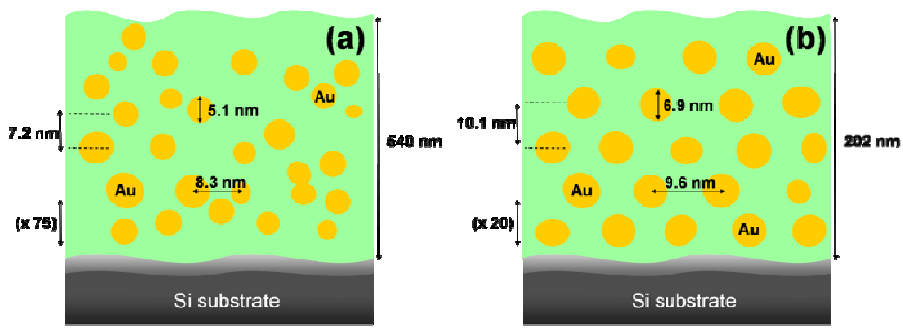

Fig. C.1.9 Schematic comparison between Au NPs morphology for sample with (a) t_{Au} = 1.6 nm and (b) t_{Au} = 2.9 nm. NP average diameter (ϕ), interparticle distance (L) and bilayer thickness (Λ) are obtained by GISAXS and XRR.

C.1.7. UV-VIS Absorption

Au NPs samples were additionally grown on quartz substrates to measure sample optical absorption in transmission mode. These samples were prepared under identical experimental conditions as the above-described multilayers to be compared in the same way. The optical absorption of these films was measured with a Cary 4000 UV-vis spectrophotometer at the ICMM, in the 200–900 nm ultraviolet-visible range.

Fig. C.1.10 shows the optical absorption coefficient as a function of wavelength of Au NP samples with t_{Au} = 1.6 nm and t_{Au} = 2.9 nm. Optical absorption from a Si_3N_4 film has been included for comparison. SPR wavelength is about 570 nm for t_{Au} = 1.6 nm and

587 nm for t_{Au} = 2.9 nm samples. Note that the SPR of t_{Au} = 2.9 nm slightly redshifts. This fact is in agreement with theory and experiments for nanoparticles much smaller than the wavelength of the absorbing light (where dipole approximation is valid, ϕ < 25 nm for gold), which predict that the maximum of the SPR clearly red shifts with increasing Au volume fraction.[9]

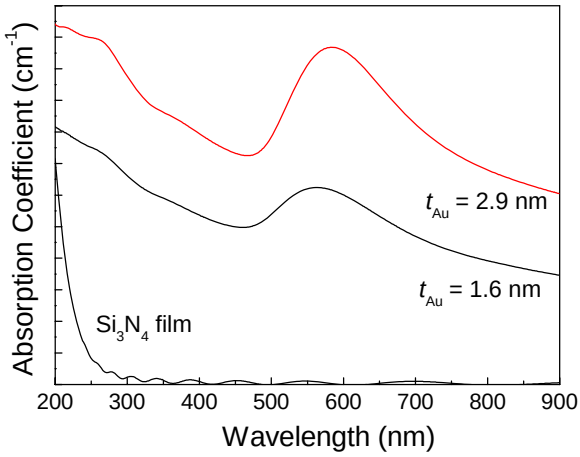

Fig. C.1.10 Optical absorption coefficient of Au NP samples with t_{Au} = 2.9 (ϕ = 6.9 nm) and t_{Au} = 1.6 nm (ϕ = 5.1 nm). A sputtered Si_3N_4 film is presented for comparison. Absorption has been normalized to total sample thickness.

In Fig. C.1.11, sample optical spectra have been qualitatively compared to the Maxwell-Garnett (M-G) effective medium model just by considering Au bulk optical properties and a volume fraction (f) equal to 29% for the case of t_{Au} = 2.9 nm and 22% for t_{Au} = 1.6 nm (calculated from RBS data). In M-G theory, ε_{eff} satisfies the equation.[26,27]

$$\frac{\varepsilon_{eff} - \varepsilon_m}{\varepsilon_{eff} + 2\varepsilon_m} = f\frac{\varepsilon - \varepsilon_m}{\varepsilon + 2\varepsilon_m} \qquad \text{(C.1.1)}$$

Where ε is the dielectric function of the metallic particles and ε_m is the dielectric function of the matrix. The dielectric function of Au has been taken from Palik database

and the medium dielectric function ε_m is taken as a constant of 4 for the Si_3N_4. The absorption coefficient of the composite can be obtained from the following formula[27]

$$\alpha = \frac{4\pi}{\lambda\sqrt{2}}\left[\left(\varepsilon_{e1}^2 + \varepsilon_{e2}^2\right)^{1/2} - \varepsilon_{e1}\right]^{1/2} \qquad (C.1.2)$$

Here ε_{e1} and ε_{e2} are the real and imaginary parts of the effective dielectric function $\varepsilon_{eff.}$

Compared to theory, slightly red-shifts are obtained for the two experimental SPR.

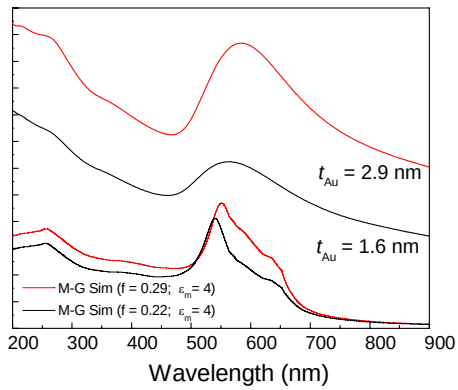

Fig. C.1.11 Optical absorption coefficient of Au NP samples with t_{Au} = 2.9 (ϕ = 6.9 nm) and t_{Au} = 1.6 nm (ϕ = 5.1 nm) compared to Maxwell-Garnet (M-G) theory using f = 0.29 and f = 0.22 (calculated from RBS data of t_{Au} = 2.9 and t_{Au} = 1.6 nm, respectively), Au bulk optical properties and the dielectric function of Si_3N_4 (ε_m = 4).

Apart from the dielectric properties of the cluster metal, it has been mentioned that the SPR spectral position depends on the size, shape and NPs organization, as well as on the surrounding medium. Therefore, there are different factors that can explain these small deviations from expected values. For the sake of clarity, we have discussed here these factor for two cases: i) the case of quasi-static regime, for what only the dipole term is assumed to contribute to the absorption (for gold, it happens for Au NPs with ϕ < 25

nm, which is our experimental situation) and where changes in the spectra are therefore referred to as intrinsic size effects as well as for ii) the non quasi-state case (ϕ > 25 nm), that is, in the extrinsic size region, where the dipole approximation is not valid.

Considering the surrounding medium, an increase of the refractive index of the Si_3N_4 matrix can induce a SPR red-shift.[1,9,28] However, this fact does not seem to explain the observed red-shift. M-G calculation has been done considering a matrix refractive index approximately equal to the Si_3N_4 bulk value of 2. Taking that into consideration, smaller index in comparison with the bulk material might be expected in our samples, but not an enhancement.

On the other hand, the size effect of the plasmon absorption does not result so evident. While for Au NPs with ϕ > 25 nm (extrinsic size region) the peak position shifts to longer wavelengths as higher order multipole terms increasingly dominate,[29] the situation is more complicated for smaller NPs, for which intrinsic size effects should dominate. Experimentally, both a blue shift and a red shift of the SPR have been found when decreasing size.[1,9] Furthermore, the magnitude of the wavelength shift in the absorption maximum for NPs in the intrinsic size region is usually small compared to the total line width of the plasmon resonance. The SPR peak position is therefore, usually not as well suited for a discussion of a size effect within the quasi-static regime.

By contrast, much more drastic effect on the surface plasmon absorption is found if the NP shape is changed. Assuming deviation from spherical shape (typically spheroidal NPs with a revolution axis perpendicular to the substrate and H/D axis ratio, which is commonly observed, for instance in Ag NPs embedded in Si_3N_4)[12,28], a decrease of the H/D axis ratio (oblate-like shape) can also induce a SPR red-shift. A little ellipsoidal deformation of the mainly spherical Au NPs can explain the small difference between theory and experimental data in the SPR position of these samples.

If we consider now the plasmon bandwidth, for the case of large Au particles (ϕ > 25 nm), it is well known that the SPR bandwidth increases with increasing size. When the wavelength becomes comparable to the dimension of the NP, it leads to an inhomogeneous polarization of the NP by the electromagnetic field. The broadening of

the SPR is usually ascribed to retardation effects, as well as the excitation of different multipole modes, with peaks at different wavelengths.[1,9,29]

For the case of smaller Au NPs, the SPR bandwidth is size-independent within the dipole approximation. However, a size effect on the SPR has been experimentally observed as the plasmon bandwidth increases with decreasing particle size. In fact, it is quite well established that the bandwidth is inversely proportional to the radius of the particle for sizes smaller than 20 nm.[1,9] Nevertheless, we have found similar bandwidths for both samples (FWHM of about 200 nm), being a bit larger for the t_{Au} = 2.9 nm sample than for the t_{Au} = 1.6 nm one (with smaller NP size), contrary to reported results.

Even so, a broadening of the size distribution of the NPs is also expected to induce a broadening of their size shape distribution. Since cluster shape is known to influence the spectral position of the SPR, such a size-induced broadening of their shape distribution may result in a broadening and maybe a spectral shift of the SPR band.[28] From this point of view, the broader NP size distribution found for t_{Au} = 2.9 nm sample in comparison with t_{Au} = 1.6 nm (see FWHM of ϕ distribution, in Table. C.1.III) might be associated with a slightly broader SPR for t_{Au} = 2.9 nm in Fig. C.1.10. For these samples, the SPR width seems more dependent of size distribution than of NPs arrange.

In view of these results, the SPR spectral position of Au NPs embedded in Si_3N_4 seems to be mainly modified by the Au volume fraction, which is varied along the sample series. The effect of the surrounding medium appears similar for both samples, with a matrix refractive experimental index close to 2.0. A slightly deviation from spherical shape for the Au NPs (oblate-like shape) may explained the small red shift observed in the SPR of both samples in comparison with M-G mean field theory. In addition, the larger NP size distribution in t_{Au} = 2.9 nm can explain its slightly broader SPR.

C.1.8 Conclusions

With the aim of growing Au NPs inside Si_3N_4 matrix in a controlled way, a series of Au/Si_3N_4 samples has been prepared by sequential sputtering technique, keeping constant the Si_3N_4 layer thickness and modifying the effective Au layer thickness (t_{Au}).

A change in the Au-layer morphology with the deposited Au amount has been evidenced by XRR and GISAXS results. While continuous Au layers leading to multilayered samples have been found for $t_{Au} \geq 4.7$ nm, non-continuous Au-layers resulting in Au NPs inside the Si_3N_4 matrix have been found for $t_{Au} \leq 2.9$ nm, being the percolation regime between these values. Approximately spherical isolated Au NPs with average sizes ranging between 7- 5 nm and a size distribution with FWHM of 40-45% have been obtained. The Au NP density is of the order of 10^{12} NP/cm^2.

Moreover, different Au NP distributions depending on the Au-layer thickness have been evidenced by GISAXS. While Au NPs (ϕ = 7 nm) with in-plane spatial correlation are found for t_{Au} = 2.9 nm sample, Au NPs (ϕ = 5 nm) without spatial correlation are found for the smallest Au-layer sample, with t_{Au} = 1.6 nm.

For both samples, UV-vis absorption spectrum shows a surface plasmon resonance (SPR) effect, revealing that, despite of its stratified character, both samples can be considered as homogeneous films in terms of their optical response.

Within the series of NPs samples, the SPR spectral position, which is the main characteristic of the nanocomposite optical properties, is mainly determined by the Au volume fraction, which is varied along the sample series, and the nature of the surrounding material, which is the same for all samples. In agreement with theory, the SPR shifts towards longer wavelengths with increasing the Au-layer effective thickness (and consequently the Au volume fraction).

A slightly deviation from spherical shape for the Au NPs (oblate-like spheroids) may explain the small red shift observed in the SPR of these samples in comparison with Maxwell-Garnet theory. In addition, the larger NP size distribution in t_{Au} = 2.9 nm

sample (ϕ = 7 nm) can explain its slightly broader SPR in comparison with t_{Au} = 1.6 nm sample (ϕ = 5 nm).

The obtained dependence of the SPR maximum on the effective Au-layer thickness makes this system tunable for optical applications requiring a specific absorption spectrum.

References

1 U. Kreibig and M Vollmer, *Optical Properties of Metal Cluster* (Berlin: Springer) Vol 25 1995.

2 C. R. Henry Surf. Sci. Rep. 31, 232 (1998).

3 T. Schalkammer, A. Leitner, F. R. Aussenegg, G. Bauer and F. Pittner, SPIE Proc.3253, 12 (1998).

4 V. P. Zharov, E. N. Galitovskaya, C. Johnson and T. Kelly, Lasers Surg. Med. 37, 219 (2005).

5 G. Schmid, *Clusters and Colloids: From Theory to Application*; (VCH: Weinheim) 1994.

6 M. Graetzel, *Electrochemistry in Colloids and Dispersions*; Ed. R. A. Mackay, J. Texter; (VCH: Weinheim, New York) 1992.

7 A. Henglein, J. Phys. Chem. 97, 8457 (1993).

8 A. P. Alivisatos, J. Phys. Chem. 100, 13226 (1996).

9 S. Link and M. A. El-Sayed, J. Phys. Chem. B103, 8410 (1999).

10 C. Sönnichsen, T Franzl, T Wilk, G. von Plessen and J Feldmann, New J. Phys. 4, 93.1-93.8 (2002).

11 J. Tourdert, D. Babonneau, L. Simonot, S. Camelio and T. Girardeau, Nanotechnology 19, 125709 (2008).

12 T. Girardeau, S. Camelio, D. Babonneau, J. Tourdert, A. Barranco, Thin Solid Films 313, 455 (2004).

13 D. Ricard, P. Roussignol, C. Flytzanis, Opt. Lett. 10, 511(1985).

14 M. Breit, V. A. Podolskiy, S. Grésillon, G. von Plessen, J. Feldmann, J. C. Rivoal, P. Gadenne, Andrey K. Sarychev and Vladimir M. Shalaev Phys. Rev. B 64, 125106 (2001).

15 Jean-Michel Lamarre, Franck Billard, Chahineze Harkati Kerboua, Michel Lequime, Sjoerd Roorda, Ludvik Martinu, Optics Communications 281, 331(2008).

16 O. L. Muskens, N. Del Fatti and F. Vallée, Nano Lett. 6, 552 (2006).

17 L. Arlemao, D. Barreca, G. Bottaro, A. Gasparotto, S. Gross, C. Maragno, E. Tondello, Coordination Chemistry Reviews 250, 1294 (2006).

18 H. Bernas, J. Chaumont, E. Cottereau, R. Meunier, A. Traverse, C. Clerc, O. Kaitasov, F. Lalu, D. Le Du, G. Moroy and M. Salomé, Nucl Instr. and Meth. B 62, 416 (1992).

19 E. Kotai, Nucl. Instrum. Methods B 85, 588 (1994).

[20] V. Holý and T. Baumbach, Phys. Rev. B 49, 10668 (1994).

[21] M. Rauscher, T. Salditt, and H. Spohn, Phys. Rev. B 52, 16855 (1995).

[22] J.S. Pedersen, J. Appl. Crystallogr. 27, 595 (1994).

[23] D. Babonneau, G. Abadias, J. Toudert, T. Girardeau, E. Fonda, J.-S. Micha, F. Petroff, J. Phys.: Condens. Mat. 20, 035218 (2008).

[24] K. Salomon, O. Milat, M. Buljan, U.V. Desnica, N. Radić, P. Dubček, and S. Bernstorff, Thin Solid Films (to be published).

[25] L. Zhang, F. Cosandey, R. Persaud and T. E. Madey, Surf. Sci. 439, 73 (1999).

[26] B. Palpant, Phys. Rev B 57, 1963 (1998).

[27] L. H. Zhou, C. H. Zhang, Y. T. Yang, B. S. Li, L. Q. Zhang, Y. C. Fu and H. H. Zhang, Nucl Instr. and Meth. B 267, 58 (2009).

[28] J. Tourdert, S. Camelio, D. Babonneau, M-F Denanot and T. Girardeau, J. Appl Phys. 98, 114316 (2005).

[29] G. C. Papavassiliou, Prog. Solid State Chem. 12, 185 (1980).

Appendix C

From Ferromagnetism to Noble Metal Nanoparticles Formation in the Si_3N_4 and ZnO Systems

C.2. Au/ZnO Multilayers

C.2.1. Motivation

As it has been explained in Appendix C.1, the refractive index of the matrix plays an important influence on the SPR.[1,2] Motivated by the Au NPs growth obtained in the transparent nitride Si_3N_4, with a refractive index of 2, we have performed a study of the Au NPs growth in ZnO oxide matrix, which is also a material previously studied by the research group and with refractive index close to 2. The aim of this work is therefore to compare how Au NPs grow and arrange inside this other ceramic matrix, and the corresponding influence on the optical properties of the nanocermet.

Similarly to the case of the Au/Si_3N_4 system, a detailed characterization of the nanocermets from the structural point of view has been performed here to fully understand their properties. In this Appendix, several experimental techniques have been combined to determine the growth mode and to provide a description of the Au NPs in terms of average size, morphology and organization in the matrix. The structural and optical properties of this system have been compared to the ones obtained for the Au/Si_3N_4 system.

C.2.2. Preparation of samples

Following the same procedure as the previously described for Au/Si_3N_4 samples (Appendix C.1), Au/ZnO multilayered films were prepared by sequential sputtering of

ZnO and Au on Si(100) and quartz substrates at room temperature. The residual pressure was near $1x10^{-7}$ mbar. ZnO layers were deposited by reactive sputtering from a pure Zn target (Goodfellow: 99.9%) using O_2/Ar mixture gas (30% O_2-rich) at a working pressure of $5.4x10^{-3}$ mbar (the ZnO growth conditions are the same as the ones used for Mn/ZnO series growth, described in Chapter 3). The deposition rate was about 3 nm/min for a DC power of ~5.5 W. Au layers were grown from a gold target (99.999%) at $5.0x10^{-3}$ mbar pressure of pure Ar. The deposition rate was about 5 nm/min for a DC power of ~10 W. Pre-sputtering was developed before multilayer growth and also between two consecutive layers. The sequence of deposition was always started and finished with a ZnO layer so Au grows always on the same type of surface.

Following the above described method, a series of five Au/ZnO samples, labelled as $[ZnO_{(135s)}/Au_{(t\text{-}sput)}]_n$ was prepared. Whereas the ZnO sputtering time per layer was maintained constant in every sample, the Au layer sputtering time (t-sput) was varied between 88 s and 7 s. The expected ZnO layer thickness is therefore approximately constant in every sample (about 3 nm here) while the expected Au layer thickness (t_{Au}) ranges from 8 to 2 nm. The number of bilayers (n) was increased in order to maintain the Au total amount approximately constant in the five samples. The prepared samples are summarized in Table C.2.I, where the sputtering deposition time of the Au and ZnO layers for each sample as well some structural and compositional parameters as bilayer thickness (Λ) or number of atoms, obtained from XRR and RBS measurements, are given.

In Table C.2.I, the labelled Au-layer "effective thickness" corresponds to the calculated Au-layer thickness (t_{Au}) using RBS and the Au bulk density (ρ_{Au} = $5.9x10^{22}$ at/cm^3) and similarly for the ZnO (RBS data and ρ_{ZnO} = $8.3x10^{22}$ at/cm^3). In the named "sample effective thickness description", it has been considered RBS-t_{Au} and the ZnO-layer thickness average among all the samples (from both XRR and RBS).

From now on, samples will be named by their sample effective thickness.

Table C.2.I Sample series description: sputtering time for the ZnO and Au-layer deposition and number of bilayers (n), XRR-obtained bilayer thickness (XRR-Λ), RBS-obtained bilayer thickness (RBS-Λ), number of Au atoms per Au-layer and calculated effective Au-layer thickness (t_{Au}), total number of Zn atoms measured by RBS (at/cm^2) and calculated and ZnO-layer thickness (t_{ZnO}) using RBS data and bulk densities (ρ_{Au} = 5.9x10^{22} at/cm^3 and ρ_{ZnO} = 8.3x10^{22} at/cm^3 respectively), sample effective thickness values considering RBS-t_{Au} and the ZnO-layer thickness average among all the samples (from both XRR and RBS).

Sample $[ZnO_{(135s)}/Au_{(t\text{-}sput)}]_n$	XRR-Λ (nm)	RBS-Λ (nm)	RBS Au-atoms per layer (at./cm^2)	RBS t_{Au} (nm)	RBS total Zn-atoms (at./cm^2)	RBS t_{ZnO} (nm)	Sample effective thickness
$[ZnO_{(135s)}/Au_{(88s)}]_5$	10.5	11.1	4.60x10^{16}	7.8	6.1x10^{16}	3.3	$[ZnO_{(3nm)}/Au_{(7.8nm)}]_5$
$[ZnO_{(135s)}/Au_{(44s)}]_{10}$	7.5	7.6	2.71x10^{16}	4.6	1.0x10^{17}	3.0	$[ZnO_{(3nm)}/Au_{(4.6nm)}]_{10}$
$[ZnO_{(135s)}/Au_{(22s)}]_{20}$	6	6.2	2.12x10^{16}	3.6	4.4x10^{17}	2.6	$[ZnO_{(3nm)}/Au_{(3.6nm)}]_{20}$
$[ZnO_{(135s)}/Au_{(11s)}]_{40}$	5	5.8	1.41x10^{16}	2.4	1.1x10^{18}	3.4	$[ZnO_{(3nm)}/Au_{(2.4nm)}]_{40}$
$[ZnO_{(135s)}/Au_{(7s)}]_{75}$	5	5.8	1.06x10^{16}	1.8	2.5x10^{18}	4.0	$[ZnO_{(3nm)}/Au_{(1.8nm)}]_{75}$

C.2.3 X-Ray Reflectivity (XRR)

The XRR curves of the Au/ZnO samples, measured with a Bruker D8 X-ray diffractometer with a Cu K_α source at the ICMM facilities, are shown in Fig. C.2.1. Maxima corresponding to heterostructure periodicity can be observed for all samples, showing that films are actually formed by alternated ZnO and Au-rich regions, leading to out-of-plane periodicity. In this case, short oscillations corresponding to finite size film interferences are observed for $[ZnO_{(3nm)}/Au_{(7.8nm)}]_5$, $[ZnO_{(3nm)}/Au_{(4.6nm)}]_{10}$ and $[ZnO_{(3nm)}/Au_{(3.6nm)}]_{20}$ samples. In comparison with XRR spectra from $[Si_3N_{4(6nm)}/Au_{(t)}]_n$ samples (depicted in Fig. C.1.1), it seems that heterostructure peaks appear better defined for these three Au/ZnO samples with n = 5, 10 and 20. By contrast, for samples with smallest t_{Au} values (n = 40 and 75), broader periodicity peaks are found for these Au/ZnO samples in comparison with the others from the Au/ZnO series. Moreover, if we compare $[Si_3N_{4(6nm)}/Au_{(2.9nm)}]_{40}$ and $[ZnO_{(3nm)}/Au_{(2.4nm)}]_{40}$ sample spectra, a number of three bilayer peaks can be clearly distinguished for the Au/Si_3N_4 sample, while only one is evidenced for Au/ZnO sample.

These results suggest that, for larger t_{Au} values ($t_{Au} \geq 3.6$ nm) where formation of continuous Au-layers is expected, sharper Au-ZnO interfaces in comparison with the Au-Si_3N_4 ones are obtained. However, for small t_{Au} values, where Au NP formation is expected, out-of-plane periodicity gets worse for the Au/ZnO system compared to the Au/Si_3N_4 one. Less well formed, or bad organized Au NPs inside ZnO are firstly evoked by comparison of XRR measurements of both Au/ZnO and Au/Si_3N_4 systems.

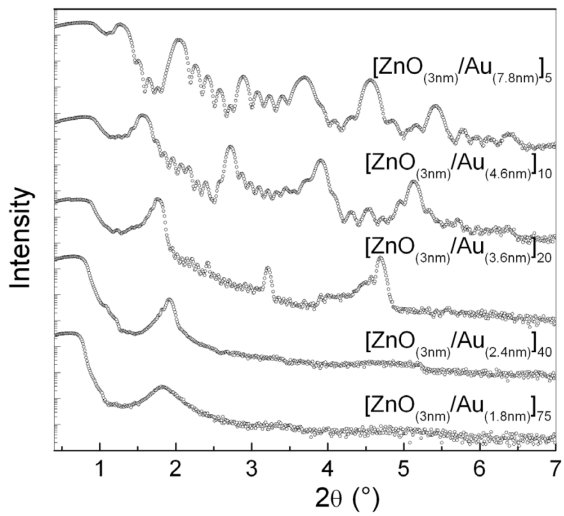

Fig. C.2.1 X-ray Reflectivity (XRR) spectra of the Au/ZnO sample series. Curves have been vertically shifted for clearness.

The bilayer thickness values calculated from XRR spectra analysis (XRR-Λ) range between 10.5 nm and 5 nm within the sample series (Table C.2.I). The evolution of the experimental bilayer thickness obtained by XRR versus the Au-layer deposition time can be seen in Fig. C.2.2. Differing from the Au/Si_3N_4 case, XRR-Λ exhibits approximately linear variation with the Au-layer sputtering time for all the sample series. A change in the Au-layer morphology cannot be related here to the existence of two different slopes within this sample series. It seems that for this system, Au-layer continuous growth is preserved until shorter Au-layer sputtering times than in the case of Au/Si_3N_4 samples. This would be in agreement with XRR results, which showed that heterostructure

charasteristic peaks appear better defined for Au/ZnO samples with n = 5, 10 and 20 in comparison with the thicker Au/Si_3N_4 ones, suggesting smaller interface roughness for Au/ZnO multilayers.

Two facts should be noted here: i) the calculation of the XRR bilayer thickness for samples with the smallest t_{Au} values (n = 40 and 75) is more complicated for the thinnest Au/ZnO samples than for the Au/Si_3N_4 ones since there are less number of broader peaks. The uncertainty in the XRR-Λ value has been considered higher for these two samples (Δ(XRR-Λ) = ± 0.7 nm compared to Δ(XRR-Λ) = ± 0.5 nm for the others). ii) Even if a clear transition between different growth regimes is not evidenced from Fig. C.2.2, non-continuous Au layers are in fact expected for the shortest Au-layer deposition times considering the gold wettability. Furthermore, the same Λ value (5 nm) has been obtained for the two shortest Au-layer deposition times (11 s and 7 s), this suggests Au NP formation at least for these Au-layer thickness (t_{Au} = 2.4 nm and 1.8 nm). Anyway, it should be noticed that the transition from Au continuous layer to Au NP growth seems much more abrupt in Au/Si_3N_4 samples, pointing out that Si_3N_4 favours the formation of Au NPs.

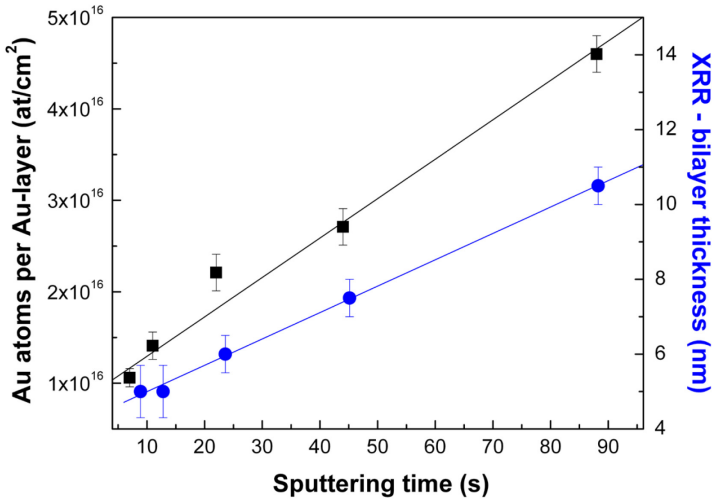

Fig.C.2.2 Number of Au atoms/cm² per layer (RBS) and bilayer thickness values measured by XRR (XRR-Λ) versus sputtering time per Au-layer deposition.

C.2.4. Rutherford Backscattering Spectroscopy (RBS)

RBS experiments were done on the JUSSIEU accelerator in France using a 1.2 MeV He^+ beam. Experimental RBS data of the Au/ZnO sample series are shown in Fig. C.2.3. Obtained results from data simulations using the RBX software[3] are summarized in Table C.2.I. The number of Au atoms per Au-layer (at/cm^2), the number of Zn atoms per ZnO-layer (at/cm^2) and their corresponding Au and ZnO-layer thickness calculated considering the Au metal bulk density (ρ_{Au} = 5.9x10^{22} at/cm^3) and ZnO bulk density (ρ_{ZnO} = 8.3x10^{22} at/cm^3) are given in the table. The total number of Au atoms per Au-layer ranges between 4.6x10^{16} and 1.06x10^{16} at/cm^2 within the sample series. The average number of Zn atoms per ZnO layer is about 2.1 x10^{16} at/cm^2.

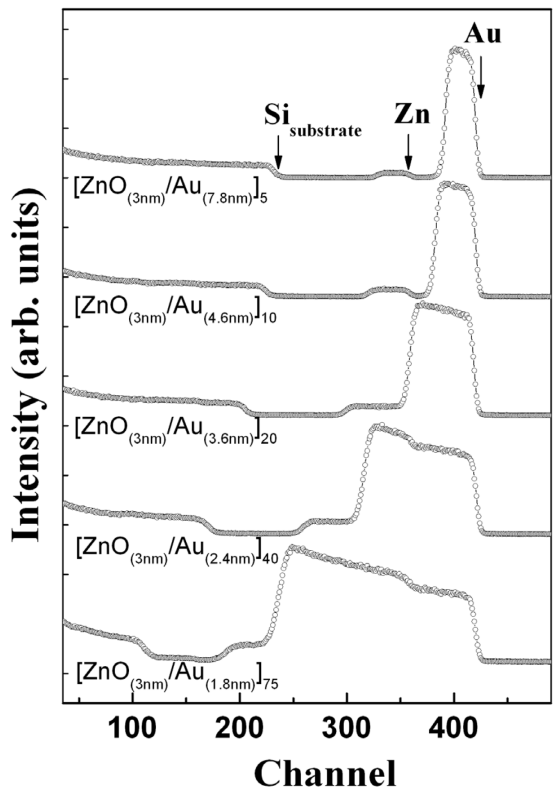

Fig. C.2.3 RBS spectra corresponding to the Au/ZnO samples.

As it was expected, the obtained amount of deposited gold results approximately proportional to its sputtering time. The linear dependence can be observed in Fig. C.2.2, where the total number of Au atoms Au-layer obtained from RBS is represented as a function of the Au-layer sputtering time.

C.2.5. X-Ray Absorption Spectroscopy (XAS)

XAS experiments at the Au L_{III}-edge were performed on the samples in order to obtain additional information about the Au electronic state and local environment in the sample series. Experiments were performed in fluorescence mode at room temperature on the SAMBA beamline at SOLEIL (Paris), in collaboration with Dr. Emiliano Fonda.

C.2.5.1. X-Ray Absorption Near-Edge Spectroscopy (XANES)

Au L_{III}-edge X-ray absorption near-edge structure (XANES) spectra of representative Au/ZnO samples and a gold metal foil are displayed in Fig. C.2.4. Direct comparison with the Au metal reference spectrum clearly evidences that Au is present in the metallic form. Although no significant differences between the sample spectra and the metallic Au reference are found, a small softening of the XANES spectral features appears, especially for the thinnest Au-layers, which would be in agreement with a decrease of the average coordination number due to NP formation.

C.2.5.2. Extended X-Ray Absorption Fine Structure (EXAFS)

EXAFS analysis was performed using Cherokee software developed by Dr. Alain Michalowicz. Simulations of the experimental data for four representative samples and a standard Au metal foil can be observed in Fig. C.2.5. Pairs and distances obtained from the data analysis have been summarized in Table C.2.II.

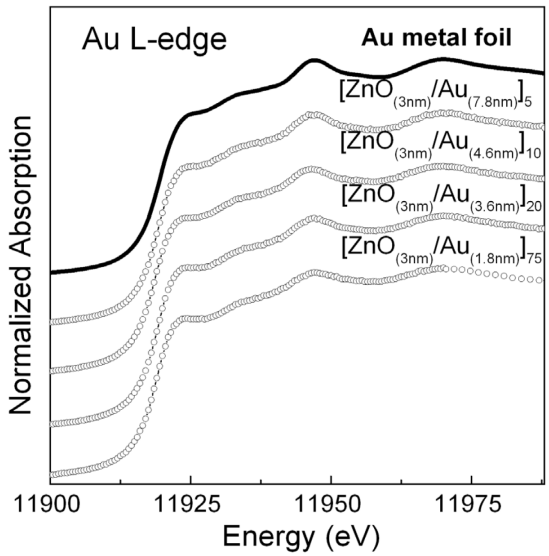

Fig.C.2.4. XANES of representative samples in comparison with the Au metal reference spectrum.

It can be observed that the Au-Au distances obtained for each sample, about 2.84 Å are slightly smaller but in agreement with the Au metal foil reference. Considering additional Au-O or Au-Zn contributions in the simulations does not seem necessary since Au-Au simulations reproduce the experimental data. Therefore, EXAFS results indicate mostly Au metal formation, either as continuous layer or as NPs, in all the sample series. If there were any Au/ZnO interdiffusion in the samples, it would be very small.

A noticeably decrease in the Au-Au coordination number N in comparison with the Au/Si_3N_4 system has been obtained. This seems related to the finite size effect (smaller Au cluster size in the Au/ZnO samples) and probably to larger Au crystalline disorder in the Au/ZnO system.

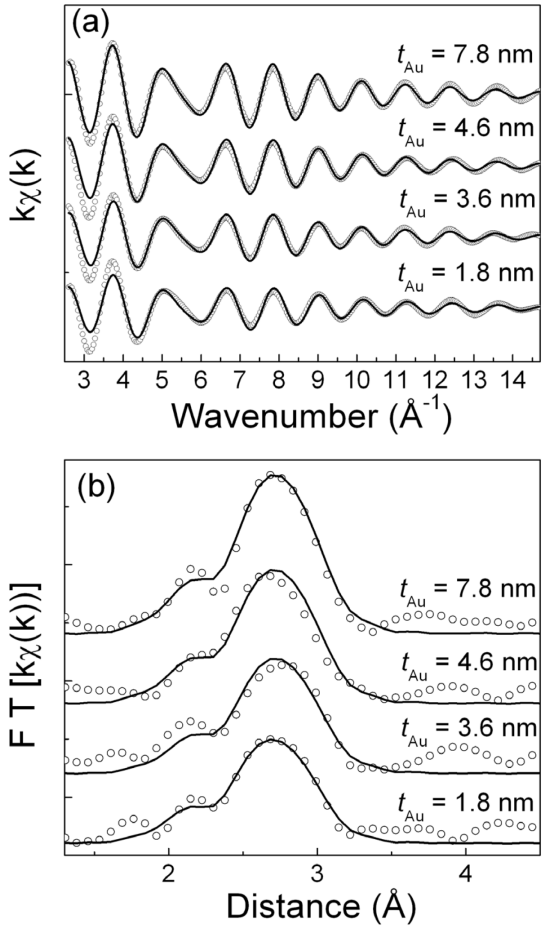

Fig. C.2.5 (a) k-space comparison between the experimental EXAFS signal (dots) and simulations (lines) at Au L_{III}-edge of samples t_{Au} = 7.8, 4.6, 3.6 and 1.8 nm. (b) Fourier transform of the (a) plotted signals; modulus (dots) and simulation (lines) are shown for comparison.

C.2.6. X-Ray Diffraction (XRD)

Diffraction measurements on the sample series were carried out in a standard laboratory diffractometer (Bruker D8 TT) by using the K_α radiation line of Cu in the θ-2θ configuration at the ICMM facilities.

XRD spectra from the Au/ZnO samples are shown in Fig. C.2.6(a), where it can

be observed that all samples show crystalline Au with (111) texture. Results from XRD analyisis are summarized in Table C.2.III, where Au(111) grain sizes in the out-of-plane direction calculated by the Scherrer equation are given. Obtained gold crystalline grain size ranges from 7.5 to 2.7 nm within the sample series.

Table C.2.II Au atomic surrounding given by EXAFS analysis. R, N and σ^2 correspond to the atomic distance, number of neighbours and Debye-Waller factor, respectively.

Sample	Au-Au		
	R (Å)	N	σ^2 (10^{-3}Å^2)
Au foil	2.85±0.01	12.0±0.5	9.6±0.5
$[ZnO_{(3nm)}/Au_{(7.8nm)}]_5$	2.84±0.01	12.0±0.5	9.9±0.5
$[ZnO_{(3nm)}/Au_{(4.6nm)}]_{10}$	2.83±0.01	10.1±0.5	9.9±0.5
$[ZnO_{(3nm)}/Au_{(3.6nm)}]_{20}$	2.83±0.01	8.7±0.5	9.9±0.5
$[ZnO_{(3nm)}/Au_{(2.4nm)}]_{40}$	2.83±0.01	8.6±0.5	9.9±0.5
$[ZnO_{(3nm)}/Au_{(1.8nm)}]_{75}$	2.84±0.01	7.9±0.5	9.9±0.5

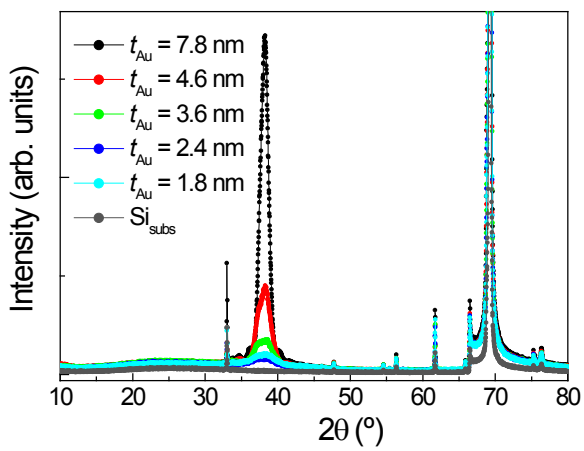

Fig. C.2.6 XRD diffraction spectra of the Au/ZnO samples and a silicon substrate.

Table. C.2.III XRD results summary: Au(111) peak position (2θ), full width at half maximum (FWHM) and its corresponding grain size in the out-of-plane direction obtained by the Scherrer equation. As well, effective Au-layer thickness (t_{Au}) calculated from RBS data and Au NP diameter (ϕ) obtained by GISAXS.

Sample	XRD-Au(111)			RBS t_{Au} (nm)	GISAXS ϕ (nm)
	2θ (°)	FWHM (°)	grain size		
$[ZnO_{(3nm)}/Au_{(7.8nm)}]_5$	38.19	7.8	7.5	7.8	-
$[ZnO_{(3nm)}/Au_{(4.6nm)}]_{10}$	38.14	4.6	4.6	4.6	-
$[ZnO_{(3nm)}/Au_{(3.6nm)}]_{20}$	38.09	3.6	3.6	3.6	-
$[ZnO_{(3nm)}/Au_{(2.4nm)}]_{40}$	38.06	2.4	2.8	2.4	4.7
$[ZnO_{(3nm)}/Au_{(1.8nm)}]_{75}$	38.13	1.8	2.7	1.8	3.7

For $t_{Au} \geq 3.6$ nm, where formation of continuous Au-layers is expected, the obtained XRD-Au grain sizes are nearly identical to the effective Au-layer thickness calculated from RBS data considering Au bulk density (t_{Au}). Therefore, the assumption of the Au bulk density ($\rho_{Au} = 5.9 \times 10^{22}$ at/cm^3) in these Au/ZnO samples becomes justified.

For samples with $t_{Au} = 2.4$ and 1.8 nm, larger nanocrystalline grain sizes in comparison with the RBS effective Au-layer thickness (t_{Au}) support the suggested non-continuous Au growth in samples with $t_{Au} \leq 2.4$ nm. Gold crystalline grain sizes close to 3 nm compared to about 2 nm of effective thickness for these samples are found. On the other hand, the Au crystalline sizes of these two samples (~3 nm) are smaller than the ones given by GISAXS, included in Table C.2.III (~ 4 and 5 nm for $t_{Au} = 2.4$ and 1.8 nm, respectively). This fact can be easily understood considering than each Au NP may consists of smaller nanocrystalline grains. Moreover, increase of the Au/ZnO interfacial regions due to Au NP formation is usually related to an enhancement of the crystalline disorder.

This situation slightly differs from the Au/Si_3N_4 case, where the Au diameters obtained from XRD were of the same order as the ones obtained by GISAXS (Table C.1.III). Another difference (not given in the table) is that, apart from Au(111),

Au(200) peak also appeared for the Au/Si_3N_4 samples, what is indicative of less textured gold nanocrystals in the Au/Si_3N_4 system.

Unlike the Au(111) diffraction peak, no additional diffraction peaks appear in the 2θ range between 30º and 40º, where the ZnO(002) peak at 2θ = 34.4º or ZnO(111) at 2θ about 36.3º might be expected. This evidences absence of crystalline ZnO phase in the out-of-plane direction or extremely small ZnO crystalline grains. It is important to emphasize here that (002) peak corresponding to the hexagonal wurtzite-ZnO (*W*-ZnO) crystal structure was observed in similar Mn/ZnO multilayered samples with equal ZnO layer thickness (~ 3 nm), described in chapter 3. Those samples were prepared following the same sequential sputtering procedure and both ZnO layers were deposited under the same experimental parameters. The ZnO(002) peak was clearly observed in samples with large enough ZnO content ($n \geq 20$), in particular in $[ZnO_{(3nm)}/Mn_{(1.5nm)}]_{20}$ and $[ZnO_{(3nm)}/Mn_{(0.1nm)}]_{75}$ samples measured with a standard diffractometer at the ICMM facilities (Fig. 3.7). For that reason, the presence of the *W*-ZnO(002) peak was expected for Au/ZnO samples with $n \geq 20$.

This declination of the ZnO crystallinity induced by the Au growth evidences strong Au-ZnO interaction at the interface in the sample series.

C.2.7. Grazing Incidence Small Angle X-Ray Scattering (GISAXS)

GISAXS measurements were performed to obtained additional information about the Au morphology and NP dimensions. The experiments were carried out on the SWING beamline at SOLEIL synchrotron (France) in collaboration with Dr. David Babonneau and Dr. Olivier Lyon.

The experimental details and data analysis procedure are the same as the ones described in section C.1.6. In this case, just some preliminary results are reported. For instance, the 2D GISAXS patterns of the Au/ZnO sample with t_{Au} = 1.8 nm is shown in Fig C.2.7a compared to the pattern corresponding to the Au/Si_3N_4 sample with t_{Au} = 1.6

nm (Fig C.2.7b), both with n = 75. The measured pattern presents features of Au NP formation.

Bilayer thicknesses and NP sizes measured by this technique are given in Table C.2.IV. For samples t_{Au} = 1.8 nm and 1.6 nm, Bragg peaks indicate layering corresponding to Λ about 4.9 nm and 4.8 nm respectively, well in agreement with the values determined by XRR. A preliminary analysis gives average NP diameters of approximately ϕ = 4.7 nm and ϕ = 3.7 nm for samples with t_{Au} = 1.8 nm and t_{Au} = 1.6 nm, respectively. Also included in Table C.2.IV are the average Au cluster dimensions determined from XRD measurements of the (111) Au reflection along the out-of-plane direction.

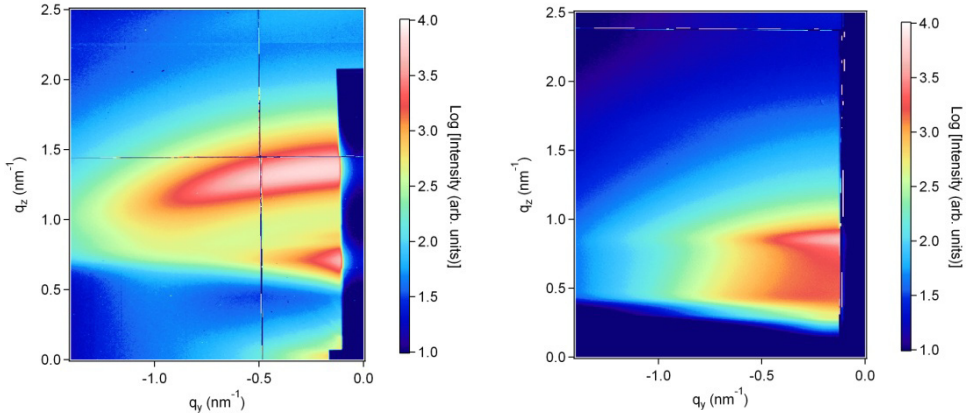

Fig. C.2.7 2D GISAXS patterns of $[ZnO_{(3nm)}/Au_{(1.8nm)}]_{75}$ sample (left) and $[Si_3N_{4(6nm)}/Au_{(1.6nm)}]_{75}$ sample (right).

As it was indicated above, the Au crystalline grain sizes calculated by XRD are slightly smaller than the ϕ values determined by GISAXS (see Table C.2.IV). This was explained considering that not the all nanoparticle contributes to crystalline order, existing Au amorphous fraction that leads to smaller XRD-ϕ values compared to GISAXS ones. The Au amorphous contribution would be more important as the Au-layer thickness is diminished, in the NP regime.

The estimated Au NP density in these samples is about $4x10^{12}$ NP/cm^2 and $7x10^{12}$ NP/cm^2 for t_{Au} = 2.4 nm and t_{Au} = 1.8 nm, respectively, which are considerably larger than in the Au/Si_3N_4 system (~$2x10^{12}$ NP/cm^2), in agreement with the smaller NP size. Higher NP density in the Au/ZnO system agrees with the shorter average in-plane interparticle distances (L), also included in the table. For instance, L = 4.8 nm has been estimated for the Au/ZnO sample with t_{Au} = 1.8 nm, while nearly double separation (L = 8.3 nm) was found for the Au/Si_3N_4 sample with t_{Au} = 1.6 nm. The NP density has been calculated here in the same manner, by the total number of Au atoms measured by RBS (at/cm^2) divided by the number of atoms per NP obtained from the volume calculated with the diameter ϕ, measured by GISAXS and the Au atomic density of $5.9x10^{22}$ at/cm^3.

Table C.2.IV Structural characterization of samples with Au NP growth: XRR-obtained bilayer thickness (XRR-Λ), GISAXS-obtained bilayer thickness (GISAXS-Λ), Au NP average diameter obtained by XRD (XRD-ϕ) and by GISAXS (GISAXS-ϕ). Au-layer NP density (NP/cm^2) has been calculated using GISAXS-ϕ, the number of Au atoms per cm^2 (RBS) and Au atomic density (ρ_{Au} = $5.9x10^{22}$ at/cm^3). In-plane interparticle distance (L) has been obtained from Au NPs density and considering both square and hexagonal NP arranges. The given L value corresponds to the average.

Sample	XRR-Λ (nm)	GISAXS-Λ (nm)	XRD-ϕ (nm)	GISAXS-ϕ (nm)	Au NPs (NP/cm^2)	L (nm)
$[ZnO_{(3nm)}/Au_{(2.4nm)}]_{40}$	5	4.9	2.8	4.7	$4.4x10^{12}$	6.0
$[ZnO_{(3nm)}/Au_{(1.8nm)}]_{75}$	5	4.8	2.7	3.7	$6.8x10^{12}$	4.8

Regarding the structural parameters summarized in the table, it can be noticed, similarly to what we observed for Au NPs in Si_3N_4, that Au NPs are also separated in plane by a value close to 3/2 of ϕ distance for both Au/ZnO samples. For each sample, the obtained average in-plane interparticle distance (L) and out-of-plane periodicity (Λ) have again similar values (about 5 nm in this case).

C.2.8. UV-VIS Absorption

Au NPs samples on quartz substrates were used to measure sample optical absorption in transmission mode. The optical absorption of these films was measured with a Cary 4000 UV-vis spectrophotometer at the ICMM, in the 200–900 nm ultraviolet-visible range.

Fig. C.2.8(a) shows the optical density spectra as a function of wavelength of samples with t_{Au} ranging from 7.8 to 2.4 nm. The absorption coefficient spectra are also given in Fig. C.2.8(b) for further comparison. The spectrum of sample with t_{Au} = 1.8 nm (75 bilayers) has not been included since its optical density results too high to be accurately measured. Optical absorption from a ZnO film has been included for comparison. For these samples, differing from the Au/Si_3N_4 system, no surface plasmon resonance (SPR) is observed. For the particular case of t_{Au} = 2.4 nm sample, for what Au NP formation ($\phi \sim 4$ nm) was pointed by GISAXS, absorption at higher wavelengths slightly differs from the other samples, where continuous Au/ZnO layers are expected. Nonetheless, SPR is not observed in the Au/ZnO samples. The absence of SPR in these as-grown samples agrees with the results recently reported by Sangpour et al.[4] about gold NPs formation in co-sputtered Au-SiO_2 thin films, where no absorption peak was observed for the as-deposited films. A broad SPR absorption band appeared after annealing at 800°C, leading to Au NP of about 30 nm size uniformly distributed on the surface.

Taking into consideration all the obtained results, it appears that for Au/ZnO samples with t_{Au} = 1.8 nm and 2.4 nm, the Au NPs pointed out by GISAXS might be in fact not as well formed as expected.

The situation could be related to the one recently observed by Lee et al. for Au and Ag-ZnO composite nanocrystals prepared by solution-phase synthesis.[5] They found that the noble metal-ZnO systems do not form a core-shell structure despite the small lattice parameter difference between Au (or Ag) and ZnO. Conversely, a dumbbell-like structure was evidenced by HRTEM studies, being the average sizes in this case ~ 4 and ~ 10 nm for the noble metals and the ZnO.

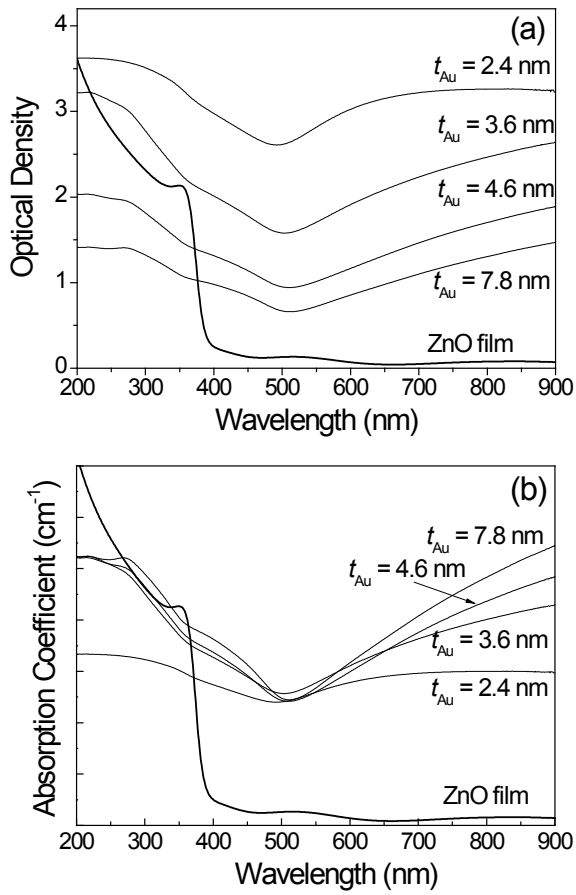

Fig. C.2.8 Optical density (a) and absorption coefficient (b) spectra of Au/ZnO samples with t_{Au} = 7.8 nm, 4.6 nm, 3.6 nm and 2.4 nm (ϕ = 5.1 nm). A sputtered ZnO film has been included for comparison.

The suggested mechanism for the formation of Au- and Ag-ZnO nanocrystals by this aqueous solution method is shown in Fig. C.2.9. They assigned the formation of dumbbell-like structures to differences in the crystalline structure between them. Due to the crystal structure mismatch (~17%), the interfacial energy would be too large, and thus to reduce the total free energy of the system, the dumbbell-like structure could form instead of core-shell structure.

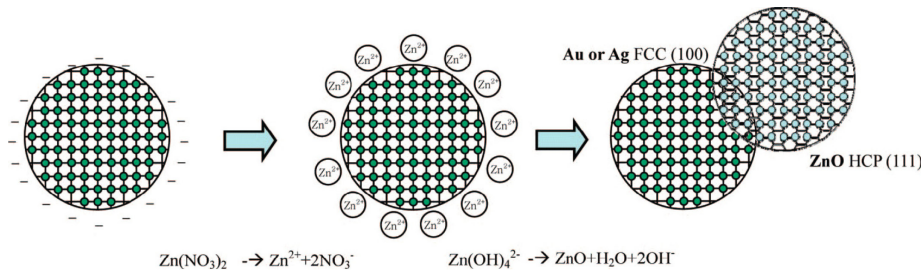

Fig. C.2.9 Mechanism for the formation of Au- and Ag-ZnO nanocrystals by solution-phase synthesis suggested by Lee et al.[5]

It should be noted that we cannot make direct comparisons since Au/ZnO preparation by sequential sputtering significantly differs from Au/ZnO growth by solution-phase synthesis. Nonetheless, the reported Au/ZnO tendency to dumbbell-like structures over core-shell ones might be associated with Au-ZnO interface tensions or defected interfacial regions in our samples that may lead to not very well formed Au NPs poorly distributed inside ZnO and nonappearance of SPR phenomenon. The existence of a significant Au-ZnO interaction at the interface has been evidenced by XRD experiments, which has shown i) declination of the ZnO crystallinity induced by the Au growth and ii) Au(111) texture favoured by the ZnO presence. Furthermore, XRR experiments have shown that out-of-plane periodicity gets declined for the Au/ZnO system compared to the Au/Si_3N_4 one for t_{Au} = 1.8 nm and 2.4 nm, evoking less well formed or worse organized Au NPs inside ZnO. Moreover, analysis of XRR-Λ values along the sample series has pointed out that formation of Au NPs is further favoured using Si_3N_4 than ZnO as matrix material by this preparation method since the transition from Au continuous layer to Au NP growth is much more abrupt as well as beginning from longer Au sputtering times in the case of Au/Si_3N_4 samples.

C.2.9. Conclusions

With the aim of growing Au NPs inside a different matrix with similar refractive index as Si_3N_4 in a controlled way, a series of Au/ZnO samples has been prepared by

sequential sputtering technique, keeping constant the ZnO layer thickness and modifying the effective Au layer thickness (t_{Au}).

A change in the Au-layer morphology with the deposited Au amount has been evidenced by XRR and GISAXS results. Continuous Au layers leading to multilayered samples have been found for $t_{Au} \geq 3.6$ nm, being the Au-layer continuous growth preserved until shorter Au-layer sputtering times than in the case of Au/ samples. Non-continuous Au-layers resulting in Au NPs inside the ZnO matrix have been evidenced for $t_{Au} = 2.4$ nm and 1.8 nm.

Smaller Au NPs have been obtained in ZnO than in the Si_3N_4 matrix. Average NP sizes between 5 – 4 nm have been found in ZnO compared to 7 – 5 nm in Si_3N_4. The Au NP density varies within the Au/ZnO series, ranging between $4x10^{12}$ NP/cm^2 and $7x10^{12}$ NP/cm^2, which are considerably larger than for the Si_3N_4 matrix (~$2x10^{12}$ NP/cm^2), according to smaller NP size and shorter average in-plane interparticle distances (L = 5 – 6 nm for ZnO versus L = 8 – 10 nm for Si_3N_4 matrix).

For the Au/ZnO samples, UV-vis absorption spectrum has not shown surface plasmon resonance (SPR) effect.

The absence of SPR phenomenon in these samples has been related to possible Au-ZnO interface tensions or defected interfacial regions in our samples that may lead to not very well formed Au NPs poorly distributed inside ZnO. Significant interaction at the Au-ZnO interface has been confirmed by XRD.

References

[1] S. Link and M. A. El-Sayed, J. Phys. Chem. B 103, 8410 (1999).

[2] L. Arlemao, D. Barreca, G. Bottaro, A. Gasparotto, S. Gross, C. Maragno, E. Tondello, Coordination Chemistry Reviews 250, 1294 (2006).

[3] E. Kotai, Nucl. Instrum. Methods B 85, 588 (1994).

[4] P. Sangpour, O. Akhavan, A. Z. Moshfegh, M. Roozbehi, Appl. Surf. Sci. 254, 286 (2007).

[5] M. Lee, T. G. Kim, W. Kim and Y. Sung, J. Phys. Chem. C 112, 10079 (2008).

GENERAL CONCLUSIONS

- Different series of Mn-Zn-O films have been prepared ($[Mn_{(t)}/ZnO_{(3nm)}]_n$ multilayers, $[MnO_{x(t)}/ZnO_{(3nm)}]_n$ multilayers and $Zn_{0.95}Mn_{0.05}O$ thin films) in order to gather further knowledge of the nature of the ferromagnetic ordering in this system. For all the samples series, room temperature ferromagnetism (RTFM) as well as an evolution of the magnetic response within each series have been observed. The sensitivity of the magnetic properties to the Mn oxidation state in each sample has been found a common characteristic is this study.

- For $[Mn_{(t)}/ZnO_{(3nm)}]_n$ multilayers, XANES studies have revealed absence of metallic Mn and that the average Mn oxidation state increases from +2.1 to +3.3 as the Mn layer thickness (t) diminishes. A weak ferromagnetic signal above room temperature has been found for multilayers with larger values of t while mostly paramagnetic-like signal has been found for samples with very thin Mn layers ($t \leq 0.7$ nm), where formation of amorphous MnO_2 clusters inside the ZnO matrix have been evidenced. For the obtained ferromagnetic samples ($t \geq 3$ nm), EXAFS, XANES, HRTEM and XRD have indicated the coexistence of Mn^{2+} in rocksalt (*RS*) and wurtzite (*W*) phases. Results suggest non-homogeneously intermixed layers, with Mn and Zn highly diffused into both ZnO and Mn oxide rich-regions, leading to both Zn-O-Mn (*W*-type) and Mn-O-Zn (*RS*-type) mixed phases. Saturation magnetization values scale with the Mn content in Zn-O-Mn (*W*-phase), what points at Mn^{2+} in ZnO wurtzite phase as the responsible of the weak ferromagnetic signal observed.

- For $[MnO_{x(t)}/ZnO_{(3nm)}]_{75}$ multilayers, $MnO_{2-\delta}$ nanograins embedded in *W*-ZnO (with Mn/Zn ratio about 4 at.%) have been obtained by oxidizing both Zn and Mn during growth. Stronger RTFM, with M_S values reaching 0.8 μ_B per Mn atom, has been found here, where results suggest ferromagnetism due to Mn^{3+} and Mn^{4+} interacting via double-exchange mechanism under the effect of the neighbouring

ZnO. The coexistence of Mn^{3+} and Mn^{4+} has been unambiguously confirmed by Mn K-edge and Mn $L_{3,2}$-edge measurements.

- These different approaches to the study of the role of interfaces and the Mn oxidation state in the Mn-Zn-O system have indicated two possible kinds of ferromagnetic interaction in this system, which are greatly influenced by the particular Mn oxidization or reduction process during growth. Reduction of an initially highly oxidized Mn phase by the surrounding ZnO effect has led to ferromagnetic order via double exchange. By contrast, just a small paramagnetic-like signal has been found in originally metallic Mn that highly oxidized during growth. For this former series, a FM signal has only been found when the average Mn oxidation state is close to +2, case where FM based on the magnetic interactions between the Mn^{2+} cations in a wurtzite Zn-O-Mn phase is suggested.

- RTFM due to Mn^{2+} in ZnO lattice forming Zn-O-Mn wurtzite phase has been also observed in Mn:ZnO films prepared by sputtering from a $Zn_{0.95}Mn_{0.05}O$ target, where a strong variation of the ferromagnetic response has been obtained by modifying the working gas type (Ar, Ar/N_2, Ar/O_2). The highest M_S values have been obtained for the Ar– and Ar/N_2–prepared Mn:ZnO films and results are in agreement with RTFM ordering in n-type Mn:ZnO mediated by electron carriers. Both preparation using Ar/O_2 and post-deposition annealings in oxygen lead to highly oxidized Mn, close to Mn^{4+} and a significant reduction of the ferromagnetism.

- It has been found that improvement of the crystal quality of samples, oxidation of Mn during growth or after deposition as well as promoting rocksalt phase over the wurtzite one are common features leading to the weakening of the ferromagnetism in this system, whose origin is mostly associated with Mn^{2+} in *W*-ZnO. High oxidization of Mn during the early growth process only favours ferromagnetism under certain particular conditions, where surrounding ZnO seem to favour MnO_2 reduction and the interaction between Mn^{3+} and Mn^{4+} by double-exchange. These specific

conditions leading to RTFM by double-exchange mechanism have been found to be more difficult to stabilize than formation of the Zn-O-Mn *W*-phase. The coexistence of Mn^{3+} and Mn^{4+} is necessary but not sufficient for the FM ordering of the system.

- Moreover, the magnetic, structural and electronic properties of Mn/Si_3N_4 multilayers have been studied in this work for the first time, reporting RTFM in this system. The origin of ferromagnetism here has been ascribed to the formation of a distorted non-centrosymmetric Mn_3N_2 phase with slightly shorter Mn-N distances. Changes in the unit cell volume have been commonly considered theoretically in order to promote transitions from the AFM ground state to a FM phase in manganese nitrides. XMCD has shown that the magnetism in the films is due to the Mn d^5 (Mn^{2+}) state and XANES calculations have confirmed the presence of a Mn_3N_2 phase with Mn T_d symmetry, what seems to be favored by the Si_3N_4 tetrahedral structure. An evolution of the magnetic properties within the sample series has been found depending on the Mn and Si_3N_4 layer thickness, explaining this variation in terms of the Mn_3N_2 phase.

- In addition, the growth of Au nanoparticles embedded in both ZnO and Si_3N_4 systems has been also studied by preparing Au/ZnO and Au/Si_3N_4 series by sequential sputtering. A change in the Au-layer morphology with the deposited Au amount has been evidenced by XRR and GISAXS in the two systems, obtaining Au NPs for $t_{Au} \leq 2.4$ mm in the ZnO matrix and for $t_{Au} \leq 2.9$ mm in the Si_3N_4 one. Average NP sizes between 5 - 4 nm have been found in ZnO compared to 7 - 5 nm in Si_3N_4. Au NP density ranges between $4x10^{12}$ NP/cm^2 and $7x10^{12}$ NP/cm^2 in the ZnO series, being considerably larger than in the Si_3N_4 matrix (~$2x10^{12}$ NP/cm^2), according to smaller NP size and shorter average in-plane interparticle distances for ZnO.

- For the Au/ZnO samples, surface plasmon resonance (SPR) effect has not been observed, fact that has been related to possible Au-ZnO interface tensions or

defected interfacial regions in our samples that may lead to not very well formed Au NPs poorly distributed inside ZnO.

- For the Au/Si_3N_4 samples, different Au NP distributions have been found by GISAXS, evidencing Au NPs (ϕ = 7 nm) with in-plane spatial correlation for t_{Au} = 2.9 nm sample while Au NPs (ϕ = 5 nm) without spatial correlation for t_{Au} = 1.6 nm. For both samples, UV-vis absorption has shown a surface plasmon resonance (SPR), which shifts towards longer wavelengths with increasing the Au-layer effective thickness, in agreement with theory. A variation of the SPR maximum with the effective Au-layer thickness has been obtained, what makes Au/Si_3N_4 system tunable for optical applications requiring a specific absorption spectrum.

CONCLUSIONES GENERALES

- Se han preparado distintas series de muestras del sistema Mn-Zn-O en forma de lámina delgada (multicapas $[Mn_{(t)}/ZnO_{(3nm)}]_n$, multicapas $[MnO_{x(t)}/ZnO_{(3nm)}]_n$ y láminas delgadas de tipo $Zn_{0.95}Mn_{0.05}O$) con el objetivo de lograr una mayor comprensión de la naturaleza del ordenamiento ferromagnético en este sistema. En todas las series de muestras estudiadas se ha observado ferromagnetismo a temperatura ambiente (RTFM) así como una evolución de la respuesta magnética en cada serie. Una característica común en todas las muestras estudiadas es la fuerte dependencia de las propiedades magnéticas con el estado de oxidación de Mn.

- En el caso de las multicapas denominadas $[Mn_{(t)}/ZnO_{(3nm)}]_n$, estudios de XANES han demostrado ausencia de Mn metálico en las muestras, así como un aumento del estado de oxidación promedio de Mn, de +2.1 a +3.3, a medida que disminuye el grosor de la capa de Mn (t) dentro de la serie. Las multicapas con los valores de t mayores presentan una pequeña señal ferromagnética a temperatura ambiente, mientras que únicamente una contribución de tipo paramagnético se ha observado en las muestras con capas de Mn muy delgadas ($t \leq 0.7$ nm), constituidas principalmente por agregados amorfos de MnO_2 en la matriz de ZnO. En las muestras ferromagnéticas, los estudios realizados mediante EXAFS, XANES, HRTEM y XRD muestran la coexistencia de Mn^{2+} en dos fases distintas, tipo cloruro sódico (*RS*) y wurtzita (*W*). Los resultados obtenidos sugieren la existencia de capas ricas en óxido de Mn (tipo *RS*) y ricas en ZnO (tipo *W*), en las que los fenómenos de interdifusión de Zn y Mn dan lugar a la formación de dos de dos fases mixtas no homogéneas denominadas Zn-O-Mn (*W*) y Mn-O-Zn (*RS*), que coexisten en estas muestras. Se ha encontrado que la imanación de saturación escala con la cantidad de Mn en la fase *W* (Zn-O-Mn), lo que apunta a que sólo el Mn^{2+} en ZnO con fase wurtzita es responsable de la pequeña señal ferromagnética observada.

- En el caso de las multicapas denominadas $[MnO_{x(t)}/ZnO_{(3nm)}]_{75}$, los estudios realizados muestran la formación de pequeños agregados de $MnO_{2-\delta}$ dentro de W-ZnO (en una relación Mn/Zn de aproximadamente 4 % at.) obtenidos mediante oxidación de Zn y de Mn durante el proceso de preparación. Se ha encontrado ferromagnetismo a temperatura ambiente, con valores de imanación de saturación (M_S) considerablemente mayores que en el caso anterior, alcanzando 0.8 μ_B por átomo de Mn. Los resultados apuntan a que el origen del ferromagnetismo en estas muestras reside en la interacción de doble-canje entre Mn^{3+} and Mn^{4+}, promovida por el efecto reductor del ZnO situado en las proximidades. La coexistencia de Mn^{3+} y Mn^{4+} ha sido corroborada mediante experimentos de XAS los bordes K y L del Mn.

- Las dos vías utilizadas para el estudio de los fenómenos de intercara y del estado de oxidación de Mn en el magnetismo del sistema Mn-Zn-O han puesto de manifiesto la posibilidad de dos tipos de interacciones ferromagnéticas distintas en este sistema, las cuales son muy dependientes del proceso particular de oxidación o reducción del Mn durante el crecimiento. Por un lado, la reducción de una fase de Mn altamente oxidada durante el depósito por el efecto del ZnO próximo se ha asociado con ferromagnetismo por doble-canje. A diferencia, Mn originariamente metálico que sufre una elevada oxidación durante el crecimiento únicamente presenta un comportamiento tipo paramagnético. Partiendo de Mn metálico, se ha encontrado orden ferromagnético únicamente en muestras con estados de oxidación promedio de Mn cercanos a +2, donde el ordenamiento ferromagnético se ha asociado con la interacción entre los cationes Mn^{2+} de una fase Zn-O-Mn tipo wurtzita.

- Se ha conseguido también ferromagnetismo a temperatura ambiente (RTFM) en muestras con Mn^{2+} en la red de ZnO formando una fase Zn-O-Mn tipo wurtzita en láminas de Mn:ZnO preparadas por pulverización de un blanco de composición $Zn_{0.95}Mn_{0.05}O$, en las que se ha observado una fuerte variación de la respuesta magnética en función del tipo de gas durante el depósito (Ar, Ar/N_2, Ar/O_2). Los valores de M_S más altos corresponden a las láminas de Mn:ZnO preparadas con Ar y

con Ar/N_2, en este orden, y los resultados obtenidos avalan la existencia de ferromagnetismo mediado por los electrones en muestras tipo n con Mn^{2+} diluido en ZnO. Tanto la preparación de láminas en atmósfera de Ar/O_2 como el recocido posterior de las muestras en atmósfera de oxígeno dan lugar a estado de oxidación promedio de Mn elevado, próximo a Mn^{4+} y una considerable reducción del ferromagnetismo.

- Factores como la mejora de la calidad cristalina de las muestras, la alta oxidación del Mn durante el crecimiento o tras la preparación, así como el aumento de fase tipo NaCl frente a wurtzita constituyen características comunes relacionadas con el deterioro del ferromagnetismo en este sistema, asociado principalmente a Mn^{2+} en *W*-ZnO.

- La alta oxidación inicial del Mn en el proceso de crecimiento únicamente favorece el ferromagnetismo en ciertas condiciones particulares, bajo las cuales el ZnO cercano al MnO_2 favorece la reducción del MnO_2 y la interacción entre Mn^{3+} y Mn^{4+} vía doble-canje. Sin embargo, los resultados obtenidos indican que las condiciones necesarias para lograr ordenamiento ferromagnético a través de doble-canje en este sistema son considerablemente más difíciles de estabilizar que la formación de Zn-O-Mn con fase wurtzita. La coexistencia de Mn^{3+} y Mn^{4+} no es suficiente para el ordenamiento ferromagnético del sistema.

- Por otro lado, las propiedades magnéticas, estructurales y electrónicas de multicapas de Mn/Si_3N_4 han sido estudiadas por vez primera, con la obtención de ferromagnetismo por encima de temperatura ambiente. El origen del ferromagnetismo se ha explicado mediante la formación de una fase no centro-simétrica y distorsionada de Mn_3N_2, con distancias Mn-N ligeramente inferiores a las existentes en Mn_3N_2, lo que está de acuerdo con las modificaciones del volumen de la celda unidad consideradas frecuentemente en estudios teóricos sobre transiciones entre estados fundamentales antiferromagnéticos y ferromagnéticos en nitruros de manganeso. XMCD ha demostrado que el magnetismo de estas muestras procede de Mn d^5 (Mn^{2+}) y cálculos de XANES han confirmado la presencia de la fase Mn_3N_2

con entorno de Mn no centrosimétrico, posiblemente favorecido por el ordenamiento tetraédrico de tipo Si-N_4 del Si_3N_4. Se ha observado una evolución de las propiedades magnéticas de las muestras al modificar los grosores de las capas de Mn y de Si_3N_4, explicando esta variación en función de la fase de Mn_3N_2 formada.

- Además, se han llevado a cabo estudios del crecimiento de nanopartículas (NPs) de Au en ambas matrices, ZnO y Si_3N_4, preparadas mediante sputtering secuencial. Estudios de XRR y GISAXS han mostrado un cambio en la morfología de la capa de Au en función de la cantidad de Au depositada, indicando formación de NPs de Au para $t_{Au} \leq 2.4$ nm, en el caso de ZnO, y para $t_{Au} \leq 2.9$ nm, en el caso de Si_3N_4. El tamaño promedio de las NPs de Au obtenidas es de 5-4 nm en la serie de ZnO y de 7-5 nm en la de Si_3N_4. La densidad de NPs de Au varía entre $4x10^{12}$ NP/cm^2 y $7x10^{12}$ NP/cm^2 en la serie de ZnO, siendo considerablemente más grande que en la serie de Si_3N_4 (~$2x10^{12}$ NP/cm^2), de acuerdo con el menor tamaño y la menor separación entre NPs en la matriz de ZnO.

- En el caso de las muestras Au/Si_3N_4, GISAXS ha evidenciado distintos tipos de distribución de las NPs, obteniéndose NPs de Au (ϕ = 7 nm) con correlación espacial en el plano para t_{Au} = 2.9 nm y NPs de Au (ϕ = 5 nm) sin correlación espacial para t_{Au} = 1.6 nm.

- Ambas distribuciones de Au/Si_3N_4 presentan resonancia de plasmón de superficie (SPR), desplazándose el máximo hacia longitudes de onda mayores al aumentar el grosor de la capa efectiva de Au, como predice la teoría. La variación obtenida en la posición del plasmón de superficie en función del grosor de Au efectivo pone de manifiesto el interés del sistema Au/Si_3N_4 en aplicaciones ópticas.

- En el caso de las muestras Au/ZnO, no se ha observado resonancia de plasmón de superficie (SPR), hecho que se ha relacionado con la existencia de tensiones o zonas defectuosas en las intercaras Au-ZnO, pudiendo dar lugar a NPs de Au peor formadas o distribuidas de manera inhomogénea dentro de la matriz.

Agradecimientos

Son muchas las personas que han contribuido de una u otra manera a la realización de este trabajo. A todas ellas quiero expresar mi más sincero agradecimiento.

En primer lugar a mi director de tesis, Carlos Prieto, por toda la dedicación, ilusión y esfuerzo puestos en este trabajo y por toda la ayuda, paciencia y confianza en mí a lo largo de estos años. Gracias, Carlos, siempre serás un referente para mí.

A Luisa Bausá, mi tutora, por su ayuda y disponibilidad.

Al grupo de investigación, Alicia de Andrés, Federico Mompeán, Rafa Jiménez y Mar García, por el apoyo recibido.

A todas las colaboraciones. Gracias a Agnès Traverse por la estancia en París, por tanta amabilidad y comprensión y por las aportaciones tanto científicas como personales. Gracias también a Johann y al grupo de CLIO. A Augusto Barrós y al Instituto de Engenharia Cerâmica e do Vidro por la estancia en Aveiro, por las medidas de TEM y por toda la ayuda ofrecida. A Javier García por las medidas y los análisis de RBS y NRA. A Jesús Chaboy por los cálculos de XANES. A Yves Huttel y a Elisa Román por las medidas de XPS. A Luisa Ruiz González y a José María González Calbet por las medidas de HRTEM. A Neil Telling y a Gerrit Van der Laan por los experimentos de XAS y de XMCD en el borde L. A Olivier Lyon y David Babonneau por las medidas y el análisis de GISAXS. A Ángel de Pablos por ayudarme con los blancos de sputtering. A Emiliano Fonda por su asistencia en SAMBA y a toda la gente de SpLine por su asistencia y apoyo en tantas ocasiones. Gracias, Germán Castro, por tu ayuda. Ha sido un placer colaborar con todos vosotros.

Al mejor becario mayor que se puede imaginar, Félix, incapaz de reflejar tanta gratitud, y a Merche, por su tan eficiente ayuda y por transmitir tanto entusiasmo.

A Ana, mi compañera de tesis y de tantos años, gracias por estar siempre ahí. A Isabel, María, Marisa, Jorge, Rocío, Edu, Ainhara, Raúl y Ainhoa, por hacer los días en el Instituto tan agradables. A Argelia, por la buena onda que nos diste. A Riccardo y los

"fotónicos", por los buenos ratos en el 004 y alrededores. A Jorge, Norbert y Luis Balo, por la ayuda con medidas y cacharreos de laboratorio varios. Al "Club Valdelatillas", al mejor personal trainer, Javi y al resto de más o menos sufridores, Mariano, Elvira, Lidia, Quique…gracias equipo por tantos buenos momentos, agujetas incluidas. Gracias también al Grupo de Teatro por tantas risas.

Gracias a todo el personal científico, técnico y administrativo del Instituto de Ciencia de Materiales y al CSIC, por la oportunidad de disfrutar una beca.

A mis compañeros de la Facultad (gracias Alberto por cuidarme tanto) incluidos los que ya no están (gracias Claudio, imposible olvidarte).

A mis compis de piso, las de siempre y los de ahora, mi pequeña familia de Meléndez, gracias por vuestra comprensión y por ese "buen rollito".

A mis amigas de la resi y a las de Albacete de toda la vida, por vuestro interés en mi trabajo durante todos estos años.

Al apoyo incondicional de toda mi familia. A mi hermana Ana, por tanta motivación, a la peque, a Toni y a mis hermanos Juanjo y Ernesto. Gracias Pepe, por tus consejos, y gracias Mamá, por darme muchísimo más que la vida.

Y gracias a ti, Emilio, por tu ayuda, por escucharme y por hacerme tan feliz cada día.

Tesis Doctoral - Madrid - 2009